Engineering synthetic and natural vesicular system for tumor-targeted drug delivery

by

Sagar Rayamajhi

B.Tech., Kathmandu University, Nepal, 2015

AN ABSTRACT OF A DISSERTATION

submitted in partial fulfillment of the requirements for the degree

DOCTOR OF PHILOSOPHY

Department of Chemistry
College of Arts and Sciences

KANSAS STATE UNIVERSITY
Manhattan, Kansas

2021

Abstract

Nanomedicine provides exciting opportunities to solve modern-world medical problems from disease diagnosis to therapy. From the first approved nanomedicine in 1995 against cancer, Doxil®, to the recent sensation, lipid nanoparticle-based mRNA vaccine against COVID-19, nanomedicine has come a long way to the state of becoming a platform medical technology. Toward this endeavor, this dissertation is focused on lipid-based vesicles systems, synthetic liposomes, and cell-secreted extracellular vesicles (EVs), where we have explored and optimized efficient engineering techniques to achieve tumor-targeted drug delivery and diagnostic capacity. Liposomes are synthetic vesicles with an aqueous core and phospholipid bilayer and EVs are natural vesicles secreted by cells with protein-lipid bilayer and aqueous core carrying cellular information in terms of proteins and nucleic acid (mRNA, miRNA, DNA). These complementary properties when paired make them highly efficient delivery vehicles in a biological environment, an overarching goal of this dissertation.

The main objective of this dissertation is to overcome two major challenges in nanoparticulate drug delivery system: 1) how to overcome endosome degradation of nanoparticles and maximize intracellular bioavailability and 2) how to overcome biological barriers for efficient delivery- rapid immune clearance, circulation stability, epithelial barriers, microenvironment barriers, cellular, and intracellular barriers. Toward this aim, we engineered a pH-sensitive liposome with pH-responsive 3ß-[N-(N',N'-dimethylaminoethane)-carbamoyl] (DC) moiety to avoid endosomal degradation. pH-sensitive liposome showed pH-responsive cationic properties which elevated the fusogenic characteristic of liposome at the acidic environment in the endosomes and facilitate endosomal escape via membrane fusion (**Chapter 3**). Although the in-vitro results were promising, the challenge to overcome the biological barrier remains. To overcome this

problem, a natural messenger of the cellular system, which has been optimized with years of evolution, EVs, was used. We optimized a simple, efficient, and reproducible EVs isolation method by combining centrifugation, ultrafiltration, and size exclusion-based chromatography. Synthetic liposomes were used to engineer an EVs-based hybrid system that contributed to increasing overall yield, stability, and added functionality (**Chapter 4**). EVs derived from mouse macrophage J774A.1 showed preferential interaction toward cancer cells, both in vitro and in vivo mouse models showing promises for tumor-targeted drug delivery. Further, a gadolinium incorporated liposome was synthesized and hybridized with EVs to engineer a hybrid system with diagnostic capacity, which showed contrast-enhanced diagnostic characteristics as confirmed by clinical magnetic resonance imaging (**Chapter 5**). Finally, EVs were optimized for their reproducibility of physicochemical and functional properties. Rigorous EVs isolation technique and characterization confirmed the EVs production is significantly higher in cancer cells compared to non-cancer (**Chapter 6**). The nanosystems engineered in this study were successful to overcome endosomal degradation via escape, have longer retention time, good biocompatibility, efficient drug loading capacity, and tumor targeting characteristic, all of which are excellent properties for drug delivery systems. With this proof of concept and design consideration, this dissertation adds an important understanding of the vesicles-based system for tumor-targeted drug delivery. We envision that future works on the molecular mechanism behind the achieved biomimicry and tumor targeting potential can lead toward the translation of a vesicle-based system for tumor-targeted drug delivery.

Engineering synthetic and natural vesicular system for tumor-targeted drug delivery

by

Sagar Rayamajhi

B.Tech., Kathmandu University, Nepal, 2015

A DISSERTATION

submitted in partial fulfillment of the requirements for the degree

DOCTOR OF PHILOSOPHY

Department of Chemistry
College of Arts and Sciences

KANSAS STATE UNIVERSITY
Manhattan, Kansas

2021

Approved by:

Major Professor
Santosh Aryal

Copyright

Abstract

Nanomedicine provides exciting opportunities to solve modern-world medical problems from disease diagnosis to therapy. From the first approved nanomedicine in 1995 against cancer, Doxil®, to the recent sensation, lipid nanoparticle-based mRNA vaccine against COVID-19, nanomedicine has come a long way to the state of becoming a platform medical technology. Toward this endeavor, this dissertation is focused on lipid-based vesicles systems, synthetic liposomes, and cell-secreted extracellular vesicles (EVs), where we have explored and optimized efficient engineering techniques to achieve tumor-targeted drug delivery and diagnostic capacity. Liposomes are synthetic vesicles with an aqueous core and phospholipid bilayer and EVs are natural vesicles secreted by cells with protein-lipid bilayer and aqueous core carrying cellular information in terms of proteins and nucleic acid (mRNA, miRNA, DNA). These complementary properties when paired make them highly efficient delivery vehicles in a biological environment, an overarching goal of this dissertation.

The main objective of this dissertation is to overcome two major challenges in nanoparticulate drug delivery system: 1) how to overcome endosome degradation of nanoparticles and maximize intracellular bioavailability and 2) how to overcome biological barriers for efficient delivery- rapid immune clearance, circulation stability, epithelial barriers, microenvironment barriers, cellular, and intracellular barriers. Toward this aim, we engineered a pH-sensitive liposome with pH-responsive 3ß-[N-(N',N'-dimethylaminoethane)-carbamoyl] (DC) moiety to avoid endosomal degradation. pH-sensitive liposome showed pH-responsive cationic properties which elevated the fusogenic characteristic of liposome at the acidic environment in the endosomes and facilitate endosomal escape via membrane fusion (**Chapter 3**). Although the in-vitro results were promising, the challenge to overcome the biological barrier remains. To overcome this

problem, a natural messenger of the cellular system, which has been optimized with years of evolution, EVs, was used. We optimized a simple, efficient, and reproducible EVs isolation method by combining centrifugation, ultrafiltration, and size exclusion-based chromatography. Synthetic liposomes were used to engineer an EVs-based hybrid system that contributed to increasing overall yield, stability, and added functionality (**Chapter 4**). EVs derived from mouse macrophage J774A.1 showed preferential interaction toward cancer cells, both in vitro and in vivo mouse models showing promises for tumor-targeted drug delivery. Further, a gadolinium incorporated liposome was synthesized and hybridized with EVs to engineer a hybrid system with diagnostic capacity, which showed contrast-enhanced diagnostic characteristics as confirmed by clinical magnetic resonance imaging (**Chapter 5**). Finally, EVs were optimized for their reproducibility of physicochemical and functional properties. Rigorous EVs isolation technique and characterization confirmed the EVs production is significantly higher in cancer cells compared to non-cancer (**Chapter 6**). The nanosystems engineered in this study were successful to overcome endosomal degradation via escape, have longer retention time, good biocompatibility, efficient drug loading capacity, and tumor targeting characteristic, all of which are excellent properties for drug delivery systems. With this proof of concept and design consideration, this dissertation adds an important understanding of the vesicles-based system for tumor-targeted drug delivery. We envision that future works on the molecular mechanism behind the achieved biomimicry and tumor targeting potential can lead toward the translation of a vesicle-based system for tumor-targeted drug delivery.

Table of Contents

List of Figures

Acknowledgements

This journey has been both challenging and beautiful, which would not have been possible without persistence, perseverance, and patience, 3P's I say. I have acquired these traits from my parents, my mother **Januka Thapa,** and my father, **Bom Bahadur Rayamajhi**. Not from their words, but their action. I have seen their continuous hard work and dedication to me and my sister, Srijana Rayamajhi, for better education and life. This dissertation is for them, for their unconditional love and support, for their wisdom and hope, for their sacrifice and strength.

I would like to dedicate my dissertation to my advisor, **Dr. Santosh Aryal.** I feel lucky to have an advisor who is like a guardian, colleague, and mentor. Looking back to my first semester to now, I have grown, both on a personal and professional level, which is significantly contributed by the mentorship and guidance from Dr. Aryal. Directly and indirectly, I have learned tremendously from him. The amount of time Dr. Aryal has given to me to teach small things, from formatting in word, making figures in PowerPoints, to experimental techniques, and writing manuscripts and grants is tremendous, and I am forever indebted to him for all his efforts to help and guide me. I am also thankful to Dr. Aryal's lab members, Dr. Arunkumar Pitchaimani, Dr. Tuyen Nguyen, Dr. Ramesh Marasini, Colin Ferrel, Jessica Marchitto, and Cesar Aparicio. Thank you Tuyen and Ramesh for training me and teaching me various things during these years. I have learned directly and indirectly a lot from you. I would like to express my sincere gratitude towards my Ph.D. committee members: Dr. Paul Smith, Dr. Ryan Rafferty, Dr. Seong-O Choi, Dr. Stefan Bossmann, and Dr. Brian Lindshield for your valuable guidance in research and course-work throughout my Ph.D. program. I am thankful to faculty and staff member of the Department of Chemistry, Nanotechnology innovation center of Kansas State (NICKS), and Anatomy & Physiology for their help and support in many ways.

I would like to acknowledge all the teachers in my life, from my first teachers at home to school, and university. I am thankful to my undergraduate supervisor Dr. Gunjan Bisht and Dr. Bhupal Govinda Shrestha for their help and support during my undergraduate thesis at Kathmandu University. Especially, I am very thankful to Dr. Bisht for her encouragement and support to write a research manuscript. It was my first experience of writing and publishing research and review papers, which became a crucial part of my application process to grad school in the USA. I am also thankful to my undergraduate project members Biplab KC, Siddhi Nath Paudel, Deepak Karna, and Sandeep Adhikari for collectively completing projects despite unforeseen circumstances. This was crucial for me to pave my journey in grad school at Kansas State University.

I am also thankful to my family and friends. My sister Srijana Rayamajhi, brother in law Ram Chhetri, and my cute niece, Amayra Chhetri. I am always thankful for your unconditional love and support. I am thankful to my wife, Sabita Ranabhat. During this journey, you have become a beautiful addition to my life and I am forever lucky to have you. Thank you for your love, support, and strength. I cannot forget my friends, specially Jardine friends, my alcohol buddies without which my 3P's would not have worked. I would like to thank my past roommate, Rijesh Karmacharya, for many things, but mainly for teaching me how to cook. You taught me what my parents could not! I am thankful to all who have supported me directly and indirectly during this journey and will continue to work with the same dedication and effort in the future. Thank you!

Dedication

To my mother and father

Januka Thapa & Bom bahadur Rayamajhi

To my mentor

Dr. Santosh Aryal

To my wife

Sabita Ranbhat

Chapter 1 - Introduction

1.1 Concept of nanotechnology and nanomedicine

In 1956, Nobel laureate and theoretical physicist Professor Richard Feynman gave a talk "there is plenty of room at the bottom" at the annual American Physical Society meeting at Caltech.[1] This talk led to the conceptual foundation of "Nanotechnology" where Feynman discussed the idea of writing an entire encyclopedia on the tip of a nail, storing information on the atomic scale, miniaturizing the computer, and developing tiny machines for medical and industrial applications. Although not termed as nanotechnology, Feynman was leading down the foundation of nanotechnology through his groundbreaking concepts. Later on, in 1974, the term "nano-technology" was first used by Norio Taniguchi.[2] In 1981, the invention of a scanning tunneling microscope led to the visualization of individual atoms, providing a crucial characterization tool for nanotechnology. Encouraged by the Feynman concept, Eric Drexler published a book in 1986 using the "nanotechnology" term proposing the idea of nanoscale assembler.[3] These developments led to the emergence of nanotechnology as a field in the 1980s, almost 20 years later Feynman conceptual visualization. Today, nanotechnology is present in our everyday life from the clothes we wear, computer and mobile device we use, the medicine we take to the number of consumable products. According to the National Nanotechnology Initiative, "Nanotechnology is science, engineering, and technology conducted at the nanoscale".[4]

One of the many exciting applications of nanotechnology is in the field of medicine, thereby giving rise to "Nanomedicine". According to nature research, "Nanomedicine is a branch of medicine that applies the knowledge and tools of nanotechnology to the prevention and treatment of disease. Nanomedicine involves the use of nanoscale materials, such as biocompatible nanoparticles and nanorobots, for diagnosis, delivery, sensing or actuation purposes in a living

organism".[5] Nanomedicine aims to overcome the limitations of conventional pharmaceutical drugs by providing targeted delivery, ability to bypass complex natural barrier, tunable pharmacokinetics, and better safety and efficacy profile. Therefore, the use of nanomedicine as a drug delivery system (DDS) and diagnostic agents is gaining rapid attention in the scientific and medicinal community. Nanomedicine, owing to its nanosize, provides ample surface area to engineer for the desired outcome. For example, we can decorate nanomedicine with a targeting moiety to achieve targeted delivery, biocompatible coatings to avoid immune clearance, and biomimicry agents to deceive the cellular system. This flexibility in engineering nanomedicine is key to develop an effective drug delivery system.

1.2 Nanomedicine in drug delivery system

The discovery of therapeutic drugs is a milestone in human civilization which has now saved millions of lives and increased the life expectancy of human populations. Although the use of plants as an herbal medicine dates back to the early days of human civilization, the discovery of modern therapeutic drugs started with the extraction of morphine from opium in 1806 as a pain medication by Friedrich Serturner.[6] The 1982 discovery of Penicillin as antibiotics by Alexander Fleming marks another milestone in the history of medicine.[7] Today, we have more than 7000 therapeutic drugs approved by the US food and drug administration (FDA) for human use. As the number of therapeutic drug use increased, concerns about its side effects and off-target toxicity evolved as major challenges. This gave rise to a search for an alternative strategy to improve drug delivery. The conventional noninvasive oral, transdermal, or topical route of drug delivery is simple and easy to administer, however, limits the bioavailability of drugs thereby limiting the therapeutic efficacy. Oral delivery of drugs often needs to face a harsh gastrointestinal environment. Similarly, free drugs administered through intravenous injection might be rapidly

degraded or cleared by the immune system thereby causing maximal deposition in the liver and spleen, with potentially toxic results, and minimum availability in the target site. To overcome these limitations of free drug and conventional delivery, the drug delivery system aims to encapsulate and solubilize the drugs in a protective delivery vehicle, an enveloped vehicle system, that can be tuned for targeted drug delivery and controlled drug release, thereby enhancing therapeutic efficacy.[8]

Various nanoparticle-based delivery vehicles are available as a drug delivery system like nanocrystal, vesicles, polymeric micelles, protein-based nanoparticles, dendrimers, carbon nanotubes, and polymer-drug conjugate.[9,10] When a therapeutic drug is incorporated in these nanoparticle-based delivery vehicles, we call them nanomedicines. Each of these vehicles has its advantages and limitations. Polymer-based nanoparticles have advantages of precise control of particle characteristic, payload flexibility, and easy surface modification, however, can be limited by the increased risk of particle aggregation and toxicity. Inorganic nanoparticles have advantages of unique electrical, magnetic, and optical properties, but can be limited by toxicity and solubility problems. Lipid-based nanoparticles have the advantages of formulation simplicity with a range of physicochemical properties, high bioavailability, payload flexibility, yet can be limited by low encapsulation efficiency.[11] In these scenarios, the selection of the nanoparticle platform should be done based upon the application and feasibility of optimizations to overcome the limitations.

This dissertation is focused on vesicles based nanomedicine for drug delivery and diagnosis. Structurally, vesicles are "core-shell" structures with an aqueous core surrounded by a bilayer shell.[12] The famous and widely used vesicles are liposomes. Liposomes are vesicles with an aqueous core and phospholipid bilayer. The amphiphilic characteristic of phospholipid gives rise to self-assembly in liposomes in an aqueous solution, where the hydrophilic polar head forms

the outer structure of the bilayer and hydrophobic lipid tails form the inner layer. Since its discovery in 1961 by Alec D Bangham, liposome has been the earliest and most widely studied vesicle system for drug delivery.[13] The attractive biological properties of liposome that makes them a desirable candidate for drug delivery are excellent biocompatibility, biologically inert, biodegradable, ability to entrap hydrophilic drugs in the aqueous core and hydrophobic drugs in the hydrophobic bilayer membrane, stability, easy preparation, and functionalization.[14] As a result, liposome-based nanomedicine was the first approved therapeutics for cancer treatment and represents a significant portion of clinically approved nanotherapeutics.[15] The first approved liposome-based nanomedicine was Doxil®, doxorubicin encapsulated liposome functionalized with Polyethylene glycol (PEG), which was approved in 1995 for ovarian cancer and AIDS-related Kaposi's sarcoma. Till now, there are at least 16 different liposomes based nanomedicine approved for clinical use with the latest one approved in 2017, where the FDA granted regular approval to a liposome-encapsulated combination of daunorubicin and cytarabine (VYXEOS, Jazz Pharmaceuticals, Inc.) for the treatment of adults with acute myelogenous leukemia (AML).[16,17] Additionally, there is around 30 liposome-based nanomedicine in active clinical trials.[17] Moreover, the recent lipid nanoparticle-based vaccine developed by Pfizer/BioNTech and Moderna against coronavirus disease 2019 (COVID-19) has further expanded the scope of lipid/liposome-based nanomedicine. These data suggest the successful translation of liposome-based drug delivery systems for the treatment of cancer and other diseases. However, the liposomal-based drug delivery system faces the challenges of rapid elimination from blood and accumulation in the reticuloendothelial cell system, primarily in the liver, and lacks the innate targeting property.[14] To overcome this challenge, liposomes are functionalized by a polymeric interface like PEG, which can prevent protein opsonization by creating a steric polymeric protecting layer over liposomes

thereby allowing for long circulation time. Likewise, functionalizing with targeting antibodies can provide targeting functionality. Such a synthetic approach has been successfully employed in the liposome-based approved medicine. It is however important to note the change in physiochemical properties with each chemical modification of liposomal system and how it affects the biomolecular corona interface in the physiological environment.

1.3 Extracellular vesicles as emerging drug delivery agent

As an alternative to synthetic vesicle system, cell-derived extracellular vesicles have emerged as a promising drug delivery system. Extracellular vesicles (EVs) are the naturally available delivery system of the cellular environment. Structurally, they are made up of lipid-protein bilayer with aqueous core carrying cellular information; proteins and nucleic acid (mRNA, miRNA, DNA). Cells secrete EVs as a normal cellular process to communicate between neighboring cells and distant cells. Hence, EVs are an ideal drug delivery candidate that naturally seeks to deliver its cargo. While previously thought as garbage disposal unit of the cell, it has been recently realized that EVs plays a crucial role in intra- and inter-cellular communication and has garnered rapid attention among researcher. The role of EVs in disease progression is now well-established. For example, cancer cell-derived EVs play a crucial role in metastases by regulating cellular processes like angiogenesis, coagulation, vascular leakiness, and reprogramming of host stromal cells for the formation of the pre-metastatic niche.[18] These functionalities of cancer cell-derived EVs can be exploited for the development of tumor-targeted diagnosis and therapeutic agents. In general, EVs have the potential to be used as biomarkers, diagnostic, therapeutic, and drug delivery agents. The major advantage of using EVs as drug delivery agents over contemporary DDS (liposomes, micelles, and polymer) is the endogenous presence of transmembrane proteins in EVs that contributes to the stability and functionality of EVs.

1.4 Scope, research questions, and implications of the dissertation

In this dissertation, we have used both the liposome and EVs based vesicular system for achieving tumor-targeted drug delivery and diagnosis (**Figure 1.1**). The dissertation has seven chapters: 1) Chapter 1 introduce the overall aspect of the dissertation, 2) Chapter 2 include a literature review focusing on the engineering approach of EVs, 3) Chapter 3 describes the formulation of pH-sensitive liposome-based drug delivery system for endosomal escape, 4)

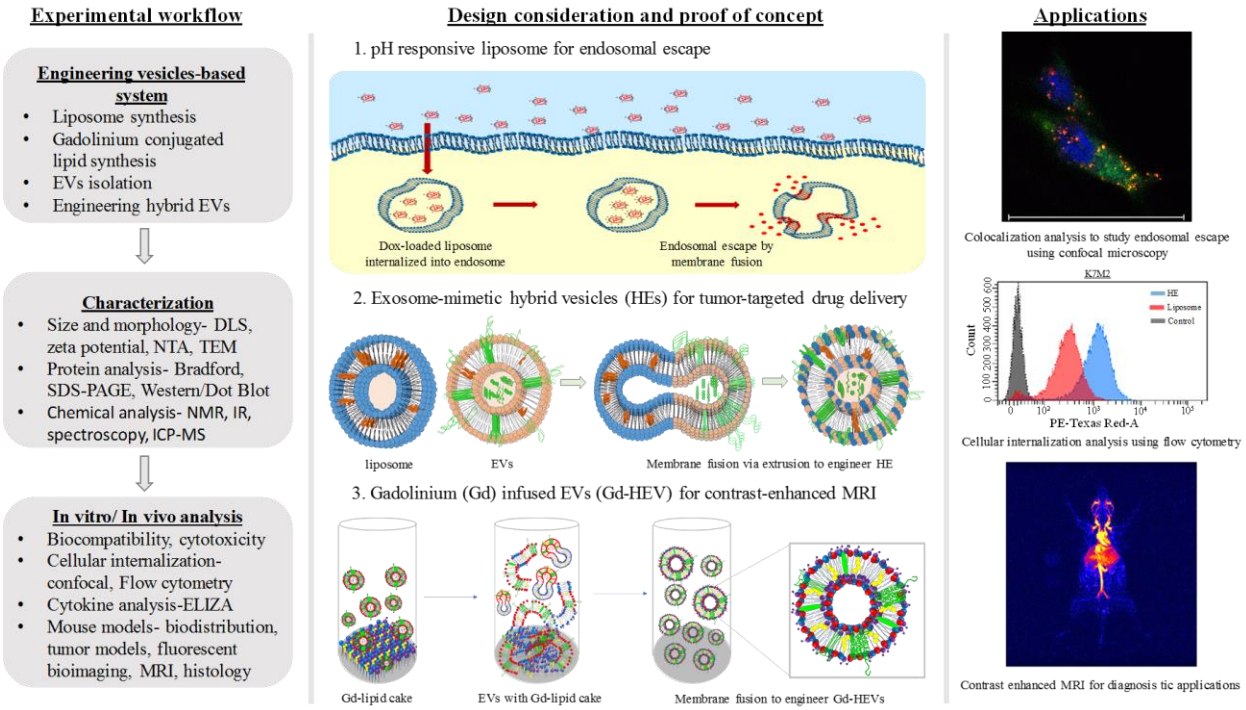

Figure 1.1 Scope of the dissertation. The general experimental workflow includes the engineering approach, characterization of engineered vesicles, and in vitro/in vivo analysis. Three major design considerations and proof of concept are presented to overcome the challenges in nanoparticulate drug delivery systems and to achieve tumor-targeted drug delivery and diagnostic potentials.

Chapter 4 discusses engineering of hybrid EVs for tumor-targeted drug delivery, 5) Chapter 5 discusses reconstruction of EVs as a magnetic resonance imaging contrast agent for cancer diagnosis, 6) Chapter 6 discusses the rigor and reproducibility of EVs production and functionality, and 7) Chapter 7 concludes the dissertation with overall summary and future outlook. In each

chapter, we have tried to address an important research question related to tumor-targeted drug delivery.

In the first research chapter, chapter 3, our research question is how to avoid the endosomal degradation of nanomedicine, which is one of the major biological barriers associated with the drug delivery system. Towards this direction, we formulated a pH-sensitive DC-liposome by using a 3ß-[N-(N',N'-dimethylaminoethane)-carbamoyl] cholesterol (DC-cholesterol). Due to the presence of DC-moiety in DC-liposome, it showed pH-responsive cationic properties with the elevation of surface charge in the acidic environment. This leads to elevated fusion behavior in an acidic environment thereby facilitating membrane fusion with the anionic endosomal membrane by electrostatic interaction, resulting in the endosomal escape and releasing the drug payload. Here, we exploited the chemistry of DC-moiety to achieve pH-dependent cationic property and the acidic environment of the endosome to achieve membrane fusion via electrostatic interaction.

Moving to our next chapter, Chapter 4, our research question was what if we used cell-derived natural vesicles derived from endogenous membrane compartment of cell (like endosome) that can naturally avoid endosomal degradation fate. For this purpose, we used EVs derived from mouse macrophage J774A.1. The reason for using an immune cell as an EV source was to exploit the cancer-targeting characteristic of immune cells. We hypothesized that EVs derived from immune cells will share the characteristic of parent cells to track and target cancers, owing to the similarity in surface protein contents. However, the application of EVs is limited by low yield and lack of membrane protein integrity due to the harsh ultracentrifugation based isolation method. To overcome this, we optimized an alternative centrifugation-ultrafiltration based method for EV isolation and hybridized it with synthetic liposome via extrusion-based membrane fusion. We called these hybrid vesicles as hybrid exosomes (HE). Further, we loaded anticancer drug,

Doxorubicin, and analyzed the tumor-targeted drug delivery potential of HE. The incorporation of liposomes in HE increased the overall yield of HE while maintaining stability and membrane integrity. Owing to the presence of EVs surface proteins, HE showed enhanced internalization toward cancer cells and HE-DOX showed higher cytotoxicity toward cancer cells compared to the normal one. This result provided proof of concept for HE to serve as a cancer-targeting drug delivery vehicle. Here, we exploited the EVs' natural surface membrane content for biomimicry and used liposome lipid content to enhance the overall yield of EV mimetic vesicles, which showed great potential for tumor-targeted drug delivery with enhanced therapeutic potential.

Next, in Chapter 5, our research question was if we can use EVs as a cancer diagnostic agent by precisely delivering diagnostic agent to the tumor. Towards this endeavor, we engineered a hybrid EVs system with a magnetic resonance imaging (MRI) contrast agent- gadolinium (Gd). We called these vesicles gadolinium infused hybrid extracellular vesicles (Gd-HEV). Gadolinium is a paramagnetic element capable of enhancing nuclear relaxation of neighboring water molecules, hence they are widely used as a bright contrast agent (T_1-agent) in clinical MRI. However, the use of commercially available Gd-based contrast agents like Magnevist® is now reporting significant toxicity issues due to nephrogenic systemic fibrosis (NSF). Also, due to the rapid elimination of CAs and low blood retention time, the dose required for clinically relevant contrast is continuously increasing. To solve these problems in CAs, which play a significant role in cancer diagnosis via MRI, we incorporated Gd in the liposome and hybridized with EVs to formulate Gd-HEV. We hypothesize that Gd-HEVs, owing to the presence of immune cell-derived EV protein cargo, can effectively disguise themselves as a biological entity, prolong the retention time for contrast enhancement, and show tumor specificity. Gd-HEV showed enhanced contrast property and higher blood retention time along with preferential accumulation toward cancer cells,

compared to Magnevist®. This result provided the proof of concept for EVs based hybrid system to be used as a tumor-targeted delivery agent for diagnosis.

In our last research chapter, chapter 6, our research question was about the rigor and reproducibility of EVs production and functionality. We observed a significant application of EVs in terms of tumor-targeted drug delivery and diagnostic agent. However, these functionalities are applicable as long as they are replicable efficiently. Although EVs make themselves a promising candidate for the DDS, EVs research may be limited by their heterologous functionality owing to their heterologous sub-populations. The different size and origin of these vesicles alter their functionality which can incredibly depend on the specific isolation procedures that dictate EV heterogeneity. Therefore, it is imperative to address the issue of reproducibility in EVs isolation and functionality to envision a realistic translational EVs research. Toward this attempt, we explored the rigor and reproducibility in EV production and functionality by varying certain parameters in the EV isolation process like incubation time and EV source (cancer vs non-cancer cell), in 3-5 independent replicate analysis. We used size exclusion chromatography to further purify EVs from possible contaminations of soluble proteins and analyzed the impact of purification in all different varying parameters.

In our concluding chapter, chapter 7, we have given concluding remarks and future implications of this dissertation. The major aim of the dissertation was focused on overcoming the two major challenges associated with nanoparticulate drug delivery system- 1) how to overcome endosome degradation of nanoparticles and maximize intracellular bioavailability and 2) how to overcome biological barriers for efficient and targeted delivery- rapid immune clearance, circulation stability, epithelial barriers, microenvironment barriers, cellular, and intracellular barriers. To achieve this aim, we designed two types of vesicular system- 1) a liposome responsive to pH environment for

endosomal escape and 2) EVs based hybrid system to achieve biomimicry and endogenous targeting functionality. By the design consideration of pH-responsive liposome and EV based hybrid system following surface functionalization and extrusion-based membrane fusion, we were able to formulate DC-liposome, HE, and Gd-HEV. These nanosystems successfully overcome endosomal degradation via escape, have longer retention time, good biocompatibility, efficient drug loading capacity, and tumor targeting characteristic, all of which are excellent properties for DDS. The research attempts in this dissertation adds an important understanding of vesicles based system for tumor-targeted drug delivery. We envision that future works on the molecular mechanism behind the achieved biomimicry and tumor targeting potential can lead toward the translation of vesicle based system for tumor-targeted drug delivery.

Chapter 2 - Literature Review: Surface functionalization strategies of extracellular vesicles

***Chapter 2**, in full, is a reprint of the material as it appears in Journal of Materials Chemistry B, 2020, Sagar Rayamajhi and Santosh Aryal. doi: 10.1039/D0TB00744G*

Abstract

Extracellular vesicles (EVs) are lipid-protein bilayer vesicular constructs secreted to the extracellular spaces by cells. All cells secrete EVs as a regular biological process that appears to be conserved throughout the evolution. Owing to the rich molecular cargo of EVs with specific lipid and protein content and documented role in cellular communication, EVs have been exploited as a versatile agent in the biomedical arena, including diagnostic, drug delivery, immunomodulatory, and therapeutic agents. With these multifaceted applications in the biomedical field, the functionalization of EVs to add diverse functionality has garnered rapid attention. EVs can be functionalized with exogenous imaging and targeting moiety that allows for the target specificity and the real-time tracking of EVs for diagnostic and therapeutic applications. Importantly, such added functionalities can be used to explore EVs biogenesis pathway and their role in cellular communication, which can lead to a better understanding of EVs cellular mechanisms and processes. In this report, we have reviewed existing EVs surface functionalization strategies and broadly classified them into three major approaches: physical, biological, and chemical approaches. The physical approach of EVs functionalization includes methods like sonication, extrusion, and freeze-thaw that can change the surface properties of EVs via membrane rearrangements. The biological approach discusses genetically and metabolically engineering cells to express protein or cargo molecule of interest in secreted EVs. The chemical approach includes different facile click type chemistries that can be used to covalently conjugate EVs lipid or protein

construct with different linker groups for diverse functionality. Different chemistry like thiol-maleimide, EDC/NHS, azide-alkyne cycloaddition, and amidation chemistry have been discussed to functionalize EVs. Finally, a comparative discussion of all approaches has been done focusing on the significances of each approach. The collective knowledge of the major approach of surface functionalization can be used to improve the limitation of one technique by combining it with another. An optimized surface functionalization approach developed accordingly can efficiently add required functionality to EVs while maintaining their natural integrity.

2.1 Background

Extracellular vesicles (EVs) are lipid and protein construct secreted by cells into extracellular spaces. Cells release EVs on a regular basis as a normal cellular process that appears to be conserved throughout evolution.[19] EVs biogenesis from cells has been observed in primitive unicellular prokaryotes to complex multicellular eukaryotes. The higher organism showed the presence of EVs in diverse body fluids, including blood, urine, saliva, breast milk, and semen.[20]

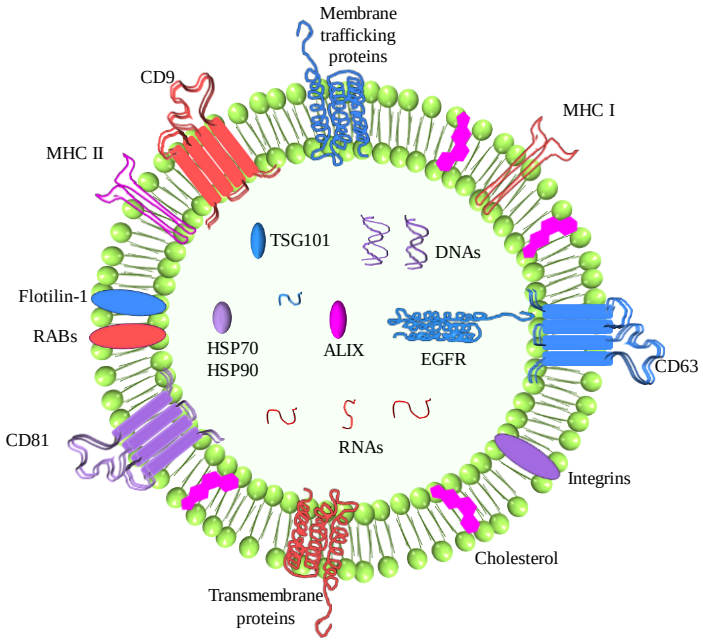

EV Cargo	
Lipids:	Sphingomyelin Phosphatidylserine Ceramide Cholesterol
Proteins:	Membrane transport/fusion protein (Annexin, flotillin, RABs) Transmembrane proteins (CD9, CD63, CD81) Antigen presentation proteins (MHC I, MHC II) Adhesion molecules (Integrin) ESCRT components Signal transduction proteins (EGFR) Cytoskeletal proteins (Actin, tubulin) Cytosolic proteins (histone, ribosomal proteins)
Nucleic acids:	mRNAs miRNAs Noncoding RNAs DNA

Figure 2.1 Schematic showing the structural components and cargo of extracellular vesicles.

EVs are released from the cell by characteristic biogenesis process which includes a cellular mechanism of formation of EVs and their release to extracellular spaces. While earlier thought as a garbage disposal process of the cell, it has now been realized that EVs play a crucial role in intra- and inter- cellular transfer of biomolecules and information. EVs carry cellular information in the form of protein and nucleic acids. The structural components of EVs include lipids, proteins, and nucleic acids (**Figure 2.1**). Common lipid components of EVs, which form the bilayer structural framework, include sphingomyelin, phosphatidylserine, ceramide, and cholesterol. The protein construct of EVs comprises of membrane proteins located in the transmembrane framework and soluble proteins residing in the aqueous core of EVs. These proteins include membrane transport/fusion proteins (annexin, flotillin, rab), transmembrane proteins (CD9, CD63, CD81), antigen presentation proteins (Major histocompatibility complex, MHC class I and II), adhesion molecules (integrins), endosomal sorting complex required for transport (ESCRT) components, signal transduction proteins (epidermal growth factor receptor, EFGR), cytoskeletal proteins (actin, cofilin, and tubulin), and cytosolic proteins (histone and ribosomal protein).[20] Nucleic acid cargo residing in the aqueous core of EVs includes messenger RNA (mRNA), microRNA (miRNA), and noncoding RNA which carries cellular information from the parent cells.

History of extracellular vesicles: from garbage disposal bag to key player in cell communication

EVs are recently experiencing explosive research interest and attention. The last ten years have seen multidisciplinary research interest in EVs from physical, biological, and chemical sciences (**Figure 2.2**). Although the research interest in EVs is recently realized, the discoveries of EVs date back to the early 1970s. EVs were initially reported in the literature in 1971 by Aaronson et al. where authors demonstrated the electron microscopy image of EVs secreted by the eukaryotic alga *Ochromonas Danica*.[21] Before 1971, although not termed as "extracellular vesicles", EVs were observed and reported as pro-coagulant platelets derived particle in 1946[22],

platelet dust in 1967[23], and matrix vesicles in 1969.[24] During this time, EVs were thought to be garbage disposal units of cellular systems and thereby were not attracting much research interest. Later in 1983, Rose Johnston, a pioneer in exosome (EVs) discovery, and Harding reported the release of transferrin receptor from erythrocyte into small vesicles. In 1987, Rose Johnston termed these small vesicles as "exosomes", which is now widely used to represent small EVs of endosomal origin. In 1996, Raposo et al. explored the immunological role of exosome with the discovery of the role of exosome secreted by B lymphocytes in adaptive immune response.[25] In 1998, Zitvogel et al. reported the role of dendritic cell-derived exosomes in the suppression of murine tumors in a T cell-dependent manner.[26] These studies slowly led to the exploration of EVs roles in cellular communication suggesting that they are not just garbage disposal bags of cells. Later, in 2006 and 2007, the discovery of exosome-mediated RNA and protein delivery from one cell to another strongly put forward the role of EVs (exosomes) in intercellular communication.[27,28] Along with this, roles of vesicles inside the cell has also been extensively studied to understand complex cellular transport mechanism. As a result, Ames E. Rothman, RandyW. Schekman and Thomas C. Südhof were awarded Nobel prize in physiology and medicine in 2013 for their discovery of the regulatory mechanism of the vesicular transport system, a major intracellular transport system.[29–31] All these pioneering studies led the foundation of EVs multifunctional roles in the cellular process thereby grasping multifaceted interest with around 94000 published articles mentioning "extracellular vesicles" term in PubMed central database as of now.

Currently, the number of EVs related immunization strategy against a variety of cancer are under clinical trials. According to the clinical trials database of NIH US national library of medicine, there are 43 ongoing phase clinical studies related to EVs and exosomes.[32] Recently, a

phase 2 clinical trial of vaccination with tumor-antigen loaded dendritic cell-derived exosomes (CSET 1437) was completed in 2018.[33,34]

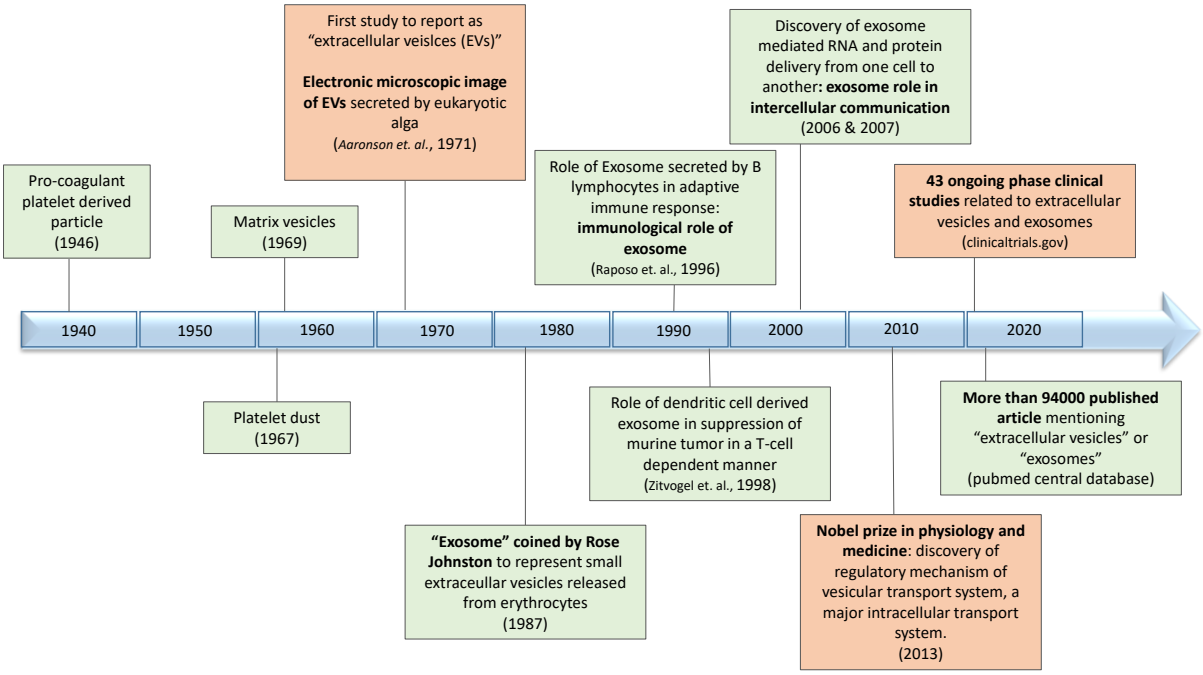

Figure 2.2 Timeline showing major events in the discovery and research of extracellular vesicles.

2.2 Extracellular vesicles classification and biogenesis

EVs can be broadly classified into exosomes, microvesicles, and apoptotic bodies based upon their origin and biogenesis. Exosomes are derived from the endosomal membrane, microvesicles are secreted by outward budding of the plasma membrane, and apoptotic bodies are formed from the plasma membrane during apoptosis.[35,36]. These vesicles vary significantly with their size. While exosomes are small EVs with a size less than 150 nm, microvesicles and apoptotic bodies size can range from 200 nm to 5 µm. Recent report suggests isolation of large extracellular vesicles, as big as 10 µm, referred to as large oncosomes, which can be categorized broadly in "microvesicles" subdivision of EVs.[37–39]Among these vesicles, special interest is towards exosome due to their specific biogenesis pathway that includes the endosomal origin and small size (50-150

nm). Exosome biogenesis includes regulated machinery of cargo sorting to form multivesicular bodies (MVB) from the inward invagination of the endosome. This process is reported to control by the endosomal sorting complex required for transport (ESCRT) machinery which includes around thirty proteins associated with four different ESCRT groups (ESCRT-0, -I, -II, and –III).[40] However, there have been reports of the formation of MVB in an ESCRT independent fashion.[41] In these cases, MVBs formations are found to be regulated by lipids (ceramide), tetraspanins (Cd63, CD81), and small integral membrane protein of lysosome and late endosome (SIMPLE).[40–43] This shows that MVB formation is the part of the exosome biogenesis process that occurs in both ESCRT dependent and ESCRT independent pathways. After the MVB formation, MVB can be fused with lysosome for degradation or in an alternative pathway, it fuses with plasma membrane thereby releasing the inner vesicular structure, exosomes, to extracellular spaces.[35] Different proteins are involved in the EVs secretion process. Proteins of ras-related proteins in brain (RAB) family, including RAB11, RAB35, RAB7, and RAB27, which are essential regulators of intracellular vesicular transport, are reported to be involved in exosome secretion process.[20] In the case of secretion of microvesicles, plasma membrane-derived EVs, ESCRT and ADP-ribosylation factor 6 (ARF6) proteins are involved.[20]

EVs are classified based upon their origin (endosome vs plasma membrane). Exosome represents endosomal derived EVs. However, it is practically very difficult to separate EVs based upon their origin as it is now evidently clearer that EVs populations are heterogeneous with lots of common protein markers.[44–47] Protein markers like CD63 and CD81 are generally represented as exosome markers and considered as proof of exosomes, which now are reported to be present in other EVs population as well.[44] Considering these factors, here, in this report, we are using "extracellular vesicles" term to represent exosomes and small EVs (size <200 nm), as per the

recommendation of minimal information for studies of extracellular vesicles 2018 (MISEV2018).[48]

2.3 EVs Surface functionalization strategies

EVs have innate functionality due to cellular origin. These vesicles have been reported to play a role in inter and intra-cellular communication.[49–53] EVs cargo consists of cellular information in terms of proteins and nucleic acid. The functional characteristic of EVs has made them a perfect candidate to be exploited in the biomedical field, as a biomarker, vehicles of immunotherapies, and therapeutic agents.[54–62] To further add desired functionality to these natural vesicles, different surface functionalization strategies have been explored which can be broadly classified into three major approaches: physical, chemical, and biological engineering methods (**Figure 2.3**).[63,64] These functionalization strategies have allowed for the added functionality in

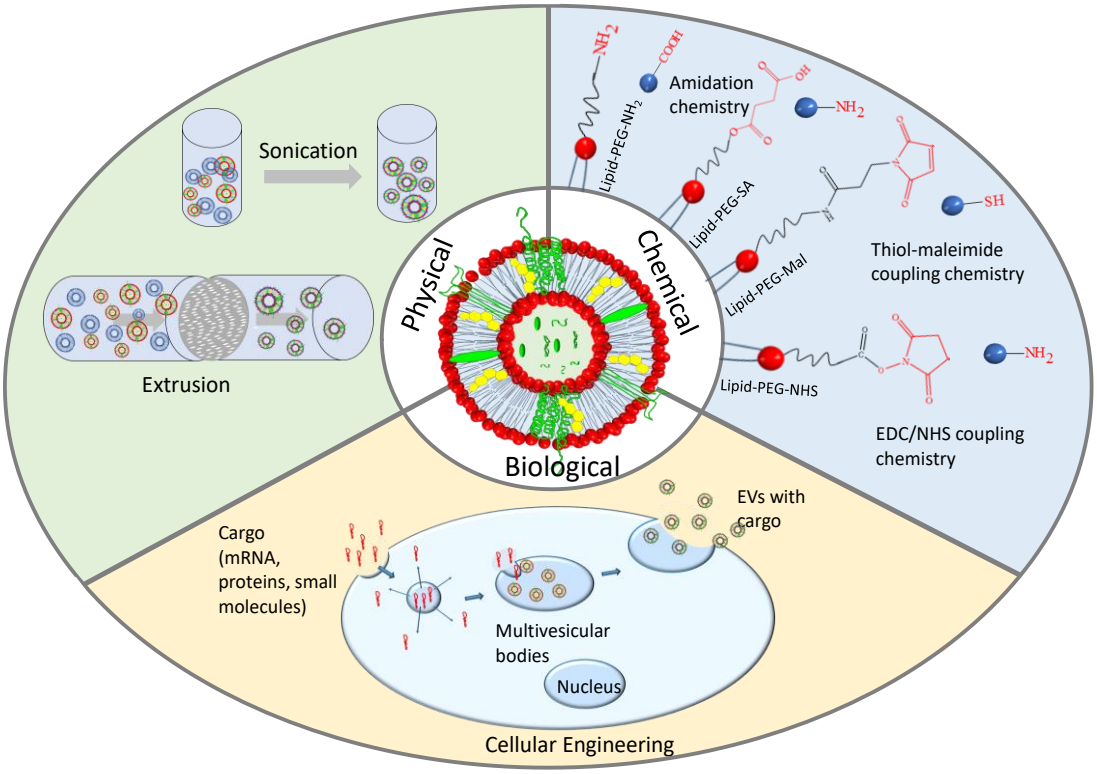

Figure 2.3 The surface functionalization capsule. Schematic showing physical, biological, and chemical strategies of surface functionalization of extracellular vesicles.

EVs while preserving the EVs membrane integrity. Some of the added functionality includes higher yield, fluorescent tags, imaging probes, immune-activating agents, and targeted therapeutic agents.[65–67] In this report, surface functionalization strategies of EVs using physical, biological, and chemical approaches will be explored independently. In the physical approach, physical methods like extrusion, sonication, and freeze-thaw will be explored for surface functionalization. Likewise, in the biological approach, EVs functionalization process by exploiting cellular machinery and EVs biogenesis process will be explored. Finally, in the chemical approach, EVs functionalization process using click chemistry like EDC/NHS chemistry and thiol-maleimide chemistry will be discussed.

2.3.1 Surface functionalization strategy: Physical method

The physical method of surface functionalization comprises of using physical force to change the surface construct of the EVs. The common method includes sonication, extrusion, and freeze-thaw, which by the physical force temporarily disrupts the lipid constructs of vesicles into their constituents. After the removal of the force, vesicles spontaneously self assembles into their natural structure. This characteristic of spontaneous self-assembly has been exploited in the surface functionalization of EVs.[65,68] Sato et al. reported functionalization of the surface of EVs by hybridizing it with PEGylated liposome using freeze-thaw facilitated membrane fusion (**Figure 2.4A**).[69] The freeze-thaw method briefly disrupts membrane construct by the temporary formation of ice crystals, thereby causing hydration-dependent phase changes and prompting membrane fusion.[69,70] The functionalization method adopted here allowed for the optimization of the properties of EVs surface to decrease their immunogenicity and increase colloidal stability, thereby improving the half-life of EVs in blood. Here, repeated freeze-thaw cycles were carried out by freezing the mixture in liquid nitrogen and thawing at room temperature, and the fusion process

was monitored by fluorescent resonance energy transfer. Although this method is simple and readily initiates membrane fusion, the repeated freeze-thaw cycle can damage the protein content of EVs.[71] Repeated changes in temperature associated with the freeze-thaw cycle can lead to the

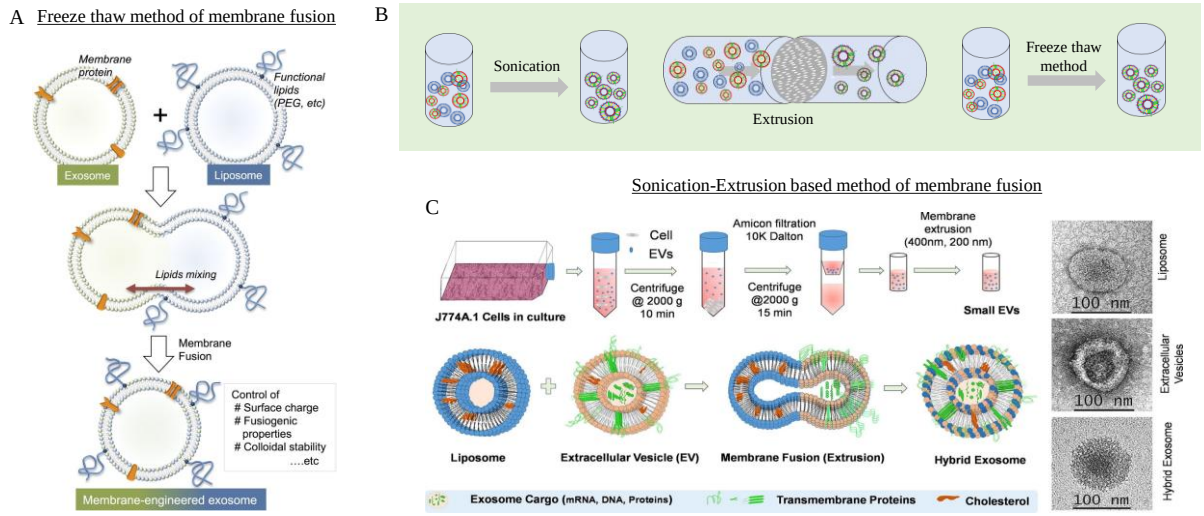

Figure 2.4 Surface functionalization strategies using physical methods. (A) Schematic showing the freeze–thaw method of membrane fusion. Reproduced from ref.[68] under the terms of Creative Commons CC BY license. Copyright 2016, Springer Nature, (B) schematic showing different physical methods for surface functionalization – sonication, extrusion, and freeze–thaw, and (C) schematic showing isolation of extracellular vesicles following the sonication–extrusion method of membrane fusion. Reproduced from S. Rayamajhi, T. D. T. Nguyen, R. Marasini and S. Aryal, Macrophage-derived exosome-mimetic hybrid vesicles for tumor-targeted drug delivery, Acta Biomater., 2019, 94, 482–494, with permission from Elsevier.[65]

denaturation of protein and therefore compromise the innate functionality of EVs. Study has shown that environmental changes like temperature and pH can alter the EVs protein content and internalization behavior, thereby changing the innate functionality of EVs.[72,73] As an alternative to this approach, we have explored the extrusion-based membrane fusion method in our recent work.[65,74] Here, EVs were hybridized with liposome using sonication followed by membrane extrusion process. This process facilitates membrane assembly by physically forcing the mixture through nanosize (400nm, 200nm, 100nm) polycarbonate membrane filter (**Figure 2.4**).[75,76] After the process is done, mixed vesicular structure self assembles to form hybrid EVs, with surface

characteristics from both liposomes and EVs. Here, the functionalization process followed increased the overall yield of EVs along with the incorporation of rhodamine B dye, which was used to track the cellular interaction of EVs *in vitro*. In another similar study, Javier et al. reported extrusion mediated hybridization of EVs with gadolinium infused liposome to formulate gadolinium infused EVs as a magnetic resonance imaging contrast agent (**Figure 2.5**).[77]

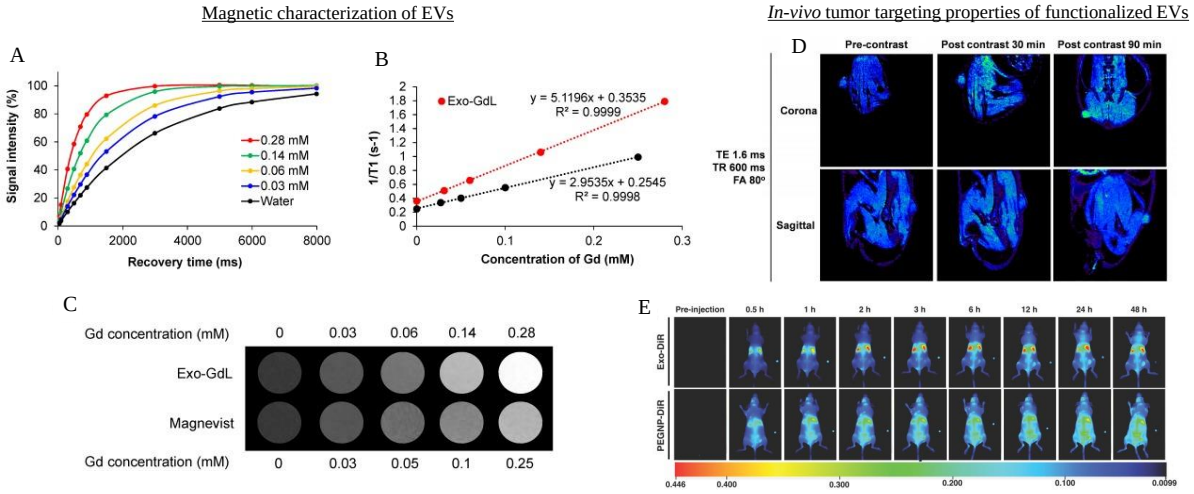

Figure 2.5 Evaluation of the magnetic properties and in vivo tumor targeting properties of surface-functionalized extracellular vesicles. (A) T_1 recovery curve of extracellular vesicles functionalized by the imaging agent gadolinium (Exo-GdL) at different concentrations of gadolinium, (B) longitudinal relaxivity (r_1) of Exo-GDL compared to the commercial contrast agent Magnevist. Exo-GdL shows a significant enhancement in r_1 as represented by the slope of the best fit line, (C) T_1 weighted image of Exo-GDL and Magnevist at different concentrations of gadolinium, (D) in vivo magnetic resonance imaging of Exo-GdL injected mice showing localization and enhancement of contrast in the tumor area, and (E) in vivo biodistribution of extracellular vesicles labeled with a near-infrared dye (Exo-DiR) showing significant localization in the tumor area compared to the control PEGylated nanoparticle. Reproduced and adapted from ref.[77] under the terms of the Creative Commons Attribution (CC BY-NC) license. The figure is adapted from three different figures from the original paper. Copyright 2019, Ivyspring International Publisher.

Gadolinium (Gd) is a widely used magnetic resonance imaging contrast agent.[78–81] With the incorporation of Gd in EVs using membrane fusion method, authors reported enhancement in the magnetic (relaxivity) and tumor-targeting properties, as confirmed by magnetic resonance imaging. They further incorporated near-infrared dye in the EVs construct using extrusion

mediated hydrophobic insertion strategy to track the biodistribution of EVs in *in-vivo* conditions. The surface-functionalized approach adopted in this study added a contrast agent and a fluorescent agent to the EVs, thereby allowing it's *in vitro* and *in vivo* tracking.[74,82]

Tamura et al reported surface functionalization of EVs with cationic polysaccharide polymer, pullulan, by simple incubation method facilitated by electrostatic interaction.[83] The EVs surface functionalized by cationic pullulan showed enhanced accumulation in hepatocellular carcinoma HepG2 cells *in vitro* compared to an unmodified one. Further functionalized EVs showed enhanced accumulation and anti-inflammatory effect *in vivo* in mice induced with liver injury, showing efficacy in the treatment of the liver injury. Another study by Sawada et al. reported surface functionalization of EVs with cationic nanogel CHP (ethylenediaimine modified cholesteryl pullulan) via the incubation method.[84] The amphiphilic cationic nanogel effectively preserves the functional integrity of EVs while enhancing internalization behavior. Polysaccharide based nanogel systems are an effective carrier for protein and nucleic acid delivery (siRNA).[85]

Here, the surface polymer engineering approach used to fabricate hybrid nanogel/EV system successfully deliver functional EVs into cells, as indicated by their ability to induce neuron-like differentiation in the recipient cells. Another study by Khvorova and group reported functionalization of EVs with cholesterol-conjugated, hydrophobically modified asymmetric siRNAs (hsiRNAs) via co-incubation for siRNA delivery.[86,87] hsiRNAs functionalized EVs were efficiently internalized by target cell and showed dose-dependent silencing of the target gene, while the size distribution and integrity of EVs remained intact.[86]

Significance of physical surface functionalization strategy

The physical method of surface functionalization allows for the simple reagent free functionalization of the EVs. Compared to biological and chemical approaches, it may be the

simplest approach without the need of additional reagent or cell-based system. The reagent free approach helps to maintain the integrity of EVs content while avoiding complex purification steps. Purifying EVs is one of the major challenges in this field and physical approach can give a major advantage by omitting this step. Along with that, the extrusion process applied in the physical approach can help to maintain the size homogeneity of EVs population, which is another important aspect in the application of EVs in the delivery field. However, one of the major disadvantages associated with the physical approach is the loss of internal cargo of EVs, which carry essential cellular information. Also, the physical approach of functionalization is limited to the application compared to a wide variety of functionalization strategies offered by a biological and chemical approach. However, can be beneficial to engineer the system where preservation of internal cargo is not necessary such as in surface functionalization of drug delivery vehicles with EVs membrane to target diseased cell as discussed by Pitchaimani et. al.[75] In this research, authors reported the selective extraction of natural killer cell-derived EVs surface membrane protein and lipid via sucrose gradient centrifugation and its integration with synthetic liposome to deliver anticancer doxorubicin to the tumor in a targeted fashion. Collectively, the physical approach can be used for quick labeling of EVs with imaging or fluorescent tag or can be used in combination with a chemical or biological approach to maintain the size homogeneity of EVs population after functionalization.

2.3.2 Surface functionalization strategy: Biological method

The biological approach for surface functionalization of EVs is a pre-production EVs engineering technique by genetically engineering cells to express proteins/cargo of interest. This method exploits cellular machinery, along with EVs biogenesis process to engineer surface characteristics of EVs (**Figure 2.6**). Generally, in this approach, cells are loaded with expression

vectors (plasmid/virus) with chimeric gene/protein which contains genes/proteins that will be part of EVs (CD63, CD9, CD81, Lamp2b) fused with a protein of interest. These chimeric genes/proteins are expressed in a cell and due to the presence of EVs related protein, they become a part of EVs and are present in secreted EVs. Exploiting this method, EVs have been functionalized with different moiety for various functionality.

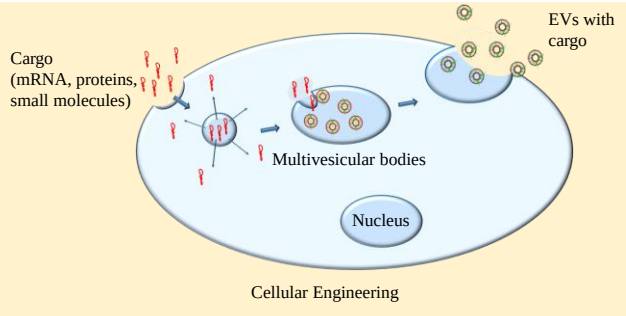

Figure 2.6 Schematic showing the functionalization strategy of extracellular vesicles using the biological approach. EVs are pre-engineered by cellular engineering of the parent cell. Cargo molecules like mRNA, proteins, and small molecules are incubated with cells which will eventually be a part of EVs.

Zachary et al. reported the development of EVs surface display technology using a biological surface functionalization method (**Figure 2.7**).[67] For this, they selected one of the highly expressed surface proteins in EVs: tetraspanins. Tetraspanins are transmembrane proteins that transverse four times in membrane with definite intra- and extra-vesicular domains.[88] CD9, CD63, and CD81 are the most common transmembrane proteins present in EVs. These proteins can be genetically engineered to display specific protein/molecule in the surface for various biological functions. Zachary et al. fused these transmembrane proteins with fluorescent reporter proteins (green fluorescent protein GFP and red fluorescent protein RFP) and expressed them in human cells, thereby creating a surface display technology for EVs. Transfected cells expressed the fluorescent signal in the endocytic region of cell suggesting successful expression of the expression vector. Further, CD63 was genetically engineered to express fluorescent reporter protein GFP in the intra-vesicular domain at the C-terminal of CD63 and RFP in the extra-vesicular domain (**Figure 2.7A**). The engineered CD63 with a dual fluorescent reporter can have dual functionality-

intravesicular GFP can explore the correct anchoring of protein in EVs membrane while extra vesicular RFP can explore different protein-protein interactions. This dual engineering method can be beneficial in accurate EVs tracking and imaging, thereby exploring the processes of EVs

Surface display using CD63 molecular scaffold

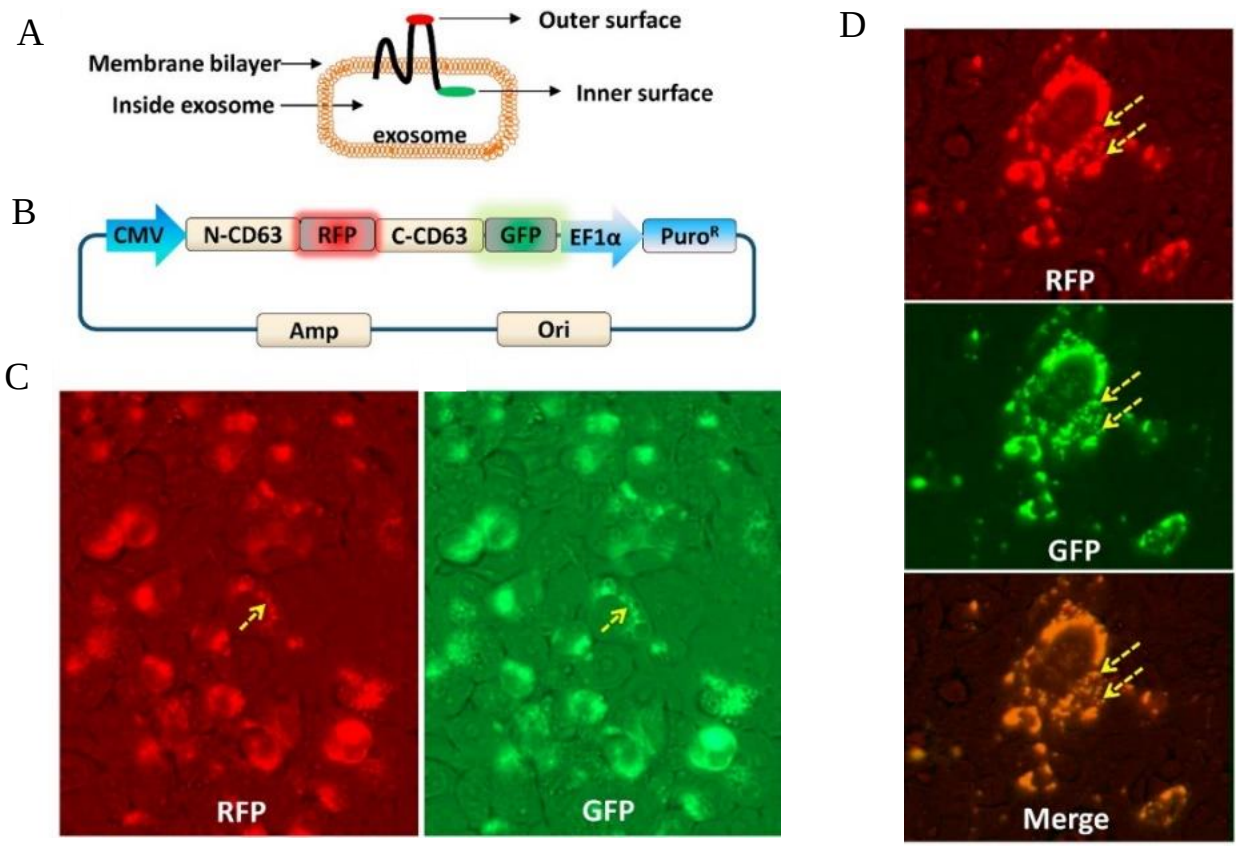

Figure 2.7 EVs' surface display using the CD63 molecular scaffold. (A) Schematic of the CD63 scaffold docking RFP to the outer and GFP to the inner vesicular space, (B) DNA construct of CD63 fusion protein with dual fluorescent markers, (C) fluorescent marker localization in HEK293 cells, and (D) colocalization analysis showing colocalization of displayed RFP and GFP in the merged figure in HEK293 cells 72 h after incubation. Reprinted and adapted from Z. Stickney, J. Losacco, S. McDevitt, Z. Zhang and B. Lu, Development of exosome surface display technology in living human cells, Biochem. Biophys. Res. Commun., 2016, 472, 53–59, with permission from Elsevier.[67]

biogenesis and release. More importantly, the choice of using CD63 as an anchoring scaffold allows simultaneous outer and inner surface engineering thereby allowing to add dual functionality, e.g. inner vesicular domain for drug packaging and outer vesicular domain for tissue

targeting. Finally, the authors showed engineered stable cell lines express CD63-GFP and secrete surface-displayed EVs. Here, EVs were engineered before their production by genetically engineering the cell exploiting the cellular machinery of EVs biogenesis. This study provided a proof-of-concept of pre-production engineering of EVs to display cargo of interest in EVs surface with potential applications in EVs tracking and imaging, protein-protein interaction, targeted drug delivery, and therapeutics.

In another study, Yim et al. developed an optogenetically engineered EV system called EXPLORs (exosome for protein loading via optically reversible protein-protein interaction) by exploiting the biological method of surface functionalization for intracellular protein delivery.[89] This novel method which uses light-based reversible protein-protein interaction for controlled loading and release of protein can overcome the current limitation in intracellular protein delivery method and protein therapeutics. Current protein therapeutics (cytokines, hormones, and monoclonal antibodies) are limited by the extracellular mechanism of action of proteins as intracellular delivery is challenging.[89] The existing method for intracellular protein delivery includes protein transduction and lipid nanoparticle-mediated protein delivery. These methods are limited by various factors, such as exposure of protein in solution, low refolding rate of recombinant proteins in target cells, lack of proper separation mechanism between protein cargo and lipid nanoparticles, and complicated protein purification steps.

Here, authors have used a photoreceptor cryptochrome 2 (CRY2) as a photosensitive agent, and CRY interacting basic-helix-loop-helix 1 (CIB1) protein module. CRY2 is activated by blue light, which on activation docks with CIB 1. This docking is light-dependent, thereby allowing for CRY2 to dock with CIB1 in the presence of light and release from CIB1 in absence of light. Authors have exploited this light-dependent reversible docking mechanism of CRY2-CIB1 to load

proteins in EVs in a controlled and reversible manner (**Figure 2.8B**). For this, they have genetically engineered DNA constructs with CRY2 genes fused with cargo protein mCherry (mCherry-CRY2), and another DNA construct with CIBN (a truncated version of CIB1) genes fused with an enhanced green fluorescent protein (EGFP) and CD9, a transmembrane protein expressed in EVs (**Figure 2.8A**). When these DNA constructs are expressed in a cell, CIBN-EGFP-CD9 will be expressed in the endosomal membrane and mCherry-CRY2 will be expressed in the cytosol. The

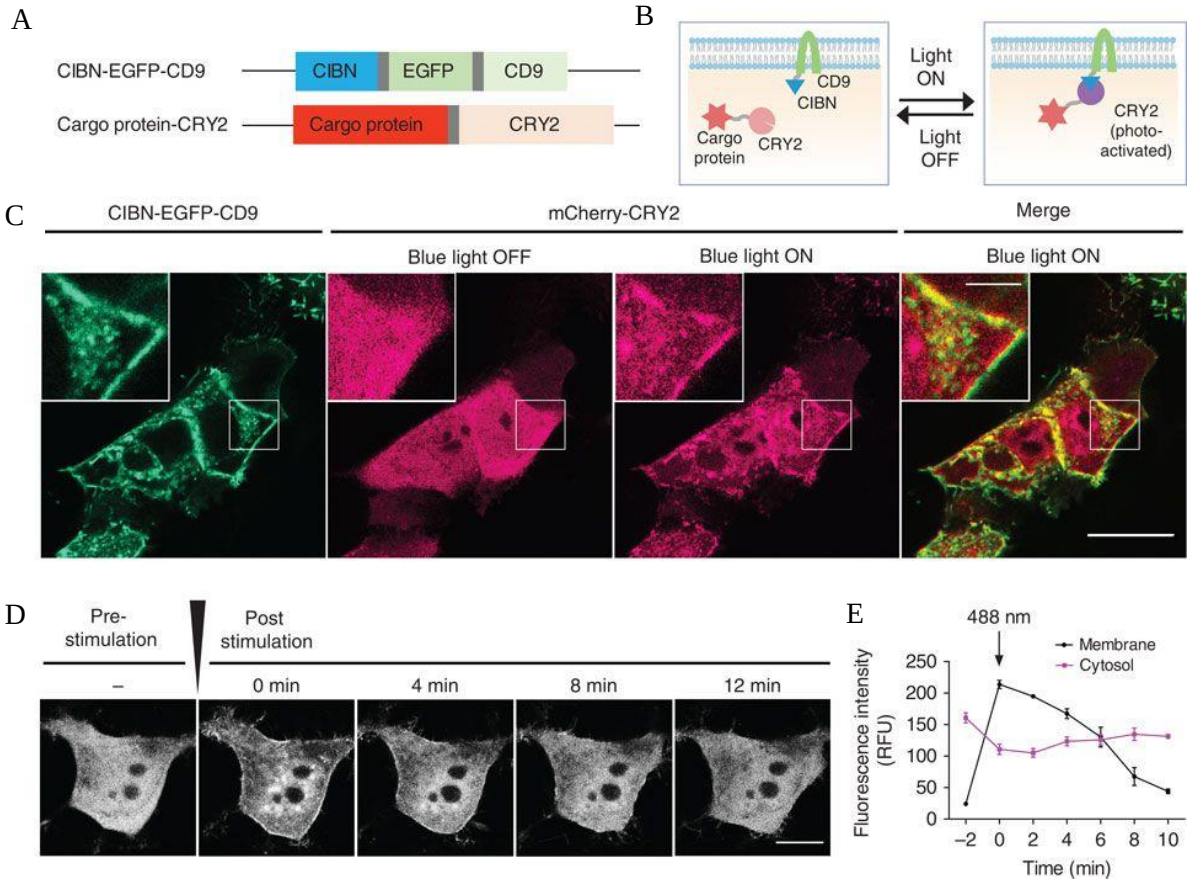

Figure 2.8 Engineering of EXPLORs (exosome for protein loading via optically reversible protein–protein interaction). (A) DNA construct for production of EGFP labeled CIBN protein anchored with CD9 and cargo protein fused with CRY2, (B) schematic showing a working mechanism of EXPLORs-light-dependent reversible protein–protein interaction, (C) confocal microscopy of transfected HEK293T cells showing light-dependent protein–protein interaction. The merged figure shows colocalization of mCherry-CRY2 with CIBN–EGFP–CD9, (D) mCherry-CRY2 distribution in a cell pre- and post-stimulation with blue light, (E) variation of mCherry fluorescence intensity with respect to light stimulation. Reproduced from ref.[89] under the terms of Creative Commons CC BY license. Copyright 2016, Springer Nature.

author confirmed their claim of reversible protein loading using fluorescence microscopy. In the absence of blue light, mCherry-CRY2 was observed to be distributed all over the cell, whereas with the treatment of blue light (488 nm laser stimulation, 15 s, 350 μW cm^{-2}), mCherry-CRY2 was localized in the endosomal compartment with CIBN-EGFP-CD9 (**Figure 2.8C**). After a certain time of post-stimulation, mCherry was again observed to be delocalized all over the cell (**Figure 2.8D and E**). This observation shows light-dependent docking and release of mCherry-CRY2 with CIBN-EGFP-CD9 which was further confirmed by immunoblot analysis. Further, successful intracellular delivery of cargo protein was shown using the engineered method.

Cheng et al. used a biological surface functionalization method to reprogram EVs as a nanoscale controller of cellular immunity (**Figure 2.9**).[90] Here, they used EVs to redirect and activate cytotoxic T cells against cancer cells by genetically displaying two distinct types of antibodies on the exosomal surface. Antibodies targeting T cell CD3 and epidermal growth factor receptor (EGFR) were fused with the transmembrane domain of human platelet-derived growth factor (PDGFR) receptor and the fusion construct was expressed in a cell by transfection. Transfected cell line secreted EVs containing both antibodies CD3 and EGFR, as confirmed by immunoblot analysis (**Figure 2.9A**). Here, they genetically engineered cells to express a fusion protein of interest which was then integrated with EVs by EVs biogenesis process to obtain surface-functionalized EVs with antibodies, termed as SMART Exos (synthetic multivalent antibodies retargeted exosomes). These SMART EVs can induce crosslink between CD3 expressing T cell and EGFR expressing triple-negative breast cancer (TNBC) cells, as confirmed by confocal microscopy, where we can see green colored SMART EVs crosslinking red-colored MDA-MB-468 cells (TNBC cells) and no-colored Jurkat cells (T cell) (**Figure 2.9B**). Overexpressed EGFR is one of the major characteristics of TNBC and can be exploited to

specifically target these cells.[91] T cell activation analysis confirmed the specificity of engineered SMART EVs in which significant activation was observed in the case of SMART EVs against EGFR positive TNBC MDA-MB-468 cells whereas nominal T cell activation was observed in EGFR negative MDA-MB-453 cells (**Figure 2.9C**). Importantly, SMART EVs expressing CD3 only or EGFR only was also showing nominal T cell activation. Also, in confocal analysis, no crosslink was observed with SMART EVs expressing one type of antibodies. This observation signifies the need for the presence of both types of antibodies in SMART EVs to induce crosslink between T cell and TNBC and subsequently induce T cell activation. This was further confirmed by the *in vitro* and *in vivo* therapeutic study, where SMART EVs expressing both antibodies showed a significant effect in EGFR positive TNBC cell or xenograft models (**Figure 2.9D and E**). Here, the authors successfully demonstrated a biological approach of surface functionalizing EVs with multiple antibodies to achieve dual targeting functionality for effectively modulating antitumor immunity. The proposed surface functionalization technique may provide a general and versatile platform technology for the development of a new class of EVs therapeutics.

Various biological surface functionalization strategy has been explored to add targeting peptide or ligands in the EVs surface to enhance the targeting characteristic of EVs. Pioneering work in this area was reported by Matthew Wood and group, where authors reported biologically engineered brain targeted EVs for the delivery of small interfering RNA (siRNA).[92] Here, the author genetically engineered lysosome-associated membrane glycoprotein 2b (Lamp2B), a protein highly expressed in EVs surface, fused to peptide obtained from rabies virus glycoprotein (RVG). Dendritic cells were transfected with plasmid encoding Lamp2B fused with RVG to produce RVG surface-functionalized EVs.[92,93] RVG peptides are neuron-specific as they bind specifically to the acetylcholine receptor and thus can provide brain targeting functionality.[94] RVG

functionalization in EVs resulted in increased brain accumulation and delivery of siRNA with subsequent knockdown of the target gene.[92] This kind of brain targeted EV based delivery system can be used in the treatment of neurodegenerative diseases like Alzheimer. A similar study carried out by Andaloussi and group explored *in vivo* biodistribution of RVG functionalized EVs, which showed higher accumulation of RVG-EVs in brain, heart, and muscle compared to non-

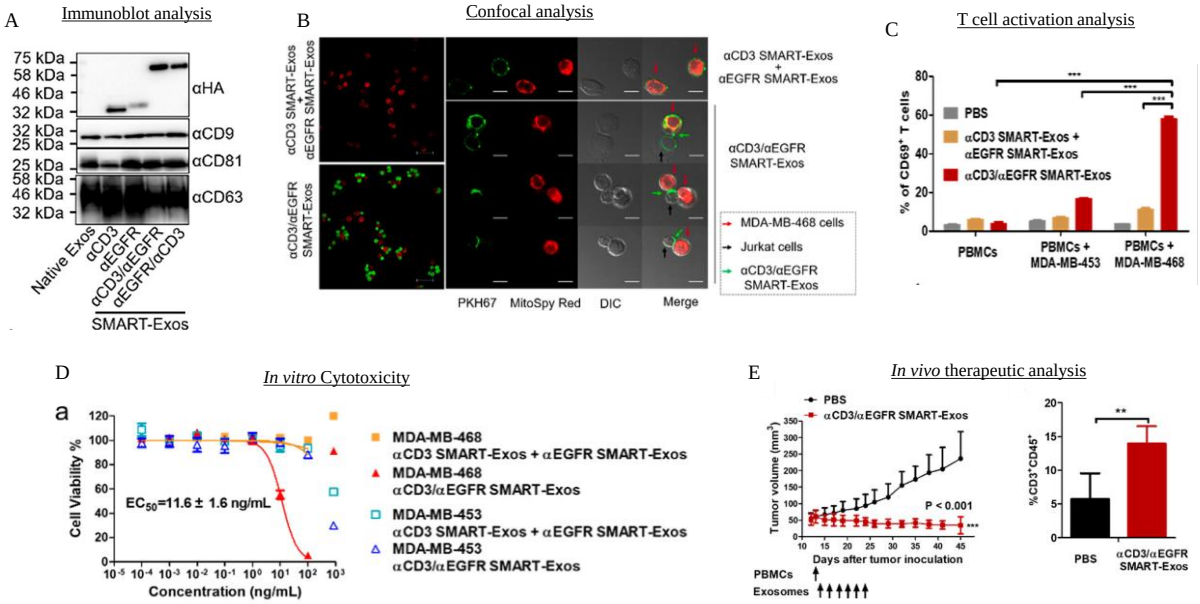

Figure 2.9 Synthetic antibodies retargeted exosomes (SMART-Exos) characterization and therapeutic analysis. (A) Immunoblot analysis showing the presence of CD3 and EGFR in different SMART-Exos, (B) confocal analysis showing crosslinking between Jurkat cells and MDA-MB-468 cells promoted by SMART-Exos expressing both CD3 and EGFR antibodies (αCD3/αEGFR SMART-Exos). SMART-Exos expressing only one kind of antibodies did not show crosslinking, (C) T cell activation assay showing the percentage of T cell activation with the treatment of SMART-Exos in human peripheral blood mononuclear cells (PBMCs) co-cultured with human breast cancer cells. αCD3/αEGFR SMART-Exos showed significant T cell activation against the triple-negative breast cancer (TNBC) cells MDA-MB-468, (D) in vitro cytotoxicity assay showing cytotoxicity of SMART-Exos in human breast cancer cells, and (E) in vivo therapeutic analysis of SMART-Exos showing sharp reduction of tumor volume along with activation of T cells with SMART-Exos treatment. Reprinted (adapted) with permission from Q. Cheng, X. Shi, M. Han, G. Smbatyan, H.-J. Lenz and Y. Zhang, Reprogramming Exosomes as Nanoscale Controllers of Cellular Immunity, J. Am. Chem. Soc., 2018, 140(48), 16413–16417.48 The figure is adapted from four different figures from the original paper. Copyright 2018 American Chemical Society.

functionalized EVs.[95] Other organs including lungs, liver, and spleen did not show a difference in the accumulation of RVG functionalized EVs and non-functionalized EVs. Brain, along with heart and muscle shows a higher expression level of acetylcholine receptor which explains the higher accumulation of RVG functionalized EVs in these organs and further confirms the specificity of RVG toward acetylcholine receptor.[95,96] In another study, Yang et al. reported using RVG functionalized EVs to deliver micro RNA, miR-124, to the ischemic region of the brain to ameliorate brain injury.[97]Another study by Tian et al. reported biological surface functionalization of EVs by αv integrin-specific iRGD (CRGDK/RGPD/EC) peptide for tumor-targeted delivery of doxorubicin.[98] Here, dendritic cells were transfected by vector expressing iRGD-Lamp2b fusion protein and EVs from transfected cell were isolated to obtain iRGD peptide-functionalized EVs. The functionalization of EVs by αv integrin-specific iRGD peptide allows specific binding toward αv integrins that are highly expressed on tumor cells and tumor-associated vascular endothelium, thereby facilitating vascular and tissue penetration of functionalized EVs.[98,99] Likewise, cardiac-specific delivery of EVs was reported by functionalizing EVs surface with cardiac targeting peptides (CTP) with peptide sequence APWHLSSQYSRT.[100] These functionalization strategies successfully functionalized EVs surface by using a genetically engineered expression vector to equip EVs with desired targeting ability.

As an alternative to the genetic engineering method of the biological approach of surface functionalization, Wang et al. have proposed a metabolic engineering and labeling strategy for the surface functionalization of EVs (**Figure 2.10**).[101] Here, authors have exploited the metabolic process of cells to functionalize EVs surface with azide moiety thereby diversifying the chemistries of EVs and expanding their functions. Authors have used two different approaches for metabolic labeling-1) residue-specific protein labeling strategy and 2) metabolic glycan labeling. Residue

specific protein labeling strategies incorporate non-canonical amino acids in newly synthesized proteins in cells.[102] Here, L-azidohomoalanine (AHA), an azide-bearing amino acid analog of methionine incorporates in newly synthesized proteins by replacing natural methionine, by residue-specific protein labeling mechanism. Thus incorporated AHA-labelled protein can be expressed in EVs by the virtue of EVs biogenesis. Likewise, glycans and glycoproteins are also expressed in EVs, and metabolic labeling of this moiety can be exploited for EVs functionalization.[103,104] Here, tetraacetylated N-azidoacetyl-D-mannosamine (ManNAz), an azidosugar, is metabolized into azido glycans during glycan biosynthesis process of the cell. These azido glycans are recruited in EVs surface during EVs biogenesis and cargo sorting process and hence expressed in secreted EVs. The confirmation of successful metabolic labeling of azide

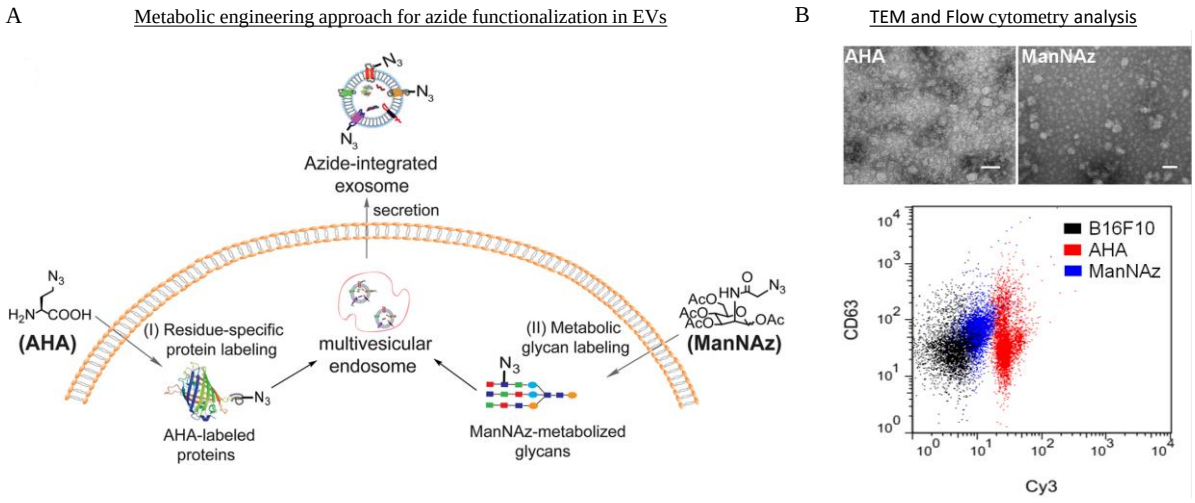

Figure 2.10 Azide functionalization in extracellular vesicles via metabolic engineering. (A) Schematic showing metabolic labeling of newly synthesized proteins by an azide labeled amino acid (AHA) via residue-specific protein labeling and glycan labeling by azido sugar (ManNAz) via the glycan biosynthesis pathway, and (B) TEM image of metabolically engineered extracellular vesicles and flow cytometry analysis to confirm the azide conjugation. Enhancement of Cy3 in metabolically engineered EVs shows successful conjugation of the azide group. CD63 was used as a marker protein for EVs. Reproduced and adapted from ref.**[101]** under the terms of Creative Commons CC BY license. The figure is adapted from two different figures from the original work. Copyright 2015, Wang et al.

moiety in secreted EVs was carried out by Cy3 conjugated dibenzobicyclooctyne (DBCO-Cy3). DBCO-Cy3 is a bright, far-red-fluorescent, probe routinely used for imaging/quantifying of azide-containing biomolecules. Cy3 DBCO reacts with azides via a copper-free "click chemistry" reaction to form a stable triazole complex, and thus acts as an analytical tool to quantify azides. Flow cytometry analysis shows enhanced Cy3 fluorescence in metabolically labeled EVs (AHA-EVs and ManNAz-EVs) compared to control EVs secreted by B16F10 cells, whereas the expression of CD63, one of the EVs marker protein, were similar in both EVs (**Figure 2.10B**). This observation clearly shows the presence of azide group in metabolically labeled EVs, and thus confirms successful metabolic labeling strategy. The functionalized azide moiety in EVs surface gives opportunities toward various azide based chemistry thus expanding the functionality of EVs. This will be discussed in detail in the chemical approach of surface functionalization.

Significance of biological surface functionalization strategy

The biological approach of surface functionalization exploits the cellular processes to functionalize the surface of EVs. In this context, a cell can be seen as a complex reaction system, which by the years of evolution has managed to carry out the various regulated interlinked chemical reaction in a highly energy-efficient way with extreme specificity. The idea of a biological approach of surface functionalization is to exploit this system to express cargo of interest in EVs surface. Here, we have discussed the genetic and metabolic engineering of a cell to specifically functionalize EVs with a cargo of interest for various functionalities. While the method is non-invasive compared to chemical functionalization strategy and thereby can preserves crucial EVs integrity and functionality, the major challenges in the biological approach can be the heterogeneity in secreted EVs population and their complicated purification process to separate functionalized EVs from the naive ones.

2.3.3 Surface functionalization strategy: Chemical method

The chemical method of surface functionalization includes the direct use of chemical reagents to add functional moiety on the surface of EVs. EVs surface is characterized by the presence of amine/carboxylic terminated phospholipid or transmembrane protein moiety which can be directly functionalized with different functional groups. Alternatively, functionalized phospholipids can also be incorporated in EVs by simple incubation following hydrophobic insertion strategy. A wide variety of simple, one step click-type chemistry can be exploited to functionalize EVs using the chemical method (**Figure 2.11**). Click chemistry is more desirable and explored in a chemical approach because of its ease of synthesis with high yield, wide in scope, and easy product separation.[105,106] In this regard, different chemical strategies like Thiol-maleimide coupling chemistry, EDC/NHS coupling chemistry, azide-alkyne cycloaddition chemistry, and

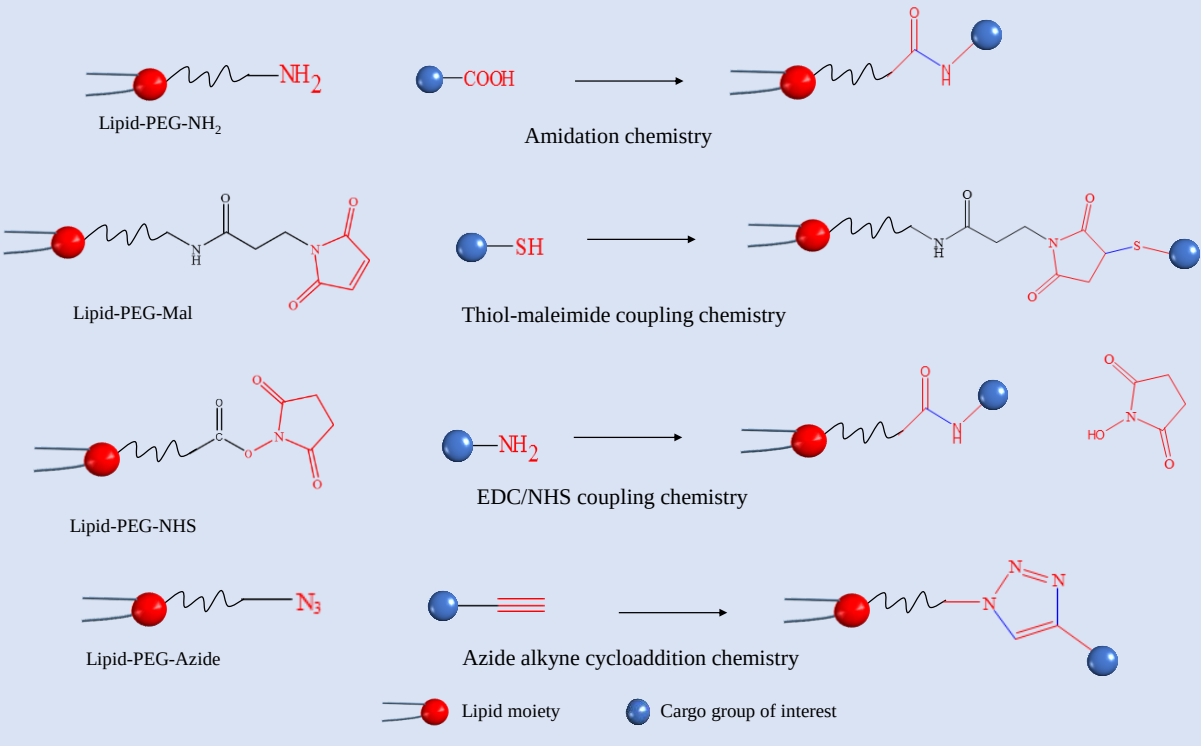

Figure 2.11 Schematic showing different facile chemistries for surface functionalization of extracellular vesicles.

amidation chemistry can be used to functionalize EVs surface with amine bearing or thiol bearing functional moiety. The coupling chemistry strategy helps to link EVs surface with ligand/cargo of interest by strong covalent bonds. For example, fluorescent dyes, imaging agents, and targeting agents can be covalently linked with EVs surface to provide the desired functionality. The chemical method of surface functionalization is post-production engineering of EVs where EVs are engineered after production using simple click chemistries. As such, the purification or separation step to isolate functionalized EVs is much simpler in the chemical method compared to the biological or physical method.

Di et al. reported functionalizing EVs with maleimide terminated lipids via hydrophobic insertion strategy.[107] The maleimide moiety in EVs surface was exploited to conjugate thiol bearing species via highly effective click chemistry to award different functionality to EVs while retaining their structural integrity and biological activity. Maleimide-EVs was conjugated with- 1) dithiol bearing molecule (1,6-hexanedithiol) to link with Mal-containing fluorescent dye (fluorescein-5-maleimide, F5M) for EVs monitoring, 2) thiol-containing magnetic particle to help in EVs separation process, and 3) thiol-containing groups to conjugate with bare gold nanoparticles through Au-S bonds for vibration detection of EVs surface cargoes (**Figure 2.12**). EVs separation or enrichment technique can be crucial to maximizing yield. Here, the functionalization approach used allows for the efficient interaction between EVs and magnetic nanoparticles. Magnetic isolation/enrichment of EVs was monitored using DID dye (**Figure 2.12D**). DID is a lipophilic environmentally sensitive dye that shows strong fluorescence when incorporated with biological membranes like EVs, whereas in aqueous solution shows negligible fluorescence. The authors used the subtraction method to calculate the capture efficiency of metal nanoparticles based upon the reduction of the fluorescent signal after capture. The method capture efficiency was around

70% for EVs from cell supernatant and 55% for EVs in serum samples. This method can be used as an alternative for a variety of immunomagnetic technique developed for EVs enrichment. The immunomagnetic technique is usually based upon antigen-antibody or receptor-aptamer specific binding thereby giving high selectivity and specificity of separation, however, are limited by high cost and low yield of EVs. In this scenario, the proposed clickable lipid probe technique with a hydrophobic insertion strategy combined with clickable magnetic enrichment can provide alternative simple, low cost, and efficient isolation/enrichment of EVs. In another strategy, gold nanoparticles (AuNPs) were immobilized with thiol-exposed EVs for characterization using surface-enhanced Raman spectroscopy (SERS) (**Figure 2.12C**). Due to the plasmonic properties of immobilized AuNPs in EVs, the molecular vibrations of EV-biomolecules can be recorded with

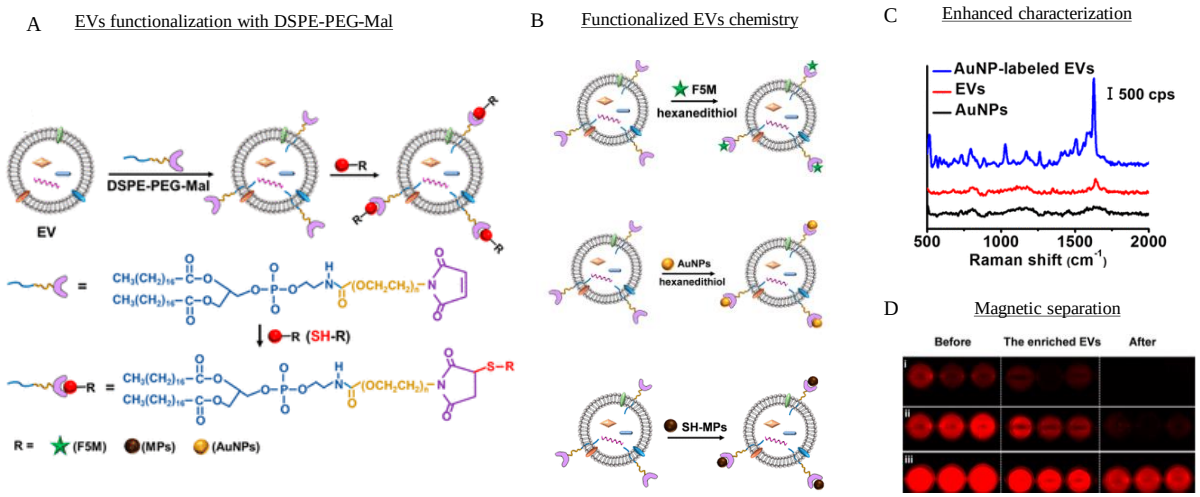

Figure 2.12 Surface functionalization of EVs with maleimide (Mal) terminated lipid for the addition of diverse surface functionalities. (A) Schematic illustration of surface functionalization of EVs by DSPE–PEG–Mal via the hydrophobic insertion strategy, (B) Mal functionalized EVs were conjugated with thiolated species by using thiol–maleimide conjugation chemistry for tracking, characterization, and separation of EVs, (C) enhanced characterization of EVs functionalized with AuNPs via Raman spectroscopy, and (D) magnetic enrichment technique of functionalized EVs. The DiD dye was used to track enrichment of EVs. The figures show enriched EVs at three different concentrations. Reprinted (adapted) with permission from H. Di, E. Zeng, P. Zhang, X. Liu, C. Zhang and J. Yang, et al., General Approach to Engineering Extracellular Vesicles for Biomedical Analysis, Anal. Chem., 2019, 91(20), 12752–12759.89 The figure is adapted from four different figures from the original paper. Copyright 2019 American Chemical Society.

high sensitivity. Here, the incorporation of Mal functionality in EVs allows for the efficient clicking with thiolated groups thereby adding significant functionality like EVs tracking, EVs enrichment, and EVs characterization.

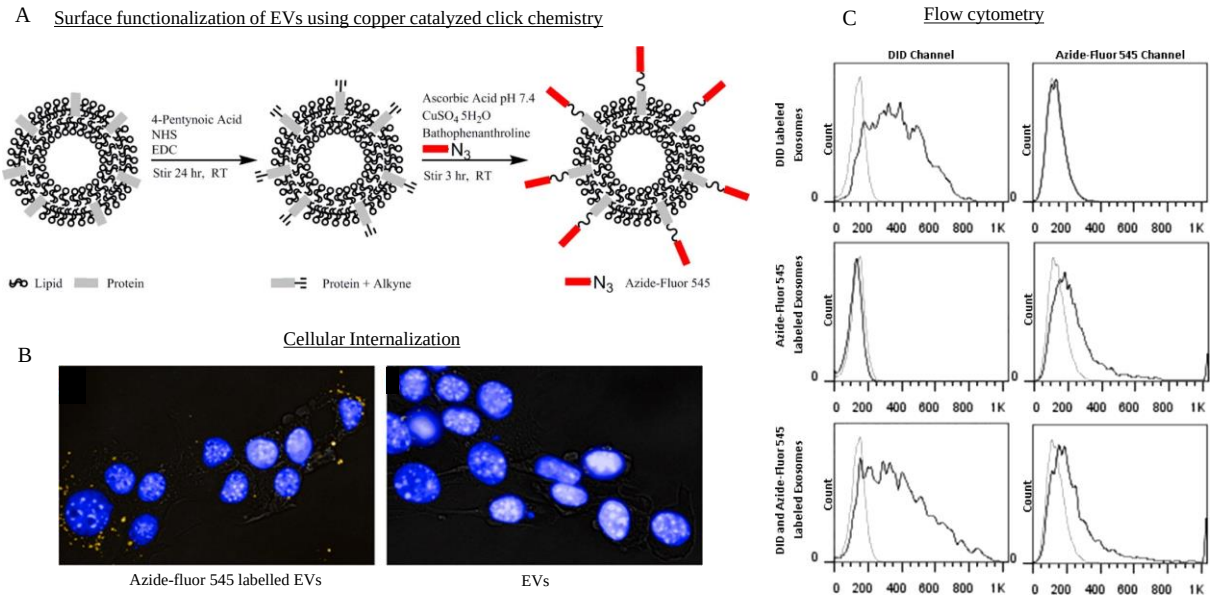

Figure 2.13 Functionalization of extracellular vesicles via copper-catalyzed click chemistry. (A) The terminal amine of EVs is activated by the terminal alkyne group via EDC/NHS coupling chemistry following the conjugation of azide-fluor 545 via copper-catalyzed azide–alkyne cycloaddition, (B) cellular internalization assay showing the internalization of azide-fluor 545 conjugated EVs in 4T1 cells. Cells were incubated for 4 h with 50 μg/mL EVs, and (C) flow cytometry analysis for the internalization behavior of EVs in 4T1 cells. EVs were fluorescently labeled with DID, azide-fluor 545, or both and analyzed using flow cytometry for an increase in fluorescence. Reproduced and adapted with permission from ref.[108], DOI: http://10.1021/bc500291r. Further permissions related to the content of this figure should be directed to ACS. Copyright 2014 American Chemical Society.

Copper-catalyzed azide-alkyne cycloaddition is another click chemistry strategy that can be utilized to functionalize EVs surface with azide functionality. Smyth et al. conjugated a terminal alkyne group to EVs using EDC/NHS coupling chemistry, where an amine group of EVs protein or lipid was cross-linked with 4-pentynoic acid by carbodiimide activation.[108] Following this functionalization with a terminal alkyne, EVs were conjugated with azide moiety (Azide-Fluor 545) using copper-catalyzed azide-alkyne cycloaddition (**Figure 2.13**). Copper-catalyzed azide-

alkyne cycloaddition is a highly efficient click reaction that forms a triazole linkage and is highly accelerated by Cu(I) catalyst. The extent of functionalization can be quantified spectrophotometrically by measuring the fluorescence of Azide-Fluor 545. The size and internalization behavior of EVs before and after Azide-Fluor conjugation did not show any marked difference, as suggested by nanoparticle tracking analysis, microscopy, and flow cytometry (**Figure 2.13B and C**). For flow cytometry, EVs were labeled with DID dye and internalization behavior was assayed in 4T1 cells. The internalization profile of unmodified EVs resembled closely with Azide-Fluor 545 functionalized EVs. With reference to these data, the authors claim that the proposed method of surface functionalization has little to no impact on EVs functionality.

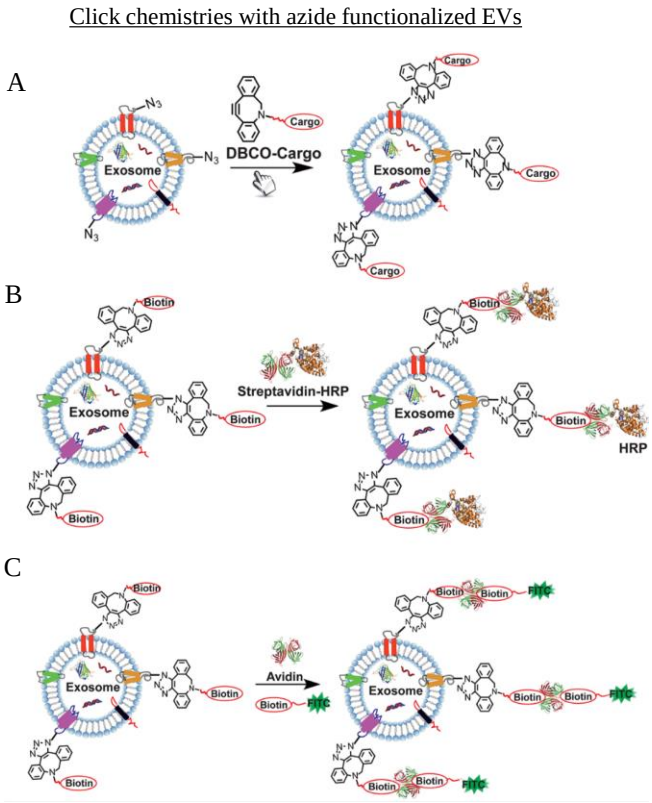

Figure 2.14 Click chemistries of azide functionalized EVs. (A) Bioorthogonal click conjugation for EV functionalization with strained alkyne group DBCO as the linker, (B) biotinylated EVs functionalized with streptavidin–HRP, and (C) incorporation of a biotinylated cargo in EVs with avidin as a linker. Reproduced and adapted from ref.[101] under the terms of Creative Commons CC BY license. Copyright 2015, Wang et al.

The azide functionalization in EVs allows for a wide range of additional functionality. E.g. azide can be linked with cargo conjugated DBCO by using azide-alkyne cycloaddition (**Figure 2.14A**). The strained alkyne group present in DBCO facilitates this reaction. Wang et al. reported biotin functionalization in EVs by using biotin linked with DBCO by PEG (DBCO-PEG_4-biotin).[101] DBCO-PEG_4-biotin was clicked with azide functionalized EVs.

Biotin is a small molecule that shows a strong binding affinity to avidin or streptavidin protein.[109] The biotinylation of EVs diversifies the EVs functionalities through various biotin-avidin interaction chemistries that can be widely used in biomedical applications (**Figure 2.14B**). Biotinylated EVs can be used in protein delivery by integrating protein of interest with streptavidin, e.g. streptavidin-horseradish peroxidase (HRP). This conjugation strategy can also be used as an analytical tool to confirm the successful biotinylation of EVs via dot blot assay. EVs can be dot blotted in the PVDF membrane followed by incubation and imaging with streptavidin-HRP. HRP can give chemiluminescence by interacting with a chemiluminescent substrate, which can be used to quantify biotinylation. Further, biotinylated EVs can be used to link biotin-conjugated cargoes of interest using avidin as a linker (**Figure 2.14C**). Therefore, the incorporation of azide functionality opens the door for various functions like biotinylation which can further diversify EVs functionality by various biotin-clicked EVs. As discussed earlier, the copper-catalyzed click chemistry allows for efficient conjugation of the functional moiety in EVs surface. However, the use of copper in biological molecules like EVs can be complicated by the associated cellular toxicity of Cu(I). To address this issue, an alternative copper-free approach of click chemistry has been developed which can provide great advantages in bio-orthogonal coupling chemistry. Gai et al. discussed the strain promoted alkyne-azide cycloaddition (SPAAC) to conjugate DBCO-liposome with azide bearing moieties.[110] Amine terminated liposome was functionalized with DBCO using DBCO-PEG_4-NHS following NHS chemistry to introduce strained alkyne (DBCO group) in a liposome (**Figure 2.15A**). Successful conjugation of DBCO can be monitored by anthracene azide assay by quantifying fluorescence of anthracene after conjugation (**Figure 2.15B**). The proposed SPAAC strategy can be utilized to functionalize any amine-terminated self-assembled vesicles including EVs. SPAAC strategy can be employed to

functionalize EVs with antibodies by using azide conjugated antibodies on DBCO functionalized EVs (**Figure 2.15C**). The extent of functionalization can be quantified using flow cytometry-based binding assay using fluorescently labeled secondary antibodies (**Figure 2.15D**).

Significance of chemical functionalization strategy

Different facile coupling chemistry like EDC/NHS chemistry, amidation chemistry, thiol-maleimide chemistry, copper-catalyzed azide-alkyne cycloaddition chemistry, and strain promoted azide-alkyne cycloaddition chemistry have been discussed as a chemical approach of surface functionalization of EVs. All these chemistries have the advantage of being easy and quick and compatible with biomolecules and therefore are widely used in functionalizing biomolecules. While these functionalization steps are rapid and quantifiable, attention should be given in the retention of membrane integrity and functionality of EVs following these strategies.

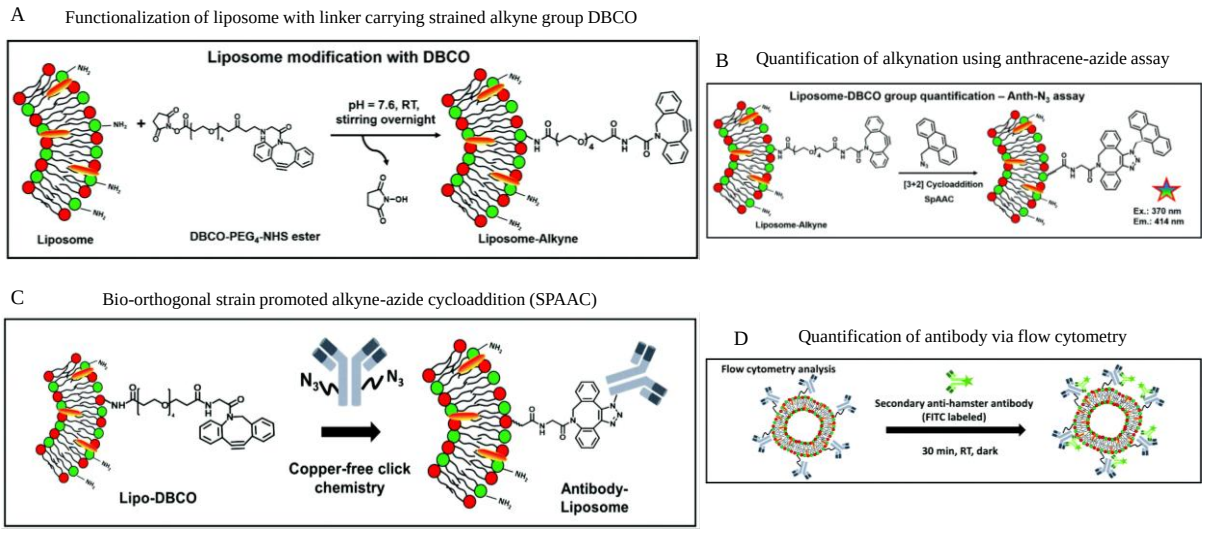

Figure 2.15 Surface functionalization of liposomes using strain promoted alkyne–azide click chemistry (SPAAC). (A) Functionalization of the amine-terminated liposome with DBCO, (B) quantification of DBCO functionalization by anthracene-azide assay, (C) functionalization of DBCO–liposome with azide integrated antibodies via SPAAC, and (D) analysis of SPAAC using flow cytometry. Reproduced and adapted from ref.[110] under a Creative Commons Attribution 3.0 Unported license with permission from the Royal Society of Chemistry. The figure is adapted from three different figures from the original work.

2.4 Comparative analysis of different surface functionalization strategies

This review discusses the physical, biological, and chemical approaches of surface functionalization of EVs membranes. While each approach has differences in their fundamental level, the aim is the same i.e. to add various functionality to EVs for biomedical application. In this regard, each approach has its own advantages and disadvantages. A physical approach like sonication, extrusion, and freeze-thaw method provides reagent free and simplest strategy for surface functionalization facilitated by membrane fusion that can integrate functionality in EVs without disrupting their natural function. However, these methods are often dependent upon and biological or chemical methods for substrate preparation, which is later utilized in membrane rearrangements. Also, there is a chance of leakage of the internal cargo of EVs which may contain crucial cellular information in the form of mRNA and proteins. Likewise, sonication and freeze-thaw method of membrane fusion can lead to heterogeneity in the size and surface property of functionalized EVs. Therefore, the extrusion process is very important to maintain the proper size and homogeneity of functionalized EVs. In this regard, the physical approach is usually advantageous when used in combination with a biological or chemical approach, and generally should be followed by the extrusion process to get the maximum benefit of this strategy. Biological and Chemical approach of functionalization is the two main independent approach of surface functionalization. Although the approaches are different, both methods use the chemistry of biomolecules to add functionality. In biological approach, we are exploiting cellular reaction system that has been optimized by years of evolution by living system whereas, in chemical approach, we use the knowledge of chemistry which is also optimized over the decades of evolving modern science. The biological approach is also called a pre-production engineering strategy as the raw materials that make up the EVs (lipids and proteins) are engineered or functionalized

before their biogenesis. Chemical approach, on the other hand, is called as post-production engineering strategies as this modification takes place after the biogenesis and extraction of EVs. The idea of using a cell's own machinery to functionalize the EVs as per our needs is fascinating, and with proper optimization, several EVs functionalization has been reported with high efficiency for adding various functionality like surface display technology, targeted imaging, and targeted drug delivery. These functionalities can have a huge impact on understanding EVs role in cellular processes and pathogenesis for biomedical applications. Despite these fascinating results and the tremendous scope of the biological approach of EVs functionalization, one of the major limitations in this method is the heterogeneous population of EVs secretion with varying levels of surface expression which makes it difficult to standardize the method. The complexity of the biological environment along with the inadequate knowledge of EVs biogenesis makes this method complex. Owing to this complexity, there can be an issue with the low yield of surface-functionalized EVs using the biological method. Here, the physical approach like extrusion can be used to maximize the yield and improve the homogeneity of the EVs population.

The chemical approach of surface functionalization provides easy and highly efficient conjugation of the different cargo of interest like antibodies, proteins, and small molecules. Due to the different click chemistry method and facile coupling strategy, these functionalizations can be done in simple steps and purified easily. Also, since it is a post-production strategy, there is no problem with EVs isolation from complex biological media as compared to the biological approach. With this perspective, the chemical approach of functionalization seems to have significant advantages with diverse functionality and simplicity. However, one major issue can be the retention of EVs integrity, functionality, and the biocompatible cellular fate of functionalized EVs. The use of chemical reagents can affect protein integrity and function. E.g. Cu(I), a catalyst

in many click reactions, has reported toxicity towards cells and can interfere with protein activity.[111] There are however Cu(I) free click chemistry that can be used to gain the same function. Nonetheless, it is crucial to explore the effect of other alternative reagents in EVs integrity and function. Therefore, while the chemical approach provides simple and diverse opportunities to functionalize EVs, special attention should be given to confirm the biocompatibility of reagents in terms of EVs membrane integrity and functionality.

2.5 Challenges in surface functionalization strategy

One of the big questions that are often not addressed in the research of surface functionalization strategy is whether the applied method interferes with the innate functionality of extracellular vesicles. This is a big question that needs to be addressed if we want to truly exploit the natural functionality of EVs. Most of the studies have shown the confirmation of surface functionalization in EVs along with the added functionality of EVs using various strategies. For example, surface display technology of EVs successfully labeled EVs with fluorescent dye to track EVs.[67] But it is unknown whether the functionalization strategy changes the innate functionality of EVs *in vitro*. For this, a comparative study with naïve EVs, without any functionalization, should be conducted. It is, however, challenging to study naïve EVs behavior without doing any engineering. As such, without labeling with fluorescent dyes or imaging agents, tracking EVs is extremely difficult. In this scenario, the analysis of the proteomics profile of EVs, before and after engineering might be helpful, as the proteomics profile is responsible for the functional role.[112–114] There has been researched effort in quantifying EVs protein after functionalization to confirm the integrity of EVs. As an example, Ming et al. quantified CD63 after the metabolic engineering of EVs to add azide functionality via flow cytometry.[101] Here, although the similar protein level of CD63 in functionalized EVs and naïve EVs may signify the retention of protein content, it does

not necessarily signify the retention in the functionality. Also, the analysis of single protein may not correlate to the extensive proteomic profile of EVs. In this scenario, analysis of whole proteomic profile along with the structures of major proteins may reflect true retention of EVs innate functionality. The structure of a protein can be assessed by a spectroscopic technique like Circular Dichroism, Raman Spectroscopy, and NMR.[115–120] These techniques provide crucial information about the secondary structure of proteins. As evident, the structure of a protein is directly linked to its function, analysis of EVs protein structures may give valuable information about the retention of protein functionality with the functionalization process.[121–125] Further, *in vitro* and *in vivo* experimentation of naïve EVs and surface functionalized EVs can be crucial to confirm the retention of naïve EVs functional integrity. The retention of functional integrity of naïve EVs with different functionalization strategies is particularly important if we want to explore the innate role of EVs in various biological processes. With the assurance of the functional integrity of EVs, different surface functionalization strategies discussed here can be applied. The surface functionalization strategy with nominal alteration in the naïve EVs functionality should be preferred.

2.6 Conclusion

EVs functionalization approaches have added various functionality to EVs which can be applied in diagnostic and therapeutic applications. All three different approaches discussed for EVs functionalization- physical, biological, and chemical have successfully functionalized EVs and added desired functionality. All three approaches have their benefits and shortcomings. The physical approach can be used in combination with a chemical or biological approach to ensure the EVs homogeneity. Biological approach, although being complex, can give naturally functionalized EVs. So, once the method is optimized, it can be beneficial for the long-term

production of functionalized EVs. Whereas, the chemical approach can give a quick one-step functionalization opportunity. Based on the need, both biological and chemical approaches can be equally beneficial. These functionalization strategies have further diversified the tremendous scope of EVs in biomedical applications. As of now, we are yet to completely understand the role of EVs in cellular processes. By properly functionalizing EVs, we can garner important information to understand EVs potential in the bio-medical field.

Chapter 3 - pH responsive cationic liposome for endosomal escape mediated drug delivery

***Chapter 3**, in full, is a reprint of the material as it appears in Colloids and Surfaces B: Biointerfaces, 2020, Sagar Rayamajhi, Jessica Marchitto, Tuyen Duong Thanh Nguyen, Ramesh Marasini, Christian Celia, and Santosh Aryal. doi: 10.1016/j.colsurfb.2020.110804*

Abstract

Endosomal degradation of the nanoparticle is one of the major biological barriers associated with the drug delivery system. Nanoparticles are internalized in the cell via different endocytosis pathways, where they are first delivered to early endosomes which mature to the late endosome and to the lysosome. During this journey, NP encounters a harsh chemical environment resulting in the degradation of NP and its content. This process is collectively called as intracellular defenses against foreign materials. Therefore, to avoid this degradative fate, the endosomal escape technique has been explored following membrane fusion or membrane destabilization mechanisms. However, these methods are limited to the application due to non-specific membrane fusion. To overcome this limitation, we have designed pH-responsive liposome made up of 3ß-[N-(N',N'-dimethylaminoethane)-carbamoyl]cholesterol hydrochloride (DC-liposome) in which the cationic nitrogen of the ammonium moiety occupies only ~2.5% of the molecule. Such a small percentage of the cationic moiety is sufficient enough to exhibit pH-responsive properties while maintaining the biocompatibility of the DC-liposome. DC-liposome showed pH-dependent cationic properties due to the protonation of DC-moiety at acidic pH. The fluorescence-based experiment confirmed pH-dependent fusogenic properties of DC-liposome. Furthermore, the endosomal colocalization study revealed higher localization of DC-liposome in the early

endosome compared to that of the late endosome, suggesting possible endosomal escape. Elevated cationic and fusogenic properties of DC-liposome at acidic pH can mediate membrane fusion with anionic endosomal membrane via electrostatic interaction, thereby causing endosomal escape. Moreover, doxorubicin-loaded DC-liposome showed higher cytotoxicity than that of free doxorubicin further supporting our clam of endosomal escape. These findings suggest the potential of DC-liposome to break the endosomal barriers to enhance the therapeutic efficacy thereby guiding us in design consideration in the field of stimuli-responsive delivery agents.

3.1 Introduction

Endosomal degradation of therapeutic agents is one of the major challenges in nanoparticulate drug delivery systems. Endosomal-lysosomal system actively encapsulates nanoparticles in endocytic vesicles and facilitates its recycling or degradation. This system includes intracellular vesicular systems including early endosome, late endosome, and lysosome, which actively participates in cargo internalization, recycling, modulation, and degradation.[126] Internalized cargo is first delivered to early endosome which plays a crucial role in determining their fate: recycling, excretion, or degradation. Depending on fate, cargo can be exported out of early endosome or continue in early endosome which matures to the late endosome and finally fuses with lysosome forming endo-lysosome vesicles for degradation.[127] Cargoes like nanoparticulate drug delivery systems are mostly internalized in the cell via different endocytosis pathways where its fate is determined.[128] Owing to the exogenous property, these nanoparticles are subjected to degradation in endo-lysosome vesicles, a unique intracellular defense mechanism.[129] Therefore, it is crucial for the nanoparticulate drug delivery system to escape early endosomes and avoid immediate degradation to maintain therapeutic efficacy.

Efforts have been made to fabricate and engineer the drug delivery system to overcome the endosomal barrier. Towards this direction, liposomal and polymeric materials have been used to fabricate nanoparticle for endosomal escape via membrane fusion or membrane destabilization.[130] A liposome is a lipid bilayer enclosed membrane structure that is widely investigated as a drug delivery system. The cationic liposome can undergo electrostatic interaction mediated membrane fusion with anionic endosome membrane thus escaping endosome.[131] Similarly, the polymeric nanoparticle can escape endosomes via membrane destabilization following osmotic rupture, particle swelling, and particle disassembly mechanism.[132–135] These technique has shown significant promises to overcome the endosomal barrier. However, the application of cationic liposomes can be limited by non-specific membrane fusion with other membrane compartments. Likewise, in polymeric materials, endosome escape mediated by membrane destabilization may be limited due to the molecular weight of cargo that can diffuse across the destabilized membrane.[134,136] To overcome these limitations, the pH-sensitive lipid-polymeric hybrid system has been developed which can selectively undergo membrane fusion at the endosomal membrane and release its payload. This system exploits the acidic pH environment of endosomal vesicles. The polymeric part shields the cationic surface in neutral pH and de-shields in acidic pH, thereby exposing the cationic surface to fuse with the anionic membrane of endosome.[137,138]

Here, we have designed pH-responsive dimethylaminoethane-carbamoyl functionalized liposome (DC-liposome) that can show pH-dependent cationic properties for endosomal escape mediated drug delivery. DC-liposome was designed using common lipid 1,2-dipalmitoyl-sn-glycero-3-phosphocholine (DPPC) and 3ß-[N-(N',N'-dimethylaminoethane)-carbamoyl]cholesterol hydrochloride (DC-Cholesterol·HCl) via thin-film hydration technique. Owing to the presence of DC - moiety, we hypothesize that DC-liposome shows pH-dependent

cationic properties that can initiate and enhance membrane fusion with anionic endosomal membrane via electrostatic interaction, thereby causing endosomal escape. Endosomal escape was analyzed using a confocal microscopy-based colocalization experiment. Further, doxorubicin, a clinical anticancer drug, was loaded in liposome to evaluate drug delivery potential. This study explores the endosome escape capability of pH-responsive DC-liposome. A better understanding of mechanistic detail of nanoparticulate drug delivery systems to overcome the endosomal barrier will greatly contribute toward the development of effective nanotherapeutics.

3.2 Materials and methods

3.2.1 Chemicals and Reagents

1,2-dipalmitoyl-sn-glycero-3-phosphocholine (DPPC) and 3ß-[N-(N',N'-dimethylaminoethane)-carbamoyl]cholesterol hydrochloride (DC-Cholesterol·HCl), Phospholipid conjugated l-α-Phosphatidylethanolamine-N-(lissamine rhodamine-B sulfonyl) (Ammonium Salt) (RhB), and l-α-Phosphatidylethanolamine-N-(4-nitrobenzo-2-oxa-1,3-diazole) (Ammonium Salt) (NBD) were purchased from Avanti Polar Lipid Inc. (Alabaster, AL, USA). CellLight^{TM} Early Endosomes-GFP and CellLight^{TM} Late Endosomes-GFP were purchased from Thermo Fisher Scientific. DAPI dye (4′,6-Diamidino-2-phenylindole dihydrochloride) and (3-(4,5-dimethylthiazol-2-yl)-2,5-diphenyl tetrazolium bromide) (MTT) reagent were purchased from Sigma-Aldrich. Doxorubicin Hydrochloride (DOX) European Pharmacopoeia (EP) Reference Standard was purchased from Sigma-Aldrich. All other reagents and chemicals were of analytical grade.

3.2.2 Cell lines

Mouse normal fibroblast (NIH/3T3) and mouse osteosarcoma (K7M2) were purchased from ATCC, Manassas, USA. Cells were maintained in Dulbecco’s Modified Eagle’s Medium

(DMEM) supplemented with 10% (v/v) Fetal Bovine Serum (FBS) and 1% streptomycin at 37 °C in 5% CO_2 environment.

3.2.3 Synthesis of dimethylaminoethane-carbamoyl functionalized liposome (DC-liposome)

Dimethylaminoethane-carbamoyl functionalized liposome (DC-liposome) was synthesized using 1,2-dipalmitoyl-sn-glycero-3-phosphocholine (DPPC) and 3ß-[N-(N',N'-dimethylaminoethane)-carbamoyl]cholesterol hydrochloride (DC-Cholesterol·HCl) in a molar ration of 7:3 via thin film hydration followed by membrane extrusion as described by Pitchaimani et al.[139] Briefly, DPPC and DC-Cholesterol·HCl were dispersed in chloroform in a molar ratio of 7:3. The mixture was then left to dry overnight to create a thin film of lipid and cholesterol. Thin-film was hydrated with phosphate buffer saline (PBS). It was then vortexed and sonicated for proper mixing and formation of a liposome. Liposomes were then extruded using 400 and 200 nm polycarbonate membrane filter, respectively, to control size homogeneity. Control liposome was formulated using DPPC and normal cholesterol following the same method. RhB and NBD labeled liposomes were synthesized using RhB and NBD conjugated lipid in a final volume concentration of 0.01% via hydrophobic insertion following thin film hydration technique.

3.2.4 Characterization

Formulated liposomes were characterized for hydrodynamic size and surface property using dynamic light scattering (DLS, Malvern ZSP). Morphology of liposomes was analyzed by using transmission electron microscopy (TEM, FEI Technai G2 Spirit BioTWIN). The stability of liposome was studied by monitoring hydrodynamic size and zeta potential over a period. Serum stability of liposome was studied by tracking optical absorbance of liposome at 560 nm wavelength in serum environment using Microplate reader (BioTek, Synergy H1 Hybrid reader). pH-

responsive characteristic of DC-liposome was analyzed by studying surface zeta potential of DC-liposome at acidic (pH 5.5), basic (pH 10), and neutral condition (pH 7.4). Liposome designed using DPPC and cholesterol (7:3 molar ratio) was used as control. Fusogenic characteristic of DC-liposome was studied using fluorescence resonance energy transfer (FRET).[140] For this, fusogenic FRET liposome with an electron acceptor was created by incorporating lipid conjugated RhB dye in cationic DC-liposome (l-α-Phosphatidylethanolamine-N-(4-nitrobenzo-2-oxa-1,3-diazole) (Ammonium Salt) and fusogenic FRET liposome with an electron acceptor was formulated by incorporating lipid conjugated NBD dye in anionic liposome (DPPC:DSPG:Chol = 5:2:3). The molar ratio of RhB to NBD in the final mixture was 7:1. For fusion study, 50 µl of cationic RhB-FRET liposome was incubated with 50 µl of anionic NBD-FRET liposome in a 96-well plate for 5 min, and the mixture was analyzed spectrofluorimetrically by exciting sample at 470 nm and recording emission spectrum between 500 nm and 700 nm, at different pH environments.

3.2.5 Drug loading and release study

Active and passive drug loading strategies were carried out to analyze the drug loading efficiency of DC-liposome. (DOX), a clinical anticancer agent was used in this study. The different initial input of DOX with different concentration viz. 25, 50, 100, 150, 200, and 400 µg/mL was used to find the optimum initial input with the highest loading efficiency. For passive loading, the membrane extrusion-based physical encapsulation technique was followed.[141] Briefly, lipid thin film was hydrated with DOX solution and mixed well. The mixture was vortexed (3 min), bath sonicated (5 min), and probe sonicated (3 min, 50% amplitude). Finally, the mixture was extruded through 400 nm and 200 nm polycarbonate membrane filter, respectively. DOX loaded DC-liposome was purified to remove unloaded DOX by Amicon Ultra-4 centrifugal filter, 10kDa (Millipore Sigma).

For active loading, an ammonium sulfate gradient was used.[142] Briefly, lipid film was hydrated with one ml of 300 mM Ammonium Sulfate and mixed well. The mixture was vortexed (3 min), bath sonicated (5 min), and probe sonicated (3 min, 50% amplitude). The mixture was extruded using a polycarbonate membrane filter to fabricate DC-liposome. Ammonium sulfate was exchanged with PBS by Amicon Ultra-4 centrifugal filter, 10 kDa (Millipore Sigma) to create a transmembrane ammonium sulfate gradient. After that, liposome was incubated with DOX for 4 h (50°C) for DOX encapsulation. Finally, DOX loaded liposome was purified to remove unloaded DOX by Amicon Ultra-4 centrifugal filter, 10 kDa (Millipore Sigma). The amount of DOX loaded was quantified spectrofluorimetrically.

DOX loading efficiency was calculated by the following equation:

% Loading Efficiency = (encapsulated DOX/ initial input of DOX) x 100

Drug release study was carried out in physiological (PBS, pH 7.4) and acidic (Acetate buffer, pH 5.5) conditions. 1 mL of DOX loaded DC-liposome (2 mg/mL) was dialyzed using 3.5 kDa dialysis membrane in 120 mL of drug release media kept at 37 °C while constant stirring (80 rpm) to maintain the sink condition during the experiments. 500 µL of release media was taken at regular intervals and replaced by fresh media. The amount of DOX in the release media was calculated spectrofluorimetrically by measuring DOX excitation and emission at 490 nm and 595 nm.

Drug release was quantified by using the following equation:

% Drug release = (DOX amount in release media/ DOX amount in 100% release) x 100

3.2.6 Biocompatibility

Biocompatibility of DC-liposome was analyzed in mouse osteosarcoma (K7M2) and mouse normal fibroblast (NIH/3T3) using MTT assay.[143,144] Briefly, 10,000 cells were seeded in

96 well plates and incubated with DC-liposome at varying concentration range (3.125, 6.25, 12.5, 25, 50, 100, and 200 µg/mL) for 48 h at 37 °C in 5% CO_2 environment. Control cells were maintained with media only. After 48 h incubation, treatment media was removed and cells were incubated with MTT reagent for 2 h. DMSO was added to dissolve the insoluble formazan crystal formed after MTT treatment, and absorbance was recorded at 550 nm using a microplate reader (BioTek, Synergy H1 Hybrid reader).

3.2.7 Endosomal escape study via confocal microscopy

Endosomal escape behavior of DC-liposome was studied using confocal microscopy.[145] For this, the co-localization experiments of RhB labeled DC-liposome with early and late endosomes were carried out. CellLight™ Early Endosomes-green fluorescent protein (GFP) and Cell Light™ Late Endosomes-GFP were used to label early and late endosomes in cells, respectively, following manufacturer protocol. Briefly, 10,000 cells were seeded in 96 well plates and incubated with 10 µL GFP for 20 h for transfection. After that, transfection media was removed with fresh media and transfected cells were incubated with rhodamine B labeled DC-liposome for 3 h. Cells were then fixed by 4% paraformaldehyde. Nucleus was stained by DAPI and cells were observed under a Confocal Laser Scanning Microscope (Carl Zeiss, LSM-700). The degree of co-localization was quantified based upon Pearson's correlation coefficient (R) using ImageJ colocalization analysis.

3.2.8 *In-Vitro* Toxicity

In-vitro toxicity of Free DOX and DOX loaded DC-liposome (DOX-DC-liposome) were analyzed in mouse osteosarcoma (K7M2) and mouse normal fibroblast (NIH/3T3) following MTT assay. Briefly, 10,000 cells were seeded in 96 well plates and incubated with Free DOX and DOX-DC-liposome at varying concentration range (µM) for 48 h at 37 °C in 5% CO_2 environment.

Control cells were maintained with media only. After 48 h incubation, treatment media was removed and cells were incubated with MTT reagent for 2 h. DMSO was added to dissolve the insoluble formazan crystal formed after MTT treatment, and absorbance was recorded at 550 nm using a microplate reader (BioTek, Synergy H1 Hybrid reader). IC50 concentration was calculated using GraphPad software following "log (inhibitor) vs. normalized response-variable slope" model.[146]

3.2.9 Statistical analysis

GraphPad software was used to analyze statistical models for IC50. All data represent the mean ± standard deviation. Biocompatibility and Cytotoxicity data include six replicates (n = 6). All other major data includes at least three replicates (n = 3).

3.3 Result and Discussion

3.3.1 Fabrication and characterization of DC-liposome

DC-liposome was designed using dimethylaminoethane carbamoyl conjugated cholesterol (DC-cholesterol), which contains ~2.5% of cationic nitrogen, and DPPC lipid (7:3 molar ratio) via thin-film hydration technique as detailed in methods. The presence of DC moiety in DC-cholesterol gives rise to characteristic cationic property in the liposome. DC-liposome was characterized for size and surface property using dynamic light scattering (DLS). Morphological properties were analyzed by transmission electron microscopy (TEM). DLS showed the average hydrodynamic size of DC-cholesterol to be 113 ± 2 nm with an impressive polydispersity index of 0.08 ± 0.03 and a positive zeta potential of 7.6 ± 1 mV (**Figure 3.1**). TEM showed the crystals of DOX at the core of the spherical DC-liposomes (**Figure 3.1B**). DC-liposome was analyzed for its hydrodynamic size and PDI for seven days to ensure its colloidal stability (**Figure 3.1C**). The nominal changes observed in both hydrodynamic size and PDI over the week of observation

confers the stability of the liposome. Further, serum stability of DC-liposome was analyzed to examine the stability of particle in serum environment spectrophotometrically. This is the measure of rapid change in serum absorbance due to the particle aggregation with serum proteins.[147,148] Aggregation is a rapid process that happens at its first touch with serum, therefore, the change in absorbance at early time points of serum and NP interaction is crucial. As shown in **Figure 3.1D**, there is no change in serum absorbance over a period suggesting a high degree of serum stability of the DC-liposome. Poly(lactic-co-glycolic acid) (PLGA) nanoparticle was used as positive control which showed aggregation in serum environment as depicted by the increase in optical

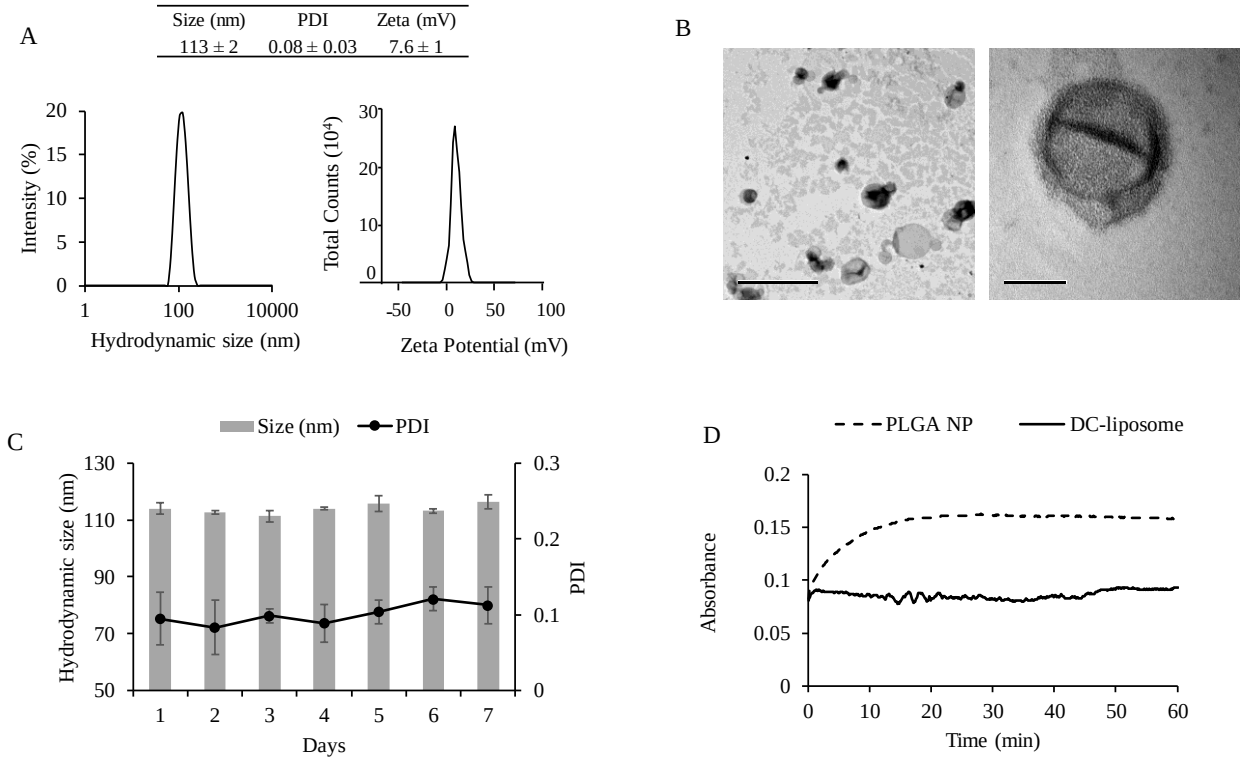

Figure 3.1 Characterization of DC-liposome. (A) Hydrodynamic size distribution and zeta potential of DC-liposome showing surface charge distribution, (B) transmission electron microscope image of DC-liposome at different magnification, (C) stability of DC-liposome over seven days in terms of hydrodynamic size and polydispersity index (PDI), and (D) serum stability of DC-liposome over sixty minute in terms of optical absorbance at 560 nm. Poly(lactic-co-glycolic acid) (PLGA) was used as positive control.

absorbance. These findings of stability assay confirmed the stability of DC-liposome in aqueous and serum environment.

3.3.2 pH-responsive characteristic of DC-liposome

Nanoparticle formulation responsive to pH gradient can be desirable for drug delivery as we can exploit the differential characteristic of nanoparticle at a specific pH.[149,150] Here, pH responsiveness of DC-liposome was characterized by tracking the change in surface charge properties of DC-liposome at physiological (pH 7.4), acidic (pH 5.5), and basic condition (pH 10). As depicted in **Figure 3.2A**, zeta potential measurement showed around 8x increment in cationic property of DC-liposome at acidic condition, from +7.6 mV at pH 7.4 to +64 mV at pH 5.5. While in basic condition, DC-liposome showed a broad distribution of zeta potential without any significant peak suggesting particle instability and breakdown. The observed distinct surface property of DC-liposome at three different pH conditions clearly showed that the surface property

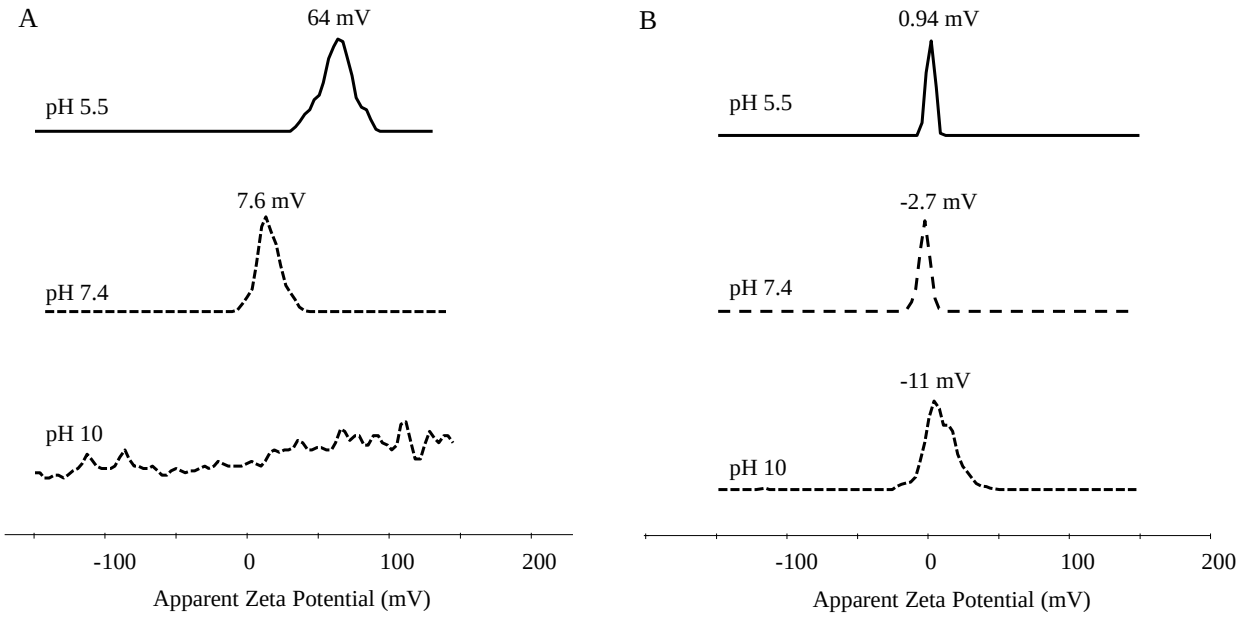

Figure 3.2 pH-responsive characteristic of DC-liposome. (A) Zeta potential of DC-liposome at different pH condition viz. pH 5.5, pH 7.4, and pH 10 showing significant variation in zeta potential with pH and (B) zeta potential of control liposome at different pH condition viz. pH 5.5, pH 7.4, and pH 10 showing minimal variation in zeta potential with pH.

of DC-liposome is a function of pH environment, confirming the pH-responsive characteristic of DC-liposome. As a control experiment, the surface property of control liposomes with normal cholesterol was analyzed at different pH environments (**Figure 3.2B**). Zeta potential measurement of control liposome showed minimal changes in zeta potential at different pH: -2.7 mV (pH 7.4), 0.94 mV (pH 5.5), and -11 mV (pH 10). The dramatic increment in cationic property observed in DC-liposome at acidic conditions may be due to the protonation of the amine group of dimethylaminoethane carbamoyl moiety in DC-cholesterol. This enhanced cationic property at acidic conditions can be exploited in endosomal escape mediated drug delivery via membrane fusion.

3.3.3 Fusogenic property of DC-liposome

Fusogenic property of DC-liposome was characterized by fluorescence resonance energy transfer (FRET) following an established protocol.[141,146,151] FRET has been widely used to analyze membrane fusion.[141,151–154] Here, two FRET liposomes were prepared and fusion behavior was studied. Cationic DC-liposome was incorporated with FRET acceptor RhB lipid and anionic liposome was formulated by incorporating FRET donor NBD lipid. The fusion behavior of these two lipids with the opposite surface charge was analyzed at three different pH environments; physiological (pH 7.4), acidic (pH 5.5) and basic (pH 10). **Figure 3.3** shows results from FRET experiments with emission spectra of anionic, cationic, and hybridized liposomes at different pH conditions. Decrement of donor fluorescent intensity at 525 nm (donor λ_{max}) and increment of acceptor fluorescent intensity at 595 nm (acceptor λ_{max}) due to fusion, suggest successful energy transfer between FRET pairs validating our clam of fusion between two liposomes. To understand how the pH environment can interfere with this fusion behavior, fusion was carried out in acidic and basic conditions. Experiments showed successful fusion in all the different pH environment,

with different efficiency. Importantly, emission spectra of acceptor showed significant increment in fluorescence at 595 nm with different pH conditions suggesting the influence of pH in the fusogenic characteristics of DC-liposome. The highest increment in acceptor fluorescent intensity

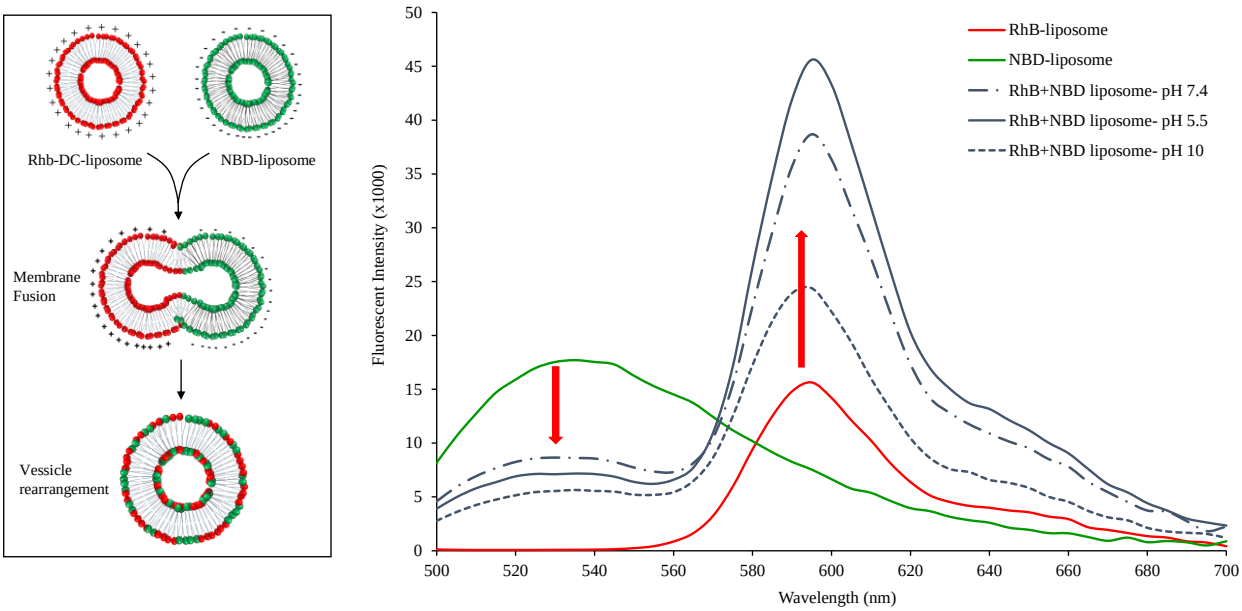

Figure 3.3 Study of the fusogenic characteristics of DC-liposome through Fluorescence Resonance Energy Transfer (FRET). DC-liposome with the positive surface charge was labeled with fluorescent acceptor RhB (λem= 595 nm). Anionic liposome was labeled with fluorescent donor NBD (λem= 525 nm). The fusion between two liposomes mediated by electrostatic interaction (schematic illustration on the right) was confirmed by FRET analysis at an excitation wavelength of 470 nm. Emission spectra of RhB+NBD liposome showed energy transfer from FRET donor NBD to FRET acceptor RhB showing successful fusion. Fusion behavior was characterized at three different pH environment (pH 5.5, pH 7.4, and pH 10).

at 595 nm was observed in acidic conditions (pH 5.5) suggesting maximum fusion. This differential fusogenic property at different pH is in accordance with the pH-responsive cationic property of DC-liposome. Here, membrane fusion is mediated by electrostatic interaction as two membranes are oppositely charged. So, high fusion characteristics at acidic pH can be attributed to enhanced cationic property of DC-liposome thereby accelerating membrane fusion. The observed enhanced fusogenic characteristic at acidic conditions can be favorable for endosomal

membrane fusion resulting in the endosomal escape. The endosomal membrane is characterized by anionic property and acidic pH environment.[155] In such a scenario, pH-responsive cationic DC-liposome can be an ideal candidate for endosome escape mediated drug delivery.

3.3.4 Drug loading and release characteristic

With the assurance of desirable pH-responsive characteristic of DC-liposome, drug loading and release behavior of DC-liposome was studied. DOX, a clinical anticancer drug, was used as a model drug. DOX was loaded with both passive and active method and loading efficiency was evaluated to investigate the influence of the loading method in drug loading efficiency. **Figure 3.4** shows DOX loading percentage and DOX content (wt%) with respect to different initial input of DOX (25, 50, 100, 150, 200, and 400 µg/mL) using active (**Figure 3.4A**) and passive (**Figure 3.S1**) loading methods. As expected, the active loading method showed higher DOX loading characteristics compared to that of the passive method, facilitated by the active ammonium sulfate transmembrane gradient. Due to ammonium gradient, free DOX actively diffuses inside liposome core and crystallize as Doxorubicin sulfate.[142] Active loading method showed DOX loading percentage from 24% to 70% and DOX content from 1.5 wt% to 2.7 wt%, at different initial input. Based upon overall DOX loading, the initial DOX input of 200 µg/mL showed the optimum result, with 59% loading efficiency and 2.7 wt% DOX content.

Similarly, passive loading method showed DOX loading percentage from 12% to 42%, and DOX content from 0.6 wt% to 1.2 wt%, at different initial input. Here, the initial input of 150 and 200 µg/mL showed the optimum result of 21% loading efficiency and 1 wt% DOX content. These numbers clearly suggest the advantage of using an active loading method for high loading efficiency. However, it is important to note that we observed a significant increment in size and PDI of DC-liposome after active loading (**Figure 3.4B**), with an average size of 196 nm (vs 113

nm) and 0.16 PDI (vs 0.08). This change in the size of the DC-liposome might be due to the effect of a transmembrane influx of DOX and the formation of DOX crystal due to active loading. Contrary to that, in the case of passive loading, there was minimal change in the average size and PDI after loading, with an average size of 143 nm (vs 113 nm) and 0.09 PDI (vs 0.08). Both active and passive loading method suggested the use of 200 µg/mL as an initial input of DOX concentration for the best loading efficiency. DOX loading assay confirmed the loading capability of DC-liposome by both active and passive loading methods.

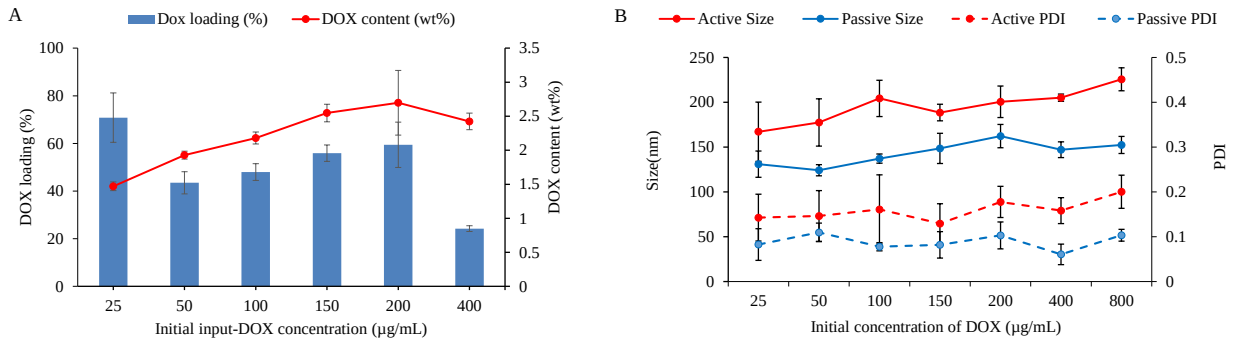

Figure 3.4 In-vitro drug loading study. (A) Doxorubicin (DOX) loading efficiency and DOX content by weight percentage with respect to carrier in different initial input concentration of DOX (µg/mL) via active loading method and (B) variation in hydrodynamic size and polydispersity index (PDI) of DC-liposome after active and passive loading with respect to different initial input concentration of DOX (µg/mL).

Further, drug release behavior was studied to characterize the drug release kinetics of DOX loaded DC-liposome (DOX-DC-liposome) under physiological condition (pH 7.4) and acidic condition (pH 5.5), as depicted in **Figure 3.5A**. DOX release assay showed an initial burst release of DOX up to 8 h followed by sustained release up to 48 h. DOX-DC-liposome showed higher drug release characteristics in the acidic environment compared to normal physiological conditions, with the release of 91% of DOX compared to 60% in normal conditions. Observed higher release at acidic conditions might be due to the elevated cationic property at the acidic

condition which can potentially result in membrane leakage and/or instability.[156,157] This elevated release characteristic at acidic pH can be attributed as another pH-responsive feature along with cationic and fusogenic properties. All these pH-responsive characteristics can collectively contribute to the endosomal escape mediated drug delivery.

3.3.5 Biocompatibility

Cationic liposomes are a favorable agent for drug delivery due to their ease of cellular internalization assisted by electrostatic interaction.[158–161] However, the major concern with the use of cationic liposomes is their associated genotoxicity. Due to the cationic surface charge, the cationic liposome can potentially damage genetic materials of the cell including DNA.[162,163] To address this issue of toxicity, the biocompatibility of cationic DC-liposome was evaluated in mouse osteosarcoma K7M2 and mouse normal fibroblast NIH/3T3 using cell viability assay for 48 h. Cell viability assay showed concentration-dependent biocompatibility with above 70% cell viability up to 50 µg/mL liposome concentration in both cancer and normal cell line (**Figure 3.5B**). Beyond that concentration, at 100 and 200 µg/mL, DC-liposome showed poor biocompatibility showing a toxic effect in K7M2. Interestingly, for NIH/3T3, DC-liposome showed

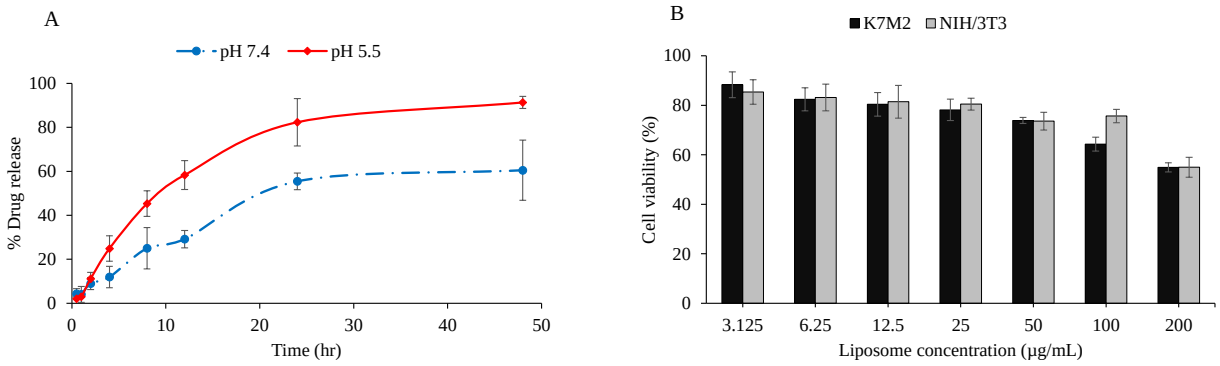

Figure 3.5 In-vitro drug release and biocompatibility study of DC-liposome. (A) DOX release characteristic of DOX loaded DC-liposome at acidic condition (Acetate buffer, pH 5.5) and normal physiological condition (PBS, pH 7.4). Biocompatibility of DC-liposome evaluated on mouse osteosarcoma K7M2 and mouse normal fibroblast NIH/3T3 in terms of percentage cell viability calculated using MTT assay. Cells were treated with DC-liposome for 48 h.

biocompatibility even at a high concentration of 100 µg/mL with 75% cell viability. At a high concentration of 200 µg/mL, DC-liposome showed significant toxicity for both K7M2 and NIH/3T3. Biocompatibility assay revealed the effect of cationic liposome on the cell is dependent upon cell type and concentration. So, it is crucial to optimize the safe concentration dose of cationic liposomes to avoid any possible toxic effect of the carrier. Here, our observations revealed good biocompatibility of DC-liposome at a concentration below 100 µg/mL.

3.3.6 Endosomal escape study

Endosomal degradation of the therapeutic agent is one of the major problems associated with nanoparticulate drug delivery technique.[164–166] Here, we hypothesized that due to the pH-responsive cationic and fusogenic properties of DC-liposome, it can escape endosome via membrane fusion. To test this hypothesis, the endosome escape study was done via confocal imaging in mouse osteosarcoma as a model cell line. Early and late endosomes in cells were labeled by green fluorescent protein (GFP) via transfection using CellLight™ Early Endosomes-GFP and Late Endosomes-GFP, respectively following manufacturer protocol as detailed in the method. DC-liposome was labeled RhB via hydrophobic insertion using membrane extrusion. RhB labeled DC-liposome was incubated with early and late endosome labeled cell independently for 3 h to study the localization of DC-liposome. **Figure 3.6** represents the confocal image for colocalization study where red color represent DC-liposome and green color represent early and late endosome. The yellow color observed in the merged figure signifies co-localization suggesting the localization of DC-liposome in the endosome. The merged figure of the confocal image revealed a higher amount of co-localization between early endosome and DC-liposome compared to late endosome and DC-liposome. To quantitatively analyze this difference, co-localization analysis was done using ImageJ following the co-localization threshold and coloc2 plugin.[167,168]

Pearson's correlation coefficient (PCC) was used as a statistic tool for quantifying colocalization.[169] PCC or Pearson's R-value ranges from -1 to +1. Higher the PCC numerical value, the higher will be the extent of co-localization. PCC analysis confirmed higher co-localization of DC-liposome with early endosome, with Pearson R-value of 0.69, compared to that of the late endosome, with Pearson's R-value of 0.44. These data show a 36% reduction in co-localization at the late endosome. This significant reduction in co-localization from DC-liposome-early endosome to DC-liposome-late endosome suggests possible endosomal escape of DC-liposome from the early endosome.

The endosome/lysosome system works in the trafficking of cargo inside the cell, it's recycling, and degradation.[126] Foreign materials are internalized in the cell by endocytosis. Primary endocytic vesicles containing internalized foreign materials deliver their content into the early endosomes. Early endosome accumulates cargo and support recycling to the plasma membrane before it matures to the late endosome. This usually takes 8-15 min.[170] After maturation, late endosome fuses to the lysosome to generate endolysosome where active degradation takes place.[126] So, it is crucial for the therapeutic agents to escape early endosomes to avoid lysosomal degradation and maintain its therapeutic effect. Here, based upon the co-localization study, DC-liposome escapes early endosomes. The mechanism of escape can be attributed to the elevated fusogenic characteristic of DC-liposome contributed by the higher cationic property at acidic pH. The endosome is characterized by the acidic environment and anionic lipid bilayer [155]. The acidic environment of endosome increases the cationic property of DC-liposome thereby increasing fusion, as depicted in graphical abstract. This leads to release of payload, here DOX. This kind of membrane fusion based endosomal escape has been hypothesized as one of the major pathways of endosomal escape in literatures [130,171–173]. Here, the unique pH-responsive characteristic of DC-

liposome has successfully assisted to escape endosome thereby facilitating maximum efficacy in drug delivery.

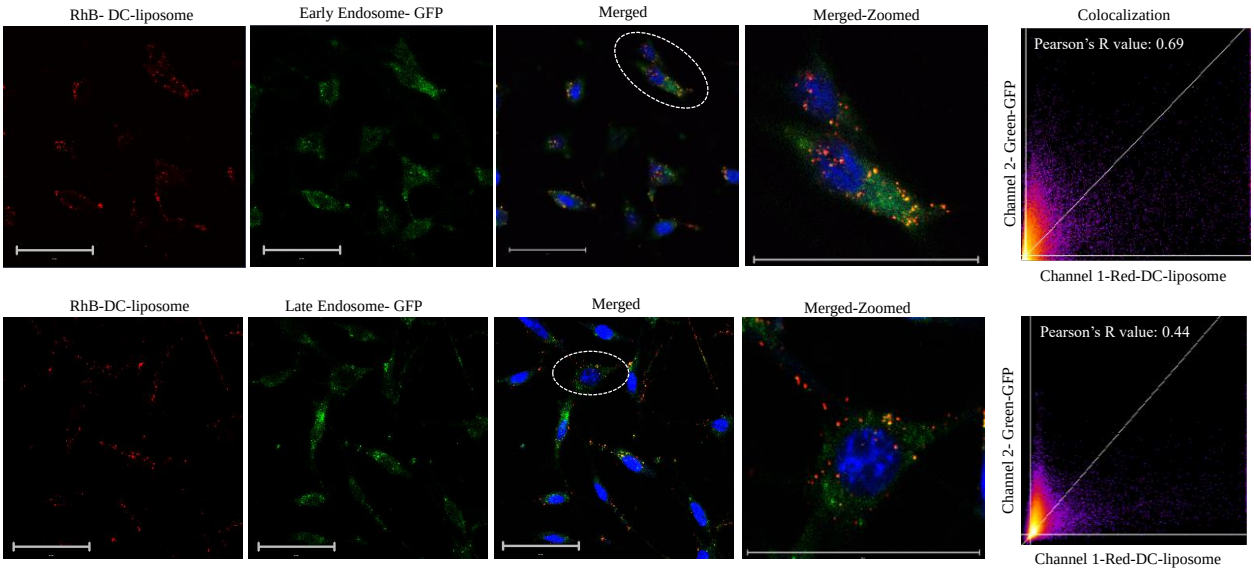

Figure 3.6 Endosomal escape study via confocal microscopy. Figure shows the confocal image of mouse osteosarcoma K7M2 showing internalization and endosomal localization of rhodamine B labeled DC-liposome (RhB-DC-liposome) (Label: 50 µm). Cells were transfected by CellLightTM Early Endosomes-green fluorescent protein (GFP) and CellLightTM Late Endosomes-GFP separately to label early endosome (top row) and late endosome (bottom row), respectively. The transfected cell line was incubated with rhodamine B labeled DC-liposome (RhB-DC-liposome) for 3 h and imaged via confocal microscopy. The colocalization of DC-liposome with early and late endosomes was analyzed separately. Yellow color in the merged figure represents co-localized DC-liposome in the endosomal compartment. Colocalization was quantitatively analyzed in terms of Pearson's correlation coefficient (R) using ImageJ colocalization analysis.

3.3.7 *In-vitro* toxicity

Finally, the therapeutic efficiency of the proposed nanosystem was evaluated. DOX loaded DC-liposome (DOX-DC-liposome) was assessed for *in-vitro* toxicity in mouse osteosarcoma K7M2 and mouse fibroblast NIH/3T3 using MTT assay (**Figure 3.7**). DOX-DC-liposome showed higher toxicity compared to free DOX in both cell lines tested. Half minimal inhibitory concentration (IC50) showed a clear distinction of elevated toxicity by DOX-DC-liposome in both cell lines. In NIH/3T3, DOX-DC-liposomes showed a significant reduction in IC50 (IC50=0.9

μM) compared to free DOX (IC50=2.1 μM). Likewise, in K7M2, DOX-DC-liposome showed IC50 of 0.42 μM and that of free DOX exhibit IC50 of 0.89 μM. Observed elevated toxicity of DOX-DC-liposome can be attributed to the endosome escape mediated release of DOX, which increases the local drug concentration thereby increasing its therapeutic efficacy. *In-vitro* toxicity assay of DOX-DC-liposome further supported the hypothesized endosomal escape mediated drug delivery.

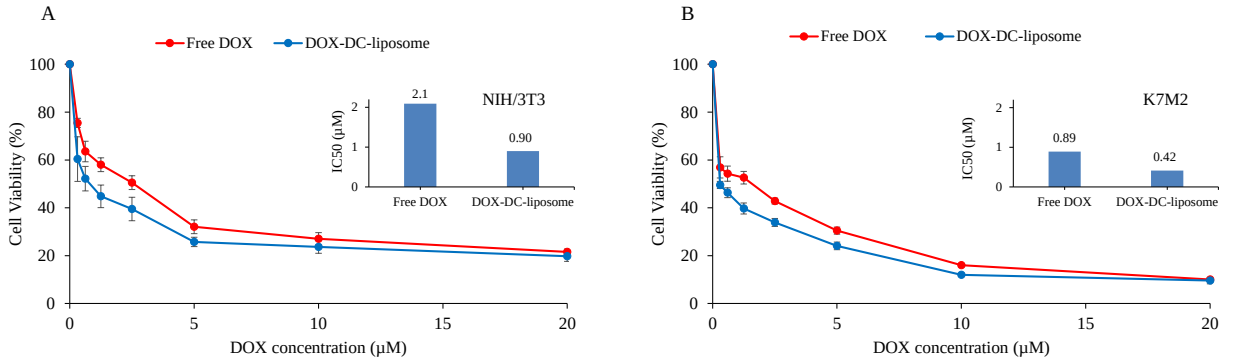

Figure 3.7 In-vitro toxicity assay. (A) Toxicity of Free DOX and DOX loaded DC-liposome (DOX-DC-liposome) on mouse normal fibroblast NIH/3T3 and (B) mouse osteosarcoma K7M2. Half minimal inhibitory concentration (IC50) shown in the inset was calculated using GraphPad software following "log(inhibitor) vs. normalized response-variable slope" model.

3.4 Conclusion

This study has successfully explored the pH-responsive characteristic of DC-liposome using surface characteristic analysis, fluorescent-based energy transfer study, and drug release kinetics. The consequences of pH-responsive characteristics have been explored in endosomal escape behavior and toxicity of drug-loaded carriers in terms of IC50. DC-liposome showed pH-responsive cationic, fusogenic, and drug release properties with higher expression in acidic conditions. With good stability at both aqueous and serum environment followed by concentration-dependent biocompatibility, DC-liposome can be considered as an ideal delivery agent. Importantly, the observed endosome escaping capability via the elevated membrane fusion

mechanism at the acidic endosomal compartment can be a rewarding characteristic for the drug delivery system. Further, the successful loading of anticancer drug, doxorubicin, and high therapeutic value of DOX-DC-liposome against cancer cells confirmed the therapeutic advantage of the proposed liposomal system. These preliminary results contribute to the proof-of-concept of using pH-responsive cationic liposomes to break the endosomal barrier in drug delivery for better therapeutic efficacy.

Chapter 4 - Macrophage-derived exosome-mimetic hybrid vesicles for tumor targeted drug delivery

***Chapter 4**, in full, is a reprint of the material as it appears in Acta Biomaterialia, 2019, Sagar Rayamajhi, Tuyen Duong Thanh Nguyen, Ramesh Marasini, and Santosh Aryal. doi: 10.1016/j.colsurfb.2020.110804*

Abstract

Extracellular vesicles (EVs) are phospholipid and protein constructs which are continuously secreted by cells in the form of smaller (30-200 nm) and larger (micron size) particles. While all of these vesicles are called as EVs, the smaller size are normally called as exosomes. Small EVs (sEVs) have now been explored as a potential candidate in therapeutics delivery owing to their endogenous functionality, intrinsic targeting property, and ability to cooperate with a host defense mechanism. Considering these potentials, we hypothesize that immune cell-derived sEVs can mimic immune cell to target cancer. However, different sEVs isolation technique reported poor yield and loss of functional properties. To solve this problem, herein we hybridized sEVs with synthetic liposome to engineer vesicles with size less than 200 nm to mimic the size of exosome and named as hybrid exosome (HE). To achieve this goal, sEVs from mouse macrophage was hybridized with synthetic liposome to engineer HE. The fluorescence-based experiment confirmed the successful hybridization process yielding HE with the size of 177±21 nm. Major protein analysis from Blot techniques reveals the presence of EV marker proteins CD81, CD63, and CD9. Differential cellular interaction of HE was observed when treated with normal and cancerous cells thereby supporting our hypothesis. Moreover, a water-soluble doxorubicin was loaded in HE. Drug-loaded HE showed enhanced toxicity against cancer

cells and pH-sensitive drug release in acidic condition, benefiting drug delivery to acidic cancer environment. These results suggest that the engineered HE would be an exciting platform for tumor-targeted drug delivery.

4.1 Introduction

Extracellular vesicles (EVs) are nano to micron sized particulates secreted by cells which later excreted to the extracellular space.[174] There are three types of EVs categories on the basis of their biogenesis and size viz.; (1) exosomes (30-150 nm), (2) micro vesicles (200-500 nm), and (3) apoptotic bodies (1-10 μm).[175] While all these vesicles are called as EVs, the smaller sized vesicles are normally called as exosomes which differentiate itself from other EVs due to its unique biogenesis. Exosome biogenesis differentiates it from other extracellular vesicles due to the endocytic origin and unique cargo sorting process to load cellular content like proteins, nucleic acid, and lipids.[176] Microvesicles and apoptotic bodies, on the other hand, are EVs subtypes derived from the plasma membrane and have the relatively large size. Since it is extremely difficult to find the particular biogenesis pathway of EVs, here, we have termed "small EVs" (sEVs) instead of "exosomes" to represent EVs of size less than 200 nm, as recommended by minimal information for studies of extracellular vesicles 2018 (MISEV2018).[177] sEVs, here, includes exosomes and small microvesicles with size below 200 nm. These vesicles are made up of the skeleton of a phospholipid bilayer that can be pictured as a typical drug delivery liposome. Therefore, sEVs have now been explored as a potential candidate in therapeutics delivery. Toward this attempt, initial studies have been carried out to understand sEV cellular internalization process, which was found to follow the path similar to that of the liposomal nanoparticulate system such as opsonization, receptor interaction, and fusion to deliver its cargo.[178] It has been reported that sEV

delivery led to higher drug accumulation in target cells and improve small molecule stability and blood circulation time, thus improving the potency of small molecule drugs.[179,180]

sEVs are secreted by most cell types including immune cells, stem cell, endothelial, and epithelial cells.[77,181–187] A variety of both membrane-bound and intracellular proteins can be found in sEVs. The most common of these include membrane transport and fusion proteins, major histocompatibility complexes, heat shock proteins, tetraspanins, proteins of the endosomal sorting complex required for transport (ESCRT) complex, and lipid raft-associated proteins.[59] They are recognized as important messengers of long distance intercellular communication and are involved in a diverse range of the biological process. Due to these unique properties, sEVs are regarded as a vector that operates intra- and inter-cellular signaling of target cells.[188] This communication skill is naturally acquired from its origin, which is specific in recognizing its target, therefore hold properties to adapt itself in harsh in vivo conditions such as communication with immune cells to convince the body that they belong to a common biological lineage.[189,190] Due to these skill-sets of sEVs, they have been exploited in drug delivery to the tumor where it deserves to recognize cancer and reduces the nonspecific distribution of the drug to a wide range of tissues and organs. Recently, Batrakova and coworkers reported a macrophage-derived exosome for targeted paclitaxel delivery to pulmonary metastases, which shows a significantly strong suppression of metastases growth and greater survival time.[191] Similarly, an array of sEVs have been evaluated for their drug delivery potentials.[179,191,191–196] A comparative study of different cell type-derived exosomes was conducted by Xiang et. al., in which researchers found the effective antitumor immunity when treated with dendritic cell-derived exosomes than that of tumor cell-derived exosomes.[197] sEVs from professional antigen presenting cells, such as dendritic cells, B cells and macrophages are known to express functional immune modulating proteins including MHC-class

I and/or MHC class-II, which preferentially induce Th1-type (cell-mediated) immune response that directs T cells to attack abnormal cells (such as cancer cells) or cells infected with intracellular parasites.[197–199]

However, the isolation of sEVs in the quantities needed for application is limited due to its poor yield.[200,201] Therefore, several techniques for sEV isolation including ultracentrifugation, ultrafiltration, precipitation, immunoaffinity-based separation, and microfluidics-based, which separate sEVs-based upon their size, density, and protein markers have been explored.[202] Yet, the preservation of structural integrity and functional properties of sEVs isolated with these techniques are a major concern. Therefore, to address these issues, membrane fusion techniques have been reported. For example, a freeze-thaw and incubation-mediated membrane fusion techniques have been explored by the researchers.[68,203,204] All these techniques have their own advantages and disadvantages in regard to ensure the purity and abundance, which is critical for the development of EV-based drug delivery. For example, Freeze thaw method can damage the sEVs protein content[73], the incubation method of membrane fusion can lead to particles with a big size and high polydispersity index, and the immunoaffinity-based separation results in the protein heterogeneity due to the difficulty in separating sEVs from the substrate. Most importantly, a major hurdle in these methods is lack of maintaining size homogeneity in the product. Among this technique, ultracentrifugation based technique is one of the most commonly used due to its simplicity and reagent-free approach, and are reported to accounts for over 56% users in the field.[205] Therefore, considered as a gold standard for sEVs isolation, however, may damage sEVs due to vigorous mechanical stress.[202,206] To address this problem, here, we have developed an optimized method for sEVs isolation by combining normal centrifugation, filtration, and size extrusion techniques to get a homogenous population of sEVs. This technique is simple, reagent-free, and uses relatively

less stress on sEVs. Further, to solve the issue of the low yield, sEV was hybridized with liposome using extrusion-based membrane fusion technique to engineer vesicles with size less than 200 nm to mimic the size of exosome and named as hybrid exosome (HE).

The aim of this membrane fusion mediated HE formulation is to take advantages of both sEV and liposomal drug delivery system, overcoming their respective shortcomings. sEVs has the advantage of being endogenous nanocarrier, but lacks the modification flexibility, and have low yield.[207] On the other hand, liposome shows prominent flexibility for surface modification facilitating for different engineering approaches but lacks the endogenous functionality.[208,209] While structurally-both sEVs and liposomes are similar having lipid bilayer with ranges in size, sEVs differs from synthetic liposome mainly by the presence of EV proteins. In this study, sEVs derived from mouse macrophage J774A.1 were hybridized with synthetic liposome to formulate HE with uniform size distribution. The aim of using macrophage as sEV source is to exploit the tumor targeting characteristic of macrophage.[210,211] Align toward this direction, we hypothesize that macrophage-derived sEVs will carry the tumor targeting properties of macrophage which can be used for cancer-specific drug delivery. Combining these two-drug delivery system would make an efficient hybrid drug delivery tool with the endogenous nature of sEVs and flexibility of liposomes that would eventually help in accelerating the development of cancer nanomedicine.

4.2 Materials and Methods

4.2.1 Chemicals and reagents

Lipid L-α-phosphatidylcholine (Egg, Chicken) (EggPC) were purchased from Avanti Polar Lipid Inc. (Alabaster, AL, USA). Cholesterol were purchased from Fisher. Mouse monoclonal antibody CD81 (5A6), CD63 (MX-49.129.5), CD9 (C-4), Integrin αM (44) also known as CD11b, TSG101 (51), Histone H3 (FL-136), and β-Actin were purchased from Santa Cruz Biotechnology.

Phospholipid conjugated l-α-Phosphatidylethanolamine-N-(lissamine rhodamine B sulfonyl) (Ammonium Salt) (Rh-B) and l-α-Phosphatidylethanolamine-N-(4-nitrobenzo-2-oxa-1,3-diazole) (Ammonium Salt) (NBD) was purchased from Avanti Polar Lipid Inc. (Alabaster, AL, USA). DAPI dye (4′,6-Diamidino-2-phenylindole dihydrochloride), (3-(4,5-dimethylthiazol-2-yl)-2,5-diphenyl tetrazolium bromide) (MTT) reagent, and Proteinase K from *Tritirachium album* was purchased from Sigma-Aldrich. Halt^{TM} Protease Inhibitor Cocktail, EDTA-Free (100X) was purchased from ThermoFisher SCIENTIFIC. All other reagents and chemical were of analytical grade.

4.2.2 Cell lines

Mouse macrophage cells (J774A.1), mouse osteosarcoma (K7M2), mouse breast cancer cell (4T1), mouse normal fibroblast (NIH/3T3) were purchased from ATCC, Manassas, USA. J774A.1, K7M2 and NIH/3T3 were maintained in Dulbecco's Modified Eagle's Medium (DMEM) supplemented with 10% (v/v) Fetal Bovine Serum (FBS) and 1% streptomycin at 37℃ in 5% CO_2 environment. 4T1 was maintained in Roswell Park Memorial Institute medium (RPMI) supplemented with 10% (v/v) Fetal Bovine Serum (FBS) and 1% streptomycin at 37℃ in 5% CO_2 environment.

4.2.3 Extracellular vesicle isolation

Small Extracellular vesicles (sEVs) were harvested from J774A.1 cells using centrifugation, filtration, and membrane extrusion techniques. J774A.1 cells were cultured in serum-free and phenol red free Dulbecco's Modified Eagle's Medium (DMEM) for 48 h at 37℃ in 5% CO_2 environment to harvest EVs. The media was collected and centrifuged at 2000 g to remove cell debris. Then the supernatant was collected and concentrated around 10 times using 10k molecular weight cut off (MWCO) amicon filter (2000 g, 15 min). The concentrated

supernatant was then extruded with 400 and 200 nm polycarbonate membrane filter consecutively to get uniform sEVs.

4.2.4 Synthesis of liposome

Liposome was synthesized by using simple thin film hydration followed by membrane extrusion as described by Pitchaimani et. al.[79] Briefly, L-α-phosphatidylcholine (Egg, Chicken) (EggPC) and Cholesterol were dispersed in chloroform in a molar ratio of 66:34. The mixture was then left to dry overnight. Then the dried film was hydrated by PBS. It was then vortexed and sonicated for proper mixing. The liposome solution was extruded using 400 and 200 nm polycarbonate membrane filter, respectively, to get nano-sized unilamellar liposomes.

4.2.5 Synthesis of hybrid exosome

Hybrid Exosomes (HE) were synthesized by simple thin film hydration followed by a membrane extrusion method. Previously isolated sEVs were used to hydrate the dry lipid layer. 200 µg protein equivalent of sEV was added to 1000 µg of lipid film in a final volume of 1 mL. It was then vortexed and sonicated (30% amplitude, 30 sec pulse on/off, for 2 min) for proper mixing. Thus formed multilamellar HE solution was extruded through 400 and 200 nm polycarbonate membrane filter, respectively, to get nano-sized unilamellar HE.

4.2.6 Characterization

Liposomes, sEVs, and HEs were characterized for hydrodynamic size and surface charge via dynamic light scattering assay (DLS, Malvern ZSP). Surface morphology of liposome, sEVs, and HEs were studied using Transmission electron microscopy (FEI Technai G2 Spirit BioTWIN). Protein quantification of sEVs were done by using Bradford assay.[212] Stability of vesicles was studied by monitoring the change in size and PDI for up to 30 days. Protein characterization of sEVs and HE were done via SDS-PAGE analysis, Dot blot assay, and western blotting. For SDS-

PAGE analysis, sEVs and HEs were mixed with sample loading buffer (1:1) with a final protein concentration of 330 µg/mL. The mixture was incubated at 90℃ for 7 minutes, and 25 µL of each sample was loaded in the wells of 4-20% Mini-PROTEAN® TGX Protein Gels. The gel was stained by Coomassie Brilliant Blue and imaged by Bio-Rad imager. For Dot blot assay, a drop of each sample (2-3 µL) was added to Polyvinylidene Fluoride (PVDF) membrane. The membrane was incubated with blocking buffer for 30 min at room temperature and then treated with primary antibodies CD81, CD63, CD9, CD11b, TSG101, β-Actin, and histone H3 (Santa Cruz). After overnight incubation with the primary antibody, the membrane was washed with wash buffer and incubated with HRP conjugated anti-mouse IgG secondary antibody (Cell signaling). The membrane was further developed using Signal Fire ECL TM Reagent and immediately imaged by Bio-imager (Kodak).

For western blotting, SDS PAGE was run as described earlier. 25 µL of samples mixed with sample loading buffer (1:1) containing 25 µg protein were loaded in the gel. After the completion of the SDS PAGE, the gel was transferred to PVDF membrane for the transfer of protein by the wet-blot method as described in our recent publications.[75,76] PVDF membrane was treated with primary antibodies β-Actin and CD63 (Santa Cruz) along with HRP conjugated anti-mouse IgG secondary antibody (Cell signaling). The membrane was further developed using Signal Fire ECL TM Reagent and immediately imaged for chemiluminescence by Bio-imager (Kodak).

4.2.7 Proteinase K assay for protein digestion

Proteinase K solution (2 mg/mL) was prepared from lyophilized proteinase K powder in 50 mM Trizma HCl buffer, pH 8.0 with 5 mM $CaCl_2$ solution as recommended by provider. For protein digestion, sEVs were incubated with proteinase K solution at 1:1 (w/w) enzyme: substrate

ratio for 2.5 h at 37 °C.[213] Control sEVs were not treated with Proteinase K. Protease inhibitor cocktail was added at a final concentration of 2x to stop the protease activity. sEVs were then washed with PBS three times using 10k MWCO amicon filter to wash out digested protein fragments and proteinase. Control sEVs and proteinase K treated sEVs were analyzed for size and protein content using DLS and Bradford assay respectively. Herein, the goal of Proteinase K assay is to validate the tumor targeting activity of sEVs as hypothesized.

4.2.8 Elucidation of hybridization

Validation of hybridization of liposome and sEVs producing HEs were done by fluorescence resonance energy transfer (FRET) study. FRET liposomes were synthesized as described in our publications.[75,80,214] FRET fluorophore lipids, NBD acting as an electron donor and Rh-B acting as an electron acceptor, were incorporated in lipid mixture in the molar ratio of 1:7 resulting in the formation of FRET liposome. For fusion analysis, 100 µl of sEVs (1mg/ml) was added to 20 µl FRET liposome (1mg/ml), mixed and bath sonicated for 5 minutes to initiate fusion. FRET liposomes, before and after fusion of sEVs, were analyzed by fluorescence spectroscopy by exciting samples at 470 nm and measuring the emission spectra between 500 to 700 nm.

Percentage FRET efficiency was calculated using the following equation:

$$\% \text{ FRET Efficiency} = (F_a/(F_a+F_d)) \times 100$$

where F_a= emission fluorescence of acceptor (Rh-B) and F_d = emission fluorescence of donor (NBD)

4.2.9 Biocompatibility Assay

Biocompatibility of vesicles was analyzed on different cell lines using MTT assay.[215] Briefly, 10,000 cells were seeded in 96 well plates for 24 h at 37℃ in 5% CO_2 environment. After that, cells were incubated with samples at varying concentration range (6.25, 12.5, 25, 50, 100,

and 200 µg/mL) for 48 h. Control cells were maintained with media only. MTT solution was added and further incubated for 2 h. DMSO was added to dissolve the insoluble formazan crystal formed after MTT treatment, and absorbance was recorded at 550 nm using microplate reader (BioTek, Synergy H1 Hybrid reader).

4.2.10 Drug loading and release study

Drug loading was carried out by physical encapsulation technique.[75] HE was prepared as described earlier and calculated amount of DOX (50 µg/ml, 100 µg/ml, 200 µg/ml and 400 µg/ml) was directly added to the hydrated lipid cake. The HE dispersion with DOX was vortexed and bath sonicated before extruding through 200 nm polycarbonate membrane filter. DOX-loaded HEs were purified by using 10k molecular weight cut off (MWCO) amicon filter where excess unloaded DOX was washed away with PBS. Amount of DOX in the wash was quantified spectrofluorimetrically by measuring DOX excitation and emission at 490 nm and 595 nm. DOX loading efficiency and percentage drug content with respect to the weight of the carrier were quantified by calculating DOX in both filtrate and HE.

DOX loading efficiency was calculated by the following equation:

% Loading Efficiency= (encapsulated DOX/Initial input of DOX) × 100

Drug release study was carried out in physiological (PBS, pH 7.4) and acidic (Acetate buffer, pH 5.5) conditions. 2 mL of 40 µg/mL of DOX encapsulated in HEs were dialyzed using 3.5 kDa dialysis membrane bag in 100 mL of drug release media kept at 37ºC while constant stirring (80 rpm). 500 µL of release media was taken at regular intervals and replaced by fresh media. The amount of DOX in the release media was calculated spectrofluorimetrically by measuring DOX excitation and emission at 490 nm and 595 nm. For control study, DOX

encapsulated liposome was prepared, and its release characteristic was studied following the same protocol.

Drug release was quantified by using the following equation:

% Drug release = (DOX amount in release media/ DOX amount in 100% release) × 100

4.2.11 In-vitro toxicity

In-vitro toxicity of Free DOX and DOX-loaded HEs were analyzed by MTT assay. Briefly, 10000 cells were seeded in 96 well plates. After 24 h, cell culture media was replaced by treatment media with Free-DOX and DOX-loaded HE (HE-DOX) and kept in incubation at 37℃ in 5% CO_2 environment for 48 h. Control cells were maintained with media only. After 48 h, media was removed and the MTT solution was added and further incubated for 2 h. DMSO was added to dissolve the insoluble formazan crystal formed after MTT treatment, and absorbance was recorded at 550 nm using microplate reader (BioTek, Synergy H1 Hybrid reader).

4.2.12 Confocal Imaging

Cellular internalization of vesicles was studied using confocal microscopy. 10,000-20,000 cells were seeded in 8 well plates for 24 h at 37℃ in 5% CO_2 environment. Cells were incubated with Rh-B labeled samples for 3 h at 37℃ in 5% CO_2 environment. Cells were then fixed by 4% Paraformaldehyde. Nucleus was stained by DAPI and cells were observed under a Confocal Laser Scanning Microscope (Carl Zeiss, LSM-700). ImageJ was used to quantify the intensity of internalized Rh-B labeled nanovesicles in terms of corrected total cell fluorescence (CTCF).

CTCF was calculated by using the following equation:

CTCF = Integrated Density – (Area of selected cell × Mean fluorescence of background readings)

4.2.13 Flow Cytometry

Cellular internalization of HEs and liposomes were further studied using flow cytometry. Cells were cultured in T25 flask up to around 80% confluency. Cell culture media was replaced by 4 mL of 50 µg/mL of Rh-B labeled HEs and liposomes, respectively. After 3 h of treatment, media was removed, and cells were washed with DPBS three times and trypsinized. Finally, 1 million cells were resuspended in 500 µl of PBS and cellular internalization was analyzed using BD LSRFortessa X-20 Special Order Research Product Flow Cytometer.

4.2.14 Statistical analysis

Different statistical model and test were carried out including T-test, F-test, and dose-response inhibition model fit using GraphPad software according to requirement. All data represent the mean ± standard deviation. Biocompatibility and Cytotoxicity data include six replicates (n=6). All other major data includes at least three replicates (n=3).

4.3 Result and Discussion

4.3.1 Extracellular vesicle isolation, hybridization, and Characterization

Small Extracellular Vesicles (sEVs) were harvested from conditioned media of mouse macrophage cells J774A.1 using differential centrifugation, filtration, and membrane extrusion technique as described in the method. Harvested sEVs were hybridized with synthetic liposomes using thin film hydration technique followed by extrusion through 400 and 200 nm size polycarbonate membranes, respectively. Synthetic liposome was prepared using L-α-phosphatidylcholine (Egg, Chicken) (EggPC) and Cholesterol in a molar ratio of 66:34 following thin film hydration technique.[75,76,79,216–218] The ratio of the liposome to sEV was optimized to 5:1. sEVs was quantified based upon protein content whereas liposome was quantified based upon lipid weights. 200 µg protein equivalent of sEVs dispersed in 1 mL Phosphate buffer saline (PBS) was

added to 1000 µg of lipid film. This initiates the hydration of lipid film to lipid cake which after extrusion results in the formation of hybrid exosomes (HE) as shown in **Figure 4.1**.

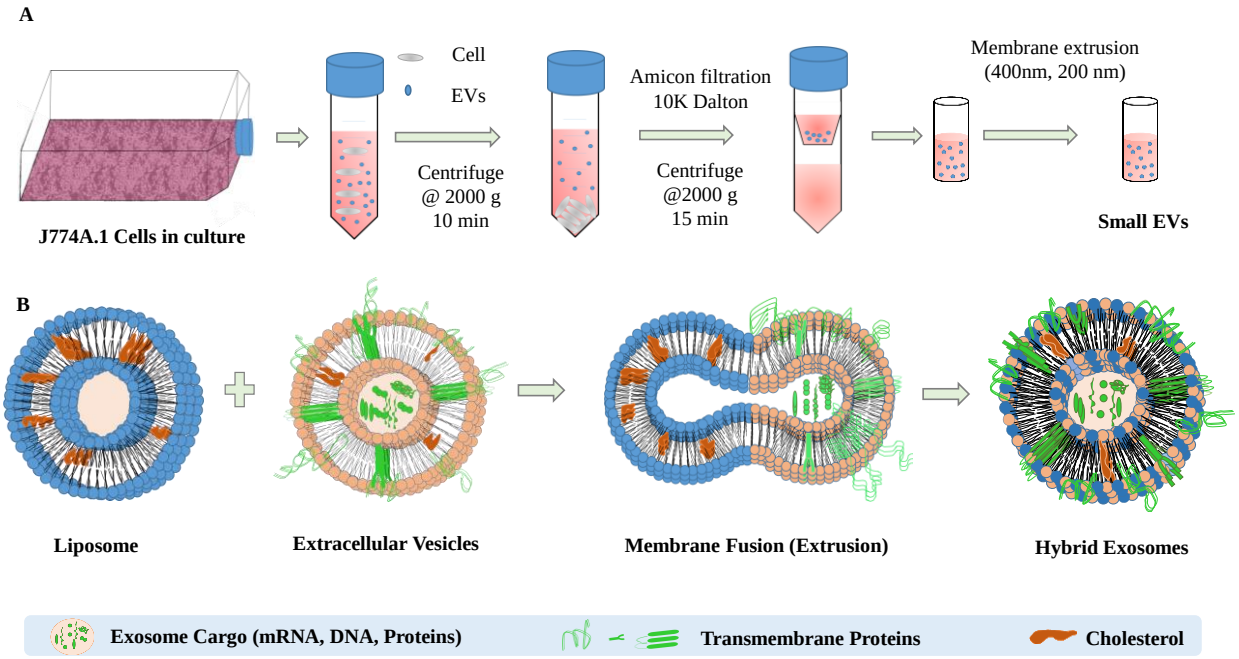

Figure 4.1 Schematic representation of the fabrication of hybrid exosome. (A) Isolation of small extracellular vesicles (EVs) from J774A.1. (B) Hybridization of immune cell-derived small extracellular vesicles (sEVs) with synthetic liposome using membrane extrusion method.

Liposomes, sEVs, and HEs were characterized for size, surface property, and protein content. **Figure 4.2** shows a comparative study on the hydrodynamic size distribution and zeta potential along with the stability of theses nanovesicles. Hydrodynamic size of liposome and sEV was found to be 131 ± 21 nm (PDI= 0.16 ± 0.05) and 139 ± 19 nm (PDI= 0.25 ± 0.02) with zeta potential of -31 ± 2 and -12 ± 1 mV, respectively. Whereas that of HE was found to be 177 ± 21 nm (PDI= 0.19 ± 0.04) and -26 ± 3 mV. While there is not much variation in the hydrodynamic size of liposome and sEV when extruded through 200 nm polycarbonate membrane, the size of HE was found to be increased to 177 nm. The increase in the size of HE is probably due to the insertion of sEV into the bilayer of synthetic liposome which increases the interaction points of water molecule thereby increasing the hydration layers. Although the size of HE is larger than the

bare liposome and sEV, the most important factor is the homogeneity in the size distribution, which can be indexed by determining the polydispersity index (PDI). We observed PDI of HE as 0.19 ± 0.04, and that of sEV was 0.25 ± 0.02. It is worth to note that the small variation in PDI broadly vary the distribution, wherein the size homogeneity is significantly greater in case of HE compared to sEV.

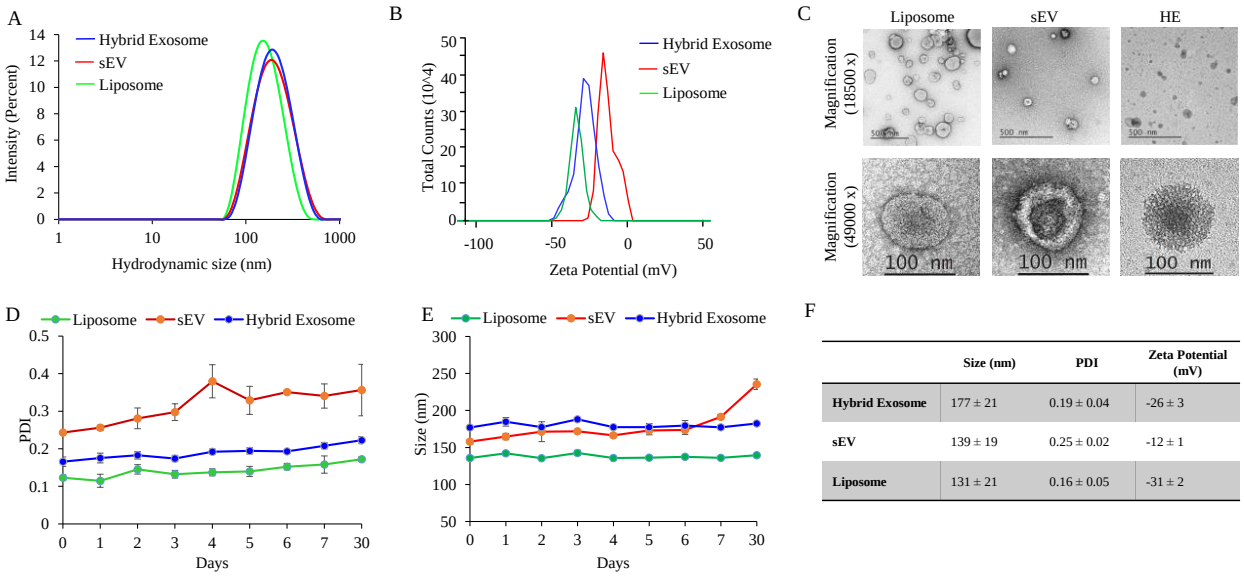

F

	Size (nm)	PDI	Zeta Potential (mV)
Hybrid Exosome	177 ± 21	0.19 ± 0.04	-26 ± 3
sEV	139 ± 19	0.25 ± 0.02	-12 ± 1
Liposome	131 ± 21	0.16 ± 0.05	-31 ± 2

Figure 4.2 Characterization of nanovesicles. (A) Hydrodynamic size distribution of liposome, small extracellular vesicle (sEV), and hybrid exosome (HE), (B) zeta Potential of nanovesicles showing surface charge distribution, (C) transmission electron microscopic image of nanovesicles at different magnification, (D & E) stability of nanovesicles over the period in terms of PDI and size, respectively, and (F) comparison between nanovesicles in terms of size, PDI, and surface charge.

Liposome, sEV, and HE were further characterized by transmission electron microscopy (TEM) to study the morphological characteristic. TEM image (**Figure 4.2C**) shows a morphological characteristic of these nanoparticles at lower and higher magnifications. Lower magnification images showed a general distribution of nanoparticles with vesicular structure. Higher magnification images of Liposome, sEV, and HE of similar size (around 100 nm in the dry state under high vacuum) were selected for comparative morphological analysis, which exhibited

a clear distinction between the nanoformulations. sEV surface showed more denser and darker characteristic compared to liposome which may be due to the presence of characteristic exosomal membrane proteins that are stained heavily with uranyl acetate staining. Similar TEM images of sEVs have been reported in other literature.[219–221] Likewise, HE showed distinct different surface morphology than that of liposome and sEV with the dense network around the surface which may be due to hybridization of exosomal proteins with the liposomal system.

To further examine the stability of these nanovesicles, we monitored their colloidal stability up to 30 days as depicted in **Figure 4.2D and E**. HE showed better stability compared to sEV, both in terms of PDI and size. During the period of 30 days, PDI of HE varied from 0.166 to 0.223 compared to 0.243 to 0.356 for sEV. Also, HE showed a minimal variation on size, from 177 nm to 182 nm, compared to sEV, from 158 nm to 235 nm. These characterization data show that incorporation of sEV in the lipid bilayer of the liposome in HE results in better stability of engineered HE compared to naive sEV.

4.3.2 Validation of hybridization

Fluorescence resonance energy transfer (FRET) and protein assay were carried out for the confirmation of hybridization between liposome and sEV. FRET has been widely used to study membrane fusion.[75,80,203,214,216,222] FRET liposomes were prepared with FRET pairs: l-α-Phosphatidylethanolamine-N-(4-nitrobenzo-2-oxa-1,3-diazole) (Ammonium salt) (PE-NBD) (Fluorescent donor, λem=525 nm) and l-α-Phosphatidylethanolamine-N-(lissamine rhodamine B sulfonyl) (Ammonium salt) (PE-Rh-B) (Fluorescent acceptor, λem=595 nm) in 1:7 molar ratio. Energy transfer in FRET liposome was monitored before and after hybridization as depicted in **Figure 4.3A**. Liposome spectra represent before hybridization, and HE spectra represent after hybridization. A diminished FRET effect was seen after hybridization which can only happen

when the distance between the FRET pair increases. This suggests that there has been the insertion of EV content in the lipid bilayer of liposome validating successful hybridization. To quantify the diminished FRET effect, FRET efficiency was calculated. **Figure 4.3B** shows quantification of time-dependent FRET efficiency in FRET Liposome and HE showing the decay of FRET efficiency in both liposomes and HE over a period. Importantly, we see 27% decrement of FRET efficiency after hybridization to HE. This decrement decreased over a period. But, we still see a decrement of 12% after 120 minutes of fusion. This observation clearly signifies a stable decrement of FRET effect after hybridization, which confirmed the successful formation of HE.

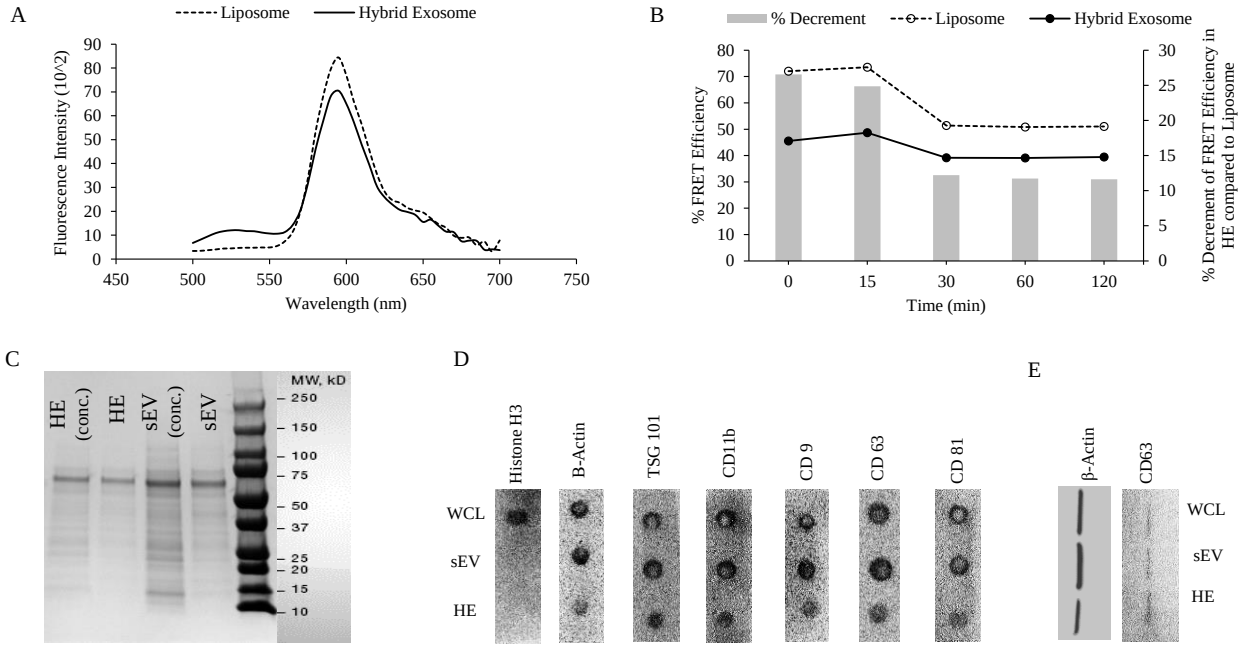

Figure 4.3 Validation of hybrid exosome formation. (A) Fluorescence Resonance Energy Transfer (FRET) study showing successful hybridization of sEV and liposome. FRET study was conducted using fluorescent donor NBD (λem=525 nm) and fluorescent acceptor RhB (λem=595 nm) at excitation wavelength of 470 nm, (B) quantification of FRET efficiency over a period and decrement of FRET efficiency after hybridization, and (C) SDS-PAGE analysis of sEV and HE. Both samples were concentrated to get distinct protein bands. (D) Dot blot assay and (E) western blot assay for the identification of EV marker proteins in whole cell lysate (WCL), small extracellular vesicle (sEV), and hybrid exosome (HE). β-Actin was used as a positive control and histone H3 was used as negative control.

Hybridization was also confirmed by protein characterization. Protein cargo of sEV is important for their unique characteristic.[75,76,223] Sodium dodecyl sulfate-polyacrylamide gel electrophoresis (SDS-PAGE) analysis showed distinct protein bands in both sEV and HE as shown in **Figure 4.3C**. Samples were concentrated to get higher signal intensity. HE showed similar protein bands like that of sEV, signifying that the sEV protein content has been conserved through the hybridization. More importantly, Dot-blot assay showed the presence of major EV marker proteins like transmembrane proteins (CD81, CD63, and CD9), tumor susceptibility gene 101 protein (TSG101), and integrin alpha M (ITGAM) protein. ITGAM is also known as CD11b protein, which is a specific protein marker of macrophage and macrophage-derived EVs (**Figure 4.3D**).[224] These proteins were present in both sEVs and HE as shown in Figure 2D, which signify the successful retention of major EV proteins through hybridization process in HE. The slight decrement of intensity in blot signal in case of HE may be due to the interference by synthetic lipid content of HE (sEV: Lipid=1:5 in HE). To further confirm the presence of EV marker protein in sEVs and HE, one of the major and widely used EV marker protein CD63 was chosen and analyzed via western blotting. Western blot assay also further confirmed the presence of CD63 in both sEVs and HEs confirming our claim.[44,188] β-actin was used as positive control and histone H3, a nuclear protein was used as a negative control in dot blot study. All three nanovesicles studied showed the presence of β-actin. However, the nuclear protein histone H3 was not present in sEV and HE, which also suggested that the isolated sEVs are free from possible nuclear contamination. Result of both positive and negative control confirms the specificity of the assay performed. These analyses further support the successful fabrication of HE with the conservation of characteristic EV protein cargoes.

4.3.3 Doxorubicin loading and release study

Next, we studied the drug loading and release kinetics to explore the potential application of HE in drug delivery. Doxorubicin (DOX) was used as a model drug. DOX was loaded in HE using membrane extrusion mediated physical method of drug loading.[75] **Figure 4.4** represents the in-vitro drug loading and release study. **Figure 4.4A** shows the optimization for the best initial input of DOX. The percentage loading efficiency of DOX with respect to various initial input concentration of DOX (50, 100, 200, 400 µg/mL) was calculated. The high loading efficiency of 82% to 99% was observed with input DOX concentration ranging from 400 µg/mL to 50 µg/mL, respectively. Based upon this data, percentage drug content with respect to the weight of the carrier was quantified gravimetrically after lyophilization. Percentage of drug content with respect to carrier increased with the increasing initial concentration of DOX from 0.9% to 5.7%. Unfortunately, HE in the case of high loading content gets aggregated as observed from the altered size and PDI. However, in the case of 100 µg/ml of initial input of DOX, size and PDI of HE after loading (176 nm, 0.25 PDI) was similar to that of before loading (168 nm, 0.27 PDI) as shown in **Figure 4.4B**. Also, the loading efficiency was 99% and the percentage drug content (%wt) with respect to the carrier was 1.8%. So, among different study groups of initial DOX input, it was found that 100 µg/mL DOX input showed the best stability in media while maintaining its loading content (**Figure 4.4C**).

With the assurance of good stability of HE, we further studied drug release to explore the release kinetics at normal physiological pH (pH 7.4, PBS) and acidic (pH 5.5, Acetate buffer) as depicted in **Figure 4.4D**. HE-DOX showed bursts release in both pH condition up to the first 8h, with enhanced drug release characteristic in acidic pH compared to physiological pH when evaluated for 48 h. The initial burst release of the drug was found to follow first order release

kinetics model (R^2 of 0.96 and 0.98). After the initial burst release, sustained drug release was observed up to 48 h. Doxorubicin-loaded liposome (Liposome-DOX) was used as control. Liposome-DOX showed similar release characteristic with that of HE-DOX with initial burst release (first order release kinetics model, R^2 0.98 and 0.99) and pH-responsive release characteristic. The initial burst release up to 12 h showed higher drug release in both pH conditions studied. After an initial burst release, both HE-DOX and Liposome-DOX show sustained release, which was slightly higher in case of Liposome-DOX compared to HE-DOX. Higher release at later time points in liposome-Dox is probably due to the fact that its surface is not passivated with transmembrane protein like in HE-DOX. All in all, our formulated HE-DOX showed a similar trend of drug release characteristic to that of control liposome signifying that the engineering method applied have retained the drug release characteristic.

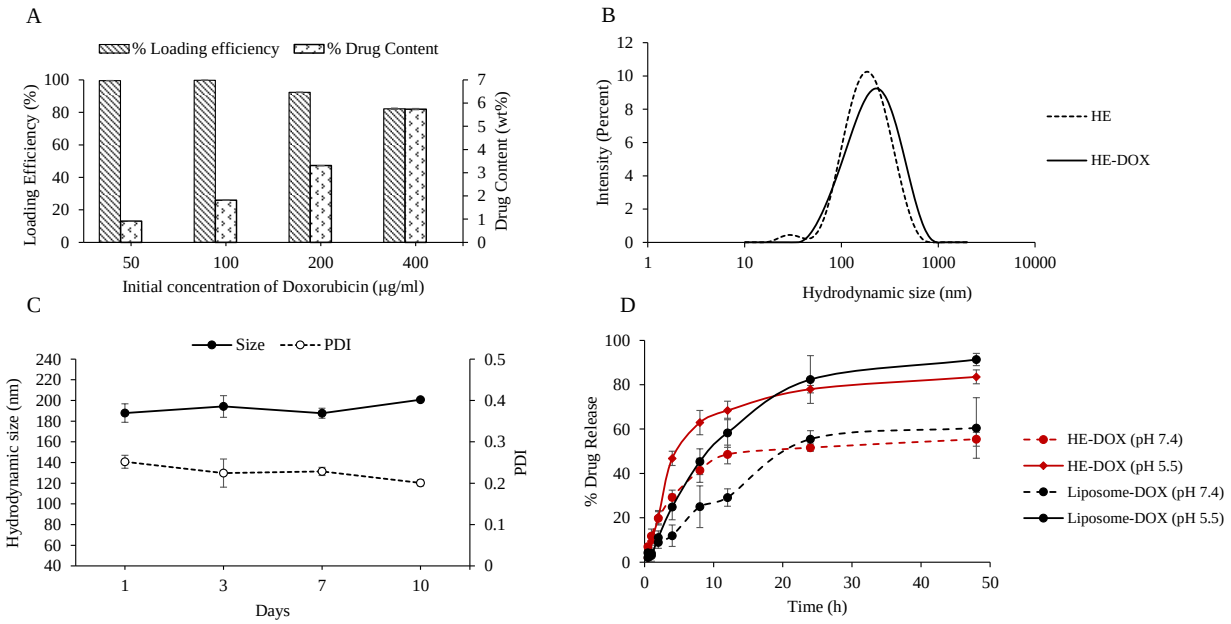

Figure 4.4 In-vitro drug loading and release study. (A) Doxorubicin loading efficiency and drug content by weight with respect to carrier in different initial concentration of Doxorubicin (µg/ml) , (B) hydrodynamic size distribution of hybrid exosome before and after DOX loading, (C) stability of DOX loaded HE (HE-DOX) over a period in terms of hydrodynamic size and PDI, and (D) percentage release of Doxorubicin from HE-DOX and control Liposome-DOX in normal physiological condition (PBS, pH 7.4) and acidic condition (Acetate buffer, pH 5.5)

Observed higher drug release in the acidic microenvironment is a desirable characteristic for drug delivery agent for cancer therapeutics. Cancer cells are often characterized by acidic microenvironment[225–227], and we found that formulated HE-DOX can release up to 83% of the drug in such acidic environment compared to 55% drug release in normal physiological condition when studied up to 48 h. Further to understand the drug burst in an acidic environment, we incubated HE and Liposome at pH 5.5 and found a broad distribution in size (**Figure 4.S8**). This broad distribution of hydrodynamic size is possible due to the aggregation and disruption in the structure of vesicles in acidic condition, which renders the faster drug release. Considering the acidic tumor microenvironment, we hypothesized that the phenomenon would benefit in suppressing tumor growth.

4.3.4 Biocompatibility

Biocompatibility of liposome, sEVs, and HE was analyzed in mouse breast cancer cell 4T1, mouse osteosarcoma K7M2, and mouse normal fibroblast NIH/3T3 as presented in **Figure 4** for 48 h of treatment. Liposome biocompatibility was analyzed with different lipid concentration, whereas in sEVs, and HE, the protein concentration was used as a handle to track biocompatibility. Liposome showed at least 80% cell viability even at high concentration (200 µg/ml) in all three cell lines. Cellular viability of liposome was found to be 93% to 80% in 4T1, 100% to 81% in K7M2, and 100% to 86% in NIH/3T3 in the concentration ranges from 6.25 to 200 µg/mL, respectively (**Figure 4.5A**). This data signifies biocompatibility of liposome even at high concentration. In case of sEVs, the range of cell viability with different protein concentration was from 92% to 95% in 4T1, 79% to 89% in K7M2, and 79% to 94% in NIH/3T3 in the concentration range from 6.25 to 1000 µg/mL (**Figure 4.5B**). Likewise, for HE, the range of cell viability with different protein concentration was from 71% to 99% in 4T1, 73% to 91% in K7M2, and 82% to

91% in NIH/3T3 in the concentration range from 6.25 to 100 µg/mL of protein **(Figure 4.5C)**. Cell viability of greater than 70% was found even at high protein concentration in both sEVs and HE. These observations reflect good biocompatibility of our HE signifying that it can be used as a safe delivery agent.

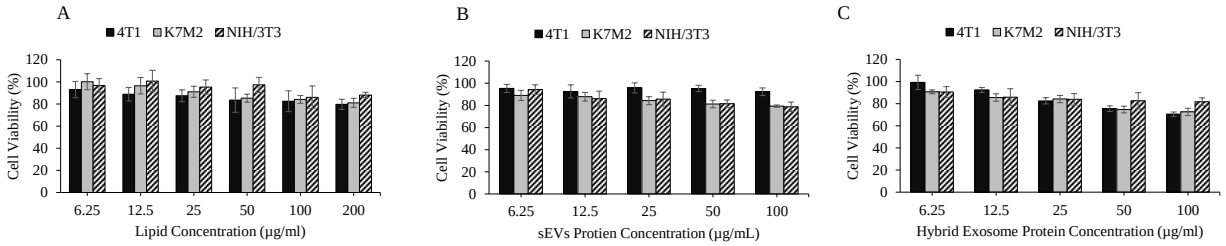

Figure 4.5 In-vitro biocompatibility study. (A) Biocompatibility of synthetic liposome, (B) small extracellular vesicles (sEVs), and (C) hybrid exosome on mouse breast cancer cell 4T1, mouse osteosarcoma K7M2, and mouse normal fibroblast NIH/3T3. Percentage cell viability was quantified using MTT assay. Cells were treated with liposome, with different lipid concentration, and small extracellular vesicles and hybrid exosome, with different protein concentration, for 48 h.

4.3.5 Cellular internalization study

Cellular internalization of HE was studied on mouse macrophage (J774A.1), mouse osteosarcoma (K7M2), mouse breast cancer (4T1), and mouse fibroblast (NIH/3T3) cells using confocal imaging and flow cytometry analysis. **Figure 4.6** shows confocal imaging of different cell lines showing internalization of Rhodamine-B (Rh-B) labeled HE and liposome and their subsequent quantification after 3 h of treatment (Detail figure can be found in **Figure 4.S3, 4.S4, 4.S5, and 4.S6**). To optimize the incubation time, we did time-dependent internalization assay of Rh-B labeled HE in NIH/3T3 and 4T1 from 1.5, 3, and 6 h time points (**Figure 4.S1 and 4.S2**). Maximum internalization was seen in 3 and 6 h incubation time with no significant differences between them. So, we decided to go with 3 h incubation time in all our further experiments.

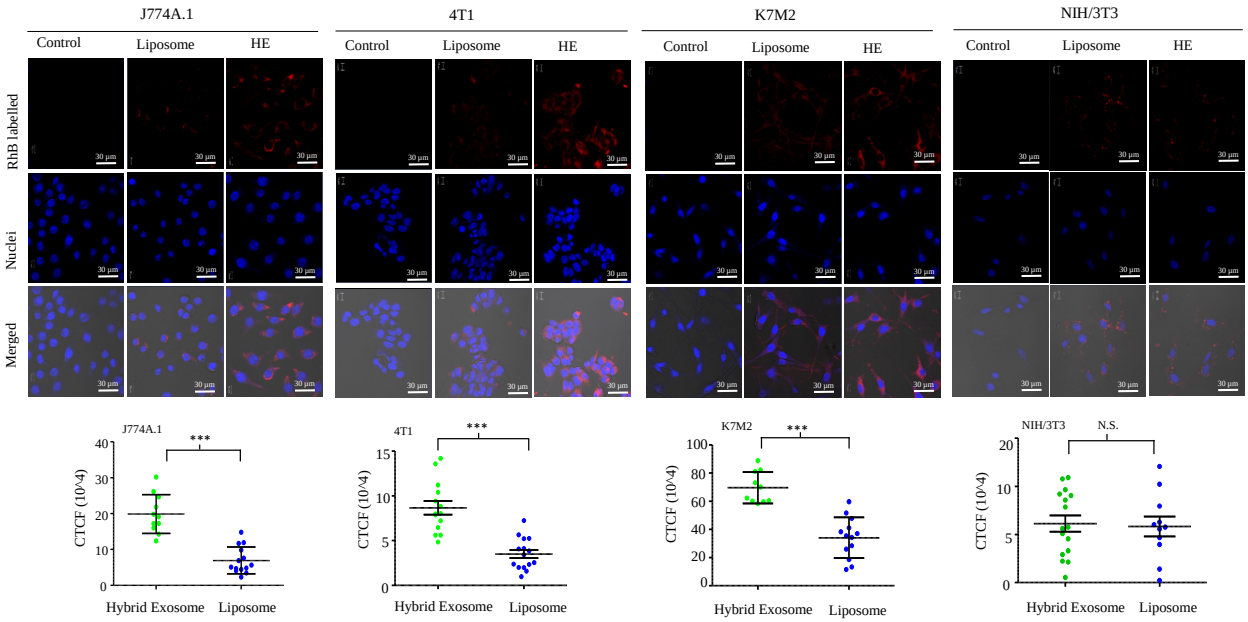

Figure 4.6 Cellular internalization study via confocal imaging. Confocal image of mouse macrophage J774A.1, mouse breast cancer cell 4T1, mouse osteosarcoma K7M2, and mouse normal fibroblast NIH/3T3 showing cellular internalization of Rhodamine labelled hybrid exosome (HE) and liposome, after 3 h incubation. Internalization was quantified in terms of corrected total cell fluorescence (CTCF) using ImageJ. (*** = $p<0.0001$, N.S= Non-significant, unpaired t test)

Nanovesicles were stained with Rh-B dye and nucleus of the cell was stained by 4′,6-diamidino-2-phenylindole (DAPI). Rh-B fluorescence intensity in the individual cell was quantified using Image-J. Untreated cells were used as control. Significant higher cellular internalization of HE compared to liposome was observed in EV parent cell J774A.1, mouse cancer cells 4T1 and K7M2, whereas there was no significant difference in the case of mouse fibroblast NIH/3T3 ($p<0.0001$, Unpaired t-test) (Figure 4.6). Likewise, a similar result was observed in the internalization behavior of sEVs which showed higher internalization in EV's parent cell and tumor cell compared to that of normal fibroblast (**Figure 4.S9**). No Rh-B signal was observed in control. This clearly shows the selectivity of sEV and HE toward its parent cells and tumor cells compared to that of normal cells. In order to further confirm this finding with a more robust quantitative analysis, a flow cytometry assay was performed in 4T1,

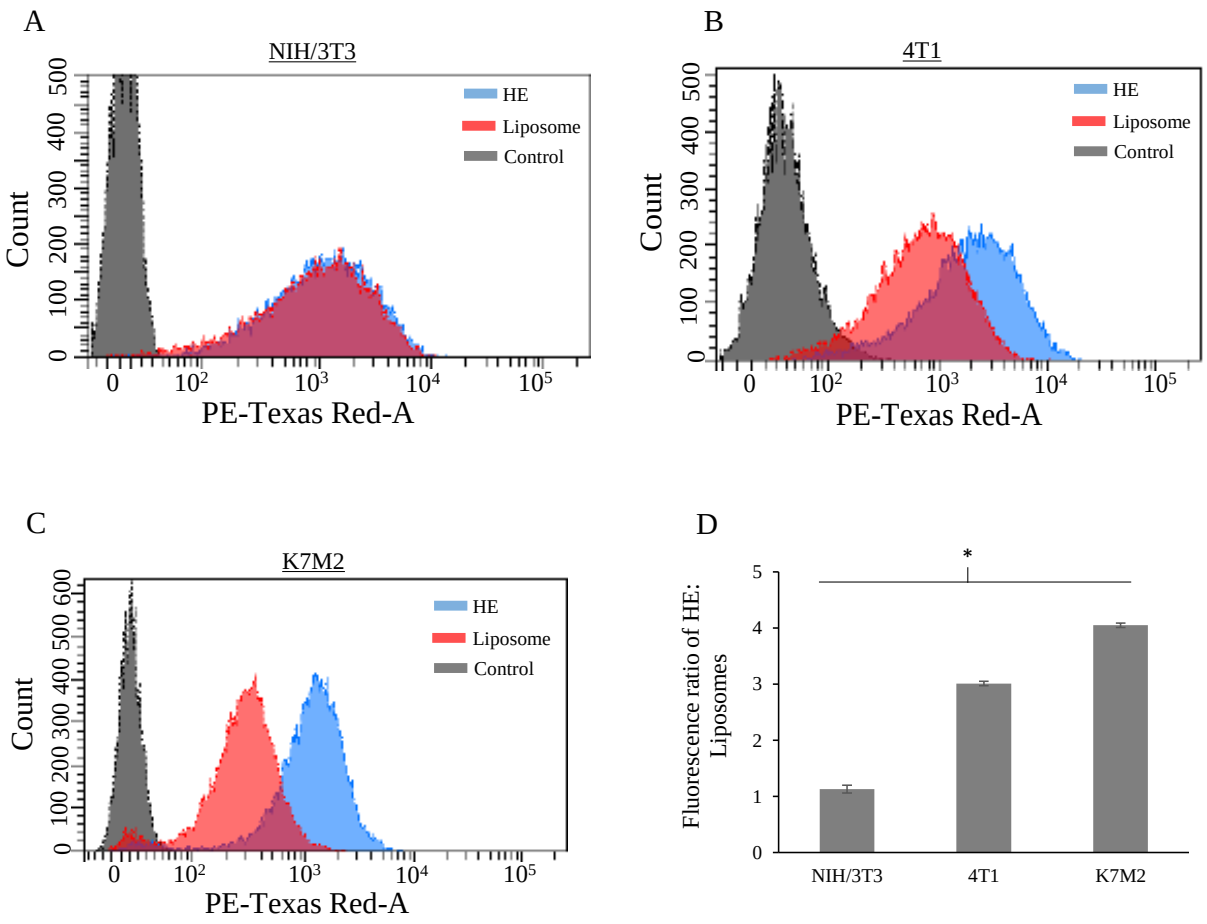

Figure 4.7 Cellular internalization study via flow cytometry. Flow cytometry analysis showing internalization of Rhodamine labelled Hybrid exosome (HE) and liposome in (A) mouse fibroblast NIH/3T3, (B) mouse breast cancer cell (4T1), and (C) mouse osteosarcoma (K7M2) after 3 h incubation, and (D) ratio of median fluorescence of HE internalization to liposome internalization in different cell lines (* = P value < 0.05, Friedman Test, one way ANOVA).

K7M2 and NIH/3T3. **Figure 4.7** shows the flow cytometry analysis on three different cell lines showing internalization of RhB labeled liposome and HE with respect to control, after 3 h of treatment. As can be seen in the fluorescence vs count plot of NIH/3T3, the fluorescent intensity of HE and liposome was similar and overlapped, signifying similar uptake characteristic of HE and liposome. Contrary to that, in case of tumor cells 4T1 and K7M2, the curve for HE shifted to the right compared to the liposome showing enhanced internalization. This observation was analyzed quantitatively by taking the median fluorescence value of nanovesicles internalized cell

and calculating the ratio of fluorescence value in HE internalized cell to liposome internalized cell, as depicted in **Figure 4.7D**. This analysis shows that HE was internalized 1.1 times higher than liposome in NIH/3T3 cell, whereas, in case of tumor cells (4T1 and K7M2), HE was internalized 3 and 4 times higher compared to the liposome, respectively. Both confocal imaging and flow cytometry analysis confirmed the selective internalization of HE towards tumor cell thereby supporting our hypothesis.

HE differs from liposome by the presence of characteristic EV surface proteins. So, the differential cancer targeting observed between HE and liposome may be due to the presence of acquired surface proteins from an immune cell in HE. We confirmed the presence of one of the main EV marker protein CD63, along with CD81, CD9, TSG101, and CD11b in HE. CD63 is a transmembrane protein that has reported to enhance cell adhesion.[228] So, herein this protein along with other surface proteins might play significant role in cellular internalization. Also, reports have shown evidence of receptor-mediated internalization of EVs including 1) Intercellular adhesion molecule 1 (ICAM1) binding to lymphocyte function associated antigen1 (LFA1), 2) phosphatidyl serine binding to T cell immunoglobulin domain and mucin domain protein 1 (TIM1), and 3) Milk fat globule EGF factor 8 protein (MFGE8) binding to integrins.[229] All these evidences increasingly suggest that EV proteins are involved in its internalization process. Further, to analyze the role of EV protein content in the observed enhanced internalization of HE, we carried out Proteinase K assay. Proteinase K is a serine protease enzyme that has a broad cleavage specificity of proteins. sEVs were treated with Proteinase K to digest the membrane proteins as described in methods. Control sEVs were not treated. **Figure 4.8** shows size, protein characterization, and cellular internalization behavior of proteinase K treated sEVs (sEV-proteinase (+)) and control sEVs (sEV-proteinase (-)). sEVs showed slight increment in hydrodyanimic size and PDI after proteinase

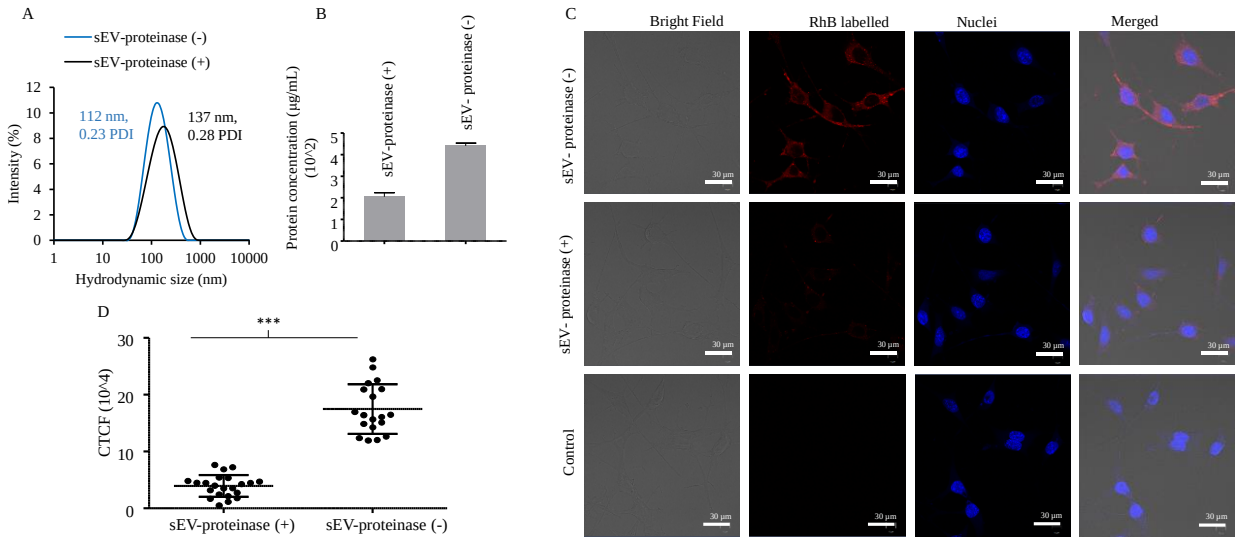

Figure 4.8 Proteinase K assay and cellular internalization study. (A) Hydrodynamic size of proteinase K treated small extracellular vesicles (sEV-proteinase (+)), and proteinase K untreated small extracellular vesicles (sEV-proteinase (-)), (B) protein quantification of sEV before and after treatment of proteinase K via Bradford assay, and (C) confocal image of mouse osteosarcoma K7M2 showing cellular internalization of Rhodamine labelled sEV-proteinase (-) and sEV-proteinase (+) after 3 h incubation. Control cells were incubated with cell culture media only. (D) Quantification of cellular internalization of sEV via ImageJ in terms of corrected total cell fluorescence (CTCF) before and after Proteinase K treatment. (***- *P value* < 0.0001, two tailed t test).

treatment, from 112 nm and 0.231 PDI to 137 nm and 0.283 PDI (**Figure 4.8A**). Protein quantification by Bradford assay showed about 50% reduction in total protein content after proteinase K treatment, from 441 µg/mL to 205 µg/mL. After proteinase K treatment of sEVs, its cellular internalization behavior was analyzed in-vitro on K7M2 cells (**Figure 4.8C**). sEVs were labeled with rhodamine B and nuclei of the cell were stained by DAPI. Cellular internalization assay showed a significant reduction of internalization of protease K treated sEVs compared to untreated one as represented by the intensity of the red signal in cells. Control cell incubated only with cell culture media did not show the red signal. Further, the intensity of internalized Rhodamine B labeled sEV-proteinase (+) and sEV-proteinase (-) was quantified using ImageJ, which showed about five times reduction of internalization in case of sEV-proteinase (+) compared

to sEV-proteinase (-). A similar result of reduction of proteinase K treated exosome was reported by Escrevente et. al., where they observed a 45 % reduction of exosome uptake by ovarian cancer cell (SKOV3) after proteinase K treatment.[230] These results clearly suggest that EV proteins are involved in its cellular internalization and observed enhanced internalization of HE in tumor cell could be due to the presence of EV proteins.

4.3.6 In-vitro cytotoxicity

In-vitro cytotoxicity of HE-DOX was studied on mouse cancer cell 4T1, K7M2, and mouse normal fibroblast NIH/3T3. **Figure 4.9** shows the comparative cytotoxicity of HE-DOX and Free DOX treatment for 48 h. It was found that the cytotoxicity profile of HE-DOX was similar to free DOX on K7M2 and NIH/3T3, whereas, interestingly, it was different in the case of 4T1. The extra sum of square F test, with LogIC50 and hillslope as a comparison parameter, was carried out to analyze the statistical difference in cytotoxicity in the different cell line. For this, cytotoxicity data were normalized and fitted in Dose-response-Inhibition model using GraphPad Prism software.[231–233] "Log (inhibitor) vs. normalized response-Variable slope" model gave best-fit equation with R-square value ranging from 0.96 up to 0.99. In case of K7M2 and NIH/3T3, F test does not reject the null hypothesis of "one curve for both datasets: HE-DOX and Free DOX", signifying that cytotoxicity profile of HE-DOX and Free-DOX is not statistically different (P value: 0.74 for K7M2, 0.98 for 4T1). Whereas, in case of 4T1, F test rejects the null hypothesis of "one curve for both dataset: He-DOX and Free DOX", signifying that cytotoxicity profile of HE-DOX and Free-DOX is significantly different (P value<0.001). This can be clearly seen in IC50 values of HE-DOX and Free-DOX in the different cell line. IC50 values of HE-DOX and Free DOX was 0.42 µM and 0.41 µM in K7M2, and 1.90 µM and 1.88 µM in NIH/3T3, showing close similarities in IC50 values in these cell lines. Contrary to that, in 4T1, HE-DOX showed relatively low IC50

value of 0.82 µM compared to 3.16 µM of Free DOX. From this comparative cytotoxicity data, we can confirm that our formulated HE-DOX is as compelling as Free DOX to arrest cancer.

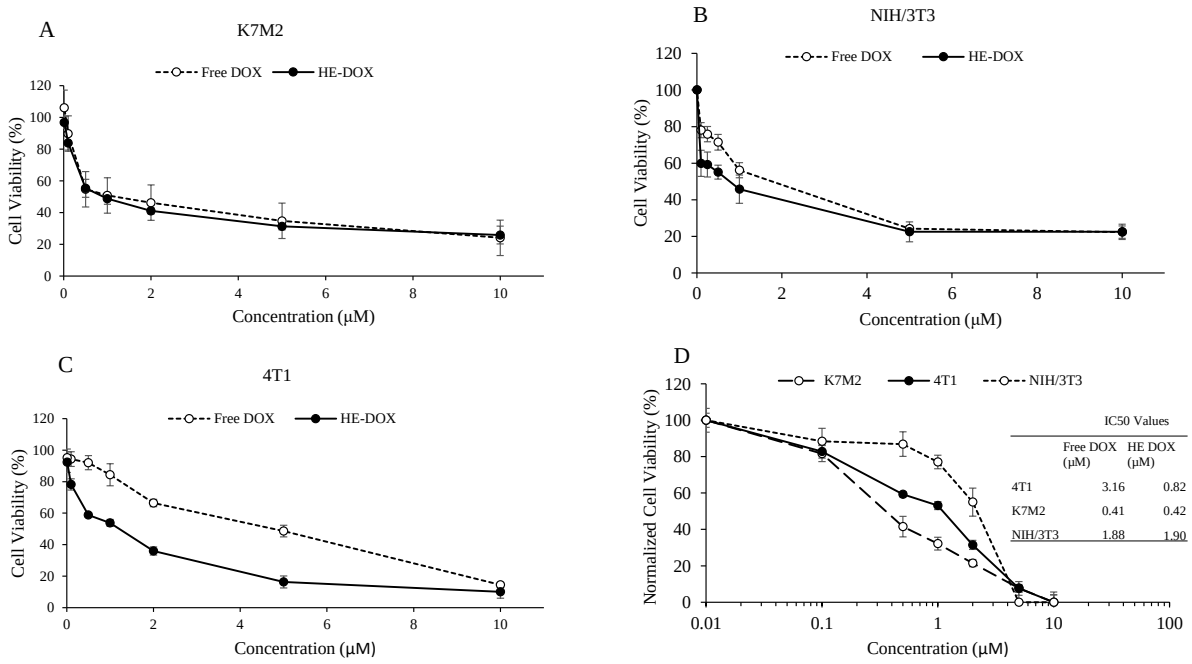

Figure 4.9 In-vitro toxicity assay. Toxicity of Free DOX and HE-DOX on mouse osteosarcoma K7M2 (A), mouse normal fibroblast NIH/3T3 (B), and mouse breast cancer cell 4T1 (C) after 48 h of incubation, and (D) comparative toxicity of HE-DOX against K7M2, 4T1, and NIH/3T3 showing IC50 value of Free DOX and HE-DOX treatment. Cell Viability data was normalized and fitted in Dose-response-Inhibition model: "Log (inhibitor) vs. normalized response-Variable slope" using GraphPad software for comparative analysis (F test, *P value*<0.0001).

To explore if there is any selectivity in cytotoxicity of HE-DOX towards tumor cell compared to a normal cell, we analyzed the difference in cytotoxicity profile of HE-DOX in mouse cancer cell K7M2, 4T1, and mouse normal fibroblast NIH/3T3. **Figure 4.9D** shows the normalized cell viability percentage with respect to the logarithmic of µM concentration of HE-DOX in three different cell lines. As can be seen in the dose-response graph, HE-DOX showed lower cell viability in tumor cell K7M2 and 4T1 compared to normal fibroblast NIH/3T3, signifying clear selectivity of cytotoxicity toward tumor cells. Quantitatively, the IC50 value of HE-DOX on K7M2 and 4T1 was 0.42 µM and 0.82 µM, which is significantly lower compared to 1.90 µM

IC50 in case of NIH/3T3. This difference in IC50 value and cytotoxicity profile of HE-DOX on three different cell line was statistically significant as confirmed by F test from Graph Pad as described earlier (P value<0.0001). From this cytotoxicity study, we were able to confirm that HE-DOX is as potent as free DOX and further shows the selectivity in cytotoxicity for tumor cells compared to the normal one. This observed enhanced cytotoxicity of HE-DOX towards tumor cell adds another advantage of using HE-DOX for tumor-targeted drug delivery platform.

Tumor cell contains lots of overexpressed surface proteins compared to normal cell.[234] Owing to this characteristic, there might be elevated events of specific receptor-mediated internalization of engineered HE in tumor cell leading to observed higher internalization. Also, since sEV is derived from an immune cell, it may carry the intrinsic characteristic of the immune cell to target tumors as discussed in the literature.[235] Immunological experiments need to be conducted to confirm these hypothesis which is out of the scope of this paper. Nonetheless, the characteristic of our formulated HE showing tumor selective enhanced internalization and cytotoxicity is very desirable in the drug delivery field for cancer therapeutics. Also from the observed interaction of HE with its parent cell (J774A.1) (**Figure 4.S7**), an outstanding opportunity to target tumor-associated macrophage, which has reported role in tumor progression and metastasis, can be pictured.[236] However, a comprehensive study is needed to picture the realistic intracellular fate of HE.

The optimized sEV isolation method used in this study is simple, reagent-free, and uses relatively less strain in sEVs compared to traditional available methods. The isolated sEVs showed homogenous size distribution with an impressive polydispersity index (139 nm, 0.25 PDI) and presence of major EV marker proteins. However, since the method does not include direct precipitation of sEVs like in ultracentrifugation method or immuno-affinity precipitation method,

isolated sEVs may contain secretory proteins and other non-vesicular compartments, which is the limitation of this optimized sEV isolation method. Additional optimization of the method like a density gradient separation method to remove the non-vesicular compartment and secreted proteins is recommended if purity is a major concern.[46] However, the method described herein is best suited for high yield and aggregation free sEV isolation with structural integrity and homogenous size distribution, which is very important to maximize intracellular drug delivery.

4.4 Conclusion

Here, the aim of engineering HE was to merge the advantage of sEV and liposome drug delivery system. By hybridizing sEV with the liposome, we have successfully formulated HE that retains the functional properties of sEVs with a higher order of colloidal stability, drug loading, and pH-sensitive sustained drug release. Engineered HE showed the differential targeting and cytotoxicity against normal and cancerous cells thereby putting itself in the group of potential tumor-targeted drug delivery candidates. These outstanding findings of HE validated our hypothesis of acquired properties of macrophage to target cancer cell. While the application of EV for therapeutic drug delivery is still in developing era, these preliminary results and hybridization approach presented would hold promises in addressing issues related to the largescale production and surface functionalization of EV mimic structures.

Chapter 5 - Strategic reconstruction of macrophage-derived extracellular vesicles as a magnetic resonance imaging contrast agent

***Chapter 5**, in full, is a reprint of the material as it appears in Biomaterials Science, 2020, Sagar Rayamajhi, Ramesh Marasini, Tuyen Duong Thanh Nguyen, Brandon L. Plattner, David Biller, and Santosh Aryal. doi:10.1039/D0BM00128G*

Abstract

Contrast agent (CA) in magnetic resonance imaging (MRI) is now an essential add-on to get high-quality contrast-enhanced anatomical images for disease diagnosis and monitoring the treatment response. However, the rapid elimination of CAs by the immune system and excretion by the renal route has limited its application. As a result, the CAs dose for effective contrast is ever-increasing, resulting in toxic side effect such as gadolinium (Gd) related nephrogenic systemic fibrosis (NSF) toxicity. Considering the widespread application of Gd-based CAs, it is now very important to revisit its formulation in order to improve local concentration and minimize dose while achieving clinical goals. Therefore, we have adapted a unique strategy to maximize Gd delivery to the target site using macrophage cell-derived extracellular vesicles (EVs) reconstructed with Gd-conjugated liposomal system herein called as gadolinium infused hybrid EVs (Gd-HEV). We hypothesize that Gd-HEV, owing to the presence of immune cell-derived EVs protein cargo, can effectively disguise themselves as a biological entity, prolong retention time for contrast enhancement, and show tumor specificity. Incorporation of Gd in nanoformulations can enhance longitudinal relaxivity r_1 by reducing the tumbling rate of paramagnetic metal complexes. Here, Gd-HEV showed higher r_1 relaxivity of 9.86 $mM^{-1}s^{-1}$ compared to 3.98 $mM^{-1}s^{-1}$ of Magnevist® at

equivalent Gd concentration, when measured in clinical 3T MRI. This will allow us to reduce clinically used Gd concentration about three-fold while maintaining contrast in clinical window thereby supporting our hypothesis. Further, Gd-HEV showed preferential cellular interaction and accumulation towards cancer cells compared to the non-cancer cell, both *in vitro* and *in vivo*. More importantly, Gd-HEV showed excellent contrast enhancement in blood vasculature with higher retention time compared to its counterpart, Magnevist®. Our study successfully showed that the incorporation of Gd in EVs framework can help to enhance contrast ability, and therefore can be a platform technology for the development of safer MRI contrast agents.

5.1 Introduction

Magnetic resonance imaging (MRI) is a widely used non-invasive imaging technology that produces high-resolution anatomical images for disease diagnosis and treatment monitoring. MRI is often accompanied by the administration of MRI contrast agents (CAs) such as gadolinium, manganese, and ferric iron-based positive CAs and iron oxide-based negative CAs to enhance the contrast of an image for improved diagnostic capability. Positive CAs are designed to make the intraluminal contents brighter whereas the negative CAs are designed to make them darker. Due to brighter image, gadolinium-based contrast agents (GBCA) are widely used in clinics accounting for 50 tons of gadolinium (Gd) administrated annually with a total global market over 1 billion dollars per year.[237] This dramatic growth of GBCAs is driven by a noninvasive technique associated with GBCA usage, and its immediate effect that can provide essential diagnostic information. However, the rapid elimination of GBCA through the renal route, extravasation in interstitial space, and nephrogenic systemic fibrosis (NSF) toxicity have limited its clinical application.[238,239] To solve this problem, GBCA has been incorporated with different types of nanoparticulate systems including liposomal, polymeric, and hybrid nanoparticulate systems with

the goal to enhance contrasts, reduce the clinically used dosage, improve precision targeting to the disease site, and to limit associated toxicities.[240–243] Here, we have proposed to incorporate GBCA in the extracellular vesicles framework to mimic endogenous functionality for immune evasion and enhanced intraluminal residence.

Extracellular vesicles (EVs) are bilayered proteolipid vesicles secreted by cells to the extracellular environment. They are distinguished into exosomes (30-150 nm), microvesicles (200-500 nm), and apoptotic bodies (1- 10 μm) based upon their size and origin.[244] Here, extracellular vesicles represent vesicles with size less than 200 nm that may constitute exosomes and small microvesicles. Throughout this paper, these vesicles are termed as "extracellular vesicles (EVs)", as per the recommendation of minimal information for studies of extracellular vesicles 2018 (MISEV2018).[245] Owing to the unique endosomal derived biogenesis which accompanies complex endosomal sorting process, EVs share characteristic of their parent cells.[246–248] For example, tumor-derived EVs have tumor homing characteristic and immune cell-derived EVs naturally seek diseased cells and exogenous material.[249,250] These parent-cell derived characteristics can be attributed to the presence of parent cell-specific protein cargoes of EVs.[251] As such, tumor-derived EVs contain tumor antigens and dendritic cells derived EVs contain MHC-II-peptide complexes.[251] EVs also share common characteristics irrespective of their origin such as their role in cell-cell communication, given that large portions of EVs derived from different cell share common cargo including cytoskeletal (actin, fibronectin), transmembrane proteins (CD9, CD63, CD81), heat shock proteins (HSP 90, HSP 70), and proteins involved in vesicular trafficking (ESCRT, Tsg101, Alix).[252–254] With this rich protein cargo content and endogenous origin, EVs can effectively communicate with the endogenous environment. In this study, our aim of incorporation of GBCA with these EVs framework is to exploit these endogenous functionalities

to develop a biomimetic contrast agent that can effectively communicate with the endogenous environment, thus avoiding rapid immune clearance. Such a feature may lead to high blood retention time where contrast agents can be monitored in the vasculature for an extended period of time thereby providing essential diagnostic information.

In this study, EVs were isolated from mouse macrophage J774A.1 cells using an optimized centrifugation-ultrafiltration method and reconstructed with Gd conjugated liposomal system by extrusion mediated membrane fusion, thus formulating gadolinium infused hybrid extracellular vesicles (Gd-HEV). Mouse macrophage J774A.1 cell were selected as the source of EVs with the expectation of improved communication with the endogenous immune system and potentially enhanced tumor-targeting functionality. We hypothesize that the reconstructed Gd-HEV, owing to the presence of EVs, can disguise themselves as a biological entity and prolong retention time for contrast enhancement. Also, due to the immunological origin of EVs, we hypothesize that Gd-HEV would show tumor specificity and preferentially accumulate in tumor tissue. To test these hypotheses, Gd-HEV were tracked *in vitro* and *in vivo* by - 1) incorporating fluorescent imaging tag, Rhodamine B conjugated lipid, to track the cellular localization, 2) near-infrared 1,1′-dioctadecyl-3,3,3′,3′-tetramethylindotricarbocyanine iodide (DiR) dye to track the *in vivo* particle localization in a tumor, and 3) 3T clinical MRI to analyze the biodistribution and contrast enhancement characteristic of particles. Furthermore, Gd-HEV was extensively evaluated for its physicochemical properties such as hydrodynamic size, surface property, protein content, colloidal and serum stability, and magnetic properties to ensure its fit for in vivo analysis. This study has demonstrated the post-production reconstruction of EVs with imaging agents to formulate Gd-HEV and monitor it's *in vitro* and *in vivo* fate. The overarching aim of formulating Gd-HEV is to

develop multimodal imaging agents with contrast enhancement, longer retention time, and differential cellular interaction for disease diagnosis and treatment monitoring.

5.2 Materials and methods

5.2.1 Materials

Lipids 1,2-distearoyl-sn-glycero-3-phosphoethanolamine (DSPE), L-α-phosphatidylcholine (Egg, Chicken) (EggPC), Phospholipid conjugated l-α-Phosphatidylethanolamine-N-(lissamine rhodamine-B sulfonyl) (Ammonium Salt) (Rh-B), and l-α-Phosphatidylethanolamine-N-(4-nitrobenzo-2-oxa-1,3-diazole) (Ammonium Salt) (NBD) were purchased from Avanti Polar Lipid Inc. (Alabaster, AL, USA). Cholesterol was purchased from Fisher. Gd (III) acetate ($Gd(OAc)_3$) was purchased from Alfa Aesar (USA). N-Hydroxysuccinimidyl ester activated 1,4,7,10-tetraazacyclododecane-1,4,7,10-tetraacetic acid (DOTA-NHS) was purchased from Macrocyclics. CellLight™ Early Endosomes-GFP was purchased from Thermo Fisher Scientific. DAPI dye (4′,6-Diamidino-2-phenylindole dihydrochloride) and (3-(4,5-dimethylthiazol-2-yl)-2,5-diphenyl tetrazolium bromide) (MTT) reagent were purchased from Sigma-Aldrich. Mouse monoclonal antibody CD63 and β-Actin were purchased from Santa Cruz Biotechnology. All other reagents and chemicals were of analytical grade.

5.2.2 Cell lines and animal model

Mouse macrophage J774A.1, mouse normal fibroblast NIH/3T3, mouse osteosarcoma K7M2, and human peripheral blood monocyte THP-1 were purchased from ATCC, Manassas, USA. Cells were maintained in Dulbecco's Modified Eagle's Medium (DMEM) supplemented with 10% (v/v) Fetal Bovine Serum (FBS) and 1% streptomycin at 37 °C in 5% CO_2 environment. For THP-1 cells, Roswell Park Memorial Institute Medium (RPMI) was used.

All animal experiments and protocols were performed in strict accordance with the NIH guidelines for the care and use of laboratory animals (NIH Publication no. 85-23 rev. 1985). The animal protocols were approved by the Institutional Animal Care and Use Committee (IACUC) and Institutional Biosafety Committee (IBC), Kansas State University, Manhattan, Kansas. Six-week-old female NU/NU nude mice were purchased from Charles River Laboratories International, Inc. and used for the study after 10 days of acclimation.

5.2.3 Synthesis of gadolinium infused liposome (Gd-Liposome)

Gadolinium lipid was synthesized by chelating Gd in DSPE-DOTA following two-step method as reported in our previous works.[255–257] First, DSPE-DOTA was synthesized via NHS coupling chemistry. Briefly, 75 mg DSPE dissolved in 10 mL chloroform containing 2% (v/v) triethylamine (TEA) was mixed with 86 mg DOTA-NHS ester and incubated for 3 h at 40°C. The product DSPE-DOTA was purified by repeated freeze-thaw cycles followed by centrifugation (4500g, 10 min, room temperature) to precipitate by-products. The supernatant was syringe filtered (0.22 µm) and lyophilized to get pure DSPE-DOTA. Thus obtained DSPE-DOTA was chelated with Gd. For this, 0.05 mmol of DSPE-DOTA in acetate buffer (pH 5.5) was treated with 0.5 mmol of $Gd(OAc)_3$ at 50 °C for 12 h. After incubation, the Gd-DOTA-DSPE (Gd-Lipid) was purified by centrifugation at 4500 *g* for 10 min at room temperature. Non-chelated Gd was removed by washing the product with acetate buffer (pH: 5.5) and distilled water, 3 times each, and then lyophilized to get pure Gd-DOTA-DSPE (Gd-Lipid).

Gd-Lipid, EggPC, and cholesterol were used in 20:50:30 molar ratio to formulate gadolinium infused liposome (Gd-Liposome) using thin-film hydration technique following membrane extrusion.[256,257] Briefly, lipid mixture equivalent to 500 µg was taken and the thin film was created by overnight solvent evaporation. The lipid film was then hydrated by 1 mL phosphate

buffer saline (PBS) followed by vortexing and sonication (bath and probe sonication, 50% amplitude, 2 min) for proper mixing resulting to the formation of liposome (500 µg/mL). Liposome solution was then extruded through a 200 nm polycarbonate membrane filter to get unilamellar liposomes. For dye labeling of Gd-Liposome, 20 µg of rhodamine B was added in 1000 µg of Gd liposome formulation to give rhodamine B labeled Gd-Liposome following thin-film hydration.

5.2.4 Synthesis of gadolinium infused hybrid extracellular vesicles (Gd-HEV)

Small extracellular vesicles (sEVs) were isolated from mouse macrophage J774A.1 using the optimized centrifugation-ultrafiltration method as described in our earlier work.[250] Briefly, cells were grown to 70% confluency (5-6 million cells) in T75 flask before adding 15 mL conditioned DMEM media without serum and phenol red. Cell culture supernatant was harvested after 48 h incubation with cells and centrifuged at 2000g for 15 min to remove cell debris. The supernatant was purified and concentrated around 10 times using a 10 k molecular weight cut off (MWCO) amicon filter (2000 g, 15 min). The concentrated supernatant was then filtered with a 220 nm filter to remove large EVs. Further, sEVs was purified using sepharose CL-4B size-exclusion chromatography[258]. The purified sEVs were quantified in terms of protein content using the Bradford assay. Generally, around 8-10 mL of purified EVs solution is obtained from 100 mL of conditioned EV media, which give a protein yield of around 300-500 µg/mL.

Gd-Liposome and sEVs were hybridized using membrane extrusion to formulate gadolinium infused hybrid extracellular vesicles (Gd-HEV). Briefly, Gd-Liposome was mixed with sEVs in a 5:1 ratio of lipid: protein weight, vortexed, sonicated (bath and probe sonication, 30% amplitude, 2 min), and finally extruded with 200 nm polycarbonate filter for hybridization. The illustration of hybridization is presented in **Schematic 1**.

5.2.5 Characterization

The physicochemical characterization of Gd-HEV was studied by dynamic light scattering (DLS, MALVERN ZSP) and transmission electron microscopy (TEM) (FEI Technai G2 Spirit BioTWIN). The stability of nanoformulations was measured in terms of hydrodynamic size (nm), polydispersity index (PDI), and serum stability over a period. For serum stability, 50 µL of 90% fetal bovine serum was added in 150 µL of nanoformulations, and absorbance was taken immediately at 540 nm using Microplate reader (BioTek, Synergy H1 Hybrid reader) at every 6 seconds with double orbital shaking till 90 min. Protein characterization of sEVs and Gd-HEV were carried out using Bradford assay, Fourier-transform infrared spectroscopy (FTIR), sodium dodecyl sulfate–polyacrylamide gel electrophoresis (SDS-PAGE), and Dot blot. For Bradford assay, Bradford reagent was used for protein quantification by measuring the absorbance at 595 nm.[259] For FTIR, Gd-HEV and sEVs were lyophilized and analyzed using icolet™ iS™ 50 FT-IR Spectrometer (Thermo Fisher). For SDS-PAGE, samples were concentrated and mixed with sample loading buffer in a 1:1 ratio. Protein concentration was maintained at 1 µg/µL. 25 µl of each sample was loaded in wells of 4-20% Mini-PROTEAN® TGX Protein Gels and gel was run in the electrophoresis chamber (200V, 25 mA) until the protein band reaches the base of gel which may take around 45- 60 minutes. After the completion of electrophoresis, the gel was stained using Coomassie Brilliant Blue and imaged by Bio-Rad imager for the analysis of protein bands. For dot blot, a drop of samples (2-4 µL) were added in Polyvinylidene Fluoride (PVDF) membrane and incubated with blocking buffer for 30 minutes at room temperature. The blocking buffer was replaced by a primary antibody of interest, here CD63 and β-Actin, and incubated overnight at 4° Celsius. The primary antibody was washed by wash buffer and replaced by HRP conjugated anti-

mouse IgG secondary antibody (Cell signaling). Following 1 h incubation, the membrane was washed and developed using Signal Fire ECL TM Reagent for imaging (Bio-imager, Kodak).

Hybridization leading to the formulation of Gd-HEV was monitored by fluorescent resonance energy transfer (FRET) as described in our earlier work.[250,260] Briefly, FRET liposome was prepared by incorporating NBD lipid (electron donor), and RhB lipid (electron acceptor) in a 1:7 molar ratio. For membrane fusion analysis, 20 µL of FRET liposome was fused with 100 µL of sEVs containing approximately 100 µg proteins. The mixture was bath sonicated for 2 minutes to initiate fusion. Emission spectra (500 to 700 nm) of FRET liposome before and after fusion with sEVs was measured by exciting the samples at 440 nm to analyze the hybridization between Gd-HEV and sEVs.

5.2.6 Gadolinium loading and release study

Three different Gd-HEV formulation was prepared to vary the molar ratio of the constituents: EggPC:Gd-Lipid: cholesterol. The ratio of EggPC: Gd-Lipid was varied while keeping cholesterol constant to make three different formulations viz. Gd-HEV-1 (EggPC:Gd-Lipid:cholesterol= 20:50:30), Gd-HEV-2 (EggPC:Gd-Lipid:cholesterol= 35:35:30), and Gd-HEV-3 (EggPC:Gd-Lipid:cholesterol= 50:20:30). Percentage Gd loading and Gd weight percentage (wt %) were calculated in each formulation using the equation given below to optimize the best formulation. The amount of Gd in fabricated Gd-HEV was quantified using inductively coupled plasma mass spectrometry (ICP-MS).

$$\% \text{ Gd loading} = (\text{Initial Gd input} / \text{Gd in fabricated Gd-HEV}) * 100$$

$$\text{Gd wt \%} = (\text{weight of Gd in Gd-HEV} / \text{weight of Gd-HEV}) * 100$$

Free Gd^{+3} ion release from Gd-HEV formulation and Magnevist® was tracked over a period of 72 h by dialysis. 1 mL of Gd-HEV and Magnevist® containing 20 µg/mL of Gd was dialyzed

using 100-500Da (molecular weight cut off) dialysis membrane in 100 mL PBS release media kept at 37 °C while constant stirring (80 rpm) to maintain the sink condition during the experiment. 1 mL of release media was taken at a regular interval and replaced by fresh media. The amount of free Gd^{+3} ion in the release media was quantified using ICP-MS and cumulative release percentage was calculated using the following equation.

% cumulative Gd release = (Gd in release media/ Gd in 100% release) x 100

5.2.7 Evaluation of magnetic properties of Gd-HEV

Magnetic characterization of Gd-HEV was done using state-of-art 3T clinical MRI (Canon Galan 3 Tesla MRI) at the Veterinary Health Center of College of Veterinary Medicine, Kansas state university. T_1 weighted image of Gd-HEV was taken at different millimolar (mM) concentrations of Gd. The longitudinal relaxation time of Gd-HEV in aqueous solution was obtained using a fast spin-echo sequence with a variable repetition time (TR= 6000, 5000, 4000, 3000, 1500, 800, 600, 400, 200 ms). Echo time (TE) was 10 ms, with slice thickness = 2 mm, flip angle (FA) = 90°, FOV = 25.6 x 25.6, and image size of 256 x 256. Longitudinal relaxivity (r_1) was calculated based upon the slope of the linear fit of $\Delta 1/T_1$ versus Gd concentration in the sample. Magnevist®, a clinical contrast agent, was used as a control contrast agent. Magnetic characterization of Magnevist® was done using the same magnetic parameters. Further, the magnetic characterization of Gd-liposome was done following the same parameter to analyze the effect of EVs content on the magnetic property of the hybrid particle. For comparative study, the amount of Gd was kept the same in Gd-HEV, Magnevist®, and Gd-Liposome.

5.2.8 *In vitro* biocompatibility

In vitro biocompatibility of Gd-HEV and Gd-Liposome on mouse osteosarcoma (K7M2) and mouse normal fibroblast (NIH/3T3) was assessed following the MTT assay.[261] 10,000 cells

were seeded in 96 well plates. After 24 h, cells were incubated with varying lipid concentrations of Gd-HEV and Gd-Liposome from 200 to 6.25 μg/mL for 48 h in 5% CO_2 environment at 37°Celcius. Cells were then washed by PBS and incubated with MTT reagent (0.5 mg/mL) for 2 h. MTT reagent was prepared by adding 5 mg MTT in 1mL PBS, syringe filtered (220 nm), and diluted to 10 mL in serum-free DMEM media. MTT reagent forms formazan crystal by reacting with mitochondria of live cells. Thus formed formazan crystal was solubilized in 100 μL DMSO and absorbance was measured at 550 nm using microplate reader (BioTek, Synergy H1 Hybrid reader).

5.2.9 *In vitro* cellular interaction of Gd-HEV

In vitro cellular interaction of Gd-HEV was evaluated in terms of its localization with early endosomes in cells. Gd-HEV was evaluated for cellular specificity among mouse osteosarcoma K7M2 and mouse normal fibroblast NIH/3T3 by tracking its internalization and localization in the early endosome. Cells were transfected by CellLight™ Early Endosomes-green fluorescent protein (GFP) following manufacturer protocol. 10,000 cells were seeded in 96 well plates and incubated with 10 μL GFP for 20 h for transfection. After that, transfection media was removed with fresh media and transfected cells were incubated with Rhodamine B labeled Gd-HEV for 3 h. Cells were then fixed by 4% Paraformaldehyde. Nuclei were stained by DAPI and cells were observed with a Confocal Laser Scanning Microscope (Carl Zeiss, LSM-700). Internalization was quantified based upon the intensity of red color inside cells produced by Rhodamine B labeled Gd-HEV using the image analysis software ImageJ. The degree of colocalization was quantified based upon Pearson's correlation coefficient (R) using ImageJ colocalization analysis.

5.2.10 *In vitro* immunogenicity assay

In vitro immunogenicity of EVs and its derivative particles were tested in human peripheral blood monocyte to assess the molecular functionality in terms of immunogenic response using cytokine release assay.[75,76,262] In brief, 500,000 THP-1 cells were seeded in 12 well plates and after 24 h, six different particles were treated and the cells were incubated for another 24 h. Gd-HEV (100 µg/mL), Gd-Liposome (100 µg/mL), EVs (20 µg/mL, equivalent EVs concentration in Gd-HEV), Magnevist (14 µg/mL, equivalent Gd concentration in Gd-HEV), LPS (6 µg/mL), and PBS were treated. Here, LPS is positive control and PBS is a negative control. The cell culture supernatant for each treatment was collected, centrifuged (2000g, 10 min, 4°C) to remove cell debris, and immediately used for cytokine analysis. Supernatants were analyzed for proinflammatory cytokines (Interleukins IL-6, IL-1β, and Tumor Necrosis Factor-alpha (TNF-α)) using quantitative enzyme-linked immunosorbent assay KIT (ELIA) (R&D Systems, Inc. Minneapolis, MN) following manufacture's protocol. The absorbance of standards, samples, and controls was measured at 450 nm with wavelength correction at 540 nm using Synergy H1 hybrid microplate reader (BioTek Instruments Inc. VT) to quantify cytokines released in each treatment.

5.2.11 *In vivo* study by fluorescence bioimaging and magnetic resonance imaging

In vivo imaging assay was performed in immunodeficient NU/NU nude mice (Charles River, 088/NU/NU homozygous) to analyze the contrast enhancement, biodistribution and tumor homing property of Gd-HEV using near infra-red fluorescent bioimaging and MRI. Mice experiments were conducted following the animal use protocol approved by KSU IACUC. Mouse osteosarcoma tumor was developed by subcutaneous injection of K7M2 cells (1x 10^6) dispersed in PBS in the lower flank of mice.[257] Mice were then monitored every other day for tumor size and

overall weight. When the tumor size reached approximately 6 mm, mice were injected with particles and imaged.

For fluorescent bioimaging, Gd-HEV and Gd-Liposome were labeled with 1,1′-dioctadecyl-3,3,3′,3′-tetramethylindotricarbocyanine iodide (DiR) dye using physical encapsulation technique. 20 µL DiR dye was added in 1000 µg Gd-HEV and extruded using a 200 nm polycarbonate membrane filter for physical encapsulation of dye in Gd-HEV. 10 mg/kg of DiR labeled Gd-HEV and Gd-Liposome in 100 µL volume was injected in tumor-bearing mice (n=3) by lateral tail vein injection. Mice were anesthetized using 2-3% isofluorane in 100% oxygen and imaged under anesthesia by the Pearl® Trilogy imaging system (LI-COR®). Images were taken at pre-injection, 1 h, 3 h, 6 h, and 24 h post-injection to analyze time-dependent biodistribution of Gd-HEV in mice. After 24 h, mice were euthanized, and organs were collected and imaged. The amount of Gd-HEV localized in the organ was quantified based upon the amount of Gd in the organ using inductively coupled plasma-mass spectroscopy (ICP-MS).

For magnetic resonance imaging, Gd-HEV with 100±10 µg equivalent of Gd in 100 µL PBS was injected in mice intravenously and imaged on a Vantage Galan™ 3T MRI clinical scanner. The MRI images of mice under anesthesia (2-3% isofluorane in 100% oxygen) were acquired before injection, at injection and post-injection at 15 mins and 60 mins. To analyze the tumor homing property, images were processed to focus tumor area. Magnevist®, a clinical contrast agent was used as a control particle and injected in mice with equivalent Gd^{3+} amount as that of Gd-HEV. The T_1-weighted MR images were recorded using a fast spin-echo sequence at TR=11.40 ms, TE=5.50 ms, FA=25º, slice thickness=1 mm, and FOV=126 mm. Images were processed for maximum intensity projection with background subtraction to reconstruct the three-dimensional image for precise representation of contrast enhancement using Medical Image

Processing, Analysis, and Visualization (MIPAV) software. All animal experiments and protocols were approved by the Institutional Animal Care and Use Committee and Institutional Biosafety Committee, Kansas State University, Manhattan.

5.2.12 Histologic Analysis

Histologic analysis of tissue section of different organs of mice injected with Gd-HEV was completed. Organs from untreated mice were used as controls. Mice were euthanized, and organs were collected after 24 post-injection with Gd-HEV. Lungs, heart, kidney, liver, and tumor were collected and immersed into 10% formaldehyde solution for tissue preservation. After fixation, tissues were trimmed onto a single glass slide and stained with hematoxylin and eosin (H&E) for histologic analysis, per standard laboratory protocols.[263]

5.2.13 Statistics

Analysis of covariance between two linear regression lines was analyzed using regression analysis and selecting "Test whether the slopes and intercepts are significantly different" option in GraphPad Prism. The statistical differences between the linear regression lines were analyzed based upon the difference in slopes and intercepts. First, the analysis of slopes is conducted to give a p-value. A P-value less than 0.05 signify that the differences in the slope of two linear regression lines are statistically significant suggesting two linear regression is significantly different. The P-value for slope more than 0.05 signifies that the slope of linear regression is not significantly different. This observation warrants the evaluation of intercepts of two linear regression lines. The P-value of intercept higher than 0.05 concludes that differences between intercepts are not significant and two linear regression are not statistically different. All major data represents Mean±SD with triplicate experiments. For biocompatibility data, the number of replication was six.

5.3 Results and discussion

5.3.1 Characterization

EVs were isolated by *in vitro* cell culture of mouse macrophage J774A.1 as detailed in methods. Gd based contrast agent incorporated in the liposomal system was hybridized with EVs construct to formulate gadolinium infused hybrid extracellular vesicles (Gd-HEV) using thin-film hydration technique followed by membrane extrusion, as depicted in **Figure 5.1**. Gd-HEV were characterized for size and surface property using dynamic light scattering. Gd-HEV showed the

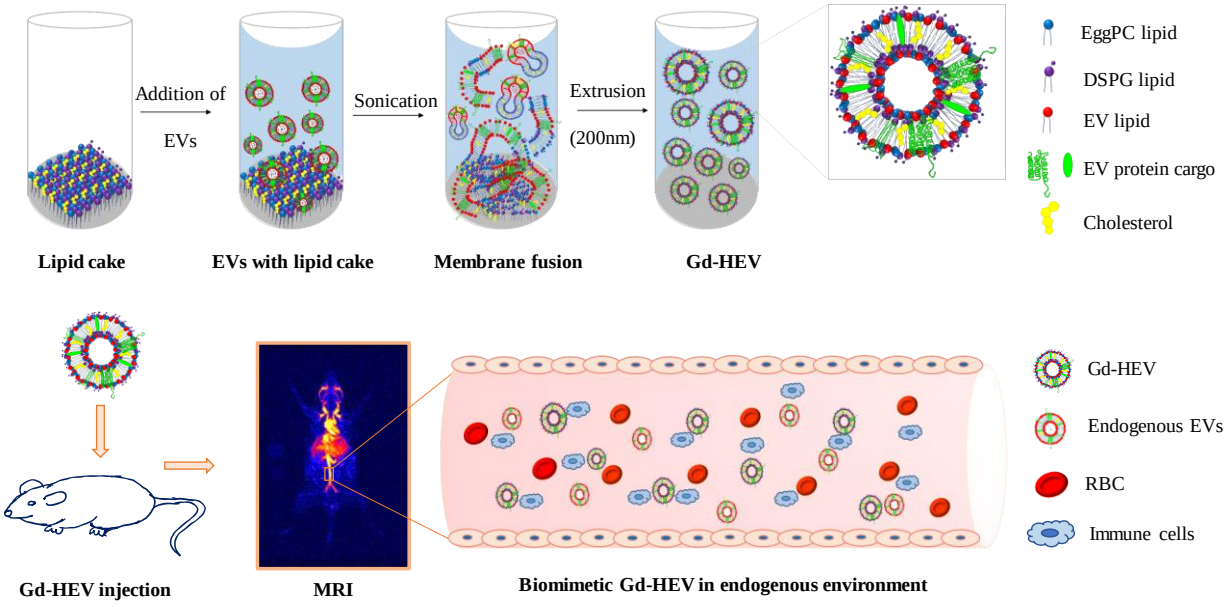

Figure 5.1 Schematic representation of the reconstruction process of extracellular vesicles with gadolinium infused lipid cake for the fabrication of gadolinium infused hybrid extracellular vesicles (Gd-HEV) via membrane fusion. Gd-HEV, being reconstructed from endogenous EVs, can communicate with the endogenous environment to avoid rapid immune clearance thereby allowing for longer blood retention time for MRI contrast enhancement.

hydrodynamic size of 127±2 nm and 0.18±0.01 PDI with size distribution similar to Gd-Liposome (138±2 nm and 0.2±0.01 PDI). Surface charge analysis showed a negative zeta potential of -33±4 mV for Gd-HEV and -37±3 mV for Gd-liposome. Size and surface charge analysis demonstrated that engineered Gd-HEV physical properties are similar to that of control Gd-liposome and is not

significantly affected by hybridization (**Figure 5.2A & B**). Moreover, the negative zeta potential further reflects the properties of the EVs, which together with liposomal properties such as monodispersed hydrodynamic characteristics confirmed the hybridization process.

Transmission electron microscopy showed the morphological characteristic of sEVs and Gd-HEV as shown in **Figure 5.2C.** Both particles are spherical entities with slight changes in surface morphology after hybridization in Gd-HEV. With the confirmation of size, surface property, and morphological characteristics, Gd-HEV were then characterized for colloidal stability in PBS and serum condition. The stability of nanoformulations is key to maintaining its efficacy in biological media. Therefore, analysis of stability in a proper solvent such as complex serum environment is crucial for *in vitro* and *in vivo* experiments. Nanoformulations can form aggregates in serum due to the formation of protein corona in its surface.[264] To evaluate the dynamic stability of Gd-HEV, Gd-HEV was subjected to serum environment and routinely compared with PLGA polymeric nanoparticle without any coatings (Figure 1F).[265]

Engineered Gd-HEV were analyzed for colloidal stability for up to 30 days in terms of size and PDI in which Gd-HEV retained its physiochemical properties (**Figure 5.2D & E**). After 15 days and 30 days, the slight increment of both size (up to 160 ± 10 nm) and PDI (up to 0.3 ± 0.05) was observed, but the integrity of the particle was still maintained. After brief agitation using sonication (30% amplitude, 30 s) the size measured shows minimal changes signifying that the increment in size overtime may be due to particle aggregation, which was then disrupted by sonication. Serum stability analysis of Gd-HEV showed stable absorbance through 90 minutes of study signifying that the particle does not aggregate in the serum environment (**Figure 5.2F**). It is significant to note that serum stability measures the serum-induced aggregation of particles, which happens immediately when putting particle in serum. Therefore, the steady absorbance observed

over a 90 minute period clearly reflects the stability of Gd-HEV in serum. To confirm this phenomenon, we used PLGA nanoparticle without surface coating to serve as a positive control. We observed a rapid increase in absorbance in its first 20 minutes of exposure to serum suggesting rapid corona formation and aggregation of the particles. The stability of Gd-HEV in the serum environment can be attributed to its biomimetic surface characteristic with transmembrane proteins derived from extracellular vesicles. These protein constructs of engineered Gd-HEV can communicate with the *in vivo* protein environment and convince the body that they are endogenous, thereby escaping rapid protein corona formation.[266,267] Along with the stability, biomimicry can aid in particle retention in blood and tissue, ultimately allowing maximum time for the particle to show its effect.

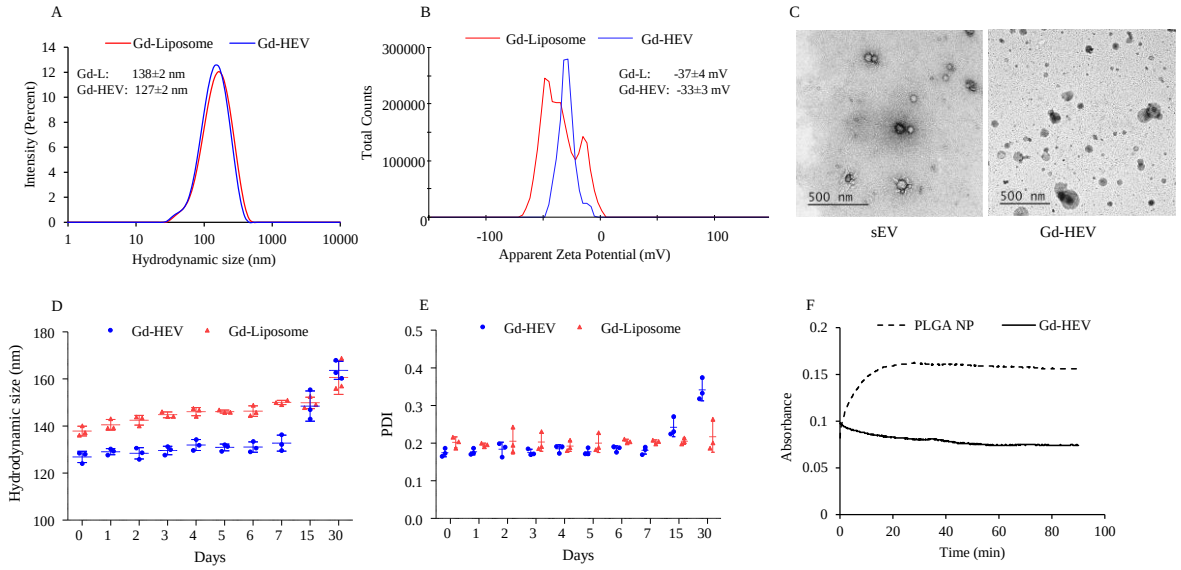

Figure 5.2 Physicochemical characterization of Gd-HEV. (A) Hydrodynamic size of Gd-HEV and Gd-Liposome, (B) zeta potential of Gd-HEV and Gd-Liposome showing surface charge characteristic, (C) transmission electron microscopy of small extracellular vesicles (sEV) and Gd-HEV showing morphological characteristic of vesicles, (D) stability of Gd-HEV and Gd-Liposome in terms of hydrodynamic size, (E) polydispersity index (PDI) over the period of 30 days, and (F) serum stability of Gd-HEV in terms of absorbance at 560 nm over 90 min of study. PLGA was used as a positive control.

Protein characterization and evaluation of hybridization

We moved forward to evaluate the retention of biomimicry in Gd-HEV with respect to naive EVs. SDS-PAGE analysis gave signature bands of different proteins present in EVs and Gd-HEV (**Figure 5.3A**). Gd-HEV showed protein bands similar to that of EVs suggesting the retention of protein content through hybridization. These proteins are the main player in the functional aspect of EVs, as such, retention of these characteristic proteins helps to maintain the biomimicry in Gd-HEV. The specific proteins from these bands were extensively characterized in our recent publication where EVs showed the presence of characteristic EV marker proteins CD9, CD63, CD81, CD11b, and TSG101.[250] Here, EVs and Gd-HEVs were characterized for the presence of one of the EVs marker protein, CD63, using dot blot. β-Actin was used as a positive control. Both, EVs and Gd-HEV showed the presence of CD63 and β-Actin (**Figure 5.3C**). Protein contents were further characterized spectroscopically using FTIR. **Figure 5.3B** represents the FTIR spectra of EVs and Gd-HEVs in terms of %Transmittance with respect to Wavenumbers (cm^{-1}). Both EVs and Gd-HEV showed a characteristic peak at around 1043-1064, 1120-1242, 1400-1465, 1576-1646, and 3726 cm^{-1}. Peaks at 1043-1064 cm^{-1} and 1120-1242 cm^{-1} represents the stretching vibration of phosphodiester and ether groups of phospholipids and cholesterol.[268,269] The sharp peak observed in the case of Gd-HEVs suggests the presence of phospholipid and cholesterol bonds that can be attributed to the hybridization of liposome with EVs. Peak around 1400-1465 cm^{-1} is due to the bending vibration of lipid and protein hydrocarbon groups. Peak around 1576-1646 cm^{-1} can be attributed to the presence of an amide bond arising from C=O stretching vibration and N-H bending vibration of the peptide bond. The broad peak observed around 3726 cm^{-1} can be attributed to N-H stretching vibration of the peptide bond along with the broad –OH stretching vibration.[268] Along with these peaks, Gd-HEV showed a specific peak at 1730, 2852, and 2923 cm^{-1} which was not observed in the case of EVs. All these specific peaks can be attributed to lipids

present in Gd-HEV. The peak at 1730 cm^{-1} is due to the presence of ester groups of phospholipids and cholesterol while the peak at 2852 and 2923 cm^{-1} is due to the symmetric and antisymmetric stretching vibration of the lipid acyl -CH_2 groups. While the presence of lipids is in EVs as well, Gd-HEV is engineered with synthetic lipids (synthetic lipids: EVs protein = 5:1). The extra hybridized synthetic lipid in EVs could explain the observed specific lipid IR peak in the case of Gd-HEV. The presence of specific protein and lipid peak in the case of Gd-HEV further validated the hybridization of EVs with synthetic liposomes.

Hybridization was further evaluated using a fluorescent-based energy transfer (FRET) experiment. FRET is a powerful biophysical technique to monitor macromolecular interaction between fluorescent molecules.[270] In FRET, an electronically excited fluorophore (FRET donor) transfers its energy to another chromophore (FRET acceptor) that has the absorption spectrum overlapped with the emission spectrum of the donor.[271] By monitoring this transfer of energy between two FRET pairs-donors and acceptors, membrane fusion can be monitored in bio-membranes.[242,260,272–274] Here, FRET liposome was prepared by integrating FRET donor NBD lipid and FRET acceptor RhB lipids in the liposomal construct as detailed in methods. When this FRET liposome is electronically excited at 440 nm to excite NBD lipid chromophore and emission spectra recorded, characteristic emission spectra as shown in **Figure 5.3D** is observed. The emission spectra have two maxima peak, with slight maxima at 525 nm and significant maxima peak at 595 nm suggesting energy transfer from FRET donor NBD (λ_{em} 525 nm) to FRET acceptor RhB (λ_{em} 595 nm). This liposome was then hybridized with EVs to formulate Gd-HEV and again the emission spectra were recorded. Emission spectra of Gd-HEV showed a decrement in maxima peak at 595 nm and increment in maxima peak at 525 nm compared to that of FRET liposome suggesting a decrease in energy transfer efficiency. FRET is distance-dependent and the decrease

in FRET efficiency suggests the increment in the distance between two fluorophores-NBD lipids and RhB lipids.[275] This strongly suggests the insertion of EVs lipid and protein content in the liposomal lipid bilayer resulting in the increment of the distance between two fluorophores. Hence, FRET experiment validated the successful hybridization between Gd-Liposome and EVs, to fabricate Gd-HEV.

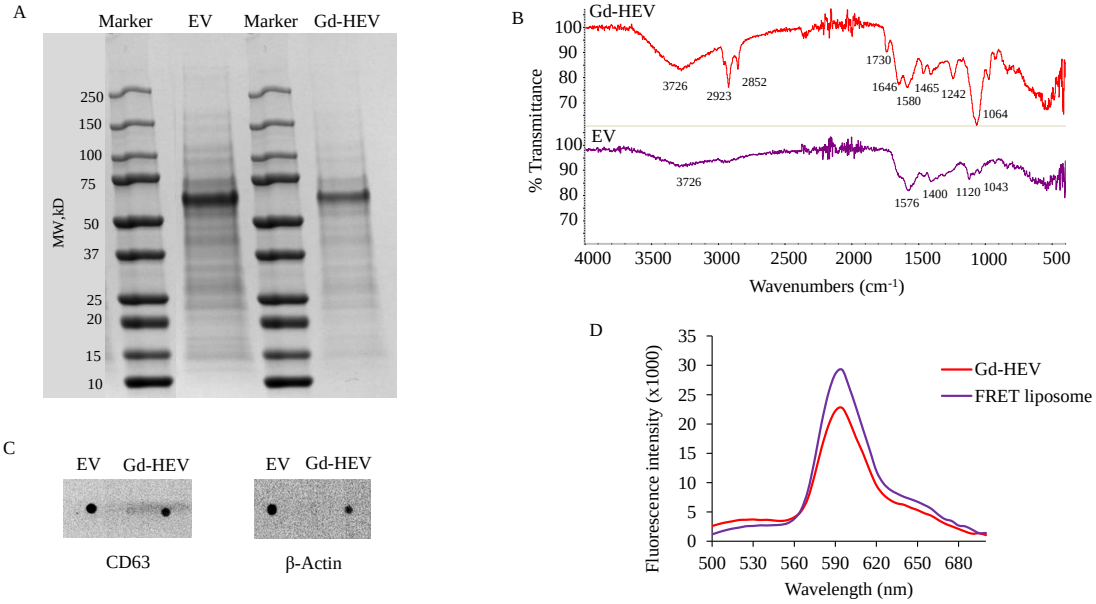

Figure 5.3 Protein characterization and evaluation of hybridization. (A) SDS-PAGE analysis of EVs and Gd-HEV showing bands of different proteins along with their molecular weights, (B) FTIR analysis of EVs and Gd-HEV showing % transmittance peaks for lipids and proteins at different wavenumber, and (C) dot blot assay for the identification of EVs marker protein CD63. β-Actin was used as a positive control. (D) FRET study showing emission spectra of FRET liposome and Gd-HEV (FRET liposome hybridized with EVs). FRET study was conducted using fluorescent donor NBD (λem = 525 nm) and fluorescent acceptor RhB (λem = 595 nm) at an excitation wavelength of 440 nm.

5.3.2 Gadolinium loading, release, and biocompatibility study

The component Gd is from the Gd-lipid conjugate which was synthesized following our protocol.[242,255,256,276] Gd lipid in Gd-HEV is responsible for the magnetic property of the particle. The amount of Gd-lipid in Gd-HEV can be crucial in maintaining the optimum magnetic property. To optimize optimum loading efficiency and wt% of Gd in Gd-HEV, three different formulations

of Gd-HEV were prepared by varying the molar ratio of Gd-Lipid and EggPC while keeping the amount of cholesterol constant. Gd-HEV-1 (20:50:30), Gd-HEV-2 (35:35:30), and Gd-HEV-3 (50:20:30) were prepared with a different molar ratio of EggPC: Gd-Lipid: Cholesterol. All three formulations gave good loading efficiency, ranging from 87 to 99%, showing the high efficiency of hydrophobic insertion strategy to incorporate Gd-lipid in Gd-HEV (**Figure 5.4A**). In the case of Gd wt%, Gd-HEV-1 showed the highest wt% with 1.9%, compared to 1.3 wt% in Gd-HEV-2, and 0.86 wt% in Gd-HEV-3. The trend of observed wt% was in accordance with the input Gd-Lipid amount in formulations. The overall wt% of three different formulations was not significantly different from each other. With similar loading efficiency and wt%, Gd-HEV formulations were analyzed in terms of stability over a period. Gd-HEV-3 gave the best stability in terms of size over a period with the average hydrodynamic size of 166±4 nm, compared to 194±12 nm in Gd-HEV-1 and 188±9 nm in case of Gd-HEV-2 (**Figure 5.S1**). This suggests that with higher wt% of Gd in Gd-HEV, stability over a period is reduced. Based on these analyses, Gd-HEV-3 formulation was deemed to be prefeered, and so this formulation was used for the remainder of this study.

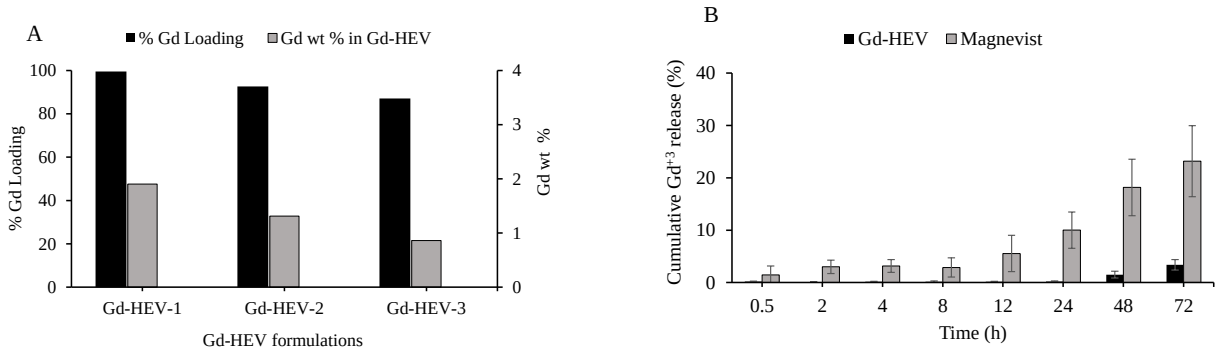

Figure 5.4 Gadolinium loading and release study. (A) Optimization of Gd-HEV formulation in terms of loading efficiency. % gadolinium loading efficiency and gadolinium wt % of three different Gd-HEV formulations with varying the molar ratios of Gd-Lipid and EggPC. Cholesterol amount was kept constant in all formulations. (B) Cumulative gadolinium ion release % from Gd-HEV and Magnevist® over a period of 72 h in PBS.

Safety issue of Gadolinium-based contrast agent

Free Gd^{+3} ion is toxic heavy metal and major health concern in the application of Gd-based contrast agent as they can compete with Ca^{2+} ion and disrupts crucial calcium homeostasis. Ca^{2+} (114 pm) has a size similar to that of Gd^{3+} (107.8 pm), as a result, Gd^{3+} can compete with Ca^{2+} to bind with enzymes and affect voltage-gated calcium channels, causing adverse biological effects.[277,278] In this scenario, retention of Gd^{+3} ion in the nanoparticulate formulation is paramount for the development of a safe gadolinium-based contrast agent. To evaluate the retention of Gd in Gd-HEV formulation, Gd release assay was carried out as described in methods (**Figure 5.4B**). Magnevist®, a widely used commercial Gd-based contrast agent was used as a control. Gd release assay in Gd-HEV showed a nominal release of free Gd^{+3} ion over a period, with non-significant release (less than 0.2%) up to 24 h, 1.5% release at 48 h, and 3.4% release at 72 h of study. This nominal release can be attributed to the macrocyclic structure of Gd-DOTA, a constituent of Gd-Lipid in Gd-HEV. Here, the macrocyclic structure of DOTA helps to chelate Gd^{+3} from all directions with eight coordination sites.[277,279] Further, the ionic radius of Gd^{+3} (107.8 pm) perfectly matches the cavity of DOTA, thereby caging Gd^{+3} in its macrocyclic structure.[280] Due to this perfect fit, mono-ionic nature, and hydrophilicity of chelator DOTA, Gd-DOTA shows high thermodynamic and kinetic stability.[280] The nominal release of free Gd^{+3} ion over a long period of 72 h shows excellent compatibility of formulated Gd-HEV as a safe contrast agent.

In the case of Magnevist®, less than 10% release was observed until 24 h. But at 48 h and 72 h, 18% and 23% of free Gd^{+3} ion were observed, respectively. The high release observed in the case of Magnevist® can be attributed to the linear structure of the contrast agent, where the Gd^{+3} ion is chelated from one side only leaving the opposite side open, making them more kinetically labile to escape the chelation [281]. Such a high release of free Gd^{+3} ion as observed with Magnveist®

is a significant health concern. A recent report suggests potential gadolinium deposition in the brain from the use of linear contrast agents, and as a result, the European Union suspended the use of four linear contrast agents including Magnevist® in 2017.[282] This scenario warrants the development of a safe biomimetic contrast agent.

The safety of formulated contrast agents, Gd-HEV and Gd-Liposome were evaluated *in vitro* in terms of cellular biocompatibility in mouse osteosarcoma K7M2 and mouse normal fibroblast NIH/3T3 using MTT assay (**Figure 5.5**). The assay showed good biocompatibility of nanoformulations in both K7M2 and NIH/3T3 cells, with over 70% cell viability even at a high concentration (200 µg/mL) following 48 h incubation of cells with particles. At a concentration of 50 µg/mL or below, the biocompatibility was more than 80%. This confirms the biocompatibility of Gd-HEV and Gd-liposome for both cancerous and non-cancerous cell lines. The observed high cellular viability and excellent retention of Gd in Gd-HEV make itself a safe biocompatible contrast agent.

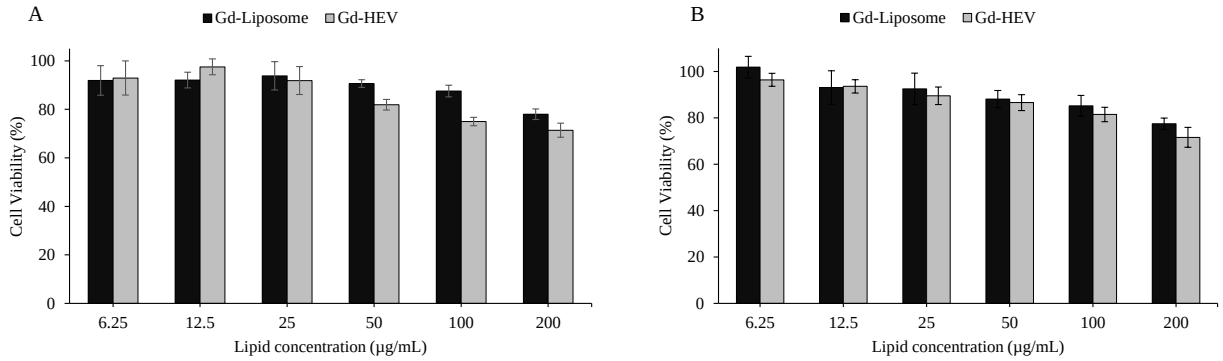

Figure 5.5 In vitro biocompatibility assay. Biocompatibility of Gd-liposome and Gd-HEV evaluated with (A) mouse osteosarcoma K7M2 and (B) mouse normal fibroblast NIH/3T3 after 48 h incubation following MTT assay.

5.3.3 Evaluation of magnetic properties

With the assurance of stability and safety of Gd-HEV, magnetic properties were evaluated for possible application in magnetic resonance imaging (MRI). Gd-HEV was characterized for

magnetic properties by measuring T_1 as a function of aqueous nanoparticles with different Gd concentrations as described in methods. T_1 weighted image of Gd-HEV at different millimolar concentration was taken using 3T clinical MRI. Magnevist® was used as a control. The input concentration of Gd in both Magnevist and Gd-HEV was maintained the same. However, the concentration of Gd as determined by ICP-MS was slightly different between Gd-HEV and Magnevist®, as depicted in the T_1 weighted image in **Figure 5.6A**. T_1 weighted image showed enhancement of contrast in the case of Gd-HEV compared to Magnevist®, at a similar concentration. Both Gd-HEV and Magnevist® showed concentration-dependent contrast, with higher signal intensity at higher concentration. The higher contrast property of Gd-HEV was further supported by the T_1 recovery curve. **Figure 5.6B** shows the %signal intensity of phantom images of Gd-HEV and Magnevist® at a particular concentration as a function of recovery time. Gd-HEV showed higher % signal intensity compared to Magnevist® at all recovery time point suggesting enhanced contrast property. Longitudinal relaxivity (r_1) as calculated by the slope of linear fit of inverse of recovery time (s^{-1}) with respect to different Gd concentration (mM) shows significant higher r_1 of 9.87 $mM^{-1}s^{-1}$ for Gd-HEV compared to 3.98 $mM^{-1}s^{-1}$ for Magnevist® (**Figure 5.6C,** p-value = 0.001, linear regression analysis of slope) at clinical 3T scanner. **Figure 5.6D** shows the r_1 relaxivity of Gd-HEV as compared to Magnevist® at different concentrations, where Gd-HEV showed around 100% increment in r_1 relaxivity compared to Magnevist® at similar Gd concentration. Observed significant contrast enhancement in the case of Gd-HEV where contrast agent Gd-DOTA is incorporated in a nanoparticulate formulation can be attributed to the reduction of the tumbling rate of paramagnetic metal complexes due to incorporation in a stable nanoparticulate formulation, thereby promoting effecting interaction between a water molecule and metal complex.[283] A similar increment in longitudinal relaxivity r_1 has been reported by Liang

et al, where naïve Gd-DOTA showed r_1 relaxivity of 4.2 $mM^{-1}s^{-1}$ compared to 10.61 $mM^{-1}s^{-1}$ (3T MRI) when incorporated to polymeric nanoparticle system.[283] Likewise, Aryal et al also reported an increment of r_1 relaxivity of Gd-DOTA to 19 $mM^{-1}s^{-1}$ (3T MRI) after insertion in the lipid bilayer of the red blood cell membrane.[242]

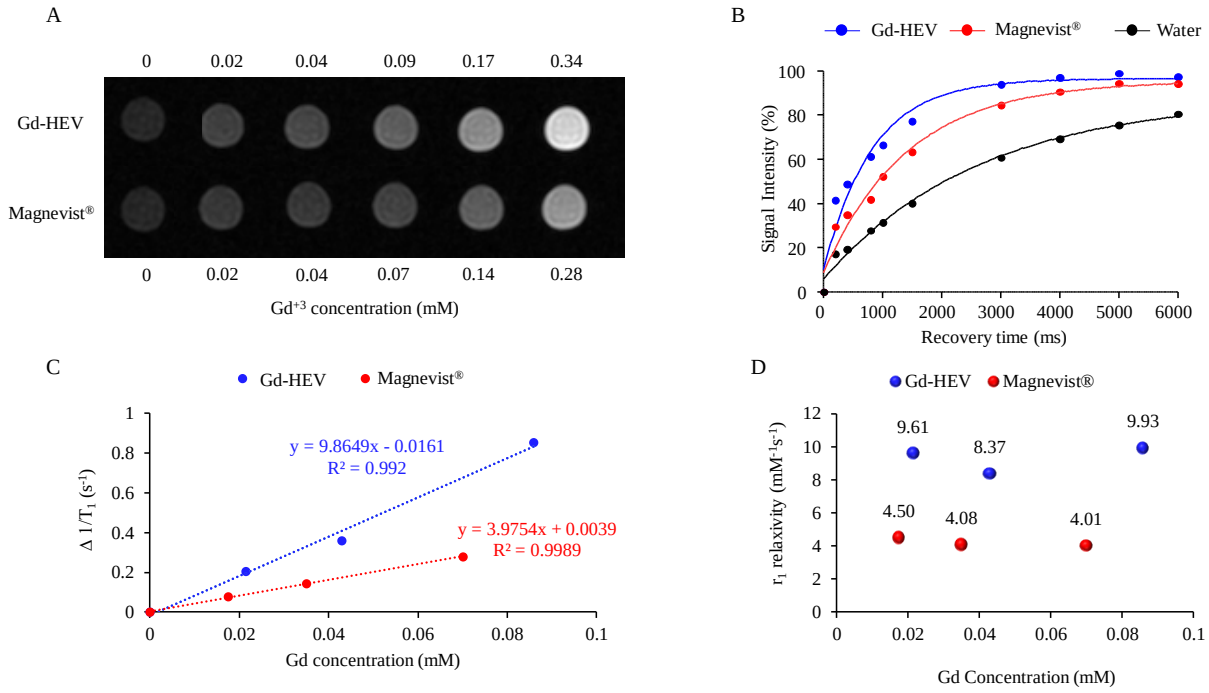

Figure 5.6 Magnetic characterization of Gd-HEV. (A) T_1 weighted image of Gd-HEV and Magnevist® at different Gd concentration showing contrast enhancement in a 3T clinical MRI system (TR=400 ms, TE=10 ms, and slice thickness=2 mm), (B) T_1 recovery curve of Gd-HEV (0.09 mM Gd), Magnevist (0.07 mM Gd), and water in terms of % signal intensity with respect to recovery time (ms) at specific Gd concentration showing different recovery characteristic, (C) linear fit of inverse of relative change in T_1 recovery time ((Δ $1/T_1$ (s^{-1})) with respect to different Gd concentration (mM) in Gd-HEV and Magnevist® (p-value = 0.001, linear regression analysis of slope). Slope of the fitted model gives longitudinal relaxivity (r_1): 9.87 $mM^{-1}s^{-1}$ for Gd-HEV and 3.98 $mM^{-1}s^{-1}$ for Magnevist®, and (D) r_1 relaxivity of Gd-HEV and Magnevist® at different concentration. Gd-HEV shows higher r_1 relaxivity compared to Magnevist®. All data were obtained using a 3T clinical MRI.

EVs protein construct does not significantly alter the longitudinal relaxivity (r_1)

To evaluate the effect of EVs transmembrane protein construct on the magnetic properties, the T_1 weighted image of Gd-HEV and Gd-Liposome was taken using 3T clinical MRI and comparative analysis of magnetic properties was performed (**Figure 5.S2**). Here, Gd-Liposomes,

with the same structural framework as Gd-HEV but devoid of EVs cargo, act as control particles. Gd-Liposome showed a concentration-dependent contrast similar to that of Gd-HEV as shown by the T_1 weighted image and T_1 recovery curve. Longitudinal relaxivity r_1 showed a slight increment in the case of Gd-HEV compared to Gd-Liposome, 9.86 vs 8.20 $mM^{-1}s^{-1}$, respectively. This observed change in longitudinal relaxivity r_1 was statistically non-significant, as computed by linear regression analysis of slope and intercept with a p-value of 0.117 and 0.118, respectively. Longitudinal relaxivity computed at three different concentrations also showed higher relaxivity for Gd-HEV compared to Gd-Liposome, however, the increment was less than 2. These analyses showed that the incorporation of EVs construct in Gd-Liposome slightly increases the longitudinal relaxivity, but the increment is non-significant. This finding can be beneficial as EVs protein content is heterogeneous and depends upon the source of parent cells.[246,284] In such a scenario, we can standardize the magnetic property using Gd-Liposome. Based on the need and application, different types of EVs could be integrated and functionalized in liposome while maintaining a similar magnetic property. It is, however, important to note that the engineering method and ratio of integration should be maintained same to envision a similar result.

5.3.4 *In vitro* cellular interaction study

The presence of EVs construct in Gd-HEV can have two main functionality- biomimicry and differential cellular interaction. The biomimicry functionality can help to escape immune clearance and increases the blood and tissue retention time of nanoconstructs.[285–289] The differential cellular interaction can help in the targeted efficacy of the nanoconstructs. EVs have been reported to share the characteristic of the parent cell and plays an important role in cellular communication.[246,266,267] In our recent work of EVs, we reported the differential internalization behavior of engineered EVs derived from macrophage.[250] Engineered EVs showed significant

higher internalization in the cancerous cells compared to non-cancer, which can be mainly attributed to the presence of EVs membrane proteins. In this study, we further explored the internalization behavior of engineered Gd-HEV by tracking its localization in early endosomes within cancer and non-cancer cell to envision the realistic differential cellular interaction of EVs. EVs are reported to internalize in the cell by various endocytosis pathways including clathrin-mediated, caveolae-mediated, macropinocytosis, phagocytosis, and lipid raft-mediated uptake.[290–292] After internalization, they are delivered to early endosome via endocytic vesicles where the fate of nanoparticles is determined.[292] Provided these engineered EVs are of endosomal origin, they are expected to avoid the endosomal degradation.[293,294]

Gd-HEV was labeled with RhB lipid via a hydrophobic insertion strategy to track its localization inside the cell.[250,257,260,276] Cells were transfected by early endosome green fluorescent protein (GFP) to label early endosomes. Localization of RhB labeled Gd-HEV was analyzed in early endosome using confocal microscopy. **Figure 5.7A** shows the confocal micrographs of K7M2 and NIH/3T3 showing the internalization of RhB labeled Gd-HEV in cells and its localization at GFP labeled early endosome. Orange yellowish color represents the colocalization of red-colored nanoparticles with green colored early endosomes. A representative single-cell image of K7M2 and NIH/3T3 was analyzed for differential colocalization study which clearly showed a higher degree of colocalization in the case of K7M2 compared to that of NIH/3T3, as represented by an orange yellowish color (**Figure 5.7B**). The degree of colocalization was analyzed quantitatively in terms of Person's R-value computed by the ImageJ® colocalization threshold plugin. **Figure 5.7C** shows a scatter plot of colocalization of Gd-HEV in early endosome in K7M2 and NIH/3T3 along with the Pearson's R-value. Higher Pearson's R-value of 0.69 in the

case of K7M2 compared to that of 0.25 in the case of NIH/3T3 clearly suggest higher

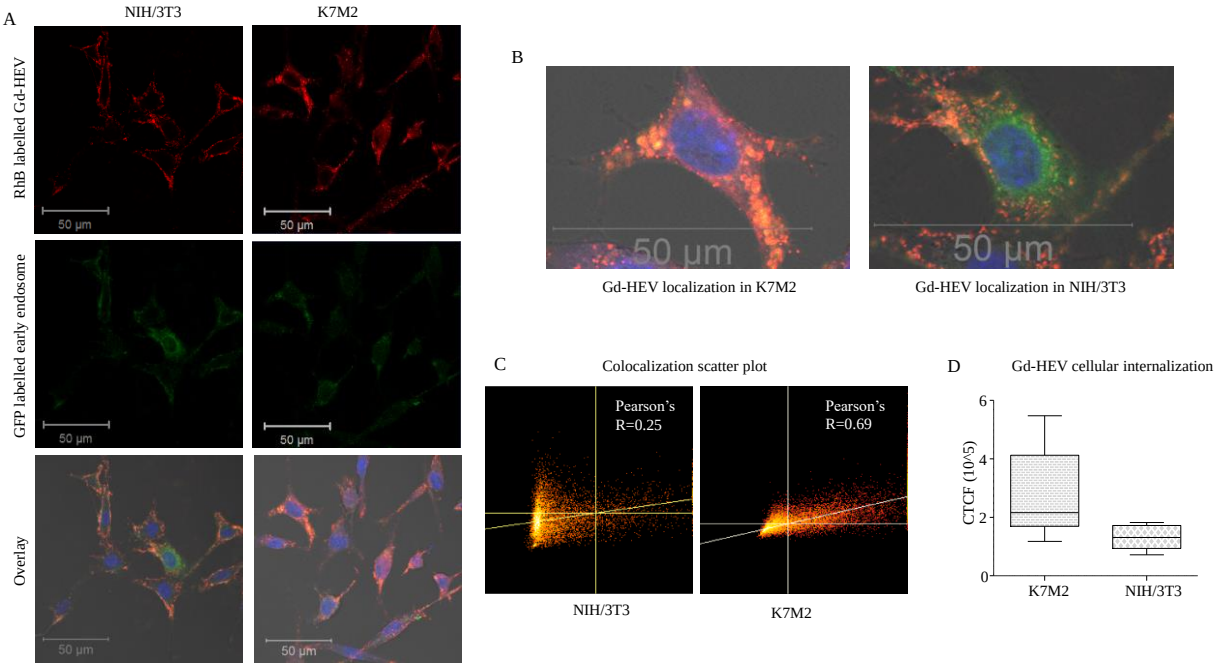

Figure 5.7 In vitro cellular interaction assay of Gd-HEV. (A) Confocal microscopic image showing internalization of Gd-HEV and its localization in early endosome in mouse normal fibroblast (NIH/3T3) and mouse osteosarcoma (K7M2). Gd-HEV was labeled by Rhodamine B. Cells were transfected by CellLightTM Early Endosomes-GFP to label early endosomes and incubated with Gd-HEV for 3 h. Overlay figure shows the colocalization of rhodamine B labeled Gd-HEV in GFP labeled early endosome, (B) representative image of the overlay figure showing differential co-localization of Gd-HEV in K7M2 compared to that of NIH/3T3 signifying different cellular internalization behavior, (C) scatter plot of Gd-HEV colocalization in NIH/3T3 and K7M2 with Pearson's R-value calculated using ImageJ colocalization threshold plugin, and (D) quantification of internalized Gd-HEV in terms of corrected total cell fluorescence (CTCF) in K7M2 and NIH/3T3. Quantification was done by ImageJ.

colocalization activity of Gd-HEV in K7M2. Higher colocalization can be related to higher cellular internalization of Gd-HEV in K7M2, as confirmed by the quantitative cellular internalization analysis based upon the intensity of the red signal in the cell (**Figure 5.7D**). *In vitro* cellular interaction study showed the differential uptake and localization of Gd-HEV towards cancer cells (K7M2) compared to non-cancer (NIH/3T3). This selective cellular interaction of Gd-HEV can be

advantageous for the development of cancer-targeted diagnostics, drug delivery, and/or imaging contrast agents.

Retention of EVs functionality through the reconstruction process

One of the crucial aspects of the engineering or reconstruction of EVs based study is the retention of molecular functionality after the reconstruction process. To exploit the native advantages of EVs based systems in drug delivery and diagnostic imaging, the molecular functionality of EVs should be conserved. We have demonstrated the retention of protein content through the reconstruction process through our protein analysis. To further analyze the retention of molecular functionality of EVs, we explored the cellular internalization behavior and immunogenic stimulation of naïve EVs and EVs after reconstruction. *In vitro* cellular internalization assay of Gd-HEV, Gd-liposome, and naïve EV was performed by confocal microscopy on mouse osteosarcoma K7M2 and mouse normal fibroblast NIH/3T3. Here, Gd-liposome acts as a control particle for Gd-HEV, which is devoid of EVs component. Gd-HEV showed enhanced cellular internalization compared to Gd-liposome and naïve EVs in K7M2 cells (**Figure 5.8A and B**). This enhancement in cellular internalization can be attributed to the combination of the liposomal component and EVs component in Gd-HEV, which can be only possible if the EVs functionality is retained. In the case of NIH/3T3, naïve EVs show minimal internalization and as a result, Gd-HEV internalization is similar compared to Gd-liposome. Here, EVs component in Gd-HEV does not contribute to the enhancement in internalization. The higher internalization behavior observed in Gd-HEV signifies the retention of EVs functionality.

To further confirm the functionality of EVs in Gd-HEV, we carried out the molecular analysis in terms of immunogenicity of EVs using ELISA.[75,76] EVs can communicate with the immune system and elicit an immune response, which can be used to track the functionality of EVs.[295] Here, we used cross-species analysis to analyze the immune response of EVs. Because our

EVs are derived from mouse immune cells (macrophages), we expect a pro-inflammatory immune response when exposed to human immune cells (monocytes). ELISA analysis showed the

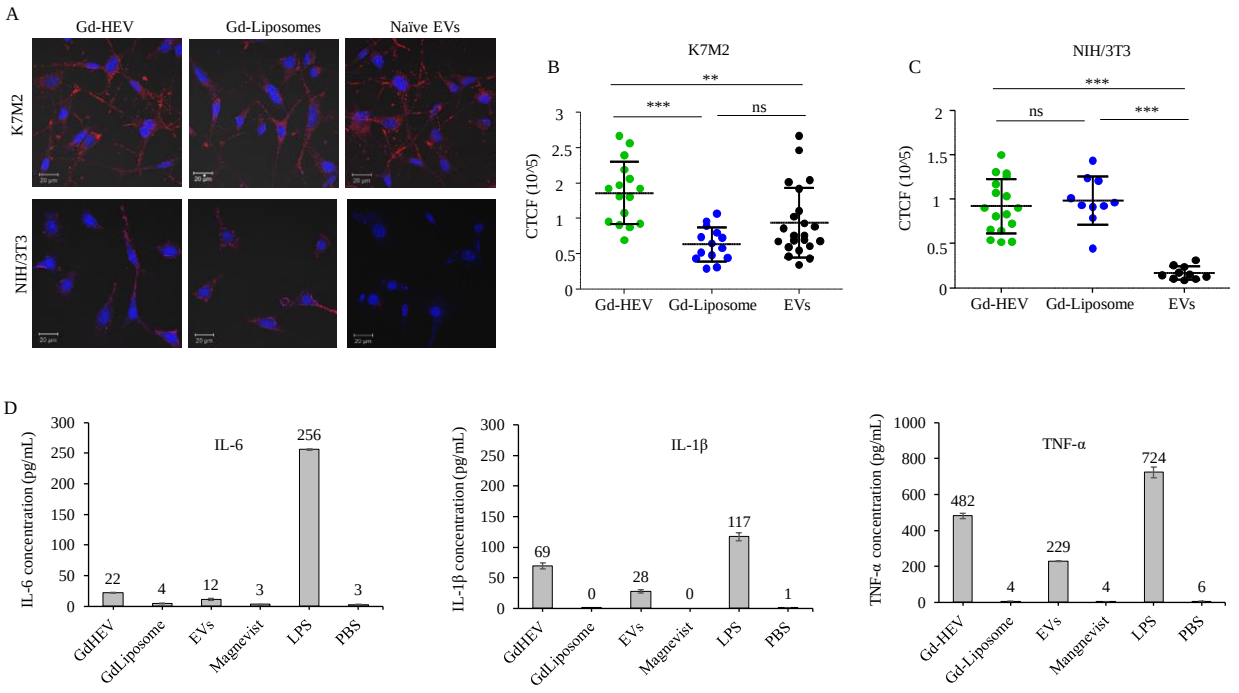

Figure 5.8 Assessment of EVs functionality after reconstruction in terms of cellular internalization and immunogenic response. (A) Confocal microscopic image of mouse osteosarcoma K7M2 and mouse fibroblast NIH/3T3 showing internalization behavior of Gd-HEV, Gd-Liposome, and naïve EVs. Particles were labeled with Rhodamine B and treated for 3h. Nuclei were stained with DAPI, (B and C) quantification of cellular internalization of Gd-HEV, Gd-Liposome, and naïve EVs in terms of corrected total cell fluorescence (CTCF) via ImageJ in K7M2 and NIH/3T3 respectively, and (D) in vitro immunogenicity assay of various nanoparticles in human peripheral blood monocyte THP-1 assessed by evaluating the release of proinflammatory cytokines (Interleukins IL-6, IL-1β, and tumor necrosis factor TNF-α) after 24 h incubation. Lipopolysaccharide (LPS, 6 µg/mL) was used as a positive control.

production of pro-inflammatory cytokines specifically in EVs and Gd-HEV treatment (**Figure 5.8D**). Gd-Liposome and Magnevist® did not induce significant cytokine production. Cytokine stimulation in THP-1 cells by EVs can be related to its immunogenic functionality. Interestingly, cytokine stimulation functionality was not only conserved in reconstructed Gd-HEV, but it was enhanced by almost double. Since Gd-liposome did not show cytokine stimulation, cytokine

stimulation in Gd-HEV is likely due to its EVs component. From this experiment, we are unable to explain the enhanced cytokine stimulation by Gd-HEV, but future work should be undertaken to further understand this phenomenon. Nonetheless, the immunogenic analysis confirms that the functionality of EVs has been retained through the reconstruction process in Gd-HEV.

5.3.5 *In vivo* biodistribution and magnetic property analysis

In vitro cellular interaction assay contributed strong evidence of the upregulated cellular interaction of Gd-HEV towards cancer cells. With this exciting finding, we went on to analyze the consequences of Gd-HEV within an *in vivo* environment. For this, NU/NU immunodeficient mouse was used as an animal model and *in vivo* biodistribution was studied using two different methods- fluorescent bioimaging and magnetic resonance imaging. For fluorescent bioimaging, Gd-HEV were labeled with near-infrared DiR dye by hydrophobic insertion strategy and injected in a mouse via tail vein injection. Gd-Liposome was used as particle control. Gd-HEV showed time-dependent localization in the tumor area when monitored up to 24 h post-injection, whereas in the case of Gd-liposome, no accumulation was seen in the tumor region (**Figure 5.9A**). Furthermore, organs were harvested after 24 h post-injection and imaged for fluorescence to assess the bioaccumulation of Gd-HEV and Gd-Liposome in different organs (**Figure 5.9B**). The fluorescence was quantified using ImageJ and a normalized fluorescence data was obtained by subtracting fluorescence of least fluorescent organ (brain) to picture relative differences of fluorescence in different organs with respect to different particles. Gd-HEV showed higher accumulation in the lungs, kidney, and tumor compared to its control particle Gd-Liposome. Overall, Gd-HEV showed enhanced bioaccumulation compared to Gd-Liposome, at equivalent liposome concentration. Since, Gd-HEV differs from Gd-liposome by EVs content, observed enhanced bioaccumulation in the case of Gd-HEV can be attributed to the EVs functionality. This

observation further supports the enhanced retention of Gd-HEV in the vasculature, thereby giving more time for enhanced bioaccumulation. Enhanced bioaccumulation observed in this study could potentially be exploited to target tumor microenvironment responsive drug/imaging agents to the tumor.

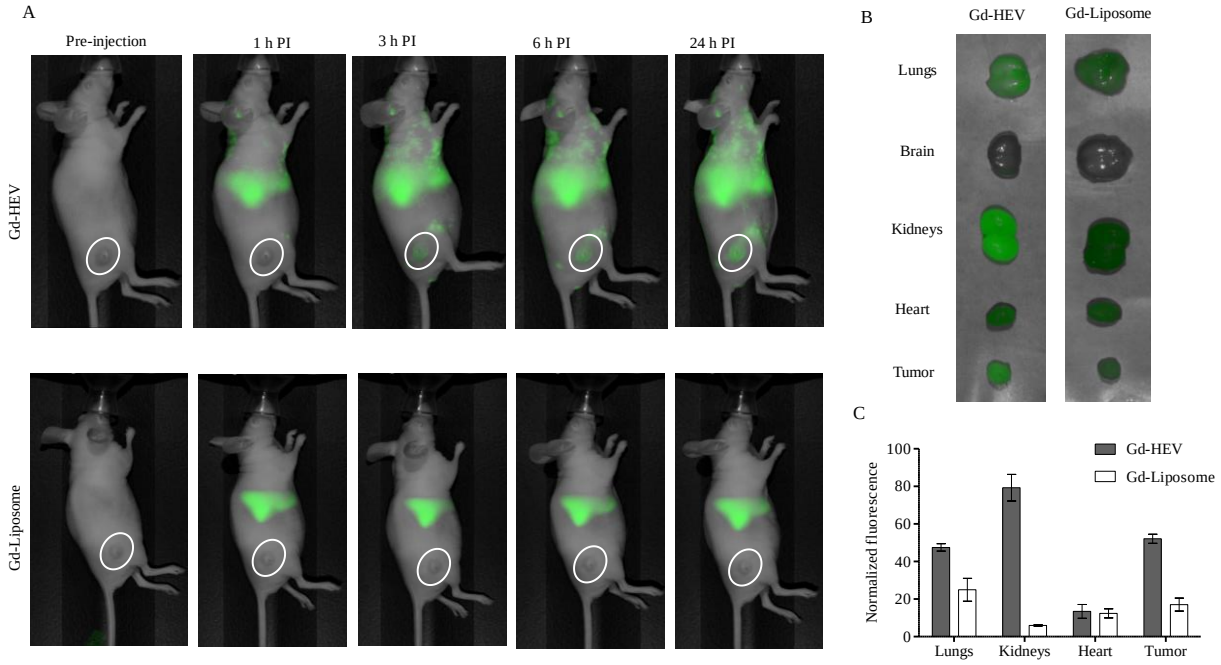

Figure 5.9 In vivo study by fluorescence bioimaging. (A) Time-dependent fluorescent image of mice injected with near-infrared DiR dye-labeled Gd-HEV and Gd-Liposome, (B) bioaccumulation of Gd-HEV and Gd-liposome in organs of mice after 24 h post-injection, and (C) quantification of fluorescence in organs harvested from Gd-HEV and Gd-Liposome treated mice. Fluorescence data were normalized by subtracting fluorescence of the least fluorescent organ (brain) to picture relative differences of fluorescence in different organs with respect to different particles.

Gd-HEV was further analyzed for biodistribution and magnetic property using magnetic resonance imaging (**Figure 5.10**). T_1 weighted MR image of mice injected with Gd-HEV was taken following tail vein injection at a specific time point. Magnevist® was used as a control contrast agent. MR image was taken at real-time during injection to map the immediate route of contrast agent during the injection. To represent this real-time route of contrast agent in a single image, Z-stack images were merged into a single image using maximum intensity projection with

background subtraction (MIPAV® software). It is important to process the images accordingly as the vasculature system in mice can be at different Z-axis and a single image cannot adequately focus the whole vasculature system of mice. The maximum intensity MR image with background subtraction showed excellent contrast enhancement illuminating the blood vasculature in the case of Gd-HEV during dynamic imaging. The image shows the clear retention of Gd-HEV in blood vasculature with no detected extravasation to interstitial spaces and tissues. In the case of Magnevist®, however, contrast can be observed in the vasculature as well as in the surrounding tissue during dynamic imaging, suggesting immediate extravasation into tissue. Also, the intensity of contrast was high in Gd-HEV compared to Magnevist® with equivalent Gd concentration, which is in accordance with the magnetic characterization data that showed higher longitudinal relaxivity r_1 of 9.87 $mM^{-1}s^{-1}$ for Gd-HEV. Most importantly, MR image taken after 15 min post-injection of Gd-HEV still showed excellent contrast in the blood vasculature with minimal extravasation in nearby tissues. Contrary to that in Magnevist® treatment, after 15 min post-injection, maximum contrast was observed accumulated in the urinary bladder, as depicted by the white arrow in **Figure 5.10A**, which is due to rapid clearance by the renal system. This kind of rapid clearance of exogenous material by the renal system is one of the major challenges in small molecular extracellular fluid agents, which can be overcome by engineering with nanoparticulate delivery system.[296–298] Moreover, the accumulation of Magnevist® in the urinary bladder following rapid renal excretion can be linked to the cause of reported nephrogenic systemic fibrosis (NSF) with severe renal impairment in patients exposed with GBCAs during MRI.[278,299] Here, Gd-HEV was successfully able to evade this rapid clearance thereby maintaining contrast in the blood vasculature. This immune evasion might be attributed to the biomimicry of Gd-HEV provided by the engineered EVs construct and the nanoparticulate size (~130 nm) that restricts Gd-HEV to

undergo glomerular filtration and escape from the renal system (particles> 8 nm do not undergo glomerular filtration).[300] After 60 min post-injection, it appears as Gd-HEV still shows contrast in blood vasculature with no evidence for accumulation in the urinary bladder, which is presumably due to the dilution of Gd-HEV over the period in the body.

Gd-HEV was analyzed for its contrast enhancement ability in the tumor area (**Figure 5.10B**). T_1 weighted image of Gd-HEV and Magnevist® at 15 min and 60 min post-injection was taken after tail vein injection in osteosarcoma tumor-bearing mice. Here, a sagittal view and a single slide of the image were chosen to focus the tumor area. The white arrow in **Figure 5.10B** represents the tumor area. Here also, Gd-HEV showed contrast enhancement compared to Magnevist which was more prominent at 60 min post-injection. Although compared to the surrounding tissue, Gd-HEV did not show much contrast enhancement in the tumor area, it was significantly high compared to control Magnevist®, at equivalent Gd concentration. This can be clinically advantageous as we can reduce the clinical dose of Gd based contrast agents like Gd-HEV to get clinically relevant contrast in the diseased site.

Organ-specific biodistribution of contrast agent was analyzed by quantitative determination of Gd present in each organ after 24 h post-injection by ICP-MS. **Figure 5.10C** shows the deposition of Gd-HEV and Magnevist® in seven different organs and blood in terms of percentage injected dose (ID) per weight of tissue (g). Magnevist® showed no significant retention in any organ except for kidney with 2.3 %ID per g tissue retention. This shows the elimination of Magnevist® from mice body within 24 h post-injection with some remaining in the kidney. Gd-HEV, on the other hand, showed retention in heart (0.30%), lungs (1.1%), tumor (0.63%), kidney (0.94%), and blood (10%). We observed that blood showed significant high retention of 10% even

after 24 h post-injection suggesting the excellent biocompatibility and blood retention characteristic of Gd-HEV.

Gd-HEV in vivo tumor specificity

In vitro cellular interaction data confirmed Gd-HEV preferentially traffics to cancer cells. These data were further supported by *in vivo* fluorescence imaging which showed time-dependent accumulation of Gd-HEV in the tumor. These observations led to the expectation that Gd-HEV

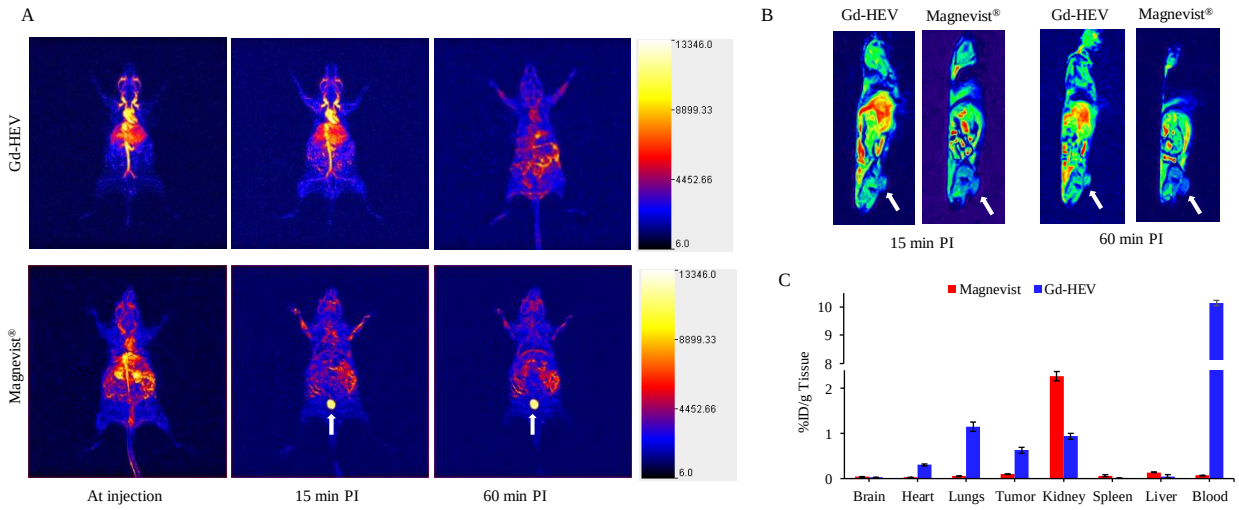

Figure 5.10 In vivo study by magnetic resonance imaging. (A) T_1 weighted MRI of a mouse injected with Gd-HEV and Magnevist® showing T_1 contrast enhancement. The image was taken at injection, 15 min, and 60 min post-injection using clinical 3T MRI. Images shown here are maximum intensity projection with background subtraction using MIPAV software, (B) T_1 weighted image of mice with sagittal view focusing tumor area as depicted by the white arrow, and (C) biodistribution of Gd-HEV and Magnevist in mice. Mice were euthanized and organs were collected after 24 h post-injection. Localization of Gd-HEV and Magnevist was quantified by tracking the amount of deposited Gd using ICP-MS.

can be used as a tumor-targeting contrast agent for MRI. However, MR image of Gd-HEV injected mice did not show significant contrast enhancement in the tumor area compared to the surrounding region. The plausible explanation for this result can be due to the low accumulation of contrast agent in the tumor. Although *in vivo* fluorescence image showed the accumulation of Gd-HEV in the tumor, when quantitative analysis was performed by tracking the amount of Gd deposited in

tumors using ICP-MS, we observed that only 0.63% of the injected dose/g tissue was localized in the tumor, after 24 h post-injection. Such low localization may not be enough to provide significant contrast enhancement.

In case of Magnevist®, the particle localization was negligible with only 0.1% localization. Though Gd-HEV showed about 6 times more localization in tumors compared to Magnevist®, the overall localization is still low to provide significant efficacy in contrast. Literature analysis suggests that this kind of low accumulation of nanoparticulate systems in the tumor is not unusual and is a major challenge in the drug delivery field.[301,302] The increasingly complex tumor microenvironment makes it extremely difficult for the nanoparticulate system to reach the actual tumor site.[303] The route for the particle to reach the tumor site is complex with lots of cellular traffic. Gd-HEV may have been hindered by this complex traffic and EVs construct did not significantly help to overcome this limitation. A possible explanation may include prolonged retention in the blood that hinders homing to tumor, therefore, reconstruction of Gd-HEV with the addition of tumor homing peptides could enhance tumor-specific delivery.

Both *in vivo* fluorescence imaging and MRI showed higher accumulation of Gd-HEV in different organs compared to control particles. While we may be able to exploit this enhanced bio-accumulation for diagnostic and therapeutic applications, it also requires the safety assurance of Gd-HEV retention in various organs. To address this concern, histologic analysis was performed by a board certified anatomic pathologist (BLP) to investigate the potential toxicity of Gd-HEV retention in various organs by hematoxylin and eosin (H&E) stained tissue sections. Untreated mice organs were used as controls. No significant lesions were observed in any organ sections, and no significant differences were observed between the tissue sections of organs treated with Gd-HEV and untreated organs (**Figure 5.11**). Treated and untreated mice showed mild incidental

changes in the lungs including alveolar collapse and hemorrhage, which is likely secondary to sampling. A section of the tumor (neoplasm) was also analyzed histologically; these were consistent with a dermal and subcutaneous anaplastic sarcoma with areas of necrosis and hemorrhage (**Figure 5.S3**). All sections examined (except the tumor) were within normal histologic limits, confirming that Gd-HEV accumulation in the heart and lungs does not induce any histological tissue damages. Because our hybrid platform is a cell-derived biomimetic platform, this result is expected.

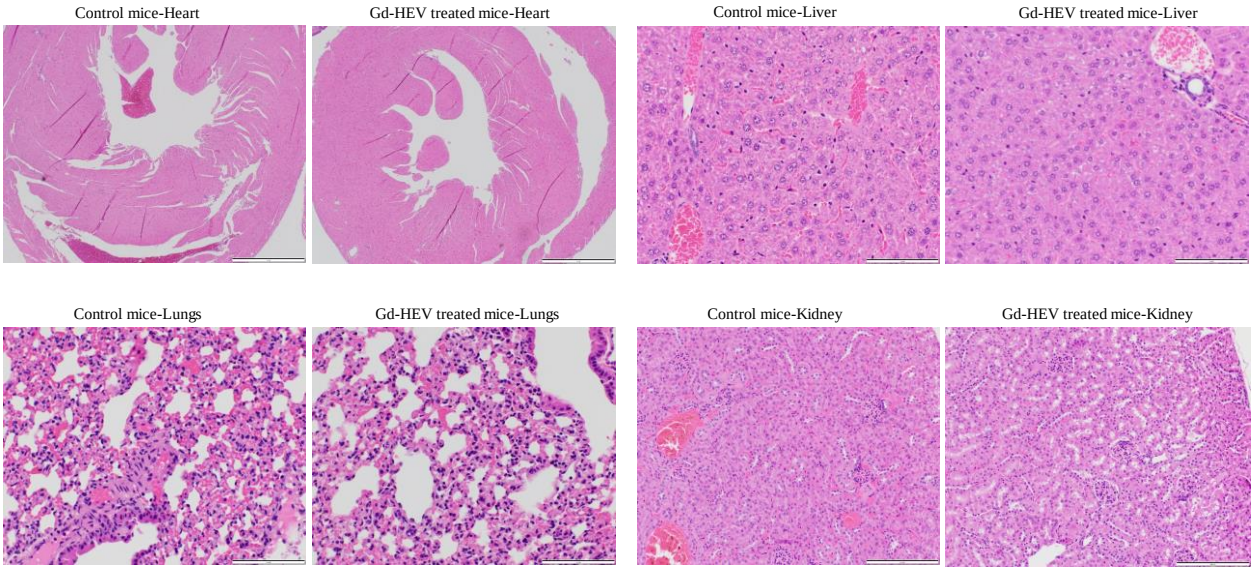

Figure 5.11 Histologic analysis of tissue sections of various organs of mice treated with Gd-HEV and untreated control mice. (Scale bar: Heart-1000µm, Lungs-100µm, Liver-100µm, Kidney-200µm).

5.4 Conclusion

This study has explored the reconstruction of EVs with gadolinium to develop a biomimetic contrast agent for contrast-enhanced MRI. The reconstruction process successfully incorporated EVs construct in Gd-HEV, with a high degree of colloidal stability and retention of protein characteristic and molecular functionality. Further, the incorporation of the lipid component in EVs along with the optimized EVs isolation method proposed in this study has increased the

overall yield and availability of EVs to reconstruct Gd-HEV. Gd-HEV showed specificity to cancer cells both *in vitro* and *in vivo*, thereby exploring its application in cancer diagnosis and treatment monitoring. Moreover, Gd-HEV showed excellent contrast enhancement and enhanced retention ability in blood vasculature allowing for proficient diagnosis with minimal dose. Further incorporation of fluorescent tags in Gd-HEV allowed for fluorescent bioimaging applications. These findings innovated a proof-of-concept towards the reconstruction of EVs based nanoparticulate modalities for the development of biomimetic multimodal imaging agents.

Chapter 6 - Rigor and reproducibility of extracellular vesicles production and functionality

Abstract

Extracellular vesicles (EVs) research has exploded with breakthrough promises in drug delivery, disease diagnosis, and therapy due to its unique functional properties acquired from the origin. However, the translational scope of EVs in these areas is challenged by the innate heterogeneity in EVs secretions which depends upon the physiological condition of the parent cell. As such, the EV's proteomic profile, cargo content, and functionality largely rely on the state of the parent cell and the isolation protocol followed. Therefore, it is important to understand the factors influencing EV production heterogeneity and functionality to ensure functional reproducibility. Toward this direction, this study aims to explore the variation of EV production and functionality with varying cellular environmental factors, particularly focusing on the impact of varying nutrient stress in EV production and functionality. In this study, we explored four types of EVs isolated by varying incubation time (12, 24, 48, and 72 h) to represent varying nutrient stress, and two cell sources- mouse osteosarcoma K7M2 and mouse fibroblast NIH/3T3 to represent cancer and non-cancer cell. An optimized ultrafiltration-size exclusion chromatography (SEC) based technique was developed for simple, efficient, and reproducible EV isolation. Each EVs isolation and subsequent characterization were carried with 3-5 independent replicates to map the reproducibility. Size analysis from nanoparticle tracking analysis showed a reproducible average size distribution ranging from 130 to 220 nm, among various incubation time and cell line. SEC characterization showed EV enrichment in fractions six to nine, with a similar trend in five independent replicates among eight different EV samples with varied incubation time and cell

source. K7M2 cells produced more EVs, both in terms of number and protein content, compared to NIH/3T3 cells, which increased with incubation time, suggesting aggressive communication in cancer cells. The optimum incubation time with the best protein recovery was identified as 48 h. Importantly, we observed changes in EV functionality in terms of cell proliferation with 72 h EVs, suggesting differential functionality of stressed EVs. This rigorous study revealed the influence of experimental conditions adapted in EV production and functionality among cancer and non-cancer cells and add crucial information in the fundamental research of EVs.

6.1 Introduction

Extracellular vesicles (EVs) are proteolipid vesicles secreted by cells into extracellular space which acts as a natural messenger in the cellular environment.[35,36,53] Owing to their innate ability to transfer cellular cargo, EVs has been widely studied as drug delivery and diagnostic agent. Research has shown promising applications of EVs in targeted delivery, biomarkers, and imaging/diagnostic agents for early disease diagnosis and therapy.[174,304–306] In our previous work, we showed preferential internalization of immune cells- derived EVs in cancer cells both in-vitro and in-vivo.[65] Further, by engineering magnetic resonance imaging (MRI) contrast agent-Gadolinium (Gd) in EVs, we demonstrated the potential of EVs as a contrast-enhanced cancer diagnostic agent.[74] Several other groups have explored the drug delivery and diagnostic potential of EVs in different disease models. Qiao et al. and Ingato et al. demonstrated that cancer/tumor cell-derived exosomes (EVs) home to their cells of origin and can be used for tumor-targeted drug delivery.[307,308] Izco et al. demonstrated systemic exosomal delivery of shRNA minicircles prevents parkinsonian pathology.[309] Alvarez-Erviti showed delivery of siRNA to the mouse brain by systemic injection of targeted exosomes.[92] Vandergriff et al. engineered cardiac homing exosomes for targeting exosomes to infarcted hearts for the treatment of myocardial infarction.[310] All these

studies report exciting avenues of EVs in the field of drug delivery and disease diagnosis. However, the translational potential of EVs can be challenged by their innate heterogeneity, in part, EVs are secreted in different sizes and different origins which can directly depend upon the state of the parent cell. Therefore, it is important to understand the factors influencing EV production heterogeneity and functionality to make sure the functionality reported can be reproduced. Toward this direction, this study aims to explore EVs production and functionality with respect to different cellular environmental factors particularly focusing on the impact of varying nutrient stress.

EVs biogenesis is directly influenced by the type and state of cells, as such the production amount, proteomic profile, and cargo content can vary depending upon cell type and its state-normal *Vs* stressed physiological conditions.[311,312] EVs are routinely isolated from cell culture using serum-free/deprived media as one of the widely used options as EV extraction media. The use of serum-free media has two specific advantages: 1) being serum-free, it avoids the inevitable contamination of endogenous EVs present in serum, and 2) the serum nutrient deprivation leads to stress-induced production of EVs resulting in higher yield and activity.[313,314] Haraszti et al. reported that the serum-deprived mesenchymal stem cells produce EVs (exosomes) up to 22-fold more effective at delivering small interfering RNA (siRNAs) to neurons compared to EVs derived from control cells.[313] Likewise, Li sun et al. reported serum deprivation elevates levels of EVs (microvesicles) with different size distributions and selectively enriched proteins in human myeloma cells.[314] These reports suggest the variations in EVs production and functionality with different cellular conditions and isolation parameters. With multiple isolation protocols, cell-type, and stress conditions, EVs production, and functionality can be varied widely, and therefore it is important to understand the effect of these variations in the functional outcome. Such

understanding can help to pinpoint key factors responsible for the variation and therefore can be crucial in maintaining the functional reproducibility in EV research and large scale production. Toward this direction, this study focuses on how different incubation time with serum deprived EV media affects the production and functionality of EVs derived from cancer cells (mouse osteosarcoma K7M2) and non-cancer cells (mouse fibroblast NIH/3T3).

Studies using serum-deprived media for the extraction of EVs have reported varied incubation times ranging from 24 h to 72 h and there has not been a detailed study about how these incubation times impact the production and functionality of the EVs. With a longer stress environment, the biogenesis of EVs can be influenced including the number, proteomic profile, and the activity of EVs, and therefore it is important to analyze such variation which can be used to develop an optimum incubation time and isolation parameters. Higher incubation time may lead to better yield, however, can be limited by the lower cell viability with a longer period of stress environment. Also, variation may come with the same batch maintained at the same condition as well. To study these variations among cell cultures maintained at identical conditions, EVs were isolated and characterized from 3-5 independent experiments following an optimized isolation protocol.

A centrifugation-ultrafiltration protocol optimized in our lab was further optimized with size exclusion chromatography (SEC) to maximize EV purity. We found a narrow variation in size, number, and protein content of EVs isolated from independent experiments maintained at the same condition, while there was significant variation in number and protein content with EVs isolated from varied incubation time. A positive correlation of EVs number and protein content with increasing incubation time was observed. Further, osteosarcoma (K7M2) cells-derived EVs showed a higher number and protein content compared to non-cancerous cell NIH/3T3. This study

successfully optimized an easy, cheap, ultracentrifugation-free, ultrafiltration-SEC-based EVs isolation method and characterized the variation of EVs production and functionality at the same and different physiological state of parent cells. The study reveals how the serum-deprived incubation time can affect the EV production and functionality among cancer and non-cancer cells and add a crucial fundamental foundation in the EVs research.

6.2 Materials and methods

6.2.1 Chemicals, reagents, and cell lines

Mouse monoclonal antibody CD63 (MX-49.129.5), HSP70, Histone H3 (FL-136), and β-Actin were purchased from Santa Cruz Biotechnology. Sepharose® CL-2B and (3-(4,5-dimethylthiazol-2-yl)-2,5-diphenyl tetrazolium bromide) (MTT) reagent were purchased from Sigma Aldrich. Mouse osteosarcoma (K7M2), and mouse normal fibroblast (NIH/3T3) were purchased from ATCC, Manassas, USA. Cell lines were maintained in Dulbecco's Modified Eagle's Medium (DMEM) supplemented with 10% (v/v) Fetal Bovine Serum (FBS) and 1% streptomycin at 37 °C in 5% CO_2 environment.

6.2.2 Isolation of EVs from the cell culture supernatant

Serum-free and phenol red-free Dulbecco's Modified Eagle's Medium (DMEM) (Thermo Fisher Scientific) was used as EV extraction media. Cells were grown in a T75 flask using complete DMEM. When the cells were around 80% confluent, complete media was removed, washed with PBS, and 10 ml of EV extraction media was added. Cells were incubated for 12, 24, 48, and 72 h to extract EVs at varying incubation times. After the respective incubation time, EV extraction media was collected and processed to isolate EVs. Cells in the cell culture flask were detached by trypsin treatment and stained by trypan blue for cell counting using an automatic cell counter. EV extraction/conditioned media was centrifuged at 300g and 4500g for 15 min each to

remove cell debris and heavier particles. Then, EV media was filtered with a 200 nm membrane filter to remove large vesicles and apoptotic bodies. The resultant filtrate was concentrated using a 10000 Dalton molecular weight amicon filter and centrifuged at 4000g for 15 min. Volume was concentrated from 10 mL to 1 mL. The one mL concentrated EV solution is subjected to Sepharose CL-2B size exclusion chromatography (SEC) to remove impurities and soluble proteins. EVs being relatively big should be able to escape the bead pore and elute while impurities and soluble proteins should be trapped in the pores of the bead. Therefore, vesicles should elute at an earlier time point thereby separating themselves from impurities.

Small-scale SEC was prepared in the lab using a small chromatography column and Sepharose CL-2B. 5 ml Sepharose CL-2B was added in the column and washed with 2 ml PBS. The column was left for 5 min to settle down. The column was 7 cm long and 1 cm wide (inner diameter). 15 fractions with 500 µL elute was collected in about 20 minutes. The fractions were characterized with UV absorbance at 280 nm, sodium dodecyl sulfate polyacrylamide gel electrophoresis (SDS-PAGE), and dot blot to analyze fraction enriched with EVs. 4 fractions (F6-F9/ F7-F10) enriched with EVs/proteins (based upon UV absorbance at 280 nm) was mixed and stored at -80 °C for further analysis.

6.2.3 Characterization of EVs

EVs were characterized for size and concentration using nanoparticle tracking analysis (NTA, Malvern NanoSight LM10). Before NTA analysis, EVs were filtered using a 220 nm syringe filter. The NTA capture and analysis settings include blue405 laser, camera level 12, slide shutter 1200, slider gain 146, frame per second 25, detect threshold 2, and temperature maintained at 25 °C. For each measurement, 5 different captures were taken and analyzed. Protein characterization of EVs was done via Bradford assay, SDS-PAGE, and dot blot. For Bradford

Assay, 100 µL of EVs sample was mixed with 500 µL of Bradford reagent and incubated for 10 min to read the absorbance at 595 nm. A standard absorbance graph was prepared using bovine serum albumin (BSA) as a standard protein. For SDS-PAGE, EVs fractions isolated from SEC were dried using lyophilizer and dissolved with 20 µL PBS. EVs sample was mixed with sample loading buffer with a 1:1 volume ratio. The mixture was incubated at 90 °C for 7 min, and 25 µL of each sample was loaded in the wells of 4–20% Mini-PROTEAN® TGX Protein Gels. The gel was stained by Coomassie Brilliant Blue and imaged by Bio-Rad imager. For Dot blot, 3 µL of each sample was added to Polyvinylidene Fluoride (PVDF) membrane. The membrane was left to absorb the drop and blocked by blocking buffer for 30 min at room temperature. The primary antibody of interest (CD63, CD81, HSP70) was added and incubated overnight. Then, the membrane was washed with wash buffer and incubated with HRP conjugated anti-mouse IgG secondary antibody (Cell signaling). The membrane was further developed using Signal Fire ECL TM Reagent and immediately imaged by Bio-imager (Kodak).

6.2.4 Cell proliferation Assay

Cell proliferation analysis K7M2 cell-derived EVs (K7M2-EVs) with various incubation times was carried out on K7M2 and NIH/3T3 cell lines using MTT assay. Briefly, 10,000 cells were seeded in 96 well plates for 24 h at 37 °C in 5% CO_2 environment. After that, the media was changed with 100 µL fresh media. Then, 100 µL of 20 µg/mL K7M2-EVs isolated at four different incubation times (12, 24, 48, 72 h) were treated to each cell line for 48 h. In control cells, 100 µL of PBS was added. After 48 h incubation, media was removed and MTT solution (5 mg/10 mL serum-free media) was added and further incubated for 2.5 h. DMSO was added to dissolve the insoluble formazan crystal formed after MTT treatment, and absorbance was recorded at 550 nm using a microplate reader (BioTek, Synergy H1 Hybrid reader). Cell proliferation behavior after

the treatment of EVs compared to untreated control was analyzed by calculating cell viability percentage.

6.3 Result and Discussion

6.3.1 Reproducibility of EVs size among identical and varied incubation time and cell-lines

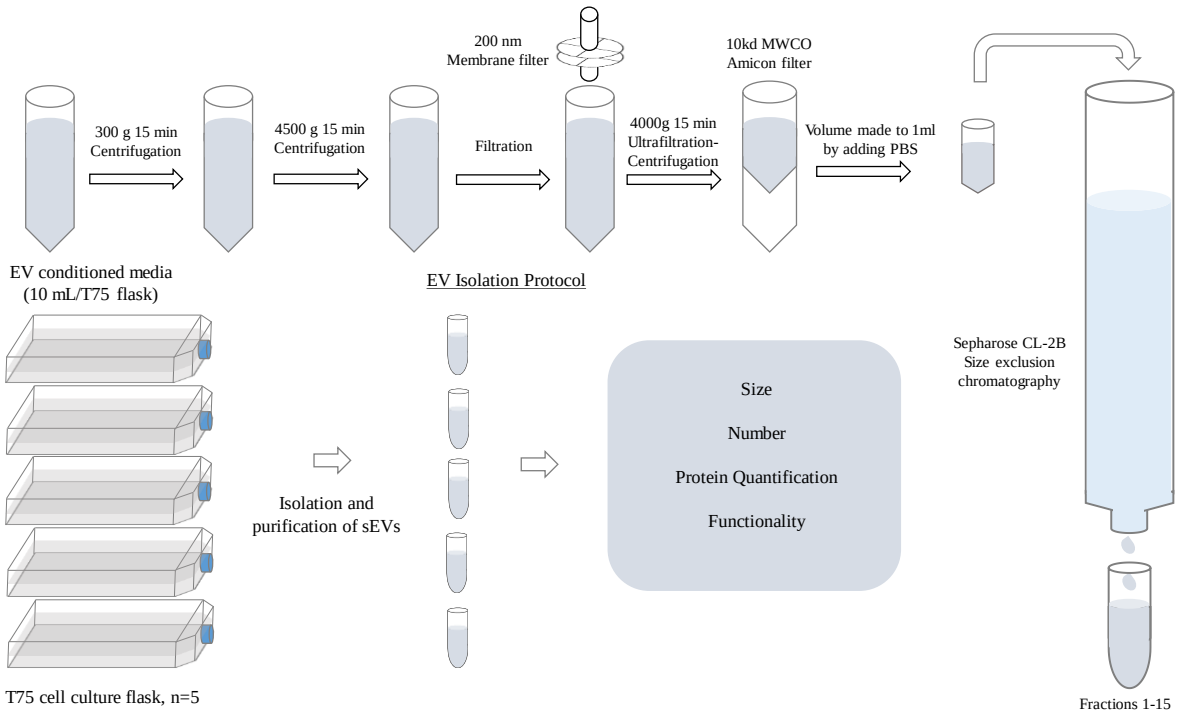

Figure 6.1 Optimization of ultrafiltration-size exclusion chromatography based EV isolation method for rigor and reproducibility analysis.

Variation in EVs size was evaluated at same and different incubation time with serum-deprived media, by carrying out 3-5 independent experiments for each time point (**Figure 6.1**). Size analysis from nanoparticle tracking analysis (NTA) showed average size distribution of K7M2 cell-derived EVs (K7M2-EVs) from 156 nm to 220 nm across various incubation times: 12, 24, 48, and 72 h. Likewise, NIH/3T3 cell-derived EVs (NIH/3T3-EVs) showed size distribution from 130 nm to 218 nm across various incubation times (**Figure 6.2**). The size of EVs

varied by as low as 20 nm to as high as 90 nm among three independent replicates at the same incubation and different incubation time, suggesting that the variation in EVs size distribution is independent of incubation time. The size analysis shows the reproducibility in EVs size at same and varied incubation time within an average size range of 130 to 220 nm, with around 20-90 nm of variation. The similarity of peak pattern of EVs size distribution among the same and different incubation time further support the reproducible size range of EVs among different incubation time and cell-lines while following experimental conditions adapter herein.

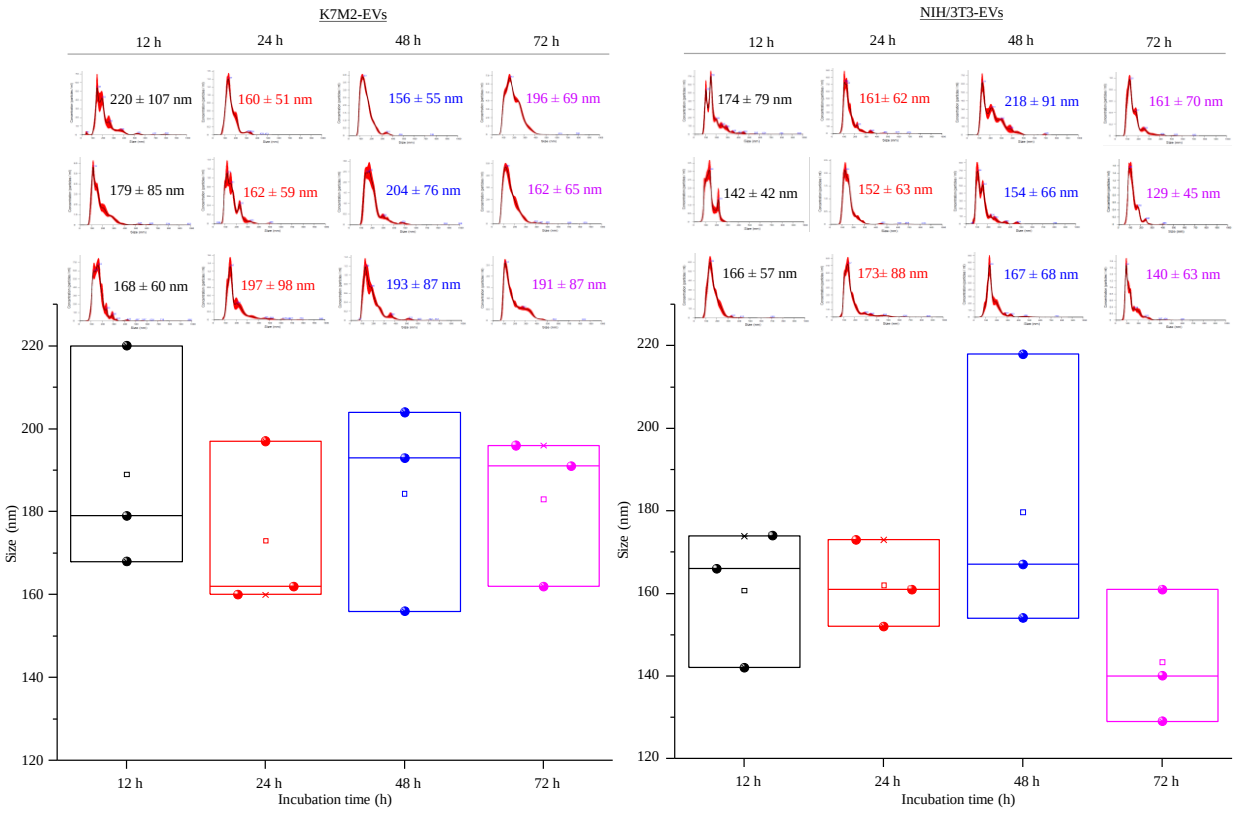

Figure 6.2 Reproducibility of EVs size among identical and varied incubation time and cell-lines. The size distribution of EVs at varied incubation times of 12, 24, 48, and 72 h, derived from K7M2 and NIH/3T3 cells. Each time point has three independent replicate analysis representing the average size, standard deviation, and overall distribution graph quantified by nanoparticle tracking analysis.

6.3.2 Size exclusion chromatography for EVs enrichment and purification

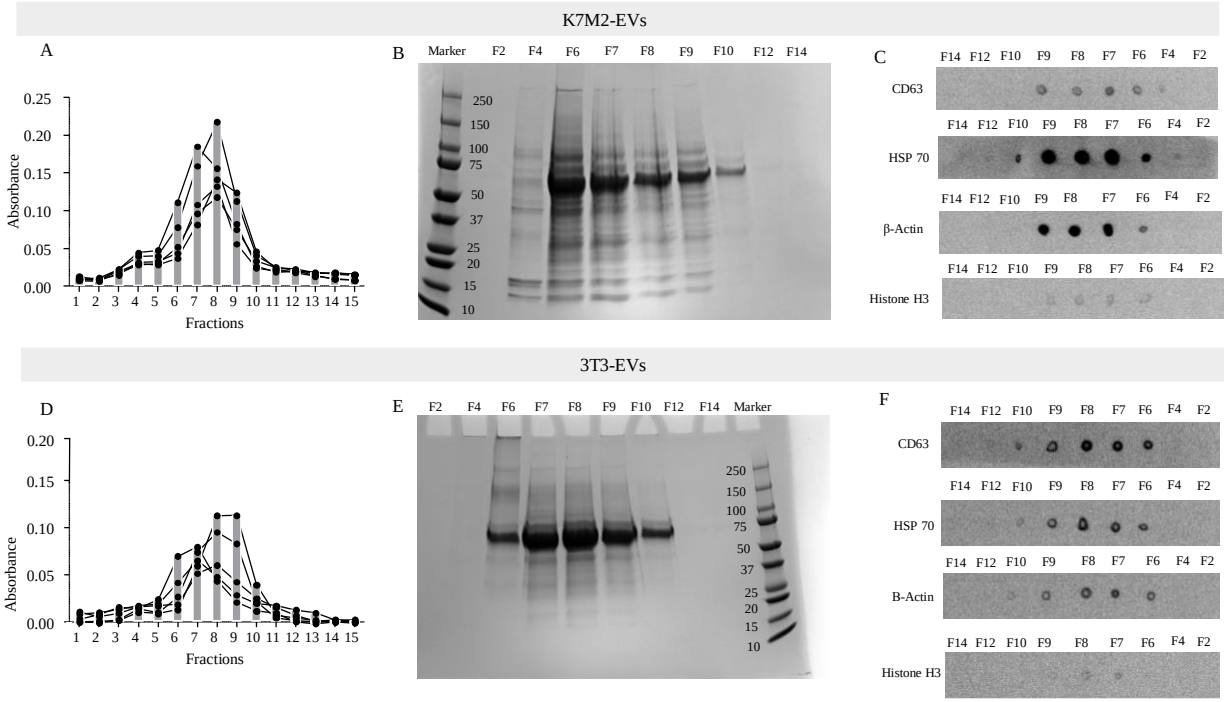

Figure 6.3 Characterization of size exclusion chromatography (SEC) based EVs enrichment and purification. (A) UV absorbance of 15 SEC fractions at 280 nm representing five different independent replicates of K7M2-EVs, (B and C) SDS-PAGE and dot blot analysis showing enrichment of EVs marker proteins CD63, HSP70 in fractions 6 to 9, in K7M2-EVs. β-Actin was used as housekeeping control and Histone H3 was used to analyze the extent of nuclear contamination in EVs. (D) UV absorbance of 15 SEC fractions at 280 nm representing five different independent replicates of NIH/3T3-EVs, and (E and F) SDS-PAGE, and dot blot analysis showing enrichment of EVs marker proteins CD63, HSP70 in fractions 6 to 9, in NIH/3T3. SEC showed a similar pattern of EV enrichment in fractions 6 to 9, in both K7M2-EVs and NIH/3T3 EVs.

EVs were isolated from the optimized ultrafiltration-size exclusion chromatography (SEC) based method as depicted in **Figure 6.1**. The ultrafiltration based method of EVs isolation has been demonstrated in our previous publications.[65,74] Here, we further characterized and optimized small-scale Sepharose® CL-2B based SEC. SEC was run to collect 15 fractions of 0.5 mL elute. **Figure 6.3** shows the characterization of SEC fractions by UV absorbance, SDS-PAGE, and dot blot. UV absorbance at 280 nm data shows peak absorbance from fractions 6 to 9, which showed a reproducible trend among five independent replicates (**Figure 6.3A**). Proteins in solution absorb

in ultraviolet range with absorbance maxima at 280 nm.[315,316] The UV absorbance data shows that proteins are enriched in certain fractions with higher absorbance. To further confirm, these proteins are indeed from EVs, SDS-PAGE and dot blot were carried out. SDS-PAGE also showed major protein bands in F6-F9 supporting the UV data. Importantly, dot blot showed the enrichment of EVs marker proteins CD63 and HSP 70 at fractions F6-F9 (**Figure 6.3C and F**). β-actin was used as housekeeping control while Histone H3, a nuclear protein was used to examine the extent of nuclear contamination in the EV sample. Negligible intensity observed in Histone H3 blot showed the isolation protocol followed lead to minimal nuclear contamination.

These characterization data confirmed that the SEC successfully enriched EVs sample in F6-F9. The working principle of SEC is based upon size-dependent differential elution time of particles and has been reported for EVs purification and enrichment.[317–320] EVs with the size range of 130-220 nm are expected to have similar elution time and elute within the range of a narrow fraction. At the same time, small soluble impurities should be trapped in the small pore of SEC beads and therefore offer separation of EVs from soluble impurities. Here, we observed maximum EVs elution within fractions 6 to 9. To further examine the efficiency and reproducibility of SEC-based EV enrichment in different cell lines, we followed the same procedure in EVs isolated from non-cancerous cell NIH/3T3 (**Figure 6.3D, E, and F**). UV absorbance data showed a peak from F6-F9, similar to that of K7M2-EVs. Further, SDS-PAGE and dot blot confirmed EVs enrichment in F6-F9, showing similar trends as that of K7M2-EVs. The observed similar trend of protein enrichment among independent replicates of EVs isolated from two different cell-lines suggests the adapted EVs isolation protocol herein is highly optimized for reproducibility and enrichment.

6.3.3 Variation of EVs protein content with varied incubation time and cell-line

EV protein content was quantified by Bradford assay and normalized with respect to the number of cells for comparative analysis. **Figure 6.4** depicts how EV protein content varies with different incubation times and the trend of variation in EVs derived from a cancer cell and normal cell. EV protein content was analyzed before and after SEC in K7M2-EVs and NIH/3T3 EVs to analyze the impact of SEC in EV protein content and yield (**Figure 6.4A and B**).

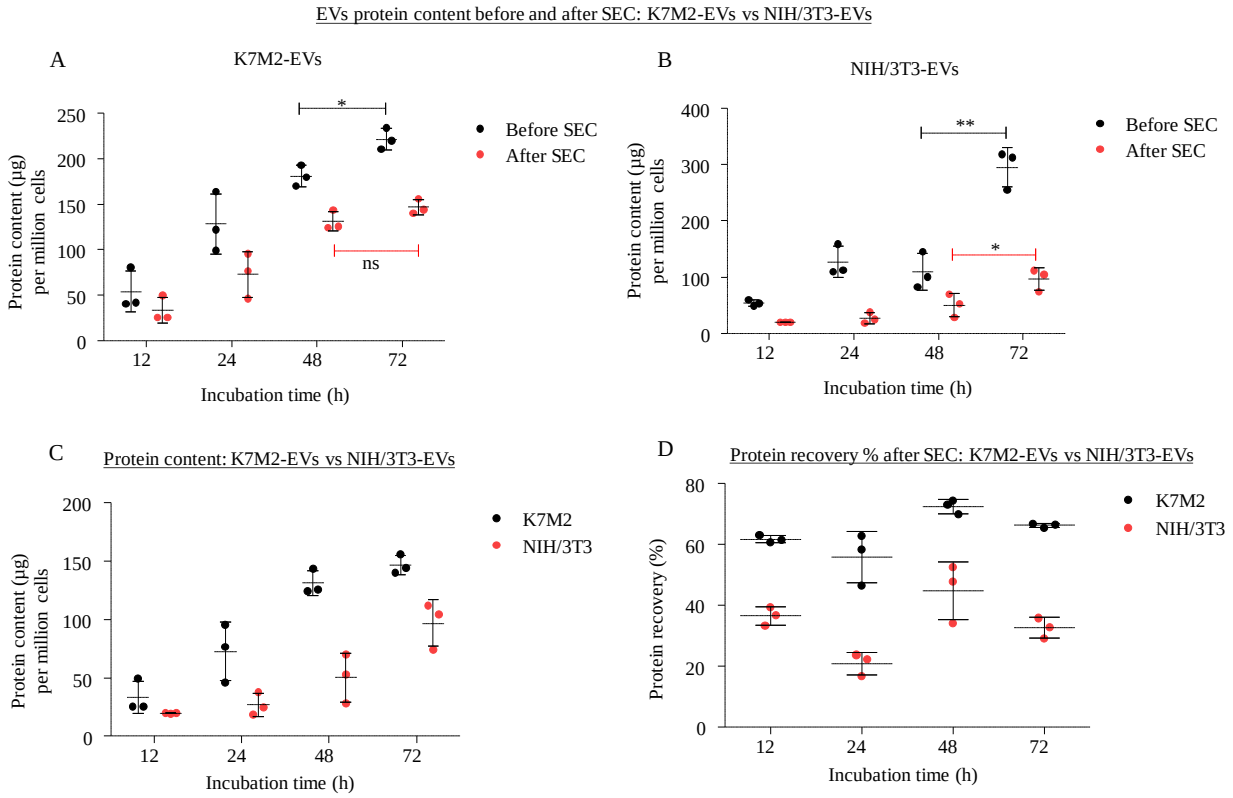

Figure 6.4 Variation of EVs protein content in K7M2-EVs vs NIH/3T3-EVs with varied incubation time. (A) K7M2- EVs protein content (µg) per million cells at varied incubation time (12, 24, 48, and 72 h), before and after SEC, (B) K7M2- EVs protein content (µg) per million cells at varied incubation time (12, 24, 48, and 72 h), before and after SEC, (C) variation of EVs protein content quantified after SEC among different incubation time in K7M2-EVs and NIH/3T3 EVs, and (D) protein recovery percentage after SEC in EVs incubated at the varied time and two different sources: K7M2-EVs and NIH/3T3 EVs (** = *P-value* < 0.005, * = *P-value* < 0.05, ns= non-significant, Unpaired t-test).

As expected, EV protein content (µg/million cells) decreased after SEC among all incubation time point samples (12, 24, 48, and 72 h) for both K7M2-EVs and NIH/3T3-EVs. This decrement can be attributed to the exclusion of soluble protein impurities after SEC, and, in part, to the procedural loss. K7M2-EVs showed an increment in protein content with incubation time, from 12h to 72 h, which showed a similar trend before and after SEC (**Figure 6.4A**). However, the increment in protein content from 48 h to 72 h after SEC was relatively low and statistically non-significant compared to the increment in protein content from 48 h to 72 h before SEC (* = P-value < 0.05, ns= non-significant, Unpaired t-test). This can be due to the increment in soluble impurities in EV-72h samples, possibly due to the reduced cell viability at higher incubation time leading to more floating dead cells. The reduction of protein recovery % after SEC at 72 h time point further supports this observation (**Figure 6.4D**). Interestingly, the EV protein content variation with varied incubation times follows a different trend in NIH/3T3-EVs, particularly before SEC (**Figure 6.4B**). Protein content before SEC shows increment from 12 h to 24 h, and a similar range in 24 h and 48 h, while increases sharply in 72 h. Here also, protein content after SEC do not increases in the same fold in 72 h sample, suggesting the sharp increase in protein content before SEC should be significantly contributed by soluble protein impurities rather than EVs. Again, lower cell viability at 72 h incubation time point leading to high floating dead cells may result in such observation. **Figure 6.4C** shows the comparison between EV protein content in K7M2-EVs and NIH/3T3-EVs at varied incubation time. In all incubation time points, from 12 h to 72 h, K7M2-EVs showed higher protein content compared to NIH/3T3-EVs. The average protein content (µg/million cells) after SEC were 33 *Vs* 19 in 12 h, 73 *Vs* 25 in 24 h, 131 *Vs* 50 in 48 h, and 140 *Vs* 97 in 72 h, in K7M2-EVs *Vs* NIH/3T3-EVs respectively. **Figure 6.4D** shows protein recovery % after the SEC in K7M2-EVs and NIH/3T3-EVs. K7M2-EVs showed higher

protein recovery % compared to NIH/3T3-EVs at all time points suggesting K7M2-EVs could have relatively fewer soluble impurities than NIH/3T3-EVs. Additionally, both EVs showed the highest recovery % in 48 h incubation time, an average of 72% for K7M2-EVs and 45% for NIH/3T3-EVs. These data conclude that EVs derived from cancer cell K7M2 show higher protein content compared to non-cancer NIH/3T3, and 48 h incubation time is optimum for best protein recovery while following the protocol discussed herein. One key difference between the K7M2-EVs and 3T3-EVs was the expression of markers proteins, strikingly HSP70 was highly expressed in K7M2-EVs compared to 3T3-EVs (**Figure 6.3C and F**). It has been reported that HSP70 is specifically overexpressed in cancer cells-derived EVs compared to non-cancer cells and our data further support this point.[321,322] This differential expression of HSP70 in cancer cell derived EVs can be exploited for the development of EV-based cancer biomarkers for early cancer diagnosis.

6.3.4 Variation of EVs concentration with varied incubation time and cell-line

EV concentration was quantified using NTA and normalized with cell number for comparative analysis. **Figure 6.5** shows the variation in EV concentration with varied incubation time in K7M2-EVs and NIH/3T3-EVs. Both EVs showed incubation time-dependent concentration (10^8/ml per million cells)- the higher the incubation time, the higher the concertation. However, the rate of increment of EVs concentration with incubation time was much higher in K7M2-EVs compared to NIH/3T3 (**Figure 6.5A and B**) suggesting aggressive cellular communication in cancer. K7M2-EVs average concentration (10^8/ml per million cells) ranges from 0.83 to 14.87 compared to 1.13 to 3.71 for NIH/3T3-EVs, from 12 h to 72 h time point. Except for the 12 h time point, the average EV concentration was higher in K7M2-EVs compared to NIH/3T3-EVs. The average EV concentration (10^8/ml per million cells) after SEC was 0.83 vs 1.13 in 12 h, 3.04 vs 2.05 in 24 h, 8.39 vs 2.44 in 48 h, and 14.87 vs 3.71 in 72 h, in K7M2-EVs

vs NIH/3T3-EVs respectively. This observation agrees with the trend of higher EV protein content in K7M2-EVs compared to NIH/3T3-EVs. As expected, with higher protein content, higher concentration was observed and vice-versa. To quantitatively analyze the relation between EVs protein content and concentration, we did correlation analysis, which showed a positive correlation of EVs protein content with the total number of EVs, as confirmed by high Pearson r and Spearman r coefficient in both K7M2-EVs (Pearson r=0.899, Spearman r=0.946) and NIH/3T3-EVs (Pearson r=0.899, Spearman r=0.879) (**Figure 6.5C and D**).

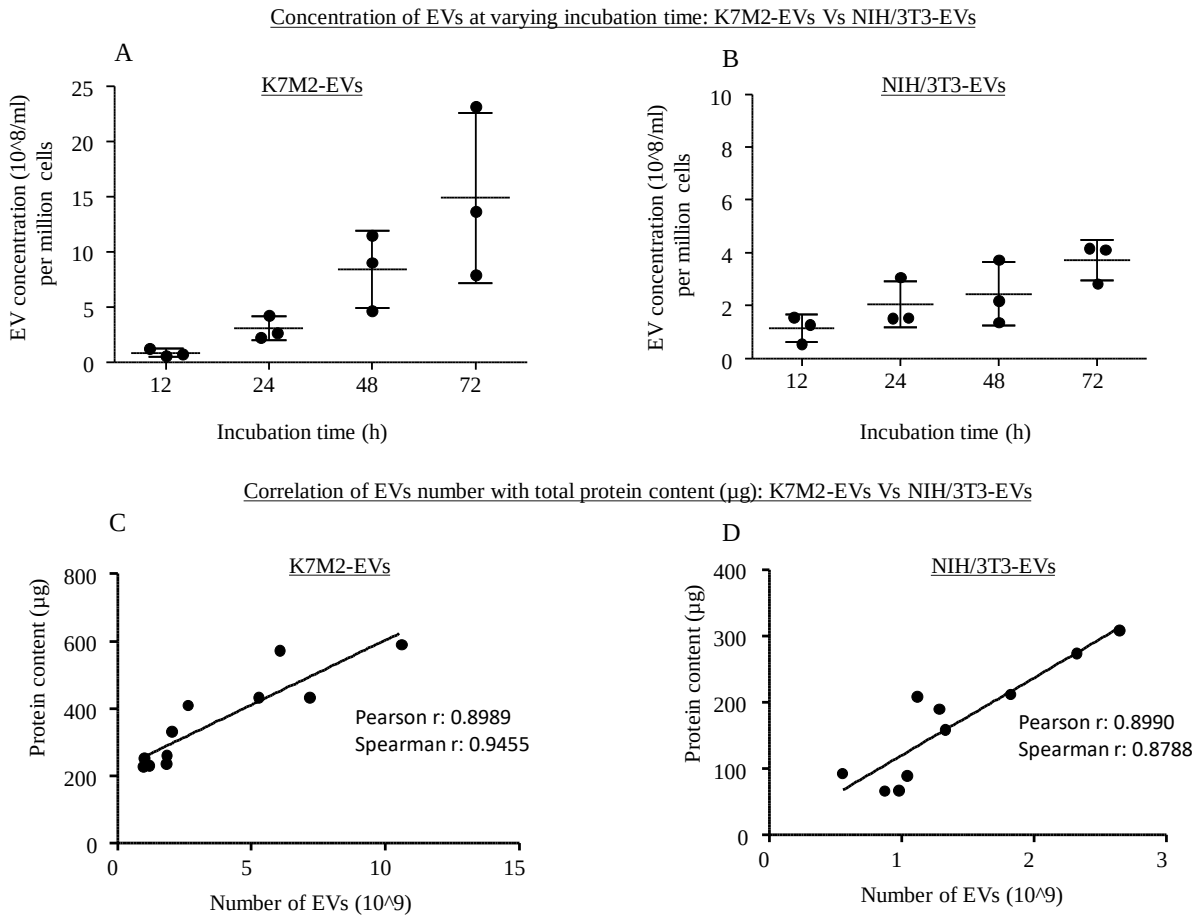

Figure 6.5 Variation of EVs concentration in K7M2-EVs vs NIH/3T3-EVs with varied incubation time. EV concentration ($1x10^8$ /million cells) at varied incubation time (12, 24, 48, 72 h) in (A) K7M2-EVs and (B) NIH/3T3 EVs. (C and D) Correlation of K7M2-EVs and NIH/3T3-EVs number with total protein content (µg). EVs number positively correlated with protein content, as represented by high Pearson r and Spearman r correlation coefficient.

6.3.5 Variation in EVs functionality with varied incubation time

We were able to characterize the variation in EVs size, protein content, and concentration with different incubation times and cell lines. To analyze whether these variations will have any functional impact, we decided to carry out a cell proliferation assay using MTT assay. EVs are reported to play role in cellular communication and may impact their proliferation rate. We treated the equivalent amount of K7M2-EVs with four different incubation times (12, 24, 48, and 72 h) to K7M2 and NIH/3T3 cells for 48 h to study the effect on cell proliferation. Cell viability data was used to analyze cell proliferation which showed an average of 100% or more cell viability compared to the untreated control, in both cell line (**Figure 6.6**) Importantly, 72 h-EVs showed significantly higher average cell viability compared to other time points, in both K7M2 cells (109%, P-value <0005) and NIH/3T3 cells (113%, P value<0.05), when compared to respective controls. This suggests that 72 h-EVs positively helped in cell proliferation in both K7M2 and NIH/3T3 cells resulting in a greater number of cells compared to the untreated control, while the rest of the EV samples have a neutral effect in cell proliferation and viability, similar to that of untreated controls. Here, all EVs samples, with an average of 100% or more cell viability shows good characteristic for a biocompatible and safe delivery agent.

One important observation here is the slightly increased proliferation characteristic with 72 h samples. This suggests that with the variation in incubation time, the functionality of EVs can be different. Although we used an equivalent amount of EV protein content (100 µl, 20 µg/mL), there were differences in functionality regarding cell proliferation. 72h-EVs are produced by most stressed cells in terms of nutrient deprivation among four different incubation time points analyzed in this study. In that regard, stressed EVs may better communicate with cells and influences cell proliferation here. A similar observation was described by Garcia et al. where the author reported

stronger pro-proliferative and pro-angiogenic effects of stressed EVs derived from nutrient-deprived cells compared to normal EVs from control conditions.[323,324] Further analysis on proteomics of EVs and cellular internalization study is required to confirm the mechanism behind the observed difference in functionality. Nevertheless, we found that the variation in incubation time may have a functional impact. Therefore, it is important to characterize probable variations in EVs isolation and processing to envision better reproducible and translational EVs research.

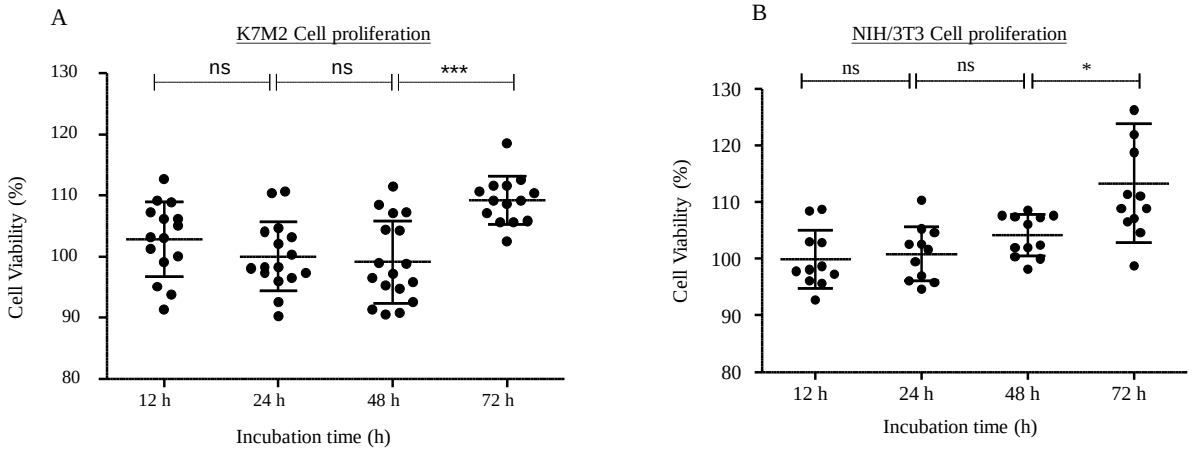

Figure 6.6 Cell proliferation assay via MTT. Cell proliferation of (A) K7M2 and (B) NIH/3T3 cells after 100 µl, 20 µg/ml K7M2-EVs (12, 24, 48, 72 h) treatment for 48 h, quantified in terms of % cell viability compared to untreated cells. (*** = P value 0.0003, (* = P value 0.0101, ns= non-significant, Mann Whitney t test).

6.4 Conclusion

The heterologous characteristic of EV production which depends upon the state of the parent cell and isolation condition has led to challenges in the reproducibility and translation of EV research. Proper characterization of EVs variation with varied isolation conditions and detail reporting of isolation parameters can aid to overcome this challenge. Here, we characterized how varied incubation times can affect the size, protein content, and concentration of EVs among cancer and non-cancer cell lines, by using an optimized ultrafiltration-SEC based method. We found that

cancer cell produces more EVs, both in terms of number and protein content, compared to the non-cancer cell, which increases with incubation time. The optimum incubation time with the best protein recovery was 48 h. The size of EVs was independent of incubation time or cell types, varying within a range of 130-220 nm. Variation in cell proliferation characteristic of 72 h-EVs suggest differential functionality of highly stressed EVs. This study has successfully optimized a reproducible ultrafiltration-SEC-based EV enrichment method and explored the variation of EVs production and functionality among cancer and non-cancer cell. Such characterization can be important steps toward the fundamental understanding of rigor and reproducibility in EV production and function to realize the translational avenues of EVs research.

Chapter 7 - Summary and Future Outlook

The lipid-based vesicular systems offer exciting opportunities for drug delivery owing to their colloidal stability, self-assembly, biocompatibility, ability to load hydrophobic to hydrophilic cargo, and a plethora of target-specific functionalizing potentials. In this regard, liposomes and EVs are two vesicles-based systems with structural similarities that are ideal for drug delivery. Liposomes are easy to prepare, control, and functionalize, while EVs have endogenous cell-derived functionality. In this dissertation, we used liposomes, EVs, and their hybrids to exploit the advantages of both systems, while mitigating respective shortcoming. Our major goal of using these systems was to overcome two major challenges associated with nanoparticulate drug delivery system- 1) how to overcome endosome degradation of nanoparticles and maximize intracellular bioavailability and 2) how to overcome biological barriers for efficient and targeted delivery- rapid immune clearance, circulation stability, epithelial barriers, microenvironment barriers, cellular, and intracellular barriers. Toward this endeavor, we engineered a pH-responsive DC-liposome, Hybrid exosome (HE), and gadolinium-infused hybrid extracellular vesicles (Gd-HEV) by using fundamental chemistry and engineering approaches.

DC-liposome showed pH-responsive cationic and fusogenic properties thereby avoiding endosomal degradation by membrane fusion (**Chapter 3**). Although the in-vitro results were promising, the challenge to overcome the biological barrier remains. To overcome this problem, a natural messenger of the cellular system, which has been optimized with years of evolution, EVs, was used. We optimized a simple, efficient, and reproducible EVs isolation method by combining centrifugation, ultrafiltration, and size exclusion-based chromatography. HE showed better overall yield, stability, and added functionality, with preferential interaction toward cancer cells, showing promises for tumor-targeted drug delivery (**Chapter 4**). Further, Gd-HEV showed optimum

stability, higher gadolinium retention, tumor-targeting property, and longer blood retention time for contrast-enhanced magnetic resonance imaging (**Chapter 5**). Overall, the engineered nanoparticles showed desirable characteristics viz. endosomal degradation via escape, longer retention time, good biocompatibility, efficient drug loading capacity, and tumor-targeting characteristic. Therefore, the demonstrated proof-of-concept and design consideration of vesicles-based drug delivery systems add important understanding on the implications of these systems to achieve efficient tumor-targeted drug delivery.

However, the translational potential of the proposed system remains challenging. The heterogeneous nature of EVs production and functionality depending on the physiological condition of the parent cell and diverse isolation parameters adds challenges in translational EVs research and demands more research in the field. We explored a part of this heterogeneity by characterizing the variation in size, protein content, concentration, and functionality of EVs among varied nutrient-stress conditions and cell lines- cancer vs non-cancer (**Chapter 6**). We found that EV protein content and the number increases with incubation time in serum-deprived condition, and cancer cell-derived EVs produces more EVs compared to non-cancer. These observations are evident that EVs production and functionality are dependent upon secreting cells. Therefore, it is important for the proper characterization of possible variation and detail reporting of isolation parameters to envision a reproducible and translational outcome. Given the exploding EV research with breakthrough promises in drug delivery, disease diagnosis, and therapy, future research should focus on accounting for the innate heterogeneity and variation in EV production and functionality. Further, exploring the molecular mechanism behind cellular communication can lead toward a better understanding of these systems to realize the translational potential of vesicle-based nanocarriers for tumor-targeted drug delivery.

References

(1) Feynman, R. P. There's Plenty of Room at the Bottom. *Reson* **2011**, *16* (9), 890. https://doi.org/10.1007/s12045-011-0109-x.

(2) Taniguchi, N. On the Basic Concept of Nanotechnology. *Proceeding of the ICPE* **1974**.

(3) Drexler, K. E. *Engines of Creation*; Anchor, 1986.

(4) What is Nanotechnology? | nano.gov https://www.nano.gov/nanotech-101/what/definition (accessed Nov 12, 2020).

(5) Nanomedicine - Latest research and news | Nature https://www.nature.com/subjects/nanomedicine (accessed Nov 12, 2020).

(6) Schmitz, R. Friedrich Wilhelm Sertürner and the Discovery of Morphine. *Pharmacy in history* **1985**, *27* (2), 61–74.

(7) Alexander Fleming Discovery and Development of Penicillin - Landmark https://www.acs.org/content/acs/en/education/whatischemistry/landmarks/flemingpenicillin.html (accessed Nov 12, 2020).

(8) Dan, N. Chapter 1 - Vesicle-Based Drug Carriers: Liposomes, Polymersomes, and Niosomes. In *Design and Development of New Nanocarriers*; Grumezescu, A. M., Ed.; William Andrew Publishing, 2018; pp 1–55. https://doi.org/10.1016/B978-0-12-813627-0.00001-6.

(9) Park, K. Nanotechnology: What It Can Do for Drug Delivery. *Journal of controlled release: official journal of the Controlled Release Society* **2007**, *120* (1–2), 1.

(10) Nanotechnology and Drug Delivery http://worldofnanoscience.weebly.com/nanotechnology-and-drug-delivery.html (accessed Nov 12, 2020).

(11) Mitchell, M. J.; Billingsley, M. M.; Haley, R. M.; Wechsler, M. E.; Peppas, N. A.; Langer, R. Engineering Precision Nanoparticles for Drug Delivery. *Nature Reviews Drug Discovery* **2020**, 1–24. https://doi.org/10.1038/s41573-020-0090-8.

(12) Dan, N. Core–Shell Drug Carriers: Liposomes, Polymersomes, and Niosomes. In *Nanostructures for Drug Delivery*; Elsevier, 2017; pp 63–105.

(13) Bangham, A. D.; Horne, R. W. Negative Staining of Phospholipids and Their Structural Modification by Surface-Active Agents as Observed in the Electron Microscope. *Journal of Molecular Biology* **1964**, *8* (5), 660-IN10. https://doi.org/10.1016/S0022-2836(64)80115-7.

(14) Torchilin, V. P. Recent Advances with Liposomes as Pharmaceutical Carriers. *Nature Reviews Drug Discovery* **2005**, *4* (2), 145–160. https://doi.org/10.1038/nrd1632.

(15) Beltrán-Gracia, E.; López-Camacho, A.; Higuera-Ciapara, I.; Velázquez-Fernández, J. B.; Vallejo-Cardona, A. A. Nanomedicine Review: Clinical Developments in Liposomal Applications. *Cancer Nanotechnology* **2019**, *10* (1), 11. https://doi.org/10.1186/s12645-019-0055-y.

(16) Research, C. for D. E. and. FDA Approves Liposome-Encapsulated Combination of Daunorubicin-Cytarabine for Adults with Some Types of Poor Prognosis AML. *FDA* **2019**.

(17) Bulbake, U.; Doppalapudi, S.; Kommineni, N.; Khan, W. Liposomal Formulations in Clinical Use: An Updated Review. *Pharmaceutics* **2017**, *9* (2), 12. https://doi.org/10.3390/pharmaceutics9020012.

(18) Becker, A.; Thakur, B. K.; Weiss, J. M.; Kim, H. S.; Peinado, H.; Lyden, D. Extracellular Vesicles in Cancer: Cell-to-Cell Mediators of Metastasis. *Cancer Cell* **2016**, *30* (6), 836–848. https://doi.org/10.1016/j.ccell.2016.10.009.
(19) Raposo, G.; Stoorvogel, W. Extracellular Vesicles: Exosomes, Microvesicles, and Friends. *J Cell Biol* **2013**, *200* (4), 373–383. https://doi.org/10.1083/jcb.201211138.
(20) Colombo, M.; Raposo, G.; Théry, C. Biogenesis, Secretion, and Intercellular Interactions of Exosomes and Other Extracellular Vesicles. *Annual Review of Cell and Developmental Biology* **2014**, *30* (1), 255–289. https://doi.org/10.1146/annurev-cellbio-101512-122326.
(21) Aaronson, S.; Behrens, U.; Orner, R.; Haines, T. H. Ultrastructure of Intracellular and Extracellular Vesicles, Membranes, and Myelin Figures Produced by Ochromonas Danica. *Journal of Ultrastructure Research* **1971**, *35* (5), 418–430. https://doi.org/10.1016/S0022-5320(71)80003-5.
(22) Chargaff, E.; West, R. The Biological Significance of the Thromboplastic Protein of Blood. *J. Biol. Chem.* **1946**, *166* (1), 189–197.
(23) Wolf, P. The Nature and Significance of Platelet Products in Human Plasma. *Br. J. Haematol.* **1967**, *13* (3), 269–288. https://doi.org/10.1111/j.1365-2141.1967.tb08741.x.
(24) Anderson, H. C. Vesicles Associated with Calcification in the Matrix of Epiphyseal Cartilage. *J. Cell Biol.* **1969**, *41* (1), 59–72. https://doi.org/10.1083/jcb.41.1.59.
(25) Raposo, G.; Nijman, H. W.; Stoorvogel, W.; Liejendekker, R.; Harding, C. V.; Melief, C. J.; Geuze, H. J. B Lymphocytes Secrete Antigen-Presenting Vesicles. *J Exp Med* **1996**, *183* (3), 1161–1172. https://doi.org/10.1084/jem.183.3.1161.
(26) Zitvogel, L.; Regnault, A.; Lozier, A.; Wolfers, J.; Flament, C.; Tenza, D.; Ricciardi-Castagnoli, P.; Raposo, G.; Amigorena, S. Eradication of Established Murine Tumors Using a Novel Cell-Free Vaccine: Dendritic Cell Derived Exosomes. *Nature Medicine* **1998**, *4* (5), 594–600. https://doi.org/10.1038/nm0598-594.
(27) Valadi, H.; Ekström, K.; Bossios, A.; Sjöstrand, M.; Lee, J. J.; Lötvall, J. O. Exosome-Mediated Transfer of MRNAs and MicroRNAs Is a Novel Mechanism of Genetic Exchange between Cells. *Nature Cell Biology* **2007**, *9* (6), 654–659. https://doi.org/10.1038/ncb1596.
(28) Ratajczak, J.; Miekus, K.; Kucia, M.; Zhang, J.; Reca, R.; Dvorak, P.; Ratajczak, M. Z. Embryonic Stem Cell-Derived Microvesicles Reprogram Hematopoietic Progenitors: Evidence for Horizontal Transfer of MRNA and Protein Delivery. *Leukemia* **2006**, *20* (5), 847–856. https://doi.org/10.1038/sj.leu.2404132.
(29) The Nobel Prize in Physiology or Medicine 2013 https://www.nobelprize.org/prizes/medicine/2013/summary/ (accessed Feb 1, 2020).
(30) Söllner, T.; Whiteheart, S. W.; Brunner, M.; Erdjument-Bromage, H.; Geromanos, S.; Tempst, P.; Rothman, J. E. SNAP Receptors Implicated in Vesicle Targeting and Fusion. *Nature* **1993**, *362* (6418), 318–324. https://doi.org/10.1038/362318a0.
(31) Perin, M. S.; Fried, V. A.; Mignery, G. A.; Jahn, R.; Südhof, T. C. Phospholipid Binding by a Synaptic Vesicle Protein Homologous to the Regulatory Region of Protein Kinase C. *Nature* **1990**, *345* (6272), 260–263. https://doi.org/10.1038/345260a0.
(32) Search of: exosome | Phase Early Phase 1, 1, 2, 3, 4 - List Results - ClinicalTrials.gov https://clinicaltrials.gov/ct2/results?term=exosome&age_v=&gndr=&type=&rslt=&phase=4&phase=0&phase=1&phase=2&phase=3&Search=Apply (accessed Mar 12, 2020).

(33) Morse, M. A.; Garst, J.; Osada, T.; Khan, S.; Hobeika, A.; Clay, T. M.; Valente, N.; Shreeniwas, R.; Sutton, M. A.; Delcayre, A.; Hsu, D.-H.; Le Pecq, J.-B.; Lyerly, H. K. A Phase I Study of Dexosome Immunotherapy in Patients with Advanced Non-Small Cell Lung Cancer. *Journal of Translational Medicine* **2005**, *3* (1), 9. https://doi.org/10.1186/1479-5876-3-9.

(34) Fuster-Matanzo, A.; Gessler, F.; Leonardi, T.; Iraci, N.; Pluchino, S. Acellular Approaches for Regenerative Medicine: On the Verge of Clinical Trials with Extracellular Membrane Vesicles? *Stem Cell Research & Therapy* **2015**, *6* (1), 227. https://doi.org/10.1186/s13287-015-0232-9.

(35) Colombo, M.; Raposo, G.; Théry, C. Biogenesis, Secretion, and Intercellular Interactions of Exosomes and Other Extracellular Vesicles. *Annual Review of Cell and Developmental Biology* **2014**, *30* (1), 255–289. https://doi.org/10.1146/annurev-cellbio-101512-122326.

(36) Raposo, G.; Stoorvogel, W. Extracellular Vesicles: Exosomes, Microvesicles, and Friends. *J Cell Biol* **2013**, *200* (4), 373–383. https://doi.org/10.1083/jcb.201211138.

(37) Di Vizio, D.; Morello, M.; Dudley, A. C.; Schow, P. W.; Adam, R. M.; Morley, S.; Mulholland, D.; Rotinen, M.; Hager, M. H.; Insabato, L.; Moses, M. A.; Demichelis, F.; Lisanti, M. P.; Wu, H.; Klagsbrun, M.; Bhowmick, N. A.; Rubin, M. A.; D'Souza-Schorey, C.; Freeman, M. R. Large Oncosomes in Human Prostate Cancer Tissues and in the Circulation of Mice with Metastatic Disease. *The American Journal of Pathology* **2012**, *181* (5), 1573–1584. https://doi.org/10.1016/j.ajpath.2012.07.030.

(38) Crescitelli, R.; Lässer, C.; Szabó, T. G.; Kittel, A.; Eldh, M.; Dianzani, I.; Buzás, E. I.; Lötvall, J. Distinct RNA Profiles in Subpopulations of Extracellular Vesicles: Apoptotic Bodies, Microvesicles and Exosomes. *Journal of Extracellular Vesicles* **2013**, *2* (1), 20677. https://doi.org/10.3402/jev.v2i0.20677.

(39) Vagner, T.; Spinelli, C.; Minciacchi, V. R.; Balaj, L.; Zandian, M.; Conley, A.; Zijlstra, A.; Freeman, M. R.; Demichelis, F.; De, S.; Posadas, E. M.; Tanaka, H.; Vizio, D. D. Large Extracellular Vesicles Carry Most of the Tumour DNA Circulating in Prostate Cancer Patient Plasma. *Journal of Extracellular Vesicles* **2018**, *7* (1), 1505403. https://doi.org/10.1080/20013078.2018.1505403.

(40) Biogenesis, Secretion, and Intercellular Interactions of Exosomes and Other Extracellular Vesicles | Annual Review of Cell and Developmental Biology https://www.annualreviews.org/doi/full/10.1146/annurev-cellbio-101512-122326?url_ver=Z39.88-2003&rfr_id=ori%3Arid%3Acrossref.org&rfr_dat=cr_pub%3Dpubmed (accessed Jan 14, 2020).

(41) Ceramide Triggers Budding of Exosome Vesicles into Multivesicular Endosomes | Science https://science.sciencemag.org/content/319/5867/1244.full (accessed Jan 14, 2020).

(42) The Intracellular Interactome of Tetraspanin-enriched Microdomains Reveals Their Function as Sorting Machineries toward Exosomes http://www.jbc.org/content/288/17/11649 (accessed Jan 14, 2020).

(43) Mutation of SIMPLE in Charcot–Marie–Tooth 1C alters production of exosomes | Molecular Biology of the Cell https://www.molbiolcell.org/doi/10.1091/mbc.e12-07-0544 (accessed Jan 14, 2020).

(44) Kowal, J.; Arras, G.; Colombo, M.; Jouve, M.; Morath, J. P.; Primdal-Bengtson, B.; Dingli, F.; Loew, D.; Tkach, M.; Théry, C. Proteomic Comparison Defines Novel Markers to Characterize Heterogeneous Populations of Extracellular Vesicle Subtypes. *Proc. Natl. Acad. Sci. U.S.A.* **2016**, *113* (8), E968-977. https://doi.org/10.1073/pnas.1521230113.

(45) Vagner, T.; Chin, A.; Mariscal, J.; Bannykh, S.; Engman, D. M.; Vizio, D. D. Protein Composition Reflects Extracellular Vesicle Heterogeneity. *PROTEOMICS* **2019**, *19* (8), 1800167. https://doi.org/10.1002/pmic.201800167.

(46) Jeppesen, D. K.; Fenix, A. M.; Franklin, J. L.; Higginbotham, J. N.; Zhang, Q.; Zimmerman, L. J.; Liebler, D. C.; Ping, J.; Liu, Q.; Evans, R.; Fissell, W. H.; Patton, J. G.; Rome, L. H.; Burnette, D. T.; Coffey, R. J. Reassessment of Exosome Composition. *Cell* **2019**, *177* (2), 428-445.e18. https://doi.org/10.1016/j.cell.2019.02.029.

(47) Ramirez, M. I.; Amorim, M. G.; Gadelha, C.; Milic, I.; Welsh, J. A.; Freitas, V. M.; Nawaz, M.; Akbar, N.; Couch, Y.; Makin, L.; Cooke, F.; Vettore, A. L.; Batista, P. X.; Freezor, R.; Pezuk, J. A.; Rosa-Fernandes, L.; Carreira, A. C. O.; Devitt, A.; Jacobs, L.; Silva, I. T.; Coakley, G.; Nunes, D. N.; Carter, D.; Palmisano, G.; Dias-Neto, E. Technical Challenges of Working with Extracellular Vesicles. *Nanoscale* **2018**, *10* (3), 881–906. https://doi.org/10.1039/C7NR08360B.

(48) Minimal information for studies of extracellular vesicles 2018 (MISEV2018): a position statement of the International Society for Extracellular Vesicles and update of the MISEV2014 guidelines: Journal of Extracellular Vesicles: Vol 7, No 1 https://www.tandfonline.com/doi/full/10.1080/20013078.2018.1535750 (accessed Jan 14, 2020).

(49) Ji, Y.; Qi, D.; Li, L.; Su, H.; Li, X.; Luo, Y.; Sun, B.; Zhang, F.; Lin, B.; Liu, T.; Lu, Y. Multiplexed Profiling of Single-Cell Extracellular Vesicles Secretion. *PNAS* **2019**, *116* (13), 5979–5984. https://doi.org/10.1073/pnas.1814348116.

(50) Sharma, P.; Mesci, P.; Carromeu, C.; McClatchy, D. R.; Schiapparelli, L.; Yates, J. R.; Muotri, A. R.; Cline, H. T. Exosomes Regulate Neurogenesis and Circuit Assembly. *PNAS* **2019**, *116* (32), 16086–16094. https://doi.org/10.1073/pnas.1902513116.

(51) Bang, C.; Thum, T. Exosomes: New Players in Cell–Cell Communication. *The International Journal of Biochemistry & Cell Biology* **2012**, *44* (11), 2060–2064. https://doi.org/10.1016/j.biocel.2012.08.007.

(52) Mathieu, M.; Martin-Jaular, L.; Lavieu, G.; Théry, C. Specificities of Secretion and Uptake of Exosomes and Other Extracellular Vesicles for Cell-to-Cell Communication. *Nat Cell Biol* **2019**, *21* (1), 9–17. https://doi.org/10.1038/s41556-018-0250-9.

(53) Paolicelli, R. C.; Bergamini, G.; Rajendran, L. Cell-to-Cell Communication by Extracellular Vesicles: Focus on Microglia. *Neuroscience* **2019**, *405*, 148–157. https://doi.org/10.1016/j.neuroscience.2018.04.003.

(54) Zhang, Z. G.; Buller, B.; Chopp, M. Exosomes — beyond Stem Cells for Restorative Therapy in Stroke and Neurological Injury. *Nature Reviews Neurology* **2019**, *15* (4), 193–203. https://doi.org/10.1038/s41582-018-0126-4.

(55) Kourembanas, S. Exosomes: Vehicles of Intercellular Signaling, Biomarkers, and Vectors of Cell Therapy. *Annual Review of Physiology* **2015**, *77* (1), 13–27. https://doi.org/10.1146/annurev-physiol-021014-071641.

(56) Nedaeinia, R.; Manian, M.; Jazayeri, M. H.; Ranjbar, M.; Salehi, R.; Sharifi, M.; Mohaghegh, F.; Goli, M.; Jahednia, S. H.; Avan, A.; Ghayour-Mobarhan, M. Circulating

Exosomes and Exosomal MicroRNAs as Biomarkers in Gastrointestinal Cancer. *Cancer Gene Therapy* **2017**, *24* (2), 48–56. https://doi.org/10.1038/cgt.2016.77.
(57) Wu, L.; Qu, X. Cancer Biomarker Detection: Recent Achievements and Challenges. *Chem. Soc. Rev.* **2015**, *44* (10), 2963–2997. https://doi.org/10.1039/C4CS00370E.
(58) Zhao, Z.; Fan, J.; Hsu, Y.-M. S.; Lyon, C. J.; Ning, B.; Hu, T. Y. Extracellular Vesicles as Cancer Liquid Biopsies: From Discovery, Validation, to Clinical Application. *Lab Chip* **2019**, *19* (7), 1114–1140. https://doi.org/10.1039/C8LC01123K.
(59) Ren, J.; He, W.; Zheng, L.; Duan, H. From Structures to Functions: Insights into Exosomes as Promising Drug Delivery Vehicles. *Biomater Sci* **2016**, *4* (6), 910–921. https://doi.org/10.1039/c5bm00583c.
(60) Hosseini, A.; Soleimani, S.; Modarres, H. P.; Emami, S. H.; Tondar, M.; Bahlakeh, G.; Hasani-Sadrabadi, M. M. Exosome-Inspired Targeting of Cancer Cells with Enhanced Affinity. *J. Mater. Chem. B* **2016**, *4* (4), 768–778. https://doi.org/10.1039/C5TB01741F.
(61) Zhang, M.; Zang, X.; Wang, M.; Li, Z.; Qiao, M.; Hu, H.; Chen, D. Exosome-Based Nanocarriers as Bio-Inspired and Versatile Vehicles for Drug Delivery: Recent Advances and Challenges. *J. Mater. Chem. B* **2019**, *7* (15), 2421–2433. https://doi.org/10.1039/C9TB00170K.
(62) Soda, N.; Rehm, B. H. A.; Sonar, P.; Nguyen, N.-T.; Shiddiky, M. J. A. Advanced Liquid Biopsy Technologies for Circulating Biomarker Detection. *J. Mater. Chem. B* **2019**, *7* (43), 6670–6704. https://doi.org/10.1039/C9TB01490J.
(63) Wan, Y.; Maurer, M.; He, H.-Z.; Xia, Y.-Q.; Hao, S.-J.; Zhang, W.-L.; Yee, N. S.; Zheng, S.-Y. Enrichment of Extracellular Vesicles with Lipid Nanoprobe Functionalized Nanostructured Silica. *Lab Chip* **2019**, *19* (14), 2346–2355. https://doi.org/10.1039/C8LC01359D.
(64) Zhu, L.; Xu, N.; Zhang, Z.-L.; Zhang, T.-C. Cell Derived Extracellular Vesicles: From Isolation to Functionalization and Biomedical Applications. *Biomater. Sci.* **2019**, *7* (9), 3552–3565. https://doi.org/10.1039/C9BM00580C.
(65) Rayamajhi, S.; Nguyen, T. D. T.; Marasini, R.; Aryal, S. Macrophage-Derived Exosome-Mimetic Hybrid Vesicles for Tumor Targeted Drug Delivery. *Acta Biomaterialia* **2019**, *94*, 482–494. https://doi.org/10.1016/j.actbio.2019.05.054.
(66) Cheng, Q.; Shi, X.; Han, M.; Smbatyan, G.; Lenz, H.-J.; Zhang, Y. Reprogramming Exosomes as Nanoscale Controllers of Cellular Immunity. *J. Am. Chem. Soc.* **2018**, *140* (48), 16413–16417. https://doi.org/10.1021/jacs.8b10047.
(67) Stickney, Z.; Losacco, J.; McDevitt, S.; Zhang, Z.; Lu, B. Development of Exosome Surface Display Technology in Living Human Cells. *Biochemical and Biophysical Research Communications* **2016**, *472* (1), 53–59. https://doi.org/10.1016/j.bbrc.2016.02.058.
(68) Sato, Y. T.; Umezaki, K.; Sawada, S.; Mukai, S.; Sasaki, Y.; Harada, N.; Shiku, H.; Akiyoshi, K. Engineering Hybrid Exosomes by Membrane Fusion with Liposomes. *Sci Rep* **2016**, *6*. https://doi.org/10.1038/srep21933.
(69) Sato, Y. T.; Umezaki, K.; Sawada, S.; Mukai, S.; Sasaki, Y.; Harada, N.; Shiku, H.; Akiyoshi, K. Engineering Hybrid Exosomes by Membrane Fusion with Liposomes. *Sci Rep* **2016**, *6* (1), 1–11. https://doi.org/10.1038/srep21933.
(70) Sugihara, K.; Jang, B.; Schneider, M.; Vörös, J.; Zambelli, T. A Universal Method for Planar Lipid Bilayer Formation by Freeze and Thaw. *Soft Matter* **2012**, *8* (20), 5525–5531. https://doi.org/10.1039/C2SM25148E.

(71) Cao, E.; Chen, Y.; Cui, Z.; Foster, P. R. Effect of Freezing and Thawing Rates on Denaturation of Proteins in Aqueous Solutions. *Biotechnology and Bioengineering* **2003**, *82* (6), 684–690. https://doi.org/10.1002/bit.10612.
(72) Cheng, Y.; Zeng, Q.; Han, Q.; Xia, W. Effect of PH, Temperature and Freezing-Thawing on Quantity Changes and Cellular Uptake of Exosomes. *Protein Cell* **2019**, *10* (4), 295–299. https://doi.org/10.1007/s13238-018-0529-4.
(73) Cao, E.; Chen, Y.; Cui, Z.; Foster, P. R. Effect of Freezing and Thawing Rates on Denaturation of Proteins in Aqueous Solutions. *Biotechnology and Bioengineering* **2003**, *82* (6), 684–690. https://doi.org/10.1002/bit.10612.
(74) Rayamajhi, S.; Marasini, R.; Nguyen, T. D. T.; Plattner, B. L.; Biller, D.; Aryal, S. Strategic Reconstruction of Macrophage-Derived Extracellular Vesicles as a Magnetic Resonance Imaging Contrast Agent. *Biomater. Sci.* **2020**. https://doi.org/10.1039/D0BM00128G.
(75) Pitchaimani, A.; Nguyen, T. D. T.; Aryal, S. Natural Killer Cell Membrane Infused Biomimetic Liposomes for Targeted Tumor Therapy. *Biomaterials* **2018**, *160*, 124–137. https://doi.org/10.1016/j.biomaterials.2018.01.018.
(76) Pitchaimani, A.; Nguyen, T. D. T.; Marasini, R.; Eliyapura, A.; Azizi, T.; Jaberi-Douraki, M.; Aryal, S. Biomimetic Natural Killer Membrane Camouflaged Polymeric Nanoparticle for Targeted Bioimaging. *Advanced Functional Materials 0* (0), 1806817. https://doi.org/10.1002/adfm.201806817.
(77) Abello, J.; Nguyen, T. D. T.; Marasini, R.; Aryal, S.; Weiss, M. L. Biodistribution of Gadolinium- and near Infrared-Labeled Human Umbilical Cord Mesenchymal Stromal Cell-Derived Exosomes in Tumor Bearing Mice. *Theranostics* **2019**, *9* (8), 2325–2345. https://doi.org/10.7150/thno.30030.
(78) Aryal, S.; Key, J.; Stigliano, C.; Ananta, J. S.; Zhong, M.; Decuzzi, P. Engineered Magnetic Hybrid Nanoparticles with Enhanced Relaxivity for Tumor Imaging. *Biomaterials* **2013**, *34* (31), 7725–7732. https://doi.org/10.1016/j.biomaterials.2013.07.003.
(79) Pitchaimani, A.; Nguyen, T. D. T.; Wang, H.; Bossmann, S. H.; Aryal, S. Design and Characterization of Gadolinium Infused Theranostic Liposomes. *RSC Adv.* **2016**, *6* (43), 36898–36905. https://doi.org/10.1039/C6RA00552G.
(80) Aryal, S.; Stigliano, C.; Key, J.; Ramirez, M.; Anderson, J.; Karmonik, C.; Fung, S.; Decuzzi, P. Paramagnetic Gd3+ Labeled Red Blood Cells for Magnetic Resonance Angiography. *Biomaterials* **2016**, *98*, 163–170. https://doi.org/10.1016/j.biomaterials.2016.05.002.
(81) Marasini, R.; Nguyen, T. D. T.; Aryal, S. Integration of Gadolinium in Nanostructure for Contrast Enhanced-Magnetic Resonance Imaging. *WIREs Nanomedicine and Nanobiotechnology n/a* (n/a), e1580. https://doi.org/10.1002/wnan.1580.
(82) Nguyen, T. D. T.; Marasini, R.; Rayamajhi, S.; Aparicio, C.; Biller, D.; Aryal, S. Erythrocyte Membrane Concealed Paramagnetic Polymeric Nanoparticle for Contrast-Enhanced Magnetic Resonance Imaging. *Nanoscale* **2020**, *12* (6), 4137–4149. https://doi.org/10.1039/D0NR00039F.
(83) Tamura, R.; Uemoto, S.; Tabata, Y. Augmented Liver Targeting of Exosomes by Surface Modification with Cationized Pullulan. *Acta Biomaterialia* **2017**, *57*, 274–284. https://doi.org/10.1016/j.actbio.2017.05.013.

(84) Sawada, S.; Sato, Y. T.; Kawasaki, R.; Yasuoka, J.; Mizuta, R.; Sasaki, Y.; Akiyoshi, K. Nanogel Hybrid Assembly for Exosome Intracellular Delivery: Effects on Endocytosis and Fusion by Exosome Surface Polymer Engineering. *Biomater. Sci.* **2020**, *8* (2), 619–630. https://doi.org/10.1039/C9BM01232J.

(85) Tahara, Y.; Akiyoshi, K. Current Advances in Self-Assembled Nanogel Delivery Systems for Immunotherapy. *Advanced Drug Delivery Reviews* **2015**, *95*, 65–76. https://doi.org/10.1016/j.addr.2015.10.004.

(86) Didiot, M.-C.; Hall, L. M.; Coles, A. H.; Haraszti, R. A.; Godinho, B. M.; Chase, K.; Sapp, E.; Ly, S.; Alterman, J. F.; Hassler, M. R.; Echeverria, D.; Raj, L.; Morrissey, D. V.; DiFiglia, M.; Aronin, N.; Khvorova, A. Exosome-Mediated Delivery of Hydrophobically Modified SiRNA for Huntingtin MRNA Silencing. *Molecular Therapy* **2016**, *24* (10), 1836–1847. https://doi.org/10.1038/mt.2016.126.

(87) Haraszti, R. A.; Miller, R.; Didiot, M.-C.; Biscans, A.; Alterman, J. F.; Hassler, M. R.; Roux, L.; Echeverria, D.; Sapp, E.; DiFiglia, M.; Aronin, N.; Khvorova, A. Optimized Cholesterol-SiRNA Chemistry Improves Productive Loading onto Extracellular Vesicles. *Molecular Therapy* **2018**, *26* (8), 1973–1982. https://doi.org/10.1016/j.ymthe.2018.05.024.

(88) Hemler, M. E. Tetraspanin Functions and Associated Microdomains. *Nature Reviews Molecular Cell Biology* **2005**, *6* (10), 801–811. https://doi.org/10.1038/nrm1736.

(89) Yim, N.; Ryu, S.-W.; Choi, K.; Lee, K. R.; Lee, S.; Choi, H.; Kim, J.; Shaker, M. R.; Sun, W.; Park, J.-H.; Kim, D.; Heo, W. D.; Choi, C. Exosome Engineering for Efficient Intracellular Delivery of Soluble Proteins Using Optically Reversible Protein–Protein Interaction Module. *Nat Commun* **2016**, *7* (1), 1–9. https://doi.org/10.1038/ncomms12277.

(90) Cheng, Q.; Shi, X.; Han, M.; Smbatyan, G.; Lenz, H.-J.; Zhang, Y. Reprogramming Exosomes as Nanoscale Controllers of Cellular Immunity. *J. Am. Chem. Soc.* **2018**, *140* (48), 16413–16417. https://doi.org/10.1021/jacs.8b10047.

(91) Reis-Filho, J. S.; Tutt, A. N. J. Triple Negative Tumours: A Critical Review. *Histopathology* **2008**, *52* (1), 108–118. https://doi.org/10.1111/j.1365-2559.2007.02889.x.

(92) Alvarez-Erviti, L.; Seow, Y.; Yin, H.; Betts, C.; Lakhal, S.; Wood, M. J. A. Delivery of SiRNA to the Mouse Brain by Systemic Injection of Targeted Exosomes. *Nature Biotechnology* **2011**, *29* (4), 341–345. https://doi.org/10.1038/nbt.1807.

(93) Wiklander, O. P. B.; Brennan, M. Á.; Lötvall, J.; Breakefield, X. O.; Andaloussi, S. E. Advances in Therapeutic Applications of Extracellular Vesicles. *Science Translational Medicine* **2019**, *11* (492). https://doi.org/10.1126/scitranslmed.aav8521.

(94) Kumar, P.; Wu, H.; McBride, J. L.; Jung, K.-E.; Hee Kim, M.; Davidson, B. L.; Kyung Lee, S.; Shankar, P.; Manjunath, N. Transvascular Delivery of Small Interfering RNA to the Central Nervous System. *Nature* **2007**, *448* (7149), 39–43. https://doi.org/10.1038/nature05901.

(95) Wiklander, O. P. B.; Nordin, J. Z.; O'Loughlin, A.; Gustafsson, Y.; Corso, G.; Mäger, I.; Vader, P.; Lee, Y.; Sork, H.; Seow, Y.; Heldring, N.; Alvarez-Erviti, L.; Smith, C. E.; Blanc, K. L.; Macchiarini, P.; Jungebluth, P.; Wood, M. J. A.; Andaloussi, S. E. Extracellular Vesicle in Vivo Biodistribution Is Determined by Cell Source, Route of Administration and Targeting. *Journal of Extracellular Vesicles* **2015**, *4* (1), 26316. https://doi.org/10.3402/jev.v4.26316.

(96) Lentz, T. L.; Burrage, T. G.; Smith, A. L.; Tignor, G. H. The Acetylcholine Receptor as a Cellular Receptor for Rabies Virus. *Yale J Biol Med* **1983**, *56* (4), 315–322.
(97) Yang, J.; Zhang, X.; Chen, X.; Wang, L.; Yang, G. Exosome Mediated Delivery of MiR-124 Promotes Neurogenesis after Ischemia. *Molecular Therapy - Nucleic Acids* **2017**, *7*, 278–287. https://doi.org/10.1016/j.omtn.2017.04.010.
(98) Tian, Y.; Li, S.; Song, J.; Ji, T.; Zhu, M.; Anderson, G. J.; Wei, J.; Nie, G. A Doxorubicin Delivery Platform Using Engineered Natural Membrane Vesicle Exosomes for Targeted Tumor Therapy. *Biomaterials* **2014**, *35* (7), 2383–2390. https://doi.org/10.1016/j.biomaterials.2013.11.083.
(99) Sugahara, K. N.; Teesalu, T.; Karmali, P. P.; Kotamraju, V. R.; Agemy, L.; Greenwald, D. R.; Ruoslahti, E. Coadministration of a Tumor-Penetrating Peptide Enhances the Efficacy of Cancer Drugs. *Science* **2010**, *328* (5981), 1031–1035. https://doi.org/10.1126/science.1183057.
(100) Kim, H.; Yun, N.; Mun, D.; Kang, J.-Y.; Lee, S.-H.; Park, H.; Park, H.; Joung, B. Cardiac-Specific Delivery by Cardiac Tissue-Targeting Peptide-Expressing Exosomes. *Biochemical and Biophysical Research Communications* **2018**, *499* (4), 803–808. https://doi.org/10.1016/j.bbrc.2018.03.227.
(101) Wang, M.; Altinoglu, S.; Takeda, Y. S.; Xu, Q. Integrating Protein Engineering and Bioorthogonal Click Conjugation for Extracellular Vesicle Modulation and Intracellular Delivery. *PLOS ONE* **2015**, *10* (11), e0141860. https://doi.org/10.1371/journal.pone.0141860.
(102) Johnson, J. A.; Lu, Y. Y.; Van Deventer, J. A.; Tirrell, D. A. Residue-Specific Incorporation of Non-Canonical Amino Acids into Proteins: Recent Developments and Applications. *Current Opinion in Chemical Biology* **2010**, *14* (6), 774–780. https://doi.org/10.1016/j.cbpa.2010.09.013.
(103) Williams, C.; Pazos, R.; Royo, F.; González, E.; Roura-Ferrer, M.; Martinez, A.; Gamiz, J.; Reichardt, N.-C.; Falcón-Pérez, J. M. Assessing the Role of Surface Glycans of Extracellular Vesicles on Cellular Uptake. *Scientific Reports* **2019**, *9* (1), 1–14. https://doi.org/10.1038/s41598-019-48499-1.
(104) Williams, C.; Royo, F.; Aizpurua-Olaizola, O.; Pazos, R.; Boons, G.-J.; Reichardt, N.-C.; Falcon-Perez, J. M. Glycosylation of Extracellular Vesicles: Current Knowledge, Tools and Clinical Perspectives. *Journal of Extracellular Vesicles* **2018**, *7* (1), 1442985. https://doi.org/10.1080/20013078.2018.1442985.
(105) Hein, C. D.; Liu, X.-M.; Wang, D. Click Chemistry, A Powerful Tool for Pharmaceutical Sciences. *Pharm Res* **2008**, *25* (10), 2216–2230. https://doi.org/10.1007/s11095-008-9616-1.
(106) Best, M. D. Click Chemistry and Bioorthogonal Reactions: Unprecedented Selectivity in the Labeling of Biological Molecules. *Biochemistry* **2009**, *48* (28), 6571–6584. https://doi.org/10.1021/bi9007726.
(107) Di, H.; Zeng, E.; Zhang, P.; Liu, X.; Zhang, C.; Yang, J.; Liu, D. General Approach to Engineering Extracellular Vesicles for Biomedical Analysis. *Anal. Chem.* **2019**, *91* (20), 12752–12759. https://doi.org/10.1021/acs.analchem.9b02268.
(108) Smyth, T.; Petrova, K.; Payton, N. M.; Persaud, I.; Redzic, J. S.; Graner, M. W.; Smith-Jones, P.; Anchordoquy, T. J. Surface Functionalization of Exosomes Using Click Chemistry. *Bioconjugate Chem.* **2014**, *25* (10), 1777–1784. https://doi.org/10.1021/bc500291r.

(109) Jain, A.; Cheng, K. The Principles and Applications of Avidin-Based Nanoparticles in Drug Delivery and Diagnosis. *Journal of Controlled Release* **2017**, *245*, 27–40. https://doi.org/10.1016/j.jconrel.2016.11.016.
(110) Gai, M.; Simon, J.; Lieberwirth, I.; Mailänder, V.; Morsbach, S.; Landfester, K. A Bio-Orthogonal Functionalization Strategy for Site-Specific Coupling of Antibodies on Vesicle Surfaces after Self-Assembly. *Polym. Chem.* **2020**, *11* (2), 527–540. https://doi.org/10.1039/C9PY01136F.
(111) Oude Blenke, E.; Klaasse, G.; Merten, H.; Plückthun, A.; Mastrobattista, E.; Martin, N. I. Liposome Functionalization with Copper-Free "Click Chemistry." *Journal of Controlled Release* **2015**, *202*, 14–20. https://doi.org/10.1016/j.jconrel.2015.01.027.
(112) Gangoda, L.; Liem, M.; Ang, C.-S.; Keerthikumar, S.; Adda, C. G.; Parker, B. S.; Mathivanan, S. Proteomic Profiling of Exosomes Secreted by Breast Cancer Cells with Varying Metastatic Potential. *PROTEOMICS* **2017**, *17* (23–24), 1600370. https://doi.org/10.1002/pmic.201600370.
(113) Carreras-Planella, L.; Soler-Majoral, J.; Rubio-Esteve, C.; Lozano-Ramos, S. I.; Franquesa, M.; Bonet, J.; Troya-Saborido, M. I.; Borràs, F. E. Characterization and Proteomic Profile of Extracellular Vesicles from Peritoneal Dialysis Efflux. *PLOS ONE* **2017**, *12* (5), e0176987. https://doi.org/10.1371/journal.pone.0176987.
(114) Bandu, R.; Oh, J. W.; Kim, K. P. Mass Spectrometry-Based Proteome Profiling of Extracellular Vesicles and Their Roles in Cancer Biology. *Experimental & Molecular Medicine* **2019**, *51* (3), 1–10. https://doi.org/10.1038/s12276-019-0218-2.
(115) Micsonai, A.; Wien, F.; Kernya, L.; Lee, Y.-H.; Goto, Y.; Réfrégiers, M.; Kardos, J. Accurate Secondary Structure Prediction and Fold Recognition for Circular Dichroism Spectroscopy. *PNAS* **2015**, *112* (24), E3095–E3103. https://doi.org/10.1073/pnas.1500851112.
(116) Cavalli, A.; Salvatella, X.; Dobson, C. M.; Vendruscolo, M. Protein Structure Determination from NMR Chemical Shifts. *PNAS* **2007**, *104* (23), 9615–9620. https://doi.org/10.1073/pnas.0610313104.
(117) Greenfield, N. J. Using Circular Dichroism Spectra to Estimate Protein Secondary Structure. *Nature Protocols* **2006**, *1* (6), 2876–2890. https://doi.org/10.1038/nprot.2006.202.
(118) Pelton, J. T.; McLean, L. R. Spectroscopic Methods for Analysis of Protein Secondary Structure. *Analytical Biochemistry* **2000**, *277* (2), 167–176. https://doi.org/10.1006/abio.1999.4320.
(119) Kruglik, S. G.; Royo, F.; Guigner, J.-M.; Palomo, L.; Seksek, O.; Turpin, P.-Y.; Tatischeff, I.; Falcón-Pérez, J. M. Raman Tweezers Microspectroscopy of circa 100 Nm Extracellular Vesicles. *Nanoscale* **2019**, *11* (4), 1661–1679. https://doi.org/10.1039/C8NR04677H.
(120) Beekman, P.; Enciso-Martinez, A.; Rho, H. S.; Pujari, S. P.; Lenferink, A.; Zuilhof, H.; Terstappen, L. W. M. M.; Otto, C.; Gac, S. L. Immuno-Capture of Extracellular Vesicles for Individual Multi-Modal Characterization Using AFM, SEM and Raman Spectroscopy. *Lab Chip* **2019**, *19* (15), 2526–2536. https://doi.org/10.1039/C9LC00081J.
(121) Hvidsten, T. R.; Lægreid, A.; Kryshtafovych, A.; Andersson, G.; Fidelis, K.; Komorowski, J. A Comprehensive Analysis of the Structure-Function Relationship in Proteins Based on Local Structure Similarity. *PLOS ONE* **2009**, *4* (7), e6266. https://doi.org/10.1371/journal.pone.0006266.

(122) Lee, D.; Redfern, O.; Orengo, C. Predicting Protein Function from Sequence and Structure. *Nature Reviews Molecular Cell Biology* **2007**, *8* (12), 995–1005. https://doi.org/10.1038/nrm2281.
(123) Thornton, J. M.; Todd, A. E.; Milburn, D.; Borkakoti, N.; Orengo, C. A. From Structure to Function: Approaches and Limitations. *Nature Structural Biology* **2000**, *7* (11), 991–994. https://doi.org/10.1038/80784.
(124) Orengo, C. A.; Todd, A. E.; Thornton, J. M. From Protein Structure to Function. *Current Opinion in Structural Biology* **1999**, *9* (3), 374–382. https://doi.org/10.1016/S0959-440X(99)80051-7.
(125) Ouzounis, C. A.; Coulson, R. M. R.; Enright, A. J.; Kunin, V.; Pereira-Leal, J. B. Classification Schemes for Protein Structure and Function. *Nature Reviews Genetics* **2003**, *4* (7), 508–519. https://doi.org/10.1038/nrg1113.
(126) Hu, Y.-B.; Dammer, E. B.; Ren, R.-J.; Wang, G. The Endosomal-Lysosomal System: From Acidification and Cargo Sorting to Neurodegeneration. *Translational Neurodegeneration* **2015**, *4* (1), 18. https://doi.org/10.1186/s40035-015-0041-1.
(127) Canton, I.; Battaglia, G. Endocytosis at the Nanoscale. *Chem. Soc. Rev.* **2012**, *41* (7), 2718–2739. https://doi.org/10.1039/C2CS15309B.
(128) Smith, S. A.; Selby, L. I.; Johnston, A. P. R.; Such, G. K. The Endosomal Escape of Nanoparticles: Toward More Efficient Cellular Delivery. *Bioconjugate Chem.* **2019**, *30* (2), 263–272. https://doi.org/10.1021/acs.bioconjchem.8b00732.
(129) Repnik, U.; Česen, M. H.; Turk, B. The Endolysosomal System in Cell Death and Survival. *Cold Spring Harb Perspect Biol* **2013**, *5* (1). https://doi.org/10.1101/cshperspect.a008755.
(130) Smith, S. A.; Selby, L. I.; Johnston, A. P. R.; Such, G. K. The Endosomal Escape of Nanoparticles: Toward More Efficient Cellular Delivery. *Bioconjugate Chem.* **2019**, *30* (2), 263–272. https://doi.org/10.1021/acs.bioconjchem.8b00732.
(131) Akita, H.; Kudo, A.; Minoura, A.; Yamaguti, M.; Khalil, I. A.; Moriguchi, R.; Masuda, T.; Danev, R.; Nagayama, K.; Kogure, K.; Harashima, H. Multi-Layered Nanoparticles for Penetrating the Endosome and Nuclear Membrane via a Step-Wise Membrane Fusion Process. *Biomaterials* **2009**, *30* (15), 2940–2949. https://doi.org/10.1016/j.biomaterials.2009.02.009.
(132) Vermeulen, L. M. P.; De Smedt, S. C.; Remaut, K.; Braeckmans, K. The Proton Sponge Hypothesis: Fable or Fact? *European Journal of Pharmaceutics and Biopharmaceutics* **2018**, *129*, 184–190. https://doi.org/10.1016/j.ejpb.2018.05.034.
(133) You, J.-O.; Auguste, D. T. Nanocarrier Cross-Linking Density and PH Sensitivity Regulate Intracellular Gene Transfer. *Nano Lett.* **2009**, *9* (12), 4467–4473. https://doi.org/10.1021/nl902789s.
(134) Selby, L. I.; Cortez-Jugo, C. M.; Such, G. K.; Johnston, A. P. R. Nanoescapology: Progress toward Understanding the Endosomal Escape of Polymeric Nanoparticles. *Wiley Interdisciplinary Reviews: Nanomedicine and Nanobiotechnology* **2017**, *9* (5), e1452. https://doi.org/10.1002/wnan.1452.
(135) Gallon, E.; Matini, T.; Sasso, L.; Mantovani, G.; Armiñan de Benito, A.; Sanchis, J.; Caliceti, P.; Alexander, C.; Vicent, M. J.; Salmaso, S. Triblock Copolymer Nanovesicles for PH-Responsive Targeted Delivery and Controlled Release of SiRNA to Cancer Cells. *Biomacromolecules* **2015**, *16* (7), 1924–1937. https://doi.org/10.1021/acs.biomac.5b00286.

(136) Su, X.; Yang, N.; Wittrup, K. D.; Irvine, D. J. Synergistic Antitumor Activity from Two-Stage Delivery of Targeted Toxins and Endosome-Disrupting Nanoparticles. *Biomacromolecules* **2013**, *14* (4), 1093–1102. https://doi.org/10.1021/bm3019906.
(137) Kono, K.; Torikoshi, Y.; Mitsutomi, M.; Itoh, T.; Emi, N.; Yanagie, H.; Takagishi, T. Novel Gene Delivery Systems: Complexes of Fusigenic Polymer-Modified Liposomes and Lipoplexes. *Gene Ther* **2001**, *8* (1), 5–12. https://doi.org/10.1038/sj.gt.3301365.
(138) Sakaguchi, N.; Kojima, C.; Harada, A.; Kono, K. Preparation of PH-Sensitive Poly(Glycidol) Derivatives with Varying Hydrophobicities: Their Ability to Sensitize Stable Liposomes to PH. *Bioconjugate Chem.* **2008**, *19* (5), 1040–1048. https://doi.org/10.1021/bc7004736.
(139) Pitchaimani, A.; Nguyen, T. D. T.; Wang, H.; Bossmann, S. H.; Aryal, S. Design and Characterization of Gadolinium Infused Theranostic Liposomes. *RSC Adv.* **2016**, *6* (43), 36898–36905. https://doi.org/10.1039/C6RA00552G.
(140) Aryal, S.; Stigliano, C.; Key, J.; Ramirez, M.; Anderson, J.; Karmonik, C.; Fung, S.; Decuzzi, P. Paramagnetic Gd3+ Labeled Red Blood Cells for Magnetic Resonance Angiography. *Biomaterials* **2016**, *98*, 163–170. https://doi.org/10.1016/j.biomaterials.2016.05.002.
(141) Pitchaimani, A.; Nguyen, T. D. T.; Aryal, S. Natural Killer Cell Membrane Infused Biomimetic Liposomes for Targeted Tumor Therapy. *Biomaterials* **2018**, *160*, 124–137. https://doi.org/10.1016/j.biomaterials.2018.01.018.
(142) Haran, G.; Cohen, R.; Bar, L. K.; Barenholz, Y. Transmembrane Ammonium Sulfate Gradients in Liposomes Produce Efficient and Stable Entrapment of Amphipathic Weak Bases. *Biochimica et Biophysica Acta (BBA) - Biomembranes* **1993**, *1151* (2), 201–215. https://doi.org/10.1016/0005-2736(93)90105-9.
(143) Ciapetti, G.; Cenni, E.; Pratelli, L.; Pizzoferrato, A. In Vitro Evaluation of Cell/Biomaterial Interaction by MTT Assay. *Biomaterials* **1993**, *14* (5), 359–364. https://doi.org/10.1016/0142-9612(93)90055-7.
(144) Marasini, R.; Pitchaimani, A.; Thanh Nguyen, T. D.; Comer, J.; Aryal, S. The Influence of Polyethylene Glycol Passivation on the Surface Plasmon Resonance Induced Photothermal Properties of Gold Nanorods. *Nanoscale* **2018**, *10* (28), 13684–13693. https://doi.org/10.1039/C8NR03026J.
(145) Babbey, C. M.; Ahktar, N.; Wang, E.; Chen, C. C.-H.; Grant, B. D.; Dunn, K. W. Rab10 Regulates Membrane Transport through Early Endosomes of Polarized Madin-Darby Canine Kidney Cells. *Mol Biol Cell* **2006**, *17* (7), 3156–3175. https://doi.org/10.1091/mbc.E05-08-0799.
(146) Rayamajhi, S.; Nguyen, T. D. T.; Marasini, R.; Aryal, S. Macrophage-Derived Exosome-Mimetic Hybrid Vesicles for Tumor Targeted Drug Delivery. *Acta Biomaterialia* **2019**, *94*, 482–494. https://doi.org/10.1016/j.actbio.2019.05.054.
(147) Choi, C. H. J.; Alabi, C. A.; Webster, P.; Davis, M. E. Mechanism of Active Targeting in Solid Tumors with Transferrin-Containing Gold Nanoparticles. *PNAS* **2010**, *107* (3), 1235–1240. https://doi.org/10.1073/pnas.0914140107.
(148) Pitchaimani, A.; Nguyen, T. D. T.; Marasini, R.; Eliyapura, A.; Azizi, T.; Jaberi-Douraki, M.; Aryal, S. Biomimetic Natural Killer Membrane Camouflaged Polymeric Nanoparticle for Targeted Bioimaging. *Advanced Functional Materials* **2019**, *29* (4), 1806817. https://doi.org/10.1002/adfm.201806817.

(149) Gao, W.; Chan, J. M.; Farokhzad, O. C. PH-Responsive Nanoparticles for Drug Delivery. *Mol. Pharmaceutics* **2010**, *7* (6), 1913–1920. https://doi.org/10.1021/mp100253e.
(150) Ding, H.; Ma, Y. Controlling Cellular Uptake of Nanoparticles with PH-Sensitive Polymers. *Scientific Reports* **2013**, *3*, 2804. https://doi.org/10.1038/srep02804.
(151) Aryal, S.; Nguyen, T. D. T.; Pitchaimani, A.; Shrestha, T. B.; Biller, D.; Troyer, D. Membrane Fusion-Mediated Gold Nanoplating of Red Blood Cell: A Bioengineered CT-Contrast Agent. *ACS Biomater. Sci. Eng.* **2017**, *3* (1), 36–41. https://doi.org/10.1021/acsbiomaterials.6b00573.
(152) Loura, L. M.; Prieto, M. J. FRET in Membrane Biophysics: An Overview. *Front. Physiol.* **2011**, *2*. https://doi.org/10.3389/fphys.2011.00082.
(153) Pornpattananangkul, D.; Olson, S.; Aryal, S.; Sartor, M.; Huang, C.-M.; Vecchio, K.; Zhang, L. Stimuli-Responsive Liposome Fusion Mediated by Gold Nanoparticles. *ACS Nano* **2010**, *4* (4), 1935–1942. https://doi.org/10.1021/nn9018587.
(154) Ha, T. Single-Molecule Fluorescence Resonance Energy Transfer. *Methods* **2001**, *25* (1), 78–86. https://doi.org/10.1006/meth.2001.1217.
(155) Geisow, M. J.; Evans, W. H. PH in the Endosome: Measurements during Pinocytosis and Receptor-Mediated Endocytosis. *Experimental Cell Research* **1984**, *150* (1), 36–46. https://doi.org/10.1016/0014-4827(84)90699-2.
(156) Paliwal, S. R.; Paliwal, R.; Vyas, S. P. A Review of Mechanistic Insight and Application of PH-Sensitive Liposomes in Drug Delivery. *Drug Delivery* **2015**, *22* (3), 231–242. https://doi.org/10.3109/10717544.2014.882469.
(157) Lee, Y.; Thompson, D. H. Stimuli-Responsive Liposomes for Drug Delivery. *Wiley Interdisciplinary Reviews: Nanomedicine and Nanobiotechnology* **2017**, *9* (5), e1450. https://doi.org/10.1002/wnan.1450.
(158) Asati, A.; Santra, S.; Kaittanis, C.; Perez, J. M. Surface-Charge-Dependent Cell Localization and Cytotoxicity of Cerium Oxide Nanoparticles. *ACS Nano* **2010**, *4* (9), 5321–5331. https://doi.org/10.1021/nn100816s.
(159) Cho, E. C.; Xie, J.; Wurm, P. A.; Xia, Y. Understanding the Role of Surface Charges in Cellular Adsorption versus Internalization by Selectively Removing Gold Nanoparticles on the Cell Surface with a I2/KI Etchant. *Nano Lett.* **2009**, *9* (3), 1080–1084. https://doi.org/10.1021/nl803487r.
(160) Miller, C. R.; Bondurant, B.; McLean, S. D.; McGovern, K. A.; O'Brien, D. F. Liposome−Cell Interactions in Vitro: Effect of Liposome Surface Charge on the Binding and Endocytosis of Conventional and Sterically Stabilized Liposomes. *Biochemistry* **1998**, *37* (37), 12875–12883. https://doi.org/10.1021/bi980096y.
(161) Akinc, A.; Battaglia, G. Exploiting Endocytosis for Nanomedicines. *Cold Spring Harb Perspect Biol* **2013**, *5* (11), a016980. https://doi.org/10.1101/cshperspect.a016980.
(162) Knudsen, K. B.; Northeved, H.; Kumar EK, P.; Permin, A.; Gjetting, T.; Andresen, T. L.; Larsen, S.; Wegener, K. M.; Lykkesfeldt, J.; Jantzen, K.; Loft, S.; Møller, P.; Roursgaard, M. In Vivo Toxicity of Cationic Micelles and Liposomes. *Nanomedicine: Nanotechnology, Biology and Medicine* **2015**, *11* (2), 467–477. https://doi.org/10.1016/j.nano.2014.08.004.
(163) Shah, V.; Taratula, O.; Garbuzenko, O. B.; Patil, M. L.; Savla, R.; Minko, M. Z. and T. Genotoxicity of Different Nanocarriers: Possible Modifications for the Delivery of Nucleic Acids http://www.eurekaselect.com/106870/article (accessed Nov 1, 2019).

(164) Bareford, L. M.; Swaan, P. W. Endocytic Mechanisms for Targeted Drug Delivery. *Advanced Drug Delivery Reviews* **2007**, *59* (8), 748–758. https://doi.org/10.1016/j.addr.2007.06.008.
(165) Degors, I. M. S.; Wang, C.; Rehman, Z. U.; Zuhorn, I. S. Carriers Break Barriers in Drug Delivery: Endocytosis and Endosomal Escape of Gene Delivery Vectors. *Acc. Chem. Res.* **2019**, *52* (7), 1750–1760. https://doi.org/10.1021/acs.accounts.9b00177.
(166) Rosenblum, D.; Joshi, N.; Tao, W.; Karp, J. M.; Peer, D. Progress and Challenges towards Targeted Delivery of Cancer Therapeutics. *Nat Commun* **2018**, *9* (1), 1–12. https://doi.org/10.1038/s41467-018-03705-y.
(167) Schindelin, J.; Arganda-Carreras, I.; Frise, E.; Kaynig, V.; Longair, M.; Pietzsch, T.; Preibisch, S.; Rueden, C.; Saalfeld, S.; Schmid, B.; Tinevez, J.-Y.; White, D. J.; Hartenstein, V.; Eliceiri, K.; Tomancak, P.; Cardona, A. Fiji: An Open-Source Platform for Biological-Image Analysis. *Nat Methods* **2012**, *9* (7), 676–682. https://doi.org/10.1038/nmeth.2019.
(168) Coloc 2 https://imagej.net/Coloc_2 (accessed Nov 7, 2019).
(169) Dunn, K. W.; Kamocka, M. M.; McDonald, J. H. A Practical Guide to Evaluating Colocalization in Biological Microscopy. *American Journal of Physiology-Cell Physiology* **2011**, *300* (4), C723–C742. https://doi.org/10.1152/ajpcell.00462.2010.
(170) Huotari, J.; Helenius, A. Endosome Maturation. *EMBO J.* **2011**, *30* (17), 3481–3500. https://doi.org/10.1038/emboj.2011.286.
(171) Varkouhi, A. K.; Scholte, M.; Storm, G.; Haisma, H. J. Endosomal Escape Pathways for Delivery of Biologicals. *Journal of Controlled Release* **2011**, *151* (3), 220–228. https://doi.org/10.1016/j.jconrel.2010.11.004.
(172) White, J. M.; Whittaker, G. R. Fusion of Enveloped Viruses in Endosomes. *Traffic* **2016**, *17* (6), 593–614. https://doi.org/10.1111/tra.12389.
(173) Cho, Y. W.; Kim, J.-D.; Park, K. Polycation Gene Delivery Systems: Escape from Endosomes to Cytosol. *Journal of Pharmacy and Pharmacology* **2003**, *55* (6), 721–734. https://doi.org/10.1211/002235703765951311.
(174) Abels, E. R.; Breakefield, X. O. Introduction to Extracellular Vesicles: Biogenesis, RNA Cargo Selection, Content, Release, and Uptake. *Cell. Mol. Neurobiol.* **2016**, *36* (3), 301–312. https://doi.org/10.1007/s10571-016-0366-z.
(175) Maas, S. L. N.; Breakefield, X. O.; Weaver, A. M. Extracellular Vesicles: Unique Intercellular Delivery Vehicles. *Trends in Cell Biology* **2017**, *27* (3), 172–188. https://doi.org/10.1016/j.tcb.2016.11.003.
(176) Bunggulawa, E. J.; Wang, W.; Yin, T.; Wang, N.; Durkan, C.; Wang, Y.; Wang, G. Recent Advancements in the Use of Exosomes as Drug Delivery Systems. *Journal of Nanobiotechnology* **2018**, *16* (1), 81. https://doi.org/10.1186/s12951-018-0403-9.
(177) Minimal information for studies of extracellular vesicles 2018 (MISEV2018): a position statement of the International Society for Extracellular Vesicles and update of the MISEV2014 guidelines: Journal of Extracellular Vesicles: Vol 7, No 1 https://www.tandfonline.com/doi/full/10.1080/20013078.2018.1535750 (accessed Jan 8, 2019).
(178) He, C.; Zheng, S.; Luo, Y.; Wang, B. Exosome Theranostics: Biology and Translational Medicine. *Theranostics* **2018**, *8* (1), 237–255. https://doi.org/10.7150/thno.21945.
(179) Kim, M. S.; Haney, M. J.; Zhao, Y.; Mahajan, V.; Deygen, I.; Klyachko, N. L.; Inskoe, E.; Piroyan, A.; Sokolsky, M.; Okolie, O.; Hingtgen, S. D.; Kabanov, A. V.; Batrakova,

E. V. Development of Exosome-Encapsulated Paclitaxel to Overcome MDR in Cancer Cells. *Nanomedicine* **2016**, *12* (3), 655–664. https://doi.org/10.1016/j.nano.2015.10.012.
(180) Saari, H.; Lázaro-Ibáñez, E.; Viitala, T.; Vuorimaa-Laukkanen, E.; Siljander, P.; Yliperttula, M. Microvesicle- and Exosome-Mediated Drug Delivery Enhances the Cytotoxicity of Paclitaxel in Autologous Prostate Cancer Cells. *J Control Release* **2015**, *220* (Pt B), 727–737. https://doi.org/10.1016/j.jconrel.2015.09.031.
(181) Bhatnagar, S.; Shinagawa, K.; Castellino, F. J.; Schorey, J. S. Exosomes Released from Macrophages Infected with Intracellular Pathogens Stimulate a Proinflammatory Response in Vitro and in Vivo. *Blood* **2007**, *110* (9), 3234–3244. https://doi.org/10.1182/blood-2007-03-079152.
(182) Clayton, A.; Turkes, A.; Navabi, H.; Mason, M. D.; Tabi, Z. Induction of Heat Shock Proteins in B-Cell Exosomes. *J. Cell. Sci.* **2005**, *118* (Pt 16), 3631–3638. https://doi.org/10.1242/jcs.02494.
(183) Nolte-'t Hoen, E. N. M.; Buschow, S. I.; Anderton, S. M.; Stoorvogel, W.; Wauben, M. H. M. Activated T Cells Recruit Exosomes Secreted by Dendritic Cells via LFA-1. *Blood* **2009**, *113* (9), 1977–1981. https://doi.org/10.1182/blood-2008-08-174094.
(184) Lai, R. C.; Yeo, R. W. Y.; Lim, S. K. Mesenchymal Stem Cell Exosomes. *Semin. Cell Dev. Biol.* **2015**, *40*, 82–88. https://doi.org/10.1016/j.semcdb.2015.03.001.
(185) Song, J.; Chen, X.; Wang, M.; Xing, Y.; Zheng, Z.; Hu, S. Cardiac Endothelial Cell-Derived Exosomes Induce Specific Regulatory B Cells. *Sci Rep* **2014**, *4*. https://doi.org/10.1038/srep07583.
(186) Skogberg, G.; Lundberg, V.; Berglund, M.; Gudmundsdottir, J.; Telemo, E.; Lindgren, S.; Ekwall, O. Human Thymic Epithelial Primary Cells Produce Exosomes Carrying Tissue-Restricted Antigens. *Immunol Cell Biol* **2015**, *93* (8), 727–734. https://doi.org/10.1038/icb.2015.33.
(187) Benito-Martin, A.; Di Giannatale, A.; Ceder, S.; Peinado, H. The New Deal: A Potential Role for Secreted Vesicles in Innate Immunity and Tumor Progression. *Front Immunol* **2015**, *6*, 66. https://doi.org/10.3389/fimmu.2015.00066.
(188) Mathivanan, S.; Ji, H.; Simpson, R. J. Exosomes: Extracellular Organelles Important in Intercellular Communication. *Journal of Proteomics* **2010**, *73* (10), 1907–1920. https://doi.org/10.1016/j.jprot.2010.06.006.
(189) Kobayashi, M.; Rice, G. E.; Tapia, J.; Mitchell, M. D.; Salomon, C. Exosomes are fingerprints of originating cells: potential biomarkers for ovarian cancer https://www.dovepress.com/exosomes-are-fingerprints-of-originating-cells-potential-biomarkers-fo-peer-reviewed-fulltext-article-RRBC (accessed Dec 22, 2018). https://doi.org/10.2147/RRBC.S58281.
(190) Kanninen, K. M.; Bister, N.; Koistinaho, J.; Malm, T. Exosomes as New Diagnostic Tools in CNS Diseases. *Biochimica et Biophysica Acta (BBA) - Molecular Basis of Disease* **2016**, *1862* (3), 403–410. https://doi.org/10.1016/j.bbadis.2015.09.020.
(191) Kim, M. S.; Haney, M. J.; Zhao, Y.; Yuan, D.; Deygen, I.; Klyachko, N. L.; Kabanov, A. V.; Batrakova, E. V. Engineering Macrophage-Derived Exosomes for Targeted Paclitaxel Delivery to Pulmonary Metastases: In Vitro and in Vivo Evaluations. *Nanomedicine: Nanotechnology, Biology and Medicine* **2018**, *14* (1), 195–204. https://doi.org/10.1016/j.nano.2017.09.011.

(192) Batrakova, E. V.; Kim, M. S. Development and Regulation of Exosome-Based Therapy Products. *Wiley Interdiscip Rev Nanomed Nanobiotechnol* **2016**, *8* (5), 744–757. https://doi.org/10.1002/wnan.1395.
(193) Haney, M. J.; Klyachko, N. L.; Zhao, Y.; Gupta, R.; Plotnikova, E. G.; He, Z.; Patel, T.; Piroyan, A.; Sokolsky, M.; Kabanov, A. V.; Batrakova, E. V. Exosomes as Drug Delivery Vehicles for Parkinson's Disease Therapy. *J Control Release* **2015**, *207*, 18–30. https://doi.org/10.1016/j.jconrel.2015.03.033.
(194) Yuan, D.; Zhao, Y.; Banks, W. A.; Bullock, K. M.; Haney, M.; Batrakova, E.; Kabanov, A. V. Macrophage Exosomes as Natural Nanocarriers for Protein Delivery to Inflamed Brain. *Biomaterials* **2017**, *142*, 1–12. https://doi.org/10.1016/j.biomaterials.2017.07.011.
(195) Batrakova, E. V.; Kim, M. S. Using Exosomes, Naturally-Equipped Nanocarriers, for Drug Delivery. *J Control Release* **2015**, *219*, 396–405. https://doi.org/10.1016/j.jconrel.2015.07.030.
(196) Haney, M. J.; Klyachko, N. L.; Zhao, Y.; Kabanov, A. V.; Batrakova, E. V. P22 - Extracellular Vesicles as Drug Delivery Vehicles for Potent Redox Enzyme Catalase to Treat Parkinson's Disease. *Free Radical Biology and Medicine* **2018**, *128*, S18. https://doi.org/10.1016/j.freeradbiomed.2018.10.396.
(197) Hao, S.; Bai, O.; Yuan, J.; Qureshi, M.; Xiang, J. Dendritic Cell-Derived Exosomes Stimulate Stronger CD8+ CTL Responses and Antitumor Immunity than Tumor Cell-Derived Exosomes. *Cell. Mol. Immunol.* **2006**, *3* (3), 205–211.
(198) Lynch, S.; Santos, S. G.; Campbell, E. C.; Nimmo, A. M. S.; Botting, C.; Prescott, A.; Antoniou, A. N.; Powis, S. J. Novel MHC Class I Structures on Exosomes. *J. Immunol.* **2009**, *183* (3), 1884–1891. https://doi.org/10.4049/jimmunol.0900798.
(199) Segura, E.; Amigorena, S.; Théry, C. Mature Dendritic Cells Secrete Exosomes with Strong Ability to Induce Antigen-Specific Effector Immune Responses. *Blood Cells Mol. Dis.* **2005**, *35* (2), 89–93. https://doi.org/10.1016/j.bcmd.2005.05.003.
(200) van Dommelen, S. M.; Vader, P.; Lakhal, S.; Kooijmans, S. A. A.; van Solinge, W. W.; Wood, M. J. A.; Schiffelers, R. M. Microvesicles and Exosomes: Opportunities for Cell-Derived Membrane Vesicles in Drug Delivery. *Journal of Controlled Release* **2012**, *161* (2), 635–644. https://doi.org/10.1016/j.jconrel.2011.11.021.
(201) Tan, S.; Wu, T.; Zhang, D.; Zhang, Z. Cell or Cell Membrane-Based Drug Delivery Systems. *Theranostics* **2015**, *5* (8), 863–881. https://doi.org/10.7150/thno.11852.
(202) Li, P.; Kaslan, M.; Lee, S. H.; Yao, J.; Gao, Z. Progress in Exosome Isolation Techniques. *Theranostics* **2017**, *7* (3), 789–804. https://doi.org/10.7150/thno.18133.
(203) Piffoux, M.; Silva, A. K. A.; Wilhelm, C.; Gazeau, F.; Tareste, D. Modification of Extracellular Vesicles by Fusion with Liposomes for the Design of Personalized Biogenic Drug Delivery Systems. *ACS Nano* **2018**, *12* (7), 6830–6842. https://doi.org/10.1021/acsnano.8b02053.
(204) Lin, Y.; Wu, J.; Gu, W.; Huang, Y.; Tong, Z.; Huang, L.; Tan, J. Exosome–Liposome Hybrid Nanoparticles Deliver CRISPR/Cas9 System in MSCs. *Advanced Science* **2018**, *5* (4), 1700611. https://doi.org/10.1002/advs.201700611.
(205) Zarovni, N.; Corrado, A.; Guazzi, P.; Zocco, D.; Lari, E.; Radano, G.; Muhhina, J.; Fondelli, C.; Gavrilova, J.; Chiesi, A. Integrated Isolation and Quantitative Analysis of Exosome Shuttled Proteins and Nucleic Acids Using Immunocapture Approaches. *Methods* **2015**, *87*, 46–58. https://doi.org/10.1016/j.ymeth.2015.05.028.

(206) Heinemann, M. L.; Ilmer, M.; Silva, L. P.; Hawke, D. H.; Recio, A.; Vorontsova, M. A.; Alt, E.; Vykoukal, J. Benchtop Isolation and Characterization of Functional Exosomes by Sequential Filtration. *Journal of Chromatography A* **2014**, *1371*, 125–135. https://doi.org/10.1016/j.chroma.2014.10.026.
(207) Engineering hybrid exosomes by membrane fusion with liposomes | Scientific Reports https://www.nature.com/articles/srep21933 (accessed Dec 19, 2018).
(208) Li, Y.; Lu, A.; Long, M.; Cui, L.; Chen, Z.; Zhu, L. Nitroimidazole Derivative Incorporated Liposomes for Hypoxia-Triggered Drug Delivery and Enhanced Therapeutic Efficacy in Patient-Derived Tumor Xenografts. *Acta Biomaterialia* **2019**, *83*, 334–348. https://doi.org/10.1016/j.actbio.2018.10.029.
(209) O'Neill, H. S.; Herron, C. C.; Hastings, C. L.; Deckers, R.; Lopez Noriega, A.; Kelly, H. M.; Hennink, W. E.; McDonnell, C. O.; O'Brien, F. J.; Ruiz-Hernández, E.; Duffy, G. P. A Stimuli Responsive Liposome Loaded Hydrogel Provides Flexible On-Demand Release of Therapeutic Agents. *Acta Biomaterialia* **2017**, *48*, 110–119. https://doi.org/10.1016/j.actbio.2016.10.001.
(210) Jadus, M. R.; Irwin, M. C.; Irwin, M. R.; Horansky, R. D.; Sekhon, S.; Pepper, K. A.; Kohn, D. B.; Wepsic, H. T. Macrophages Can Recognize and Kill Tumor Cells Bearing the Membrane Isoform of Macrophage Colony-Stimulating Factor. *Blood* **1996**, *87* (12), 5232–5241.
(211) Lewis, C. E.; Pollard, J. W. Distinct Role of Macrophages in Different Tumor Microenvironments. *Cancer Res.* **2006**, *66* (2), 605–612. https://doi.org/10.1158/0008-5472.CAN-05-4005.
(212) Kruger, N. J. The Bradford Method for Protein Quantitation. In *The Protein Protocols Handbook*; Walker, J. M., Ed.; Humana Press: Totowa, NJ, 2002; pp 15–21. https://doi.org/10.1385/1-59259-169-8:15.
(213) Petrotchenko, E. V.; Serpa, J. J.; Hardie, D. B.; Berjanskii, M.; Suriyamongkol, B. P.; Wishart, D. S.; Borchers, C. H. Use of Proteinase K Non-Specific Digestion for Selective and Comprehensive Identification of Interpeptide Crosslinks: Application to Prion Proteins. *Molecular & Cellular Proteomics* **2012**, mcp.M111.013524. https://doi.org/10.1074/mcp.M111.013524.
(214) Aryal, S.; Nguyen, T. D. T.; Pitchaimani, A.; Shrestha, T. B.; Biller, D.; Troyer, D. Membrane Fusion-Mediated Gold Nanoplating of Red Blood Cell: A Bioengineered CT-Contrast Agent. *ACS Biomater. Sci. Eng.* **2017**, *3* (1), 36–41. https://doi.org/10.1021/acsbiomaterials.6b00573.
(215) Marasini, R.; Pitchaimani, A.; Nguyen, T. D. T.; Comer, J.; Aryal, S. The Influence of Polyethylene Glycol Passivation on the Surface Plasmon Resonance Induced Photothermal Properties of Gold Nanorods. *Nanoscale* **2018**, *10* (28), 13684–13693. https://doi.org/10.1039/C8NR03026J.
(216) Pornpattananangkul, D.; Olson, S.; Aryal, S.; Sartor, M.; Huang, C.-M.; Vecchio, K.; Zhang, L. Stimuli-Responsive Liposome Fusion Mediated by Gold Nanoparticles. *ACS Nano* **2010**, *4* (4), 1935–1942. https://doi.org/10.1021/nn9018587.
(217) Nguyen, T. D. T.; Pitchaimani, A.; Bahadur Koirala, M.; Muhammad, F.; Aryal, S. Engineered Biomimetic Nanoabsorbent for Cellular Detoxification of Chemotherapeutics. *RSC Advances* **2016**, *6* (39), 33003–33008. https://doi.org/10.1039/C6RA02026G.

(218) Hu, C.-M. J.; Zhang, L.; Aryal, S.; Cheung, C.; Fang, R. H.; Zhang, L. Erythrocyte Membrane-Camouflaged Polymeric Nanoparticles as a Biomimetic Delivery Platform. *PNAS* **2011**, *108* (27), 10980–10985. https://doi.org/10.1073/pnas.1106634108.
(219) Muller, L.; Mitsuhashi, M.; Simms, P.; Gooding, W. E.; Whiteside, T. L. Tumor-Derived Exosomes Regulate Expression of Immune Function-Related Genes in Human T Cell Subsets. *Scientific Reports* **2016**, *6*, 20254. https://doi.org/10.1038/srep20254.
(220) Guerreiro, E. M.; Vestad, B.; Steffensen, L. A.; Aass, H. C. D.; Saeed, M.; Øvstebø, R.; Costea, D. E.; Galtung, H. K.; Søland, T. M. Efficient Extracellular Vesicle Isolation by Combining Cell Media Modifications, Ultrafiltration, and Size-Exclusion Chromatography. *PLOS ONE* **2018**, *13* (9), e0204276. https://doi.org/10.1371/journal.pone.0204276.
(221) Eirin, A.; Zhu, X.-Y.; Puranik, A. S.; Woollard, J. R.; Tang, H.; Dasari, S.; Lerman, A.; van Wijnen, A. J.; Lerman, L. O. Comparative Proteomic Analysis of Extracellular Vesicles Isolated from Porcine Adipose Tissue-Derived Mesenchymal Stem/Stromal Cells. *Scientific Reports* **2016**, *6*, 36120. https://doi.org/10.1038/srep36120.
(222) Aryal, S.; Hu, C.-M. J.; Zhang, L. Synthesis of Ptsome: A Platinum-Based Liposome-like Nanostructure. *Chem. Commun.* **2012**, *48* (20), 2630–2632. https://doi.org/10.1039/C2CC18176B.
(223) Schey, K. L.; Luther, J. M.; Rose, K. L. Proteomics Characterization of Exosome Cargo. *Methods* **2015**, *87*, 75–82. https://doi.org/10.1016/j.ymeth.2015.03.018.
(224) Kim, D.; Kim, T. H.; Wu, G.; Park, B. K.; Ha, J.-H.; Kim, Y.-S.; Lee, K.; Lee, Y.; Kwon, H.-J. Extracellular Release of CD11b by TLR9 Stimulation in Macrophages. *PLOS ONE* **2016**, *11* (3), e0150677. https://doi.org/10.1371/journal.pone.0150677.
(225) Kato, Y.; Ozawa, S.; Miyamoto, C.; Maehata, Y.; Suzuki, A.; Maeda, T.; Baba, Y. Acidic Extracellular Microenvironment and Cancer. *Cancer Cell Int* **2013**, *13*, 89. https://doi.org/10.1186/1475-2867-13-89.
(226) Shamsi, M.; Saghafian, M.; Dejam, M.; Sanati-Nezhad, A. Mathematical Modeling of the Function of Warburg Effect in Tumor Microenvironment. *Scientific Reports* **2018**, *8* (1), 8903. https://doi.org/10.1038/s41598-018-27303-6.
(227) Corbet, C.; Feron, O. Tumour Acidosis: From the Passenger to the Driver's Seat. *Nature Reviews Cancer* **2017**, *17* (10), 577–593. https://doi.org/10.1038/nrc.2017.77.
(228) Tugues, S.; Honjo, S.; König, C.; Padhan, N.; Kroon, J.; Gualandi, L.; Li, X.; Barkefors, I.; Thijssen, V. L.; Griffioen, A. W.; Claesson-Welsh, L. Tetraspanin CD63 Promotes Vascular Endothelial Growth Factor Receptor 2-B1 Integrin Complex Formation, Thereby Regulating Activation and Downstream Signaling in Endothelial Cells in Vitro and in Vivo. *J. Biol. Chem.* **2013**, *288* (26), 19060–19071. https://doi.org/10.1074/jbc.M113.468199.
(229) Théry, C.; Ostrowski, M.; Segura, E. Membrane Vesicles as Conveyors of Immune Responses. *Nat. Rev. Immunol.* **2009**, *9* (8), 581–593. https://doi.org/10.1038/nri2567.
(230) Escrevente, C.; Keller, S.; Altevogt, P.; Costa, J. Interaction and Uptake of Exosomes by Ovarian Cancer Cells. *BMC Cancer* **2011**, *11* (1), 108. https://doi.org/10.1186/1471-2407-11-108.
(231) KC, B.; Paudel, S. N.; Rayamajhi, S.; Karna, D.; Adhikari, S.; Shrestha, B. G.; Bisht, G. Enhanced Preferential Cytotoxicity through Surface Modification: Synthesis, Characterization and Comparative in Vitro Evaluation of TritonX-100 Modified and

Unmodified Zinc Oxide Nanoparticles in Human Breast Cancer Cell (MDA-MB-231). *Chemistry Central Journal* **2016**, *10* (1), 16. https://doi.org/10.1186/s13065-016-0162-3.
(232) Anderson, J. L.; Park, A.; Akiyama, R.; Tap, W. D.; Denny, C. T.; Federman, N. Evaluation of In Vitro Activity of the Class I PI3K Inhibitor Buparlisib (BKM120) in Pediatric Bone and Soft Tissue Sarcomas. *PLoS ONE* **2015**, *10* (9), e0133610. https://doi.org/10.1371/journal.pone.0133610.
(233) Bisht, G.; Rayamajhi, S.; KC, B.; Paudel, S. N.; Karna, D.; Shrestha, B. G. Synthesis, Characterization, and Study of In Vitro Cytotoxicity of ZnO-Fe3O4 Magnetic Composite Nanoparticles in Human Breast Cancer Cell Line (MDA-MB-231) and Mouse Fibroblast (NIH 3T3). *Nanoscale Research Letters* **2016**, *11* (1), 537. https://doi.org/10.1186/s11671-016-1734-9.
(234) Kampen, K. R. Membrane Proteins: The Key Players of a Cancer Cell. *J Membrane Biol* **2011**, *242* (2), 69–74. https://doi.org/10.1007/s00232-011-9381-7.
(235) Bae, S.; Brumbaugh, J.; Bonavida, B. Exosomes Derived from Cancerous and Non-Cancerous Cells Regulate the Anti-Tumor Response in the Tumor Microenvironment. *Genes Cancer* **2018**, *9* (3–4), 87–100. https://doi.org/10.18632/genesandcancer.172.
(236) Mantovani, A.; Schioppa, T.; Porta, C.; Allavena, P.; Sica, A. Role of Tumor-Associated Macrophages in Tumor Progression and Invasion. *Cancer Metastasis Rev* **2006**, *25* (3), 315–322. https://doi.org/10.1007/s10555-006-9001-7.
(237) Wahsner, J.; Gale, E. M.; Rodríguez-Rodríguez, A.; Caravan, P. Chemistry of MRI Contrast Agents: Current Challenges and New Frontiers. *Chem. Rev.* **2019**, *119* (2), 957–1057. https://doi.org/10.1021/acs.chemrev.8b00363.
(238) Aime, S.; Caravan, P. Biodistribution of Gadolinium-Based Contrast Agents, Including Gadolinium Deposition. *Journal of Magnetic Resonance Imaging* **2009**, *30* (6), 1259–1267. https://doi.org/10.1002/jmri.21969.
(239) Runge, V. M.; Dickey, K. M.; Williams, N. M.; Peng, X. Local Tissue Toxicity in Response to Extravascular Extravasation of Magnetic Resonance Contrast Media. *Investigative Radiology* **2002**, *37* (7), 393.
(240) Naseri, N.; Ajorlou, E.; Asghari, F.; Pilehvar-Soltanahmadi, Y. An Update on Nanoparticle-Based Contrast Agents in Medical Imaging. *Artificial Cells, Nanomedicine, and Biotechnology* **2018**, *46* (6), 1111–1121. https://doi.org/10.1080/21691401.2017.1379014.
(241) Marangoni, V. S.; Neumann, O.; Henderson, L.; Kaffes, C. C.; Zhang, H.; Zhang, R.; Bishnoi, S.; Ayala-Orozco, C.; Zucolotto, V.; Bankson, J. A.; Nordlander, P.; Halas, N. J. Enhancing T1 Magnetic Resonance Imaging Contrast with Internalized Gadolinium(III) in a Multilayer Nanoparticle. *PNAS* **2017**, *114* (27), 6960–6965. https://doi.org/10.1073/pnas.1701944114.
(242) Aryal, S.; Stigliano, C.; Key, J.; Ramirez, M.; Anderson, J.; Karmonik, C.; Fung, S.; Decuzzi, P. Paramagnetic Gd3+ Labeled Red Blood Cells for Magnetic Resonance Angiography. *Biomaterials* **2016**, *98*, 163–170. https://doi.org/10.1016/j.biomaterials.2016.05.002.
(243) Marasini, R.; Nguyen, T. D. T.; Aryal, S. Integration of Gadolinium in Nanostructure for Contrast Enhanced-Magnetic Resonance Imaging. *WIREs Nanomedicine and Nanobiotechnology n/a* (n/a), e1580. https://doi.org/10.1002/wnan.1580.

(244) Maas, S. L. N.; Breakefield, X. O.; Weaver, A. M. Extracellular Vesicles: Unique Intercellular Delivery Vehicles. *Trends in Cell Biology* **2017**, *27* (3), 172–188. https://doi.org/10.1016/j.tcb.2016.11.003.

(245) Théry, C.; Witwer, K. W.; Aikawa, E.; Alcaraz, M. J.; Anderson, J. D.; Andriantsitohaina, R.; Antoniou, A.; Arab, T.; Archer, F.; Atkin-Smith, G. K.; Ayre, D. C.; Bach, J.-M.; Bachurski, D.; Baharvand, H.; Balaj, L.; Baldacchino, S.; Bauer, N. N.; Baxter, A. A.; Bebawy, M.; Beckham, C.; Zavec, A. B.; Benmoussa, A.; Berardi, A. C.; Bergese, P.; Bielska, E.; Blenkiron, C.; Bobis-Wozowicz, S.; Boilard, E.; Boireau, W.; Bongiovanni, A.; Borràs, F. E.; Bosch, S.; Boulanger, C. M.; Breakefield, X.; Breglio, A. M.; Brennan, M. Á.; Brigstock, D. R.; Brisson, A.; Broekman, M. L.; Bromberg, J. F.; Bryl-Górecka, P.; Buch, S.; Buck, A. H.; Burger, D.; Busatto, S.; Buschmann, D.; Bussolati, B.; Buzás, E. I.; Byrd, J. B.; Camussi, G.; Carter, D. R.; Caruso, S.; Chamley, L. W.; Chang, Y.-T.; Chen, C.; Chen, S.; Cheng, L.; Chin, A. R.; Clayton, A.; Clerici, S. P.; Cocks, A.; Cocucci, E.; Coffey, R. J.; Cordeiro-da-Silva, A.; Couch, Y.; Coumans, F. A.; Coyle, B.; Crescitelli, R.; Criado, M. F.; D'Souza-Schorey, C.; Das, S.; Chaudhuri, A. D.; Candia, P. de; Junior, E. F. D. S.; Wever, O. D.; Portillo, H. A. del; Demaret, T.; Deville, S.; Devitt, A.; Dhondt, B.; Vizio, D. D.; Dieterich, L. C.; Dolo, V.; Rubio, A. P. D.; Dominici, M.; Dourado, M. R.; Driedonks, T. A.; Duarte, F. V.; Duncan, H. M.; Eichenberger, R. M.; Ekström, K.; Andaloussi, S. E.; Elie-Caille, C.; Erdbrügger, U.; Falcón-Pérez, J. M.; Fatima, F.; Fish, J. E.; Flores-Bellver, M.; Försönits, A.; Frelet-Barrand, A.; Fricke, F.; Fuhrmann, G.; Gabrielsson, S.; Gámez-Valero, A.; Gardiner, C.; Gärtner, K.; Gaudin, R.; Gho, Y. S.; Giebel, B.; Gilbert, C.; Gimona, M.; Giusti, I.; Goberdhan, D. C.; Görgens, A.; Gorski, S. M.; Greening, D. W.; Gross, J. C.; Gualerzi, A.; Gupta, G. N.; Gustafson, D.; Handberg, A.; Haraszti, R. A.; Harrison, P.; Hegyesi, H.; Hendrix, A.; Hill, A. F.; Hochberg, F. H.; Hoffmann, K. F.; Holder, B.; Holthofer, H.; Hosseinkhani, B.; Hu, G.; Huang, Y.; Huber, V.; Hunt, S.; Ibrahim, A. G.-E.; Ikezu, T.; Inal, J. M.; Isin, M.; Ivanova, A.; Jackson, H. K.; Jacobsen, S.; Jay, S. M.; Jayachandran, M.; Jenster, G.; Jiang, L.; Johnson, S. M.; Jones, J. C.; Jong, A.; Jovanovic-Talisman, T.; Jung, S.; Kalluri, R.; Kano, S.; Kaur, S.; Kawamura, Y.; Keller, E. T.; Khamari, D.; Khomyakova, E.; Khvorova, A.; Kierulf, P.; Kim, K. P.; Kislinger, T.; Klingeborn, M.; II, D. J. K.; Kornek, M.; Kosanović, M. M.; Kovács, Á. F.; Krämer-Albers, E.-M.; Krasemann, S.; Krause, M.; Kurochkin, I. V.; Kusuma, G. D.; Kuypers, S.; Laitinen, S.; Langevin, S. M.; Languino, L. R.; Lannigan, J.; Lässer, C.; Laurent, L. C.; Lavieu, G.; Lázaro-Ibáñez, E.; Lay, S. L.; Lee, M.-S.; Lee, Y. X. F.; Lemos, D. S.; Lenassi, M.; Leszczynska, A.; Li, I. T.; Liao, K.; Libregts, S. F.; Ligeti, E.; Lim, R.; Lim, S. K.; Linē, A.; Linnemannstöns, K.; Llorente, A.; Lombard, C. A.; Lorenowicz, M. J.; Lörincz, Á. M.; Lötvall, J.; Lovett, J.; Lowry, M. C.; Loyer, X.; Lu, Q.; Lukomska, B.; Lunavat, T. R.; Maas, S. L.; Malhi, H.; Marcilla, A.; Mariani, J.; Mariscal, J.; Martens-Uzunova, E. S.; Martin-Jaular, L.; Martinez, M. C.; Martins, V. R.; Mathieu, M.; Mathivanan, S.; Maugeri, M.; McGinnis, L. K.; McVey, M. J.; Jr, D. G. M.; Meehan, K. L.; Mertens, I.; Minciacchi, V. R.; Möller, A.; Jørgensen, M. M.; Morales-Kastresana, A.; Morhayim, J.; Mullier, F.; Muraca, M.; Musante, L.; Mussack, V.; Muth, D. C.; Myburgh, K. H.; Najrana, T.; Nawaz, M.; Nazarenko, I.; Nejsum, P.; Neri, C.; Neri, T.; Nieuwland, R.; Nimrichter, L.; Nolan, J. P.; Hoen, E. N. N.-'t; Hooten, N. N.; O'Driscoll, L.; O'Grady, T.; O'Loghlen, A.; Ochiya, T.; Olivier, M.; Ortiz, A.; Ortiz, L. A.; Osteikoetxea, X.; Østergaard, O.; Ostrowski, M.; Park, J.; Pegtel, D. M.; Peinado, H.;

Perut, F.; Pfaffl, M. W.; Phinney, D. G.; Pieters, B. C.; Pink, R. C.; Pisetsky, D. S.; Strandmann, E. P. von; Polakovicova, I.; Poon, I. K.; Powell, B. H.; Prada, I.; Pulliam, L.; Quesenberry, P.; Radeghieri, A.; Raffai, R. L.; Raimondo, S.; Rak, J.; Ramirez, M. I.; Raposo, G.; Rayyan, M. S.; Regev-Rudzki, N.; Ricklefs, F. L.; Robbins, P. D.; Roberts, D. D.; Rodrigues, S. C.; Rohde, E.; Rome, S.; Rouschop, K. M.; Rughetti, A.; Russell, A. E.; Saá, P.; Sahoo, S.; Salas-Huenuleo, E.; Sánchez, C.; Saugstad, J. A.; Saul, M. J.; Schiffelers, R. M.; Schneider, R.; Schøyen, T. H.; Scott, A.; Shahaj, E.; Sharma, S.; Shatnyeva, O.; Shekari, F.; Shelke, G. V.; Shetty, A. K.; Shiba, K.; Siljander, P. R.-M.; Silva, A. M.; Skowronek, A.; II, O. L. S.; Soares, R. P.; Sódar, B. W.; Soekmadji, C.; Sotillo, J.; Stahl, P. D.; Stoorvogel, W.; Stott, S. L.; Strasser, E. F.; Swift, S.; Tahara, H.; Tewari, M.; Timms, K.; Tiwari, S.; Tixeira, R.; Tkach, M.; Toh, W. S.; Tomasini, R.; Torrecilhas, A. C.; Tosar, J. P.; Toxavidis, V.; Urbanelli, L.; Vader, P.; Balkom, B. W. van; Grein, S. G. van der; Deun, J. V.; Herwijnen, M. J. van; Keuren-Jensen, K. V.; Niel, G. van; Royen, M. E. van; Wijnen, A. J. van; Vasconcelos, M. H.; Jr, I. J. V.; Veit, T. D.; Vella, L. J.; Velot, É.; Verweij, F. J.; Vestad, B.; Viñas, J. L.; Visnovitz, T.; Vukman, K. V.; Wahlgren, J.; Watson, D. C.; Wauben, M. H.; Weaver, A.; Webber, J. P.; Weber, V.; Wehman, A. M.; Weiss, D. J.; Welsh, J. A.; Wendt, S.; Wheelock, A. M.; Wiener, Z.; Witte, L.; Wolfram, J.; Xagorari, A.; Xander, P.; Xu, J.; Yan, X.; Yáñez-Mó, M.; Yin, H.; Yuana, Y.; Zappulli, V.; Zarubova, J.; Žėkas, V.; Zhang, J.; Zhao, Z.; Zheng, L.; Zheutlin, A. R.; Zickler, A. M.; Zimmermann, P.; Zivkovic, A. M.; Zocco, D.; Zuba-Surma, E. K. Minimal Information for Studies of Extracellular Vesicles 2018 (MISEV2018): A Position Statement of the International Society for Extracellular Vesicles and Update of the MISEV2014 Guidelines. *Journal of Extracellular Vesicles* **2018**, *7* (1), 1535750. https://doi.org/10.1080/20013078.2018.1535750.

(246) Sancho-Albero, M.; Navascués, N.; Mendoza, G.; Sebastián, V.; Arruebo, M.; Martín-Duque, P.; Santamaría, J. Exosome Origin Determines Cell Targeting and the Transfer of Therapeutic Nanoparticles towards Target Cells. *Journal of Nanobiotechnology* **2019**, *17* (1), 16. https://doi.org/10.1186/s12951-018-0437-z.

(247) Stoorvogel, W. Resolving Sorting Mechanisms into Exosomes. *Cell Research* **2015**, *25* (5), 531–532. https://doi.org/10.1038/cr.2015.39.

(248) Colombo, M.; Moita, C.; Niel, G. van; Kowal, J.; Vigneron, J.; Benaroch, P.; Manel, N.; Moita, L. F.; Théry, C.; Raposo, G. Analysis of ESCRT Functions in Exosome Biogenesis, Composition and Secretion Highlights the Heterogeneity of Extracellular Vesicles. *J Cell Sci* **2013**, *126* (24), 5553–5565. https://doi.org/10.1242/jcs.128868.

(249) Garofalo, M.; Villa, A.; Crescenti, D.; Marzagalli, M.; Kuryk, L.; Limonta, P.; Mazzaferro, V.; Ciana, P. Heterologous and Cross-Species Tropism of Cancer-Derived Extracellular Vesicles. *Theranostics* **2019**, *9* (19), 5681–5693. https://doi.org/10.7150/thno.34824.

(250) Rayamajhi, S.; Nguyen, T. D. T.; Marasini, R.; Aryal, S. Macrophage-Derived Exosome-Mimetic Hybrid Vesicles for Tumor Targeted Drug Delivery. *Acta Biomaterialia* **2019**, *94*, 482–494. https://doi.org/10.1016/j.actbio.2019.05.054.

(251) Choi, D.-S.; Kim, D.-K.; Kim, Y.-K.; Gho, Y. S. Proteomics, Transcriptomics and Lipidomics of Exosomes and Ectosomes. *PROTEOMICS* **2013**, *13* (10–11), 1554–1571. https://doi.org/10.1002/pmic.201200329.

(252) Wu, C.-H.; Li, J.; Li, L.; Sun, J.; Fabbri, M.; Wayne, A. S.; Seeger, R. C.; Jong, A. Y. Extracellular Vesicles Derived from Natural Killer Cells Use Multiple Cytotoxic Proteins

and Killing Mechanisms to Target Cancer Cells. *Journal of Extracellular Vesicles* **2019**, *8* (1), 1588538. https://doi.org/10.1080/20013078.2019.1588538.
(253) Niel, G. van; D'Angelo, G.; Raposo, G. Shedding Light on the Cell Biology of Extracellular Vesicles. *Nat Rev Mol Cell Biol* **2018**, *19* (4), 213–228. https://doi.org/10.1038/nrm.2017.125.
(254) Kowal, J.; Arras, G.; Colombo, M.; Jouve, M.; Morath, J. P.; Primdal-Bengtson, B.; Dingli, F.; Loew, D.; Tkach, M.; Théry, C. Proteomic Comparison Defines Novel Markers to Characterize Heterogeneous Populations of Extracellular Vesicle Subtypes. *PNAS* **2016**, *113* (8), E968–E977. https://doi.org/10.1073/pnas.1521230113.
(255) Pitchaimani, A.; Nguyen, T. D. T.; Wang, H.; H. Bossmann, S.; Aryal, S. Design and Characterization of Gadolinium Infused Theranostic Liposomes. *RSC Advances* **2016**, *6* (43), 36898–36905. https://doi.org/10.1039/C6RA00552G.
(256) Aryal, S.; Key, J.; Stigliano, C.; Ananta, J. S.; Zhong, M.; Decuzzi, P. Engineered Magnetic Hybrid Nanoparticles with Enhanced Relaxivity for Tumor Imaging. *Biomaterials* **2013**, *34* (31), 7725–7732. https://doi.org/10.1016/j.biomaterials.2013.07.003.
(257) Abello, J.; Nguyen, T. D. T.; Marasini, R.; Aryal, S.; Weiss, M. L. Biodistribution of Gadolinium- and near Infrared-Labeled Human Umbilical Cord Mesenchymal Stromal Cell-Derived Exosomes in Tumor Bearing Mice. *Theranostics* **2019**, *9* (8), 2325–2345. https://doi.org/10.7150/thno.30030.
(258) Benedikter, B. J.; Bouwman, F. G.; Vajen, T.; Heinzmann, A. C. A.; Grauls, G.; Mariman, E. C.; Wouters, E. F. M.; Savelkoul, P. H.; Lopez-Iglesias, C.; Koenen, R. R.; Rohde, G. G. U.; Stassen, F. R. M. Ultrafiltration Combined with Size Exclusion Chromatography Efficiently Isolates Extracellular Vesicles from Cell Culture Media for Compositional and Functional Studies. *Scientific Reports* **2017**, *7* (1), 1–13. https://doi.org/10.1038/s41598-017-15717-7.
(259) The Bradford Method for Protein Quantitation | Springer Nature Experiments https://experiments.springernature.com/articles/10.1385/1-59259-169-8:15 (accessed Dec 11, 2019).
(260) Pitchaimani, A.; Nguyen, T. D. T.; Aryal, S. Natural Killer Cell Membrane Infused Biomimetic Liposomes for Targeted Tumor Therapy. *Biomaterials* **2018**, *160*, 124–137. https://doi.org/10.1016/j.biomaterials.2018.01.018.
(261) Ciapetti, G.; Cenni, E.; Pratelli, L.; Pizzoferrato, A. In Vitro Evaluation of Cell/Biomaterial Interaction by MTT Assay. *Biomaterials* **1993**, *14* (5), 359–364. https://doi.org/10.1016/0142-9612(93)90055-7.
(262) Ortega, M. T.; Riviere, J. E.; Choi, K.; Monteiro-Riviere, N. A. Biocorona Formation on Gold Nanoparticles Modulates Human Proximal Tubule Kidney Cell Uptake, Cytotoxicity and Gene Expression. *Toxicology in Vitro* **2017**, *42*, 150–160. https://doi.org/10.1016/j.tiv.2017.04.020.
(263) Chan, J. K. C. The Wonderful Colors of the Hematoxylin–Eosin Stain in Diagnostic Surgical Pathology: *International Journal of Surgical Pathology* **2014**. https://doi.org/10.1177/1066896913517939.
(264) Pino, P. del; Pelaz, B.; Zhang, Q.; Maffre, P.; Nienhaus, G. U.; Parak, W. J. Protein Corona Formation around Nanoparticles – from the Past to the Future. *Mater. Horiz.* **2014**, *1* (3), 301–313. https://doi.org/10.1039/C3MH00106G.

(265) Choi, C. H. J.; Alabi, C. A.; Webster, P.; Davis, M. E. Mechanism of Active Targeting in Solid Tumors with Transferrin-Containing Gold Nanoparticles. *PNAS* **2010**, *107* (3), 1235–1240. https://doi.org/10.1073/pnas.0914140107.
(266) Pitt, J. M.; Kroemer, G.; Zitvogel, L. Extracellular Vesicles: Masters of Intercellular Communication and Potential Clinical Interventions. *J Clin Invest* **2016**, *126* (4), 1139–1143. https://doi.org/10.1172/JCI87316.
(267) Tetta, C.; Ghigo, E.; Silengo, L.; Deregibus, M. C.; Camussi, G. Extracellular Vesicles as an Emerging Mechanism of Cell-to-Cell Communication. *Endocrine* **2013**, *44* (1), 11–19. https://doi.org/10.1007/s12020-012-9839-0.
(268) Mihály, J.; Deák, R.; Szigyártó, I. C.; Bóta, A.; Beke-Somfai, T.; Varga, Z. Characterization of Extracellular Vesicles by IR Spectroscopy: Fast and Simple Classification Based on Amide and CH Stretching Vibrations. *Biochimica et Biophysica Acta (BBA) - Biomembranes* **2017**, *1859* (3), 459–466. https://doi.org/10.1016/j.bbamem.2016.12.005.
(269) Marasini, R.; Pitchaimani, A.; Thanh Nguyen, T. D.; Comer, J.; Aryal, S. The Influence of Polyethylene Glycol Passivation on the Surface Plasmon Resonance Induced Photothermal Properties of Gold Nanorods. *Nanoscale* **2018**, *10* (28), 13684–13693. https://doi.org/10.1039/C8NR03026J.
(270) Chirio-Lebrun, M.-C.; Prats, M. Fluorescence Resonance Energy Transfer (FRET): Theory and Experiments. *Biochemical Education* **1998**, *26* (4), 320–323. https://doi.org/10.1016/S0307-4412(98)80010-1.
(271) Loura, L. M.; Prieto, M. J. FRET in Membrane Biophysics: An Overview. *Front. Physiol.* **2011**, *2*. https://doi.org/10.3389/fphys.2011.00082.
(272) Pornpattananangkul, D.; Olson, S.; Aryal, S.; Sartor, M.; Huang, C.-M.; Vecchio, K.; Zhang, L. Stimuli-Responsive Liposome Fusion Mediated by Gold Nanoparticles. *ACS Nano* **2010**, *4* (4), 1935–1942. https://doi.org/10.1021/nn9018587.
(273) Piffoux, M.; Silva, A. K. A.; Wilhelm, C.; Gazeau, F.; Tareste, D. Modification of Extracellular Vesicles by Fusion with Liposomes for the Design of Personalized Biogenic Drug Delivery Systems. *ACS Nano* **2018**, *12* (7), 6830–6842. https://doi.org/10.1021/acsnano.8b02053.
(274) Aryal, S.; Nguyen, T. D. T.; Pitchaimani, A.; Shrestha, T. B.; Biller, D.; Troyer, D. Membrane Fusion-Mediated Gold Nanoplating of Red Blood Cell: A Bioengineered CT-Contrast Agent. *ACS Biomater. Sci. Eng.* **2017**, *3* (1), 36–41. https://doi.org/10.1021/acsbiomaterials.6b00573.
(275) Osad'ko, I. S. Dependence of FRET Efficiency on Distance in Single Donor-Acceptor Pairs. *J. Chem. Phys.* **2015**, *142* (12), 125102. https://doi.org/10.1063/1.4915279.
(276) Pitchaimani, A.; Nguyen, T. D. T.; Marasini, R.; Eliyapura, A.; Azizi, T.; Jaberi-Douraki, M.; Aryal, S. Biomimetic Natural Killer Membrane Camouflaged Polymeric Nanoparticle for Targeted Bioimaging. *Advanced Functional Materials* **2019**, *29* (4), 1806817. https://doi.org/10.1002/adfm.201806817.
(277) Sherry, A. D.; Caravan, P.; Lenkinski, R. E. Primer on Gadolinium Chemistry. *Journal of Magnetic Resonance Imaging* **2009**, *30* (6), 1240–1248. https://doi.org/10.1002/jmri.21966.
(278) Rogosnitzky, M.; Branch, S. Gadolinium-Based Contrast Agent Toxicity: A Review of Known and Proposed Mechanisms. *Biometals* **2016**, *29* (3), 365–376. https://doi.org/10.1007/s10534-016-9931-7.

(279) Clough, T. J.; Jiang, L.; Wong, K.-L.; Long, N. J. Ligand Design Strategies to Increase Stability of Gadolinium-Based Magnetic Resonance Imaging Contrast Agents. *Nature Communications* **2019**, *10* (1), 1–14. https://doi.org/10.1038/s41467-019-09342-3.
(280) Port, M.; Idée, J.-M.; Medina, C.; Robic, C.; Sabatou, M.; Corot, C. Efficiency, Thermodynamic and Kinetic Stability of Marketed Gadolinium Chelates and Their Possible Clinical Consequences: A Critical Review. *Biometals* **2008**, *21* (4), 469–490. https://doi.org/10.1007/s10534-008-9135-x.
(281) Dai, L.; Jones, C. M.; Chan, W. T. K.; Pham, T. A.; Ling, X.; Gale, E. M.; Rotile, N. J.; Tai, W. C.-S.; Anderson, C. J.; Caravan, P.; Law, G.-L. Chiral DOTA Chelators as an Improved Platform for Biomedical Imaging and Therapy Applications. *Nature Communications* **2018**, *9* (1), 1–10. https://doi.org/10.1038/s41467-018-03315-8.
(282) Anonymous. EMA's final opinion confirms restrictions on use of linear gadolinium agents in body scans https://www.ema.europa.eu/en/news/emas-final-opinion-confirms-restrictions-use-linear-gadolinium-agents-body-scans (accessed Dec 11, 2019).
(283) Liang, X.; Li, Y.; Li, X.; Jing, L.; Deng, Z.; Yue, X.; Li, C.; Dai, Z. PEGylated Polypyrrole Nanoparticles Conjugating Gadolinium Chelates for Dual-Modal MRI/Photoacoustic Imaging Guided Photothermal Therapy of Cancer. *Advanced Functional Materials* **2015**, *25* (9), 1451–1462. https://doi.org/10.1002/adfm.201402338.
(284) Roy, S.; Lin, H.-Y.; Chou, C.-Y.; Huang, C.-H.; Small, J.; Sadik, N.; Ayinon, C. M.; Lansbury, E.; Cruz, L.; Yekula, A.; Jones, P. S.; Balaj, L.; Carter, B. S. Navigating the Landscape of Tumor Extracellular Vesicle Heterogeneity. *Int J Mol Sci* **2019**, *20* (6). https://doi.org/10.3390/ijms20061349.
(285) Fadeel, B. Hide and Seek: Nanomaterial Interactions With the Immune System. *Front. Immunol.* **2019**, *10*. https://doi.org/10.3389/fimmu.2019.00133.
(286) Yang, G.; Chen, S.; Zhang, J. Bioinspired and Biomimetic Nanotherapies for the Treatment of Infectious Diseases. *Front Pharmacol* **2019**, *10*. https://doi.org/10.3389/fphar.2019.00751.
(287) Lang, T.; Yin, Q.; Li, Y. Progress of Cell-Derived Biomimetic Drug Delivery Systems for Cancer Therapy. *Advanced Therapeutics* **2018**, *1* (7), 1800053. https://doi.org/10.1002/adtp.201800053.
(288) Yu, Z.; Zhou, P.; Pan, W.; Li, N.; Tang, B. A Biomimetic Nanoreactor for Synergistic Chemiexcited Photodynamic Therapy and Starvation Therapy against Tumor Metastasis. *Nature Communications* **2018**, *9* (1), 1–9. https://doi.org/10.1038/s41467-018-07197-8.
(289) Qin, M.; Du, G.; Sun, X. Biomimetic Cell-Derived Nanocarriers for Modulating Immune Responses. *Biomater. Sci.* **2019**. https://doi.org/10.1039/C9BM01444F.
(290) Mulcahy, L. A.; Pink, R. C.; Carter, D. R. F. Routes and Mechanisms of Extracellular Vesicle Uptake. *Journal of Extracellular Vesicles* **2014**, *3* (1), 24641. https://doi.org/10.3402/jev.v3.24641.
(291) Mathieu, M.; Martin-Jaular, L.; Lavieu, G.; Théry, C. Specificities of Secretion and Uptake of Exosomes and Other Extracellular Vesicles for Cell-to-Cell Communication. *Nature Cell Biology* **2019**, *21* (1), 9–17. https://doi.org/10.1038/s41556-018-0250-9.
(292) van Niel, G.; D'Angelo, G.; Raposo, G. Shedding Light on the Cell Biology of Extracellular Vesicles. *Nature Reviews Molecular Cell Biology* **2018**, *19* (4), 213–228. https://doi.org/10.1038/nrm.2017.125.
(293) Murphy, D. E.; Jong, O. G. de; Brouwer, M.; Wood, M. J.; Lavieu, G.; Schiffelers, R. M.; Vader, P. Extracellular Vesicle-Based Therapeutics: Natural versus Engineered

Targeting and Trafficking. *Exp Mol Med* **2019**, *51* (3), 1–12. https://doi.org/10.1038/s12276-019-0223-5.
(294) Mathieu, M.; Martin-Jaular, L.; Lavieu, G.; Théry, C. Specificities of Secretion and Uptake of Exosomes and Other Extracellular Vesicles for Cell-to-Cell Communication. *Nat Cell Biol* **2019**, *21* (1), 9–17. https://doi.org/10.1038/s41556-018-0250-9.
(295) Cheng, L.; Wang, Y.; Huang, L. Exosomes from M1-Polarized Macrophages Potentiate the Cancer Vaccine by Creating a Pro-Inflammatory Microenvironment in the Lymph Node. *Molecular Therapy* **2017**, *25* (7), 1665–1675. https://doi.org/10.1016/j.ymthe.2017.02.007.
(296) Desai, N. Challenges in Development of Nanoparticle-Based Therapeutics. *AAPS J* **2012**, *14* (2), 282–295. https://doi.org/10.1208/s12248-012-9339-4.
(297) Sercombe, L.; Veerati, T.; Moheimani, F.; Wu, S. Y.; Sood, A. K.; Hua, S. Advances and Challenges of Liposome Assisted Drug Delivery. *Front. Pharmacol.* **2015**, *6*. https://doi.org/10.3389/fphar.2015.00286.
(298) Rosenblum, D.; Joshi, N.; Tao, W.; Karp, J. M.; Peer, D. Progress and Challenges towards Targeted Delivery of Cancer Therapeutics. *Nature Communications* **2018**, *9* (1), 1–12. https://doi.org/10.1038/s41467-018-03705-y.
(299) Grobner, T. Gadolinium – a Specific Trigger for the Development of Nephrogenic Fibrosing Dermopathy and Nephrogenic Systemic Fibrosis? *Nephrol Dial Transplant* **2006**, *21* (4), 1104–1108. https://doi.org/10.1093/ndt/gfk062.
(300) Longmire, M.; Choyke, P. L.; Kobayashi, H. Clearance Properties of Nano-Sized Particles and Molecules as Imaging Agents: Considerations and Caveats. *Nanomedicine* **2008**, *3* (5), 703–717. https://doi.org/10.2217/17435889.3.5.703.
(301) Wilhelm, S.; Tavares, A. J.; Dai, Q.; Ohta, S.; Audet, J.; Dvorak, H. F.; Chan, W. C. W. Analysis of Nanoparticle Delivery to Tumours. *Nature Reviews Materials* **2016**, *1* (5), 1–12. https://doi.org/10.1038/natrevmats.2016.14.
(302) Torrice, M. Does Nanomedicine Have a Delivery Problem? *ACS Cent. Sci.* **2016**, *2* (7), 434–437. https://doi.org/10.1021/acscentsci.6b00190.
(303) Balkwill, F. R.; Capasso, M.; Hagemann, T. The Tumor Microenvironment at a Glance. *J Cell Sci* **2012**, *125* (23), 5591–5596. https://doi.org/10.1242/jcs.116392.
(304) Kibria, G.; Ramos, E. K.; Wan, Y.; Gius, D. R.; Liu, H. Exosomes as a Drug Delivery System in Cancer Therapy: Potential and Challenges. *Mol. Pharmaceutics* **2018**, *15* (9), 3625–3633. https://doi.org/10.1021/acs.molpharmaceut.8b00277.
(305) Milane, L.; Singh, A.; Mattheolabakis, G.; Suresh, M.; Amiji, M. M. Exosome Mediated Communication within the Tumor Microenvironment. *J Control Release* **2015**, *219*, 278–294. https://doi.org/10.1016/j.jconrel.2015.06.029.
(306) Ha, D.; Yang, N.; Nadithe, V. Exosomes as Therapeutic Drug Carriers and Delivery Vehicles across Biological Membranes: Current Perspectives and Future Challenges. *Acta Pharmaceutica Sinica B* **2016**, *6* (4), 287–296. https://doi.org/10.1016/j.apsb.2016.02.001.
(307) Qiao, L.; Hu, S.; Huang, K.; Su, T.; Li, Z.; Vandergriff, A.; Cores, J.; Dinh, P.-U.; Allen, T.; Shen, D.; Liang, H.; Li, Y.; Cheng, K. Tumor Cell-Derived Exosomes Home to Their Cells of Origin and Can Be Used as Trojan Horses to Deliver Cancer Drugs. *Theranostics* **2020**, *10* (8), 3474–3487. https://doi.org/10.7150/thno.39434.

(308) Ingato, D.; Edson, J. A.; Zakharian, M.; Kwon, Y. J. Cancer Cell-Derived, Drug-Loaded Nanovesicles Induced by Sulfhydryl-Blocking for Effective and Safe Cancer Therapy. *ACS Nano* **2018**, *12* (9), 9568–9577. https://doi.org/10.1021/acsnano.8b05377.
(309) Izco, M.; Blesa, J.; Schleef, M.; Schmeer, M.; Porcari, R.; Al-Shawi, R.; Ellmerich, S.; de Toro, M.; Gardiner, C.; Seow, Y.; Reinares-Sebastian, A.; Forcen, R.; Simons, J. P.; Bellotti, V.; Cooper, J. M.; Alvarez-Erviti, L. Systemic Exosomal Delivery of ShRNA Minicircles Prevents Parkinsonian Pathology. *Molecular Therapy* **2019**, *27* (12), 2111–2122. https://doi.org/10.1016/j.ymthe.2019.08.010.
(310) Vandergriff, A.; Huang, K.; Shen, D.; Hu, S.; Hensley, M. T.; Caranasos, T. G.; Qian, L.; Cheng, K. Targeting Regenerative Exosomes to Myocardial Infarction Using Cardiac Homing Peptide. *Theranostics* **2018**, *8* (7), 1869–1878. https://doi.org/10.7150/thno.20524.
(311) Yuana, Y.; Sturk, A.; Nieuwland, R. Extracellular Vesicles in Physiological and Pathological Conditions. *Blood Reviews* **2013**, *27* (1), 31–39. https://doi.org/10.1016/j.blre.2012.12.002.
(312) Yáñez-Mó, M.; Siljander, P. R.-M.; Andreu, Z.; Zavec, A. B.; Borràs, F. E.; Buzas, E. I.; Buzas, K.; Casal, E.; Cappello, F.; Carvalho, J.; Colás, E.; Silva, A. C.; Fais, S.; Falcon-Perez, J. M.; Ghobrial, I. M.; Giebel, B.; Gimona, M.; Graner, M.; Gursel, I.; Gursel, M.; Heegaard, N. H. H.; Hendrix, A.; Kierulf, P.; Kokubun, K.; Kosanovic, M.; Kralj-Iglic, V.; Krämer-Albers, E.-M.; Laitinen, S.; Lässer, C.; Lener, T.; Ligeti, E.; Linē, A.; Lipps, G.; Llorente, A.; Lötvall, J.; Manček-Keber, M.; Marcilla, A.; Mittelbrunn, M.; Nazarenko, I.; Hoen, E. N. M. N.-'t; Nyman, T. A.; O'Driscoll, L.; Olivan, M.; Oliveira, C.; Pállinger, É.; Portillo, H. A. del; Reventós, J.; Rigau, M.; Rohde, E.; Sammar, M.; Sánchez-Madrid, F.; Santarém, N.; Schallmoser, K.; Ostenfeld, M. S.; Stoorvogel, W.; Stukelj, R.; Grein, S. G. V. der; Vasconcelos, M. H.; Wauben, M. H. M.; Wever, O. D. Biological Properties of Extracellular Vesicles and Their Physiological Functions. *Journal of Extracellular Vesicles* **2015**, *4* (1), 27066. https://doi.org/10.3402/jev.v4.27066.
(313) Haraszti, R. A.; Miller, R.; Dubuke, M. L.; Rockwell, H. E.; Coles, A. H.; Sapp, E.; Didiot, M.-C.; Echeverria, D.; Stoppato, M.; Sere, Y. Y.; Leszyk, J.; Alterman, J. F.; Godinho, B. M. D. C.; Hassler, M. R.; McDaniel, J.; Narain, N. R.; Wollacott, R.; Wang, Y.; Shaffer, S. A.; Kiebish, M. A.; DiFiglia, M.; Aronin, N.; Khvorova, A. Serum Deprivation of Mesenchymal Stem Cells Improves Exosome Activity and Alters Lipid and Protein Composition. *iScience* **2019**, *16*, 230–241. https://doi.org/10.1016/j.isci.2019.05.029.
(314) Sun, L.; Wang, H.; Zhu, X.; Wu, P.; Chen, W.; Zou, P.; Li, Q.; Chen, Z. Serum Deprivation Elevates the Levels of Microvesicles with Different Size Distributions and Selectively Enriched Proteins in Human Myeloma Cells in Vitro. *Acta Pharmacologica Sinica* **2014**, *35* (3), 381–393. https://doi.org/10.1038/aps.2013.166.
(315) Goldring, J. P. D. Spectrophotometric Methods to Determine Protein Concentration. In *Western Blotting: Methods and Protocols*; Kurien, B. T., Scofield, R. H., Eds.; Methods in Molecular Biology; Springer: New York, NY, 2015; pp 41–47. https://doi.org/10.1007/978-1-4939-2694-7_7.
(316) Anthis, N. J.; Clore, G. M. Sequence-Specific Determination of Protein and Peptide Concentrations by Absorbance at 205 Nm. *Protein Science* **2013**, *22* (6), 851–858. https://doi.org/10.1002/pro.2253.

(317) Benedikter, B. J.; Bouwman, F. G.; Vajen, T.; Heinzmann, A. C. A.; Grauls, G.; Mariman, E. C.; Wouters, E. F. M.; Savelkoul, P. H.; Lopez-Iglesias, C.; Koenen, R. R.; Rohde, G. G. U.; Stassen, F. R. M. Ultrafiltration Combined with Size Exclusion Chromatography Efficiently Isolates Extracellular Vesicles from Cell Culture Media for Compositional and Functional Studies. *Scientific Reports* **2017**, *7* (1), 15297. https://doi.org/10.1038/s41598-017-15717-7.

(318) Gaspar, L. S.; Santana, M. M.; Henriques, C.; Pinto, M. M.; Ribeiro-Rodrigues, T. M.; Girão, H.; Nobre, R. J.; Almeida, L. P. de. Simple and Fast SEC-Based Protocol to Isolate Human Plasma-Derived Extracellular Vesicles for Transcriptional Research. *Molecular Therapy - Methods & Clinical Development* **2020**, *18*, 723–737. https://doi.org/10.1016/j.omtm.2020.07.012.

(319) Mol, E. A.; Goumans, M.-J.; Doevendans, P. A.; Sluijter, J. P. G.; Vader, P. Higher Functionality of Extracellular Vesicles Isolated Using Size-Exclusion Chromatography Compared to Ultracentrifugation. *Nanomedicine: Nanotechnology, Biology and Medicine* **2017**, *13* (6), 2061–2065. https://doi.org/10.1016/j.nano.2017.03.011.

(320) Jose Chirayil, C.; Abraham, J.; Kumar Mishra, R.; George, S. C.; Thomas, S. Chapter 1 - Instrumental Techniques for the Characterization of Nanoparticles. In *Thermal and Rheological Measurement Techniques for Nanomaterials Characterization*; Thomas, S., Thomas, R., Zachariah, A. K., Mishra, R. K., Eds.; Micro and Nano Technologies; Elsevier, 2017; pp 1–36. https://doi.org/10.1016/B978-0-323-46139-9.00001-3.

(321) Cordonnier, M.; Chanteloup, G.; Isambert, N.; Seigneuric, R.; Fumoleau, P.; Garrido, C.; Gobbo, J. Exosomes in Cancer Theranostic: Diamonds in the Rough. *Cell Adhesion & Migration* **2017**, *11* (2), 151–163. https://doi.org/10.1080/19336918.2016.1250999.

(322) Elmallah, M. I. Y.; Cordonnier, M.; Vautrot, V.; Chanteloup, G.; Garrido, C.; Gobbo, J. Membrane-Anchored Heat-Shock Protein 70 (Hsp70) in Cancer. *Cancer Letters* **2020**, *469*, 134–141. https://doi.org/10.1016/j.canlet.2019.10.037.

(323) Garcia, N. A.; Ontoria-Oviedo, I.; González-King, H.; Diez-Juan, A.; Sepúlveda, P. Glucose Starvation in Cardiomyocytes Enhances Exosome Secretion and Promotes Angiogenesis in Endothelial Cells. *PLOS ONE* **2015**, *10* (9), e0138849. https://doi.org/10.1371/journal.pone.0138849.

(324) Abramowicz, A.; Widłak, P.; Pietrowska, M. Different Types of Cellular Stress Affect the Proteome Composition of Small Extracellular Vesicles: A Mini Review. *Proteomes* **2019**, *7* (2), 23. https://doi.org/10.3390/proteomes7020023.

Appendix A - Supporting information for Chapter 3

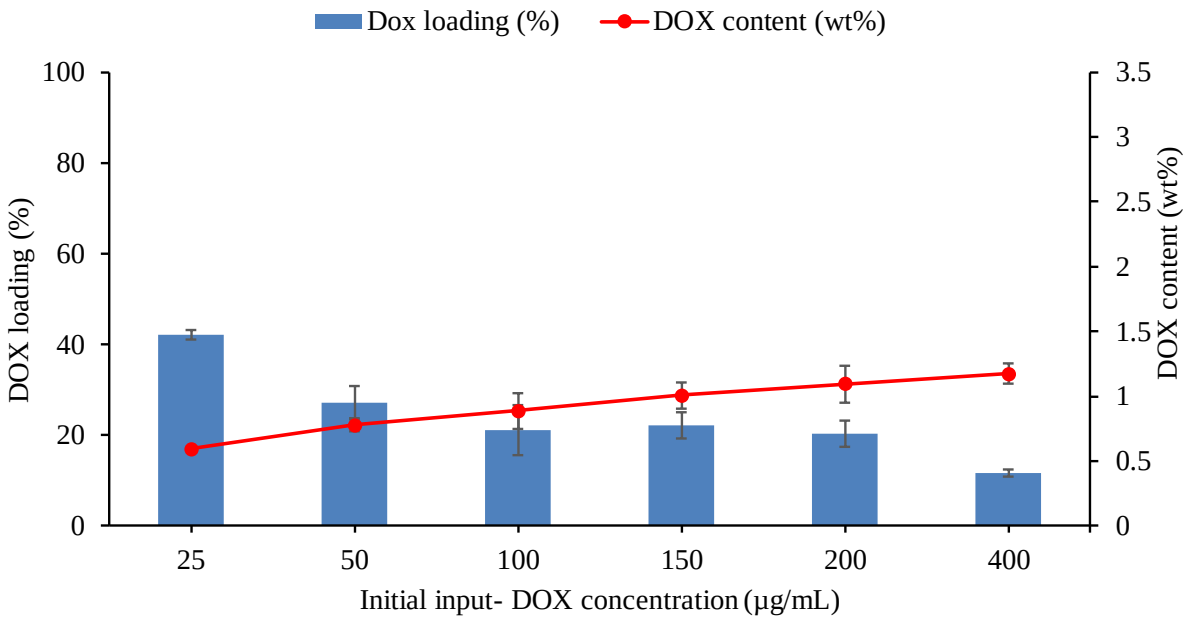

Figure 3.S1 *In-vitro* drug loading via passive method. Doxorubicin (DOX) loading efficiency and DOX content by weight percentage with respect to carrier in different initial input concentration of DOX (µg/mL).

Appendix B - Supporting information for Chapter 4

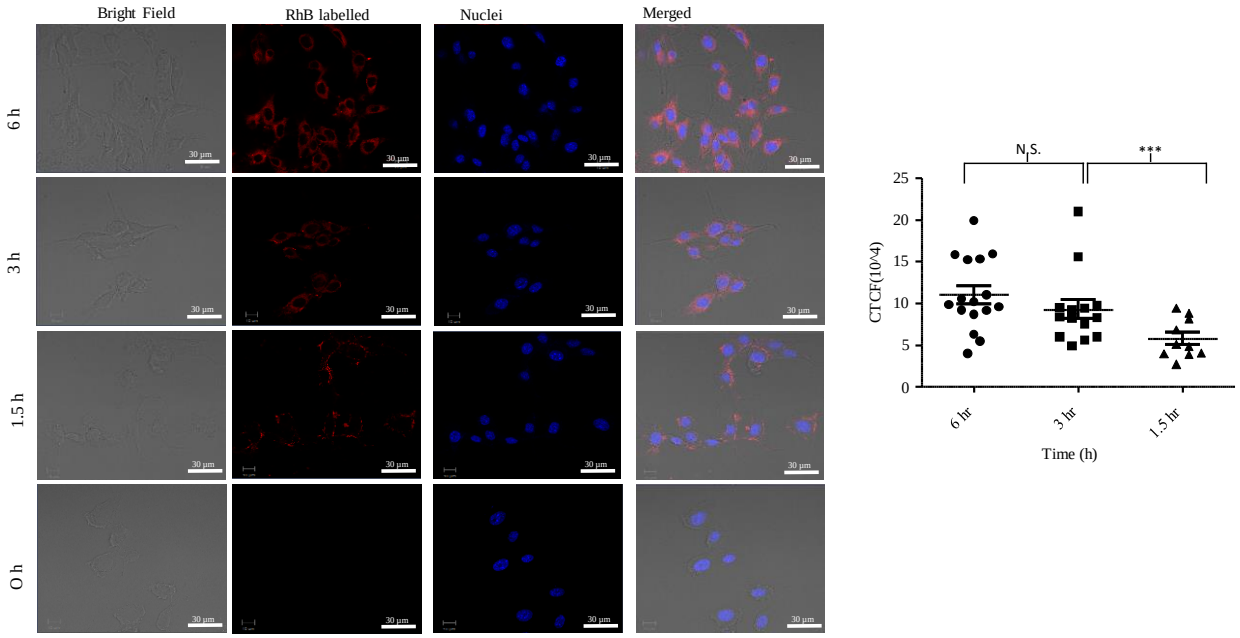

Figure 4.S1 Confocal image of mouse fibroblast NIH/3T3 showing time dependent internalization of RhB labelled hybrid exosomes in 3T3, after 0, 1.5, 3, and 6 h treatment. Internalization was quantified in terms of Corrected Total Cell Fluorescence (CTCF) using ImageJ (*** = $p<0.0001$, N.S= Non-significant, t test).

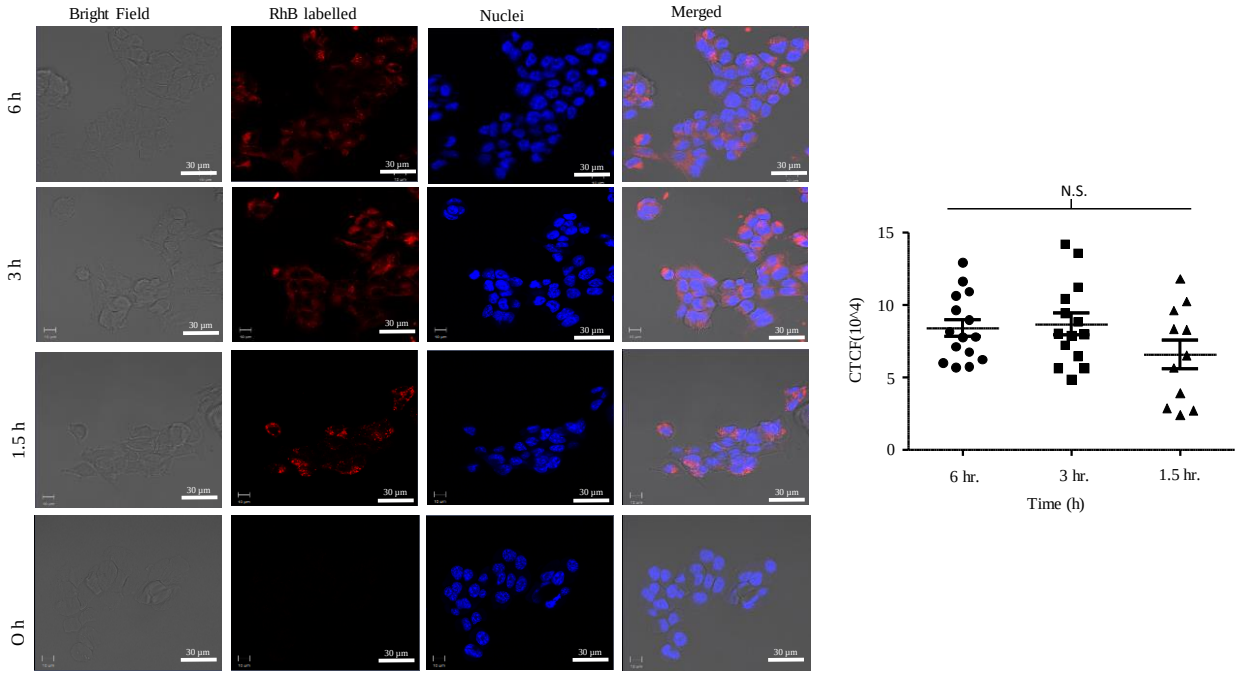

Figure 4.S2 Confocal image of mouse breast cancer cells 4T1 showing time dependent internalization of RhB labelled hybrid exosomes in 3T3, after 0, 1.5, 3, and 6 h treatment. Internalization was quantified in terms of Corrected Total Cell Fluorescence (CTCF) using ImageJ (*** = $p<0.0001$, N.S= Non-significant, t test).

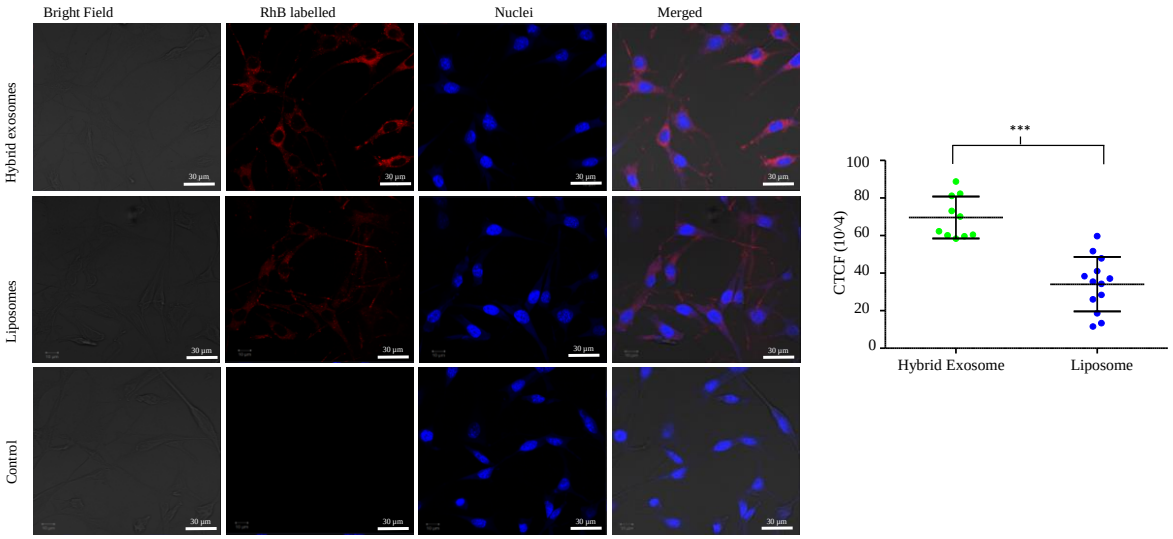

Figure 4.S3 Confocal image of mouse osteosarcoma K7M2 showing internalization of RhB labelled hybrid exosomes and liposomes after 3 h incubation. Nuclei was stained with DAPI. Internalization was quantified in terms of Corrected Total Cell Fluorescence (CTCF) using ImageJ (*** = $p<0.0001$, N.S= Non-significant, t test).

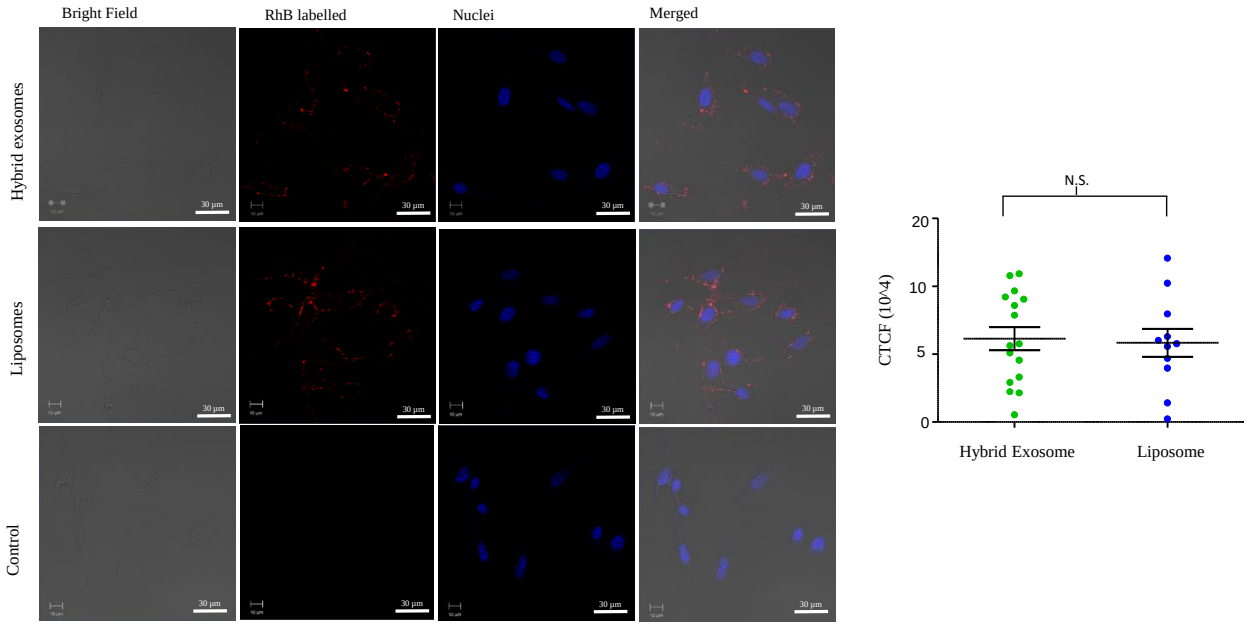

Figure 4.S4 Confocal image of mouse normal fibroblast NIH/3T3 showing internalization of RhB labelled hybrid exosomes and liposomes after 3 h incubation. Nuclei was stained with DAPI. Internalization was quantified in terms of Corrected Total Cell Fluorescence (CTCF) using ImageJ (*** = $p<0.0001$, N.S= Non-significant, t test).

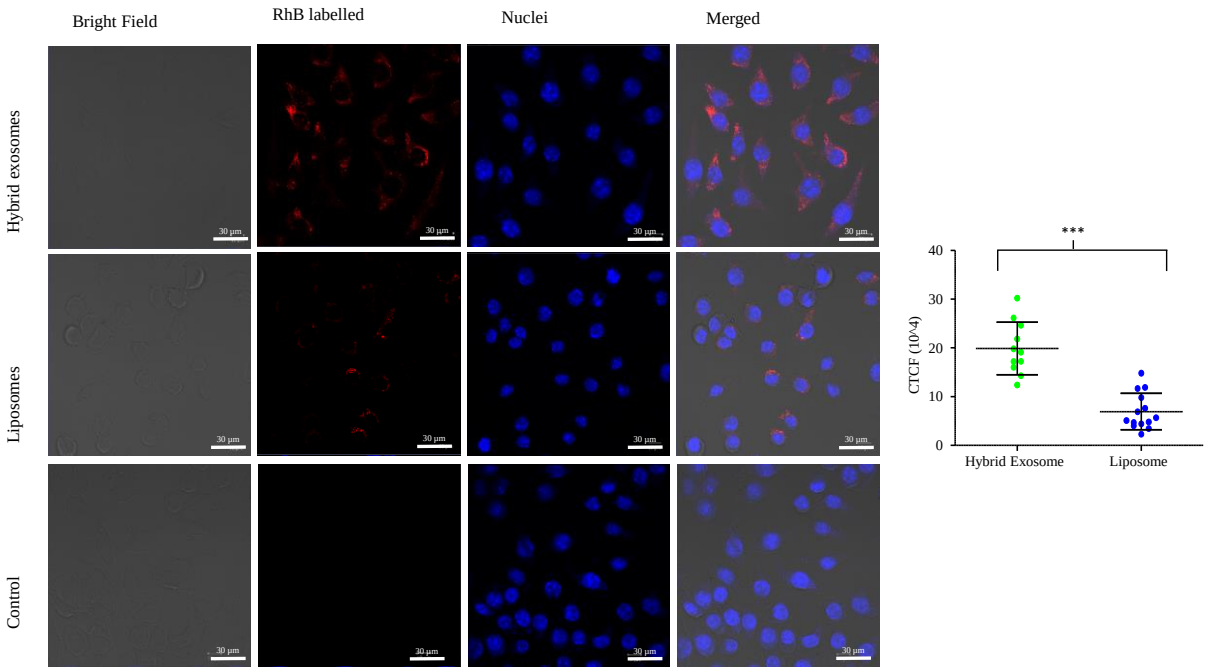

Figure 4.S5 Confocal image of mouse macrophage cells J774A.1 showing internalization of RhB labelled hybrid exosomes and liposomes after 3 h incubation. Nuclei was stained with DAPI. Internalization was quantified in terms of Corrected Total Cell Fluorescence (CTCF) using ImageJ (*** = $p<0.0001$, N.S= Non-significant, t test).

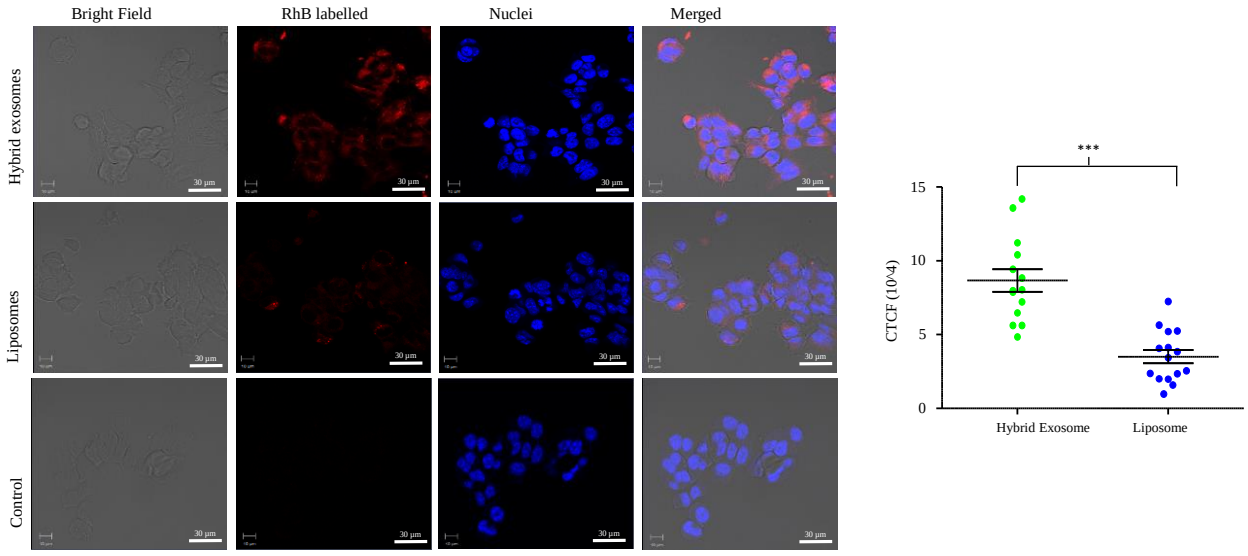

Figure 4.S6 Confocal image of mouse breast cancer cells 4T1 showing internalization of RhB labelled hybrid exosomes and liposomes after 3 h incubation. Nuclei was stained with DAPI. Internalization was quantified in terms of Corrected Total Cell Fluorescence (CTCF) using ImageJ (*** = $p<0.0001$, N.S= Non-significant, t test).

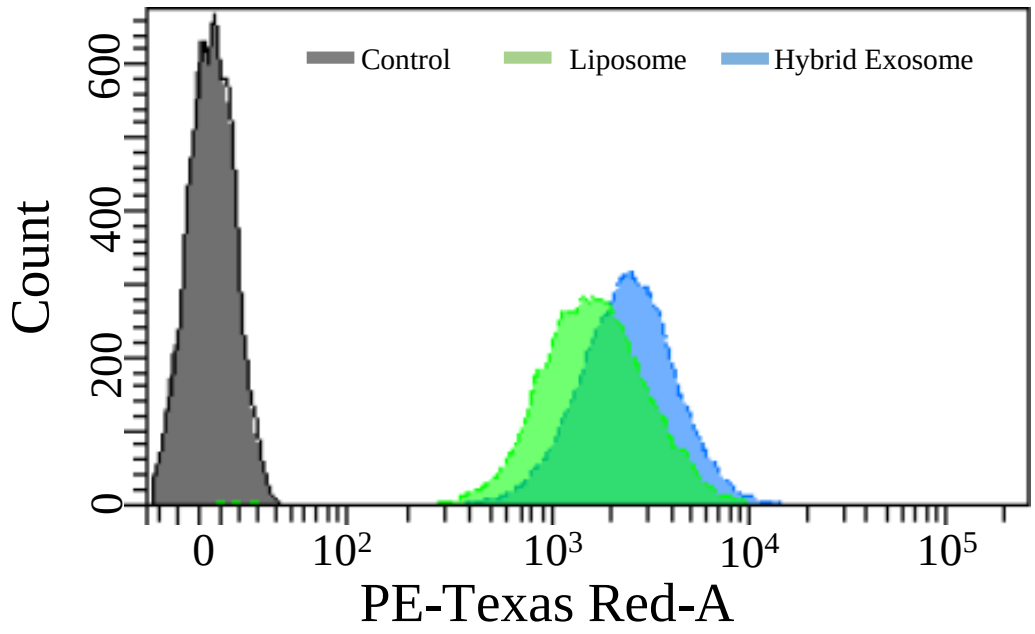

Figure 4.S7 Flow cytometry analysis showing internalization of Rhodamine labelled hybrid exosome and liposome in mouse macrophage J774A.1, after 3 h incubation. Hybrid exosome showed enhanced internalization compared to liposome.

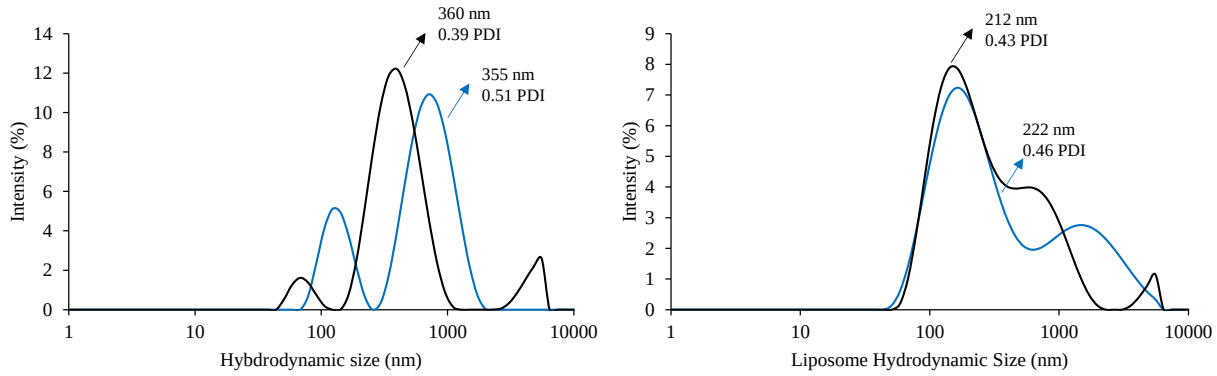

Figure 4.S8 Hydrodynamic size distribution of hybrid exosome (left) and liposome (right) in acidic condition (pH 5.5, Acetate buffer). Two independent size analysis shows broad size distribution of hybrid exosome and liposome in acidic condition with elevated size and PDI.

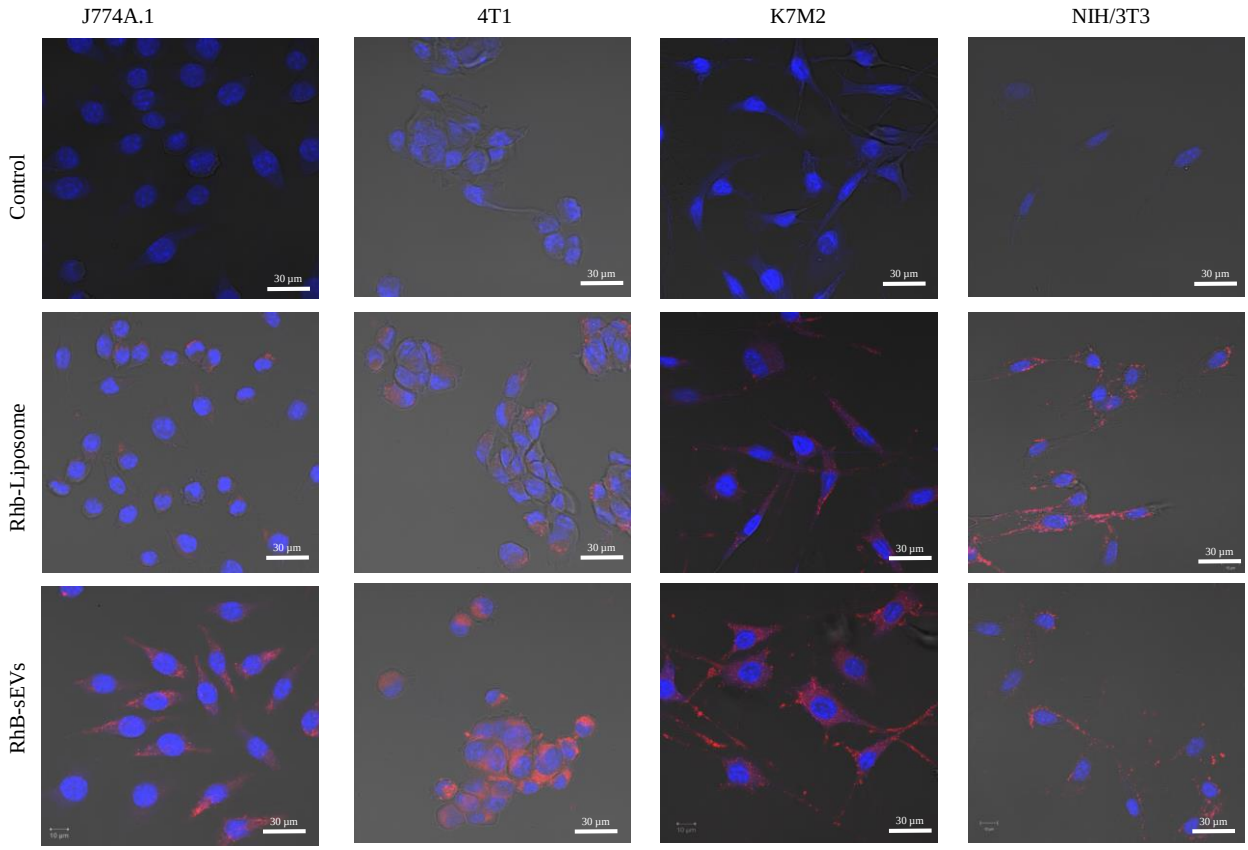

Figure 4.S9 Confocal image of mouse macrophage J774A.1, mouse breast cancer cell 4T1, mouse osteosarcoma K7M2, and mouse normal fibroblast NIH/3T3 showing cellular internalization of Rhodamine (RhB) labelled small extracellular vesicles (sEVs) and Liposome, after 3 h incubation. Nuclei were stained by DAPI. All images are merged versions.

Appendix C - Supporting information for Chapter 5

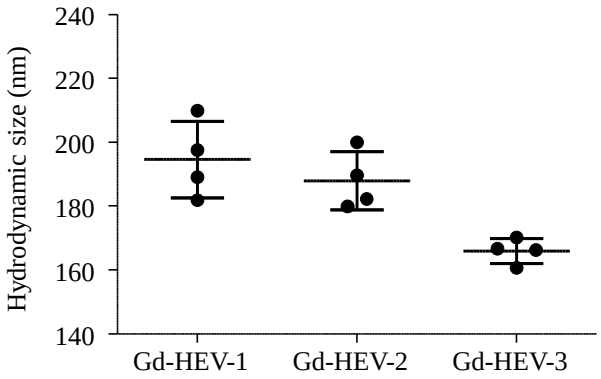

Figure 5.S1 Hydrodynamic size of three different formulations of Gd-HEV with the different molar ratios of constituents. Graph shows hydrodynamic size at four different days for each formulation (days 0, 3, 6, and 10).

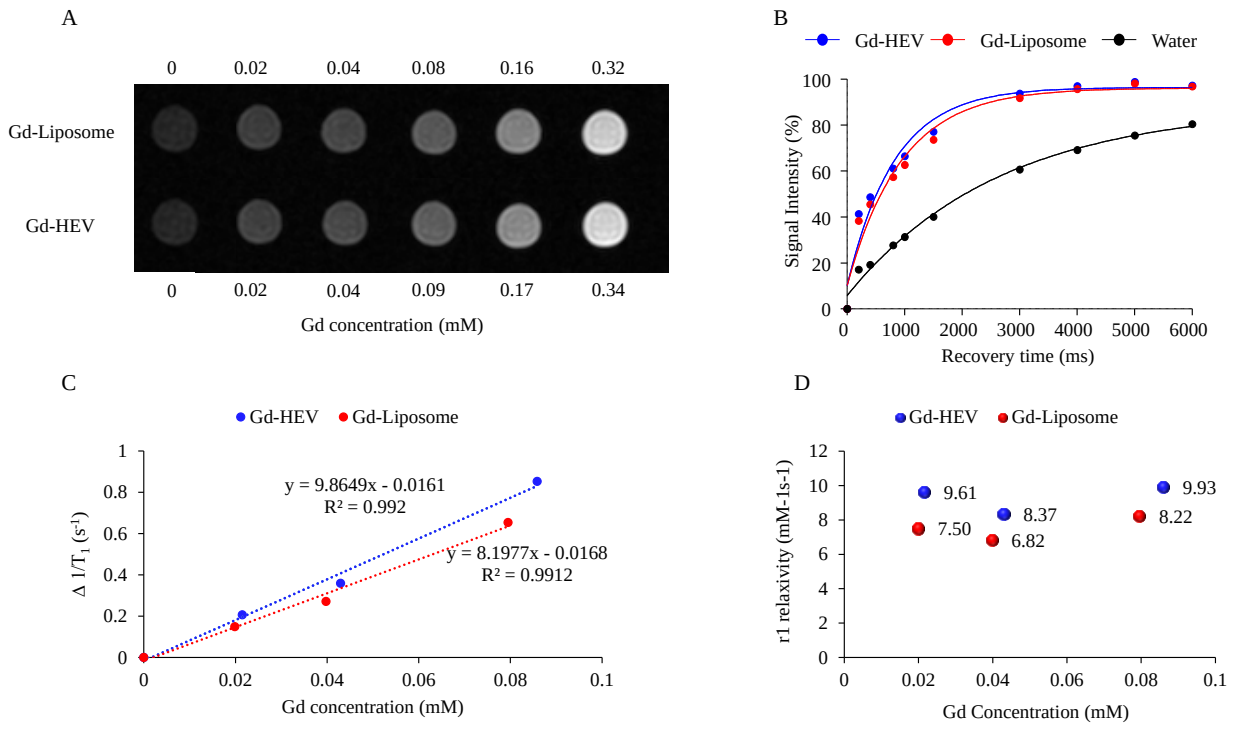

Figure 5.S2 Comparison of magnetic characterization of Gd-HEV and Gd-liposome. (A) T_1 weighted image of Gd-HEV and Gd-Liposome at different Gd concentration showing contrast enhancement in a 3T clinical MRI system (TR=400 ms, TE=10 ms, and slice thickness=2 mm), (B) T_1 recovery curve of Gd-HEV (0.09 mM Gd), Gd-Liposome (0.08 mM Gd), and water in terms of % signal intensity with respect to recovery time (ms) at specific Gd concentration showing different recovery characteristic, (C) Linear fit of inverse of relative change in T_1 recovery time ($(\Delta\ 1/T_1\ (s^{-1}))$ with respect to different Gd concentration (mM) in Gd-HEV and Gd-Liposome (p-value = 0.117 and 0.118, linear regression analysis of slopes and intercept, respectively). Slope of the fitted model gives longitudinal relaxivity (r_1): 9.87 $mM^{-1}s^{-1}$ for Gd-HEV and 8.20 $mM^{-1}s^{-1}$ for Gd-Liposome, (D) r_1 relaxivity of Gd-HEV and Gd-Liposome at different concentration. All data were obtained using a 3T clinical MRI.

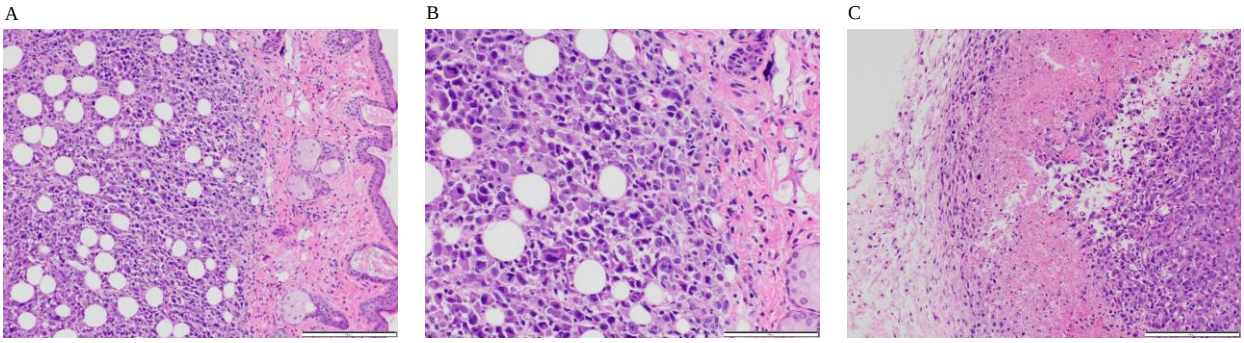

Figure 5.S3 Histologic analysis of tissue sections of the tumor. (A and B) Image showing the dermal anaplastic sarcoma and (C) Image showing the subcutaneous anaplastic tumor along with areas of necrosis and hemorrhage (Scale bar: A-200µm, B-100µm, C-200µm).

Histological features of tumor: Within the dermis and extending through the cutaneous trunci muscle into the subcutaneous adipose tissue is a multilobular and well-demarcated neoplasm composed of neoplastic polygonal to spindle-shaped cells arranged in dense sheets and clusters supported by a fibrovascular stroma. The cells have a moderate amount of eosinophilic cytoplasm, a single large round to oval nucleus with 1-3 prominent magenta or basophilic nucleoli. There is moderate to marked anisocytosis and anisokaryosis; there are increased numbers of mitotic figures (up to 10 figures, some are bizarre) per high powered 40X field of view. Within the dermal nodule, approximately 5% of the mass is necrotic characterized by necrotic karyorrhectic debris. The neoplastic cells extend into the superficial dermal collagen, and also through the underlying skeletal muscle and into the subcutaneous space where they form a distinct nodule. Here, the cell features are similar, though approximately 60% of this nodule is composed of necrotic debris intermixed with degenerate neutrophils and hemorrhage. The nodule is surrounded by loose fibrous connective tissue.

Appendix D - List of Abbreviation

Name	Abbreviation
1,1'-Dioctadecyl-3,3,3',3'-Tetramethylindotricarbocyanine Iodide	DiR
1,2-dipalmitoyl-sn-glycero-3-phosphocholine	DPPC
1,2-distearoyl-sn-glycero-3-phosphoethanolamine	DSPE
1,2-distearoyl-sn-glycero-3-phosphoglycerol, sodium salt	DSPG
1,4,7,10-Tetraazacyclododecane-1,4,7,10-tetraacetic acid mono-N-hydroxysuccinimide ester	DOTA-NHS-ester
1-ethyl-3-(3-dimethylaminopropyl)carbodiimide hydrochloride	EDC
3-(4,5-dimethylthiazol-2-yl)-2,5-diphenyl tetrazolium bromide	MTT
3ß-[N-(N',N'-dimethylaminoethane)-carbamoyl]cholesterol hydrochloride	DC-Cholesterol·HCl
4′,6-diamidino-2-phenylindole	DAPI
American Type Cell Culture	ATCC
Analysis of variance	ANOVA
Area under the curve	AUC
Confocal Laser Scanning Microscope	CLSM
Corrected total cell fluorescence	CTCF
Dimethyl sulfoxide	DMSO
Doxorubicin	DOX
Dulbecco's Modified Eagle Medium	DMEM
Dynamic Light Scattering	DLS
Echo time	TE
Endosomal sorting complex required for transport	ESCRT
Enhanced Permeability and Retention effect	EPR effect
Extracellular vesicle	EV
Fetal bovine serum	FBS
Field of view	FOV
Fluorescence-activated cell sorting	FACS
Food and Drug Administration	FDA
Fourier-transform infrared spectroscopy	FT-IR
Gadolinium	Gd
Gadolinium (III) acetate hydrate	$Gd(OAc)_3$
Gadolinium infused hybrid extracellular vesicles	Gd-HEV
Gadolinium lipid	Gd-lipid or Gd-L
Gadolinium-based contrast agent	GBCA
Hybrid exosomes	HE
Inductively coupled plasma mass spectrometry	ICP-MS
Injected dose	ID
Institutional Animal Care and Use Committee	IACUC

Institutional Biosafety Committee	IBC
Interleukin	IL
Kilo Dalton	kDa
Lipid L-α-phosphatidylcholine (Egg, Chicken)	EggPC
Longitudinal relaxation time	T_1
Longitudinal relaxivity	r_1
Longitudinal surface plasmon resonance	LSPR
L-α-Phosphatidylethanolamine-N-(7-nitro-2-1,3-benzoxadiazol-4-yl) (Ammonium Salt) (Egg-Transphosphatidylated, Chicken)	Egg NBD PE
L-α-Phosphatidylethanolamine-N-(lissamine rhodamine B sulfonyl) (Ammonium Salt) (Egg-Transphosphatidylated, Chicken)	Egg Liss Rhod PE
Magnetic Resonance Imaging	MRI
Micro gram	µg
Micro liter	µL
Mili liter	mL
Molar	M
Molecular weight	MW
Molecular weight cut off	MWCO
Mononuclear phagocyte system	MPS
Nanometer	nm
Nanoparticle	NP
Near-infrared	NIR
Nephrogenic systemic fibrosis	NSF
N-hydroxysuccinimide	NHS
Phosphate buffered saline	PBS
Poly(lactic-co-glycolic acid)	PLGA
Polydispersity index	PDI
Polyethylene glycol	PEG
Repetition time	TR
Reticuloendothelial system	RES
Rhodamine dye	RhB
Small extracellular vesicle	sEV
Transforming growth factor-β	TGF-β
Transmission Electron Micrograph	TEM
Transverse relaxation time	T_2
Transverse relaxivity	r_2
Transverse surface plasmon resonance	TSPR
Tumor microenvironment	TME
Tumor necrosis factor	TNF
Ultraviolet-visible spectroscopy	UV-Vis

Appendix E - List of Publications

1. **Rayamajhi, S**., & Aryal, S. (2020). Surface functionalization strategies of extracellular vesicles. **Journal of Materials Chemistry B**, 2020, 8, 4552-4569.

2. **Rayamajhi, S.**, Marasini, R., Nguyen, T. D., Plattner, B., Biller, D., & Aryal, S. (2020). Strategic reconstruction of macrophage-derived extracellular vesicles as a magnetic resonance imaging contrast agent. **Biomaterials Science**, 8, 2887-2904.

3. **Rayamajhi, S.**, Marchitto, J., Nguyen, T. D. T., Marasini, R., Celia, C., & Aryal, S. (2020). pH-responsive cationic liposome for endosomal escape mediated drug delivery. **Colloids and Surfaces B: Biointerfaces**, 110804.

4. Nguyen, T. D., Marasini, R., **Rayamajhi, S**., Aparicio, C., Biller, D., & Aryal, S. (2020). Erythrocyte membrane concealed paramagnetic polymeric nanoparticle for contrast-enhanced magnetic resonance imaging. **Nanoscale**, 12 (6), 4137-4149.

5. Marasini, R., Nguyen, T. D. T., **Rayamajhi, S**., & Aryal, S. (2020). Synthesis and characterization of a tumor-seeking LyP-1 peptide integrated lipid–polymer composite nanoparticle. **Materials Advances**, 1, 469-480.

6. **Rayamajhi, S**., Nguyen, T. D. T., Marasini, R., & Aryal, S. (2019). Macrophage-derived exosome-mimetic hybrid vesicles for tumor targeted drug delivery. **Acta Biomaterialia**, 94, 482-494.

Appendix F - Copyright permissions

1) Chapter 2 is a whole article reproduction from Rayamajhi, S., & Aryal, S. (2020). Surface functionalization strategies of extracellular vesicles. Journal of Materials Chemistry B, 8, 4552- Reproduced by permission of The Royal Society of Chemistry.

Surface functionalization strategies of extracellular vesicles

S. Rayamajhi and S. Aryal, *J. Mater. Chem. B*, 2020, **8**, 4552
DOI: 10.1039/D0TB00744G

2) Chapter 3 is a full article reproduction from Rayamajhi, S., Marchitto, J., Nguyen, T. D. T., Marasini, R., Celia, C., & Aryal, S. (2020). pH-responsive cationic liposome for endosomal escape mediated drug delivery. Colloids and Surfaces B: Biointerfaces, 188, 110804. (Permission not required as state below)

3) Chapter 4 is a full article reproduction from Rayamajhi, S., Nguyen, T. D. T., Marasini, R., & Aryal, S. (2019). Macrophage-derived exosome-mimetic hybrid vesicles for tumor targeted drug delivery. Acta biomaterialia, 94, 482-494. (Permission not required as state below)

4) Chapter 5 is a full article reproduction from Rayamajhi, S., Marasini, R., Nguyen, T. D. T., Plattner, B. L., Biller, D., & Aryal, S. (2020). Strategic reconstruction of macrophage-derived extracellular vesicles as a magnetic resonance imaging contrast agent. Biomaterials Science, 8, 2887- Reproduced by permission of The Royal Society of Chemistry.

Strategic reconstruction of macrophage-derived extracellular vesicles as a magnetic resonance imaging contrast agent

S. Rayamajhi, R. Marasini, T. D. T. Nguyen, B. L. Plattner, D. Biller and S. Aryal, *Biomater. Sci.*, 2020, **8**, 2887
DOI: 10.1039/D0BM00128G